Independent and joint multifractal characterization of atmospheric variability in real and controlled environments

Jerry Jose

École des Ponts ParisTech

THÈSE DE DOCTORAT

de l'École des Ponts ParisTech

Independent and joint multifractal characterization of atmospheric variability in real and controlled environments

Caractérisation multifractale indépendante et conjointe de la variabilité atmosphérique en environnement réel et contrôlé

École doctorale N° 531, Sciences, Ingénierie et Environnement (SIE)

Spécialité : Sciences et Techniques de l'Environnement

Thèse préparée au sein des laboratoires HM&Co et CEREA

Thèse soutenue le 22 Mars 2023 , par

Jerry JOSE

Composition du jury :

Marie-Claire TEN VELDHUIS Professeure, Delft University of Technology	Rapporteur
Martin, OBLIGADO Professeur associé, Université Grenoble Alpes	Rapporteur
Li-Pen, WANG Professeur associé, National Taiwan University	*Examinateur*
Denis, MARO Directeur de recherche, Institut de radioprotection et de sûreté nucléaire	*Examinateur*
Ioulia, TCHIGUIRINSKAIA Directrice de Recherche, École des Ponts ParisTech	*Examinatrice*
Daniel, SCHERTZER Professeur, École des Ponts ParisTech	*Directeur de thèse*
Auguste, GIRES Professeur associé, École des Ponts ParisTech	*Co-encadrant de thèse*
Yelva, ROUSTAN Professeur associé, École des Ponts ParisTech	*Co-encadrant de thèse*

Independent and joint multifractal characterization of atmospheric variability in real and controlled environments

Jerry Jose

HM&Co, Hydrology Meteorology & Complexity Laboratory

CEREA, Centre d'Enseignement et de Recherche en Environnement Atmosphérique

École des Ponts ParisTech

Acknowledgements:-

Author greatly acknowledges École des Ponts ParisTech for granting the interlab thesis scholarship that enabled this work. Partial financial support and access to instrumentation facilities from ANR JCJC RW-Turb project (ANR-19-CE05-0022-01) is acknowledged. Access to sense-city experimental facilities and support from the IFSTTAR and Université Gustave Eiffel team, are also acknowledged.

Abstract.

Atmospheric fields exhibit extreme variability over a wide range of spatial and temporal scales; they are also intermittent, which means that their activity is often concentrated at smaller and smaller scales. Conventional statistical tools fall short in capturing this and detecting extremes. However, the characterization of geophysical fields with their underlying complexities and correlations is ever important in prediction, modelling and understanding the weather conditions we live in, which is even more relevant now in the context of climate change.

The heterogeneous properties of atmospheric fields come form the governing non-linear equations of turbulence (Navier-Stokes), which still remains an unsolved problem regardless of its ubiquitousness. By using the concept of multiplicative cascades, it is possible to statistically reproduce the symmetries of said equations for geophysical fields; and multifractal tools expand upon this for characterizing the variability across scales by assuming same elementary process at each scale. In this dissertation, the scale invariant framework of UM, and the derived analysis technique of Joint Multifractals (JMF) are used for studying various fields in a two folded way – by examining the fields individually, and jointly, in real and controlled situations. The fields are studied in four focus areas: rainfall and kinetic energy, rainfall and wind, temperature and humidity, and rainfall and particles.

Using UM, rainfall intensity and rainfall kinetic energy (at TARANIS observatory, ENPC) are studied and a scale invariant relationship is postulated that doesn't rely on any assumptions of drop size distribution. This equation is backed by theoretical formulation and is shown to provide reliable estimates on par with commonly used equations in literature. Since kinetic energy requires relatively complex instrumentation, such a relation allows reliable retrieval of energy indirectly from commonly available precipitation data. This approach is further tested with rainfall simulations inside sense-city climate chamber using JMF.

The effect of rainfall on available wind power and power extracted by turbine are not well known. Towards this, high-resolution data from a meteorological mast (at pays d'Othe wind farm, France) are analysed along with turbine power in the purview of the Rainfall Wind Turbine or Turbulence (RW-Turb) project. JMF tools were used to study various directly measured and derived fields in RW-Turb according to rainy and dry conditions, and an overall increasing correlation with rainfall rate is observed, which is worth exploring in future.

The third focus area of temperature and humidity is explored partly with RW-Turb project and partly with sense-city climate chamber. A few known days (rainy and dry) were simulated inside sense-city in Descartes campus where ENPC is, for mimicking temperature and pressure variation observed in real conditions. Using JMF, the joint correlation between the fields in real and simulated conditions is evaluated, with efforts to account for the gap in estimation.

For the fourth focus area, aerosol concentration (nm and μm) from Cherbourg-Octeville, France was analysed alongside rain measurements for understanding scavenging of atmospheric particles by rainfall (below cloud scavenging). Preliminary analysis showed multifractal behaviour; this is of specific interest since the concentrations do not always follow the expected decreasing trend with rainfall. Along with this, multifractal properties of light attenuation by aerosols and their implications in atmospheric visibility are also studied using UM framework.

Using the various results obtained, the unifying aspect of atmospheric fields - extreme variability, intermittency and scale invariance are illustrated. Through analysis of observational and controlled data, and numerical simulations, the utility of UM in trend detection, simulations and predictions are also commented on.

keywords: atmospheric variability, multifractals, joint multifractals, precipitation, wind energy

Résumé

Les champs atmosphériques présentent une variabilité extrême sur une large gamme d'échelles spatiales et temporelles. Ils sont également intermittents, ce qui signifie que leur activité est souvent concentrée à des échelles de plus en plus petites. La caractérisation des champs géophysiques avec leurs complexités et corrélations sous-jacentes est toujours cruciale dans la compréhension, la modélisation et la prévision des conditions météorologiques dans lesquelles nous vivons, ce qui est de plus en plus important, notamment dans le contexte du changement climatique.

L'hétérogénéité des champs atmosphériques vient des équations non linéaires qui régissent la turbulence (Navier-Stokes), et qui reste d'ailleurs un problème non résolu en dépit de son caractère ubiquitaire. En utilisant le concept de cascades multiplicatives, il est possible de reproduire statistiquement les symétries desdites équations pour des champs géophysiques ; et les outils multifractals étendent cela pour caractériser la variabilité à travers les échelles en supposant les mêmes processus élémentaires à chaque échelle. Dans cette thèse, le cadre des Multifractals Universels UM et les techniques d'analyse multifractales conjointes (JMF) sont utilisés pour étudier divers champs de manière double - en examinant d'abord les champs individuellement, puis conjointement pour caractériser leur corrélation à travers les échelles, en situations réelles et contrôlées. Les champs sont étudiés selon quatre axes : pluie et énergie cinétique, pluie et vent, température et humidité, pluie et particules.

À l'aide des UM, le taux de pluie et l'énergie cinétique des précipitations sont étudiées, et une relation invariante d'échelle est établie, qui ne repose sur aucune hypothèse de distribution de la taille des gouttes. Cette équation est étayée par une formulation théorique et s'avère fournir des estimations fiables comparables aux équations couramment utilisées dans la littérature. Cette approche est ensuite testée avec des simulations de précipitations à l'intérieur de sense-city à l'aide des JMF.

L'effet des précipitations sur la puissance éolienne disponible et la puissance extraite par les éoliennes n'est pas bien connu. Dans ce but, des données à haute résolution issues d'un mât météorologique (ferme éolienne des Pays d'Othe, France) ainsi que la puissance produite par les éoliennes sont analysées dans le cadre du projet Rainfall Wind Turbine ou Turbulence (RW-Turb). Les outils JMF ont été utilisés pour étudier divers champs directement mesurés ou reconstitués et une corrélation globale plus forte avec l'accroissement du taux de précipitation est observée.

Le troisième volet de cette thèse est exploré en partie avec le projet RW-Turb et en partie avec sense-city. Quelques jours connus (pluvieux et secs) ont été simulés à l'intérieur de la chambre climatique sense-city du campus Descartes où se trouve l'ENPC, pour reproduire les variations de température et d'humidité observées en conditions réelles. À l'aide de JMF, la corrélation à travers les échelles entre les champs en conditions réelles et simulées est évaluée, avec des efforts pour

tenir compte des écarts d'estimation.

Pour le quatrième volet, les données de concentration de particules d'aérosols de Cherbourg-Octeville, en France, ont été analysées, parallèlement aux mesures de pluie. L'analyse préliminaire effectuée sur diverses classes de particules (nm et μm) montre comportement multifractal. Les propriétés multifractales de l'atténuation de la lumière par les aérosols et leurs implications dans la visibilité atmosphérique sont également été étudiées avec le cadre UM.

A partir des différents résultats obtenus, les aspects unificateurs des champs atmosphériques, à savoir l'extrême variabilité, l'intermittence et l'invariance d'échelle sont illustrés. Grâce à l'analyse des données en conditions réelles et contrôlées, et des simulations numériques, l'utilité des UM dans la détection des tendances, les simulations et les prévisions sont également commentées.

Mots clés: variabilité atmosphérique ; multifractales ; multifractales conjointes ; précipitations ; l'énergie éolienne

Contents

List of Figures

List of Tables

Introduction.

'Climate is what you expect, weather is what you get'. This famous aphorism, often attributed to Mark Twain, is losing relevance in the current context of climate change, and we are often left with a reality far from our long-term as well as short-term expectations. According to the WMO, the past 8 years are on track to be the eight warmest years on record (WMO et al., 2022). In terms of extreme events and their occurrence, climate change is constantly found to be the major cause for aggravated numbers. For example, as per World Weather Attribution's research, climate change made the 2019 European heatwave as much as 100 times more likely (WWA, 2019). According to IPCC AR6, cities are often hotspots for climate extremes due to their concentration of population and infrastructure in one location (Masson-Delmotte et al., 2021), and globally 68% of people are projected to be living in urban areas by United Nations (UN, 2019). Understanding climate patterns and variability has been always important because of its local as well as global impact on our health, and socio-economic progress (Hansen et al., 2006; Sinha et al., 2015); and with rapid urbanization and increasing impacts of climate change, it is now all the more critical.

Characterizing climate is difficult because of the complex interactions involved in the atmosphere between various interrelated processes and their extreme spatiotemporal variability over a wide range of scales. Geophysical fields also exhibit strong intermittency, which means that their activity is often concentrated at smaller and smaller scales. Analysis of climate trends can only reveal overall variation within a specific period of time and doesn't fully capture the complex small-scale variability and intermittency, and extremes of the process. Understanding this complexity is important in safely predicting and modelling weather and climate phenomenon, which has implications for agriculture, water management, air quality and human health, renewable energy production, sustainable urbanization et cetera (Holleman et al., 2020; Cristiano et al., 2017). Against this backdrop, in this dissertation, we aim towards characterizing multiple atmospheric fields and their correlation using long term high-resolution data and numerical simulations. The studied fields are selected from various application areas of interest, broadly following three UN Sustainable Development Goals (SDG) - climate action, sustainable cities and communities, and affordable and clean energy (Sachs et al., 2022). The overarching objective is to characterize various atmospheric fields in a scale invariant way, along with their small scale variability and intermittency, and coupling with other fields they interact with. This information is then used to quantify the gap between the behaviour of fields in real and controlled environments, and to account for measurement limitations in statistical analysis.

The heterogeneous properties of atmospheric fields come from the governing non-linear equations of turbulence (Navier-Stokes), which still remains an unsolved problem regardless of its ubiquitousness. By using the concept of multiplicative cascades, it is possible to statistically reproduce the symmetries of said equations for geophysical fields and utilize the scaling properties to understand long range memories. Multifractal tools, and specifically the widely used framework of

Universal Multifractals (UM) utilize these concepts and enable the characterization of fields by assigning scale invariant singularities to intensities across various scales. Multifractal analysis is often performed on various fields individually; here the framework of UM and the derived analysis technique of Joint Multifractals (JMF) are used for studying various fields individually and in correlation. This is done in real and controlled conditions with the previously stated objectives - analyzing the fields individually, and along with the fields they might be correlated with. For studying controlled environments, simulations inside the climate chamber of sense-city and data from a functional wind farm are used. The various fields studied here are precipitation or rain rate, rainfall kinetic energy, extinction coefficient of atmospheric particles, wind velocity, wind power available, power produced by wind turbines, air density, temperature, humidity and aerosol particle concentration. These fields are studied in four focus areas:

- rainfall and kinetic energy,
- rainfall and wind,
- temperature and humidity, and
- rainfall and particles.

The thesis is organized into three chapters, and the fields mentioned along with their instrumentation overlaps throughout the research. In the first chapter, the details of various data sets used for research are introduced with details of measurement campaigns and instrumentation. The tools used for analysis are presented thereafter with their need and context for the application. The various multifractals tools, notably UM and JMF are also illustrated with various samples from the data sets.

The second chapter concerns the individual analysis of atmospheric fields, and the first and fourth focus areas are addressed there specifically. Understanding rainfall as a single parameter (as usually done in $\mathrm{mm\,h^{-1}}$) doesn't capture the complexity of the process as the spatio temporal spread of drop size distribution and their velocities have far-ranging effects on the kinetic energy of rain and in turn in various forms of erosion in soil and structures. Using UM, rainfall intensity and rainfall kinetic energy are studied here from data in Paris region and a scale invariant relationship is developed which doesn't rely on the ad hoc assumption of gamma distribution; the relationship is also shown to provide reliable results on par with commonly used equations in literature. In the second part of this chapter, aerosol particles are examined individually in the context of atmospheric visibility. More precisely, light attenuation by aerosol particles is considered as the objective field over subjectively measured atmospheric visibility which is often represented as MOR (Meteorological observable range). Here we argue the usage of the extinction coefficient as the parameter for simulating visibility since the usage of MOR comes with an inherent statistical bias thanks to the instrumental and application limits. This is illustrated through observations and numerical

simulations.

The third chapter deals with joint analysis of all focus areas and is presented in three sub sections. The first sub section deals with the small scale variations in wind turbulence and its coupling with rainfall, using data from a meteorological mast in a functional wind farm at pays d'Othe, 110 km southeast of Paris. UM analysis during rain and dry conditions revealed an increasing variability in wind power during rain; and within rain events, JMF revealed an overall increasing correlation between wind power available (also for wind velocity and air density) and rainfall rate. Here, the biases in statistical analysis of actual power production by turbines and the actual sampling resolution of various instruments relevant for studying variability are identified in the framework of UM using real data and numerical simulations. The second sub section deals with simulated rainfall and climatic conditions inside the climate chamber of sense-city; this part also aims to check the efficiency of controlled environments in reproducing the small scale variability of atmospheric fields. Using simulated rainfall experimentation inside sense-city, the validity of the rainfall - kinetic energy UM relation developed in chapter 1 is tested for artificial rain. The theoretical framework is also used to quantify the gap between rainfall simulations inside the chamber (which is known to underestimate kinetic energy) and real rain outside. Variations in temperature and humidity are also studied here, with real data and sense-city simulations. Few known days are simulated inside the chamber and the efficiency of reproduction is examined with JMF framework. The last sub section deals with rainfall and particles, where size resolved aerosol concentrations (in nm and µm ranges) are examined alongside rainfall measurements. Preliminary analysis on various particle classes showed multifractal behaviour; this is of specific interest since the evolution of concentration during scavenging is influenced by many different processes and not just rainfall, and UM can be used for analysing the complexity.

Using the framework of UM and JMF, various geophysical fields are studied individually and jointly here. The biases encountered in statistical analysis and the importance of identifying the real underlying field are illustrated. The overall results of the dissertation open up discussions on the need for understanding atmospheric fields in relation to their coupling with related fields.

1. Data and Methods

In this chapter, all the data-sets used for analysis are introduced along with the methodologies employed for their analysis. In first part, section 1.1, the make and functioning of various instruments are introduced and explained in detail. They mainly consist of long-term and ongoing high-resolution measurements from optical disdrometers, meteorological stations and 3D sonic anemometers at three locations in France, which for brevity, can be grouped into two groups - observatories inside ENPC campus and campaigns outside the campus. Campus bound instrumentation includes TARANIS (measurement station at the top of University building) and Sense-city climate chamber. Outside campaigns consists of RW-Turb (on a meteorological mast in an operational wind farm and aerosol particle measurement by IRSN. The type of instruments overlap at the two set of locations, and similar data is analyzed towards different campaign objectives.

The intention of this chapter is to compile all the data that was analyzed along the course of various studies, and use them to illustrate the methodology employed. This is done in second part, section 1.1. The second part is also aimed at introducing fractals and multifractals, and how they are used in understanding extremely variable geophysical fields across various scales. The methodologies are illustrated by using portions of data from section 1.1.

1.1. Data collection and instrumentation

Fig. 1.1 shows the overall location of various observatories and measurement campaigns used in this thesis; details are expanded in upcoming sub sections. They employ instrumentation towards high-resolution measurement of size resolved parameters (rain and particles) along with other associated atmospheric fields (wind, temperature, relative humidity, light attenuation etc.).

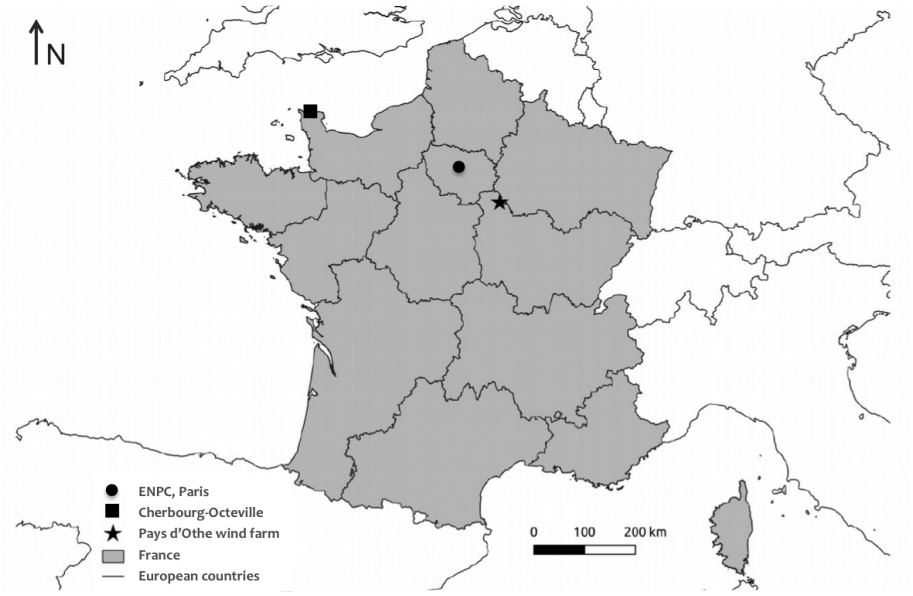

Figure 1.1: Approximate location of data-set/campaigns inside and outside ENPC campus.

1.1.1. Disdrometer data at TARANIS observatory

1.1.1.1 Location and overview

Disdrometers provide real time measurement of rain along with the rain drop size distribution according to diameter and velocity of falling drops; they are often associated with other meteorological sensors such as visibility, temperature, relative humidity etc. At TARANIS observatory, three optical disdrometers are continuously monitoring data in natural conditions; this has been used many times throughout the research presented here. TARANIS observatory (exTreme and multi-scAle RAiNdrop parIS observatory, Gires et al., 2018) is part of the Fresnel Platform of École des Ponts ParisTech (*https://hmco.enpc.fr/Page/Fresnel-Platform/en*); and is operated by Hydrology Meteorology and Complexity laboratory of École des Ponts ParisTech (HM&Co-ENPC). The intention here is to completely characterize the rain (which is often expressed as a singular parameter in $\mathrm{mm\,h^{-1}}$) with its full complexity considering the temporal variability in drop size distribution (DSD). The location of the observatory and picture of the disdrometers are given in Fig. 1.2 and Fig. 1.3.

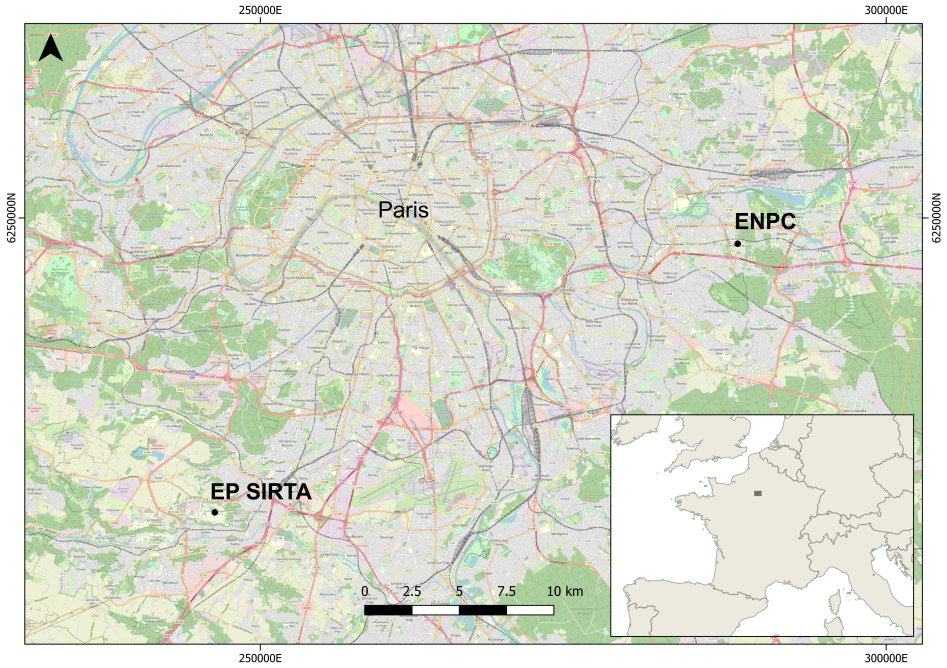

Figure 1.2: Location of TARANIS observatory with respect to Paris region (basemap from openstreetmap.org); ENPC shows the permanent location of the disdrometers and EP SIRTA shows the brief time for which they were moved as part of a national measurement campaign (relevant for section 2.1).

1.1.1.2 Overview of instrument functioning and outputs

The three optical disdrometers available here are two OTT Parsivel[2] (see Battaglia et al., 2010 or the device documentation OTT, 2014) and one PWS 100 (see Ellis et al., 2006 or the device documentation Campbell-Scientific-Ltd, 2012).

Figure 1.3: Disdrometers devices on TARANIS observatory (*https://hmco.enpc.fr/portfolio-archive/taranis-observatory/*); two OTT Parsivel^2 devices can be seen on the same base arranged perpendicular to each other, PWS 100 is in the background (in white colour) and can be identified by its receptors positioned at different angles to transmitter (pictures: ©Jerry Jose).

The OTT Parsivel^2 are occlusion based devices with a transmitter that creates laser sheet and an intercepting receiver directly aligned with it. The size (equivolumic diameter) and fall velocity are assessed from changes (decrease in amplitude of intensity and duration of the decrease) in received laser intensity due to the passing of rainfall drops through a sampling area of 54 cm^2. An ellipsoidal shape model with a standard relation between the axis ratio and the equivolumic diameter are assumed for drops in the process.

The PWS 100 consists of a transmitter that generates four horizontal parallel laser sheets, and two receptors which are not aligned with the transmitter. The signal received by each receptor corresponds to the light refracted by drops and contains four consecutive peaks associated with each laser sheet. From the delay between those peaks, fall velocity and diameter of the drops are estimated. PWS100 has a sampling area of 40 cm^2. Computations assuming spherical shape of droplets are performed here with a later correction for oblateness before final data generation (Gires et al., 2017a).

Both disdrometers have a collection time step of 30 s and provide main output as a matrix containing the number of drops ($n_{i,j}$) recorded during the time step Δt according to classes of equivolumic diameter (index i defined by a centre D_i and a width ΔD_i both expressed in mm)

and fall velocity (index j and defined by a centre v_j and a width Δv_j, both expressed in ms^{-1}). For Parsivel[2] there are 32 classes of ΔD_i from 0.062 mm to 24.5 mm and Δv_j from $0.05\,\mathrm{m\,s}^{-1}$ to $20.8\,\mathrm{m\,s}^{-1}$. And for PWS the same ranges from 0.05 to 27.2 (ΔD_i, mm) and 0.05 to 27.2 (Δv_j, $\mathrm{m\,s}^{-1}$) in 34 classes. Width of diameter and velocity classes are not similar for all classes, as they are designed to be more and more refined towards smaller values.

From the raw matrix, the drop size distribution (DSD, denoted $N(D)$) of rainfall can be obtained ($\mathrm{m}^{-3}\,\mathrm{mm}^{-1}$) which represents the number of drops per unit volume within each diameter class (within an equivolumic diameter between D_i and D_{i+1}). A binned or discrete DSD is used here according to the instrument specifications:

$$N(D_i) = \frac{1}{S_{eff}(D_i)\Delta D_i \Delta t} \sum_j \frac{n_{i,j}}{v_j} \tag{1}$$

where $S_{eff}(D_i)$ is the sampling area of disdrometer in mm^2 (which can be slightly adjusted according to drop size to account for side effects), Δt is the time step duration in hr and ρ_{wat} is the volumic mass of water ($10^3\,\mathrm{kg\,m}^{-3}$). Here $N(D_i)\Delta D_i$ gives the number of drops with a diameter in the class i per unit volume (in m^{-3}). The studied rainfall parameters - rain rate ($\mathrm{mm\,h}^{-1}$), and time specific kinetic energy ($\mathrm{J\,m}^{-2}\,\mathrm{h}^{-1}$) were obtained from raw matrix using following expression for each time step:

$$R = \frac{\pi}{6\Delta t} \sum_{i,j} \frac{n_{i,j} D_i^3}{S_{eff}(D_i)} \tag{2}$$

$$KE = \frac{\rho_{wat}\pi}{6\Delta t} \sum_{i,j} \frac{n_{i,j} D_i^3 v_j^2}{S_{eff}(D_i)} \tag{3}$$

The measured parameters - R, KE, and DSD are discussed in more details in section 2.1. Details of the devices, their functioning and data collection can be found in Gires et al. (2018). Interested readers are directed to *https://zenodo.org/record/1240168* (doi:10.5281/zenodo.1125582) where two month data from TARANIS is made available for public along with the raw files and scripts required for extracting the data. Daily overall information can be accessed through quicklooks of observatory page, latest calendar link can be accessed here: *https://hmco.enpc.fr/calendars/Calendars_Carnot_2/Calendar_Carnot_2.html*. Quicklook for a rainy day 27/10/2019 is shown in Fig. 1.4; this day was used as reference to mimic real conditions in sense-city (section 3.2.2). Temporal evolution of the number of rain drops according to various diameter class (D vs time with $\log N(D)$ in colour bar, middle left), velocity plots of drops (D vs V - renormalized plots as the parameters do not have the same bin size - with $\log N(D)$ in colour bar, middle right; solid line corresponds

to terminal fall velocity of drops for equivolumic diameter according to Lhermitte 1988), drop size distribution ($N(D)D^3$ vs D in lower left, here $N(D)$ is multiplied by D^3 to illustrate better the total volume of observed rainfall according to various drop diameters) for all three disdrometers can be seen alongside the evolution of rainfall (rainfall rate - upper left, cumulative rainfall depth - upper right) and temperature (bottom left). The temperature sensor for Parsivel^2 are very basic and does not fulfill meteorological standards (as seen in the T plot, bottom left); they are plotted here only for indication. And if required, temperature sensor from PWS at the same location is recommended; this is used in section 3.2.2.

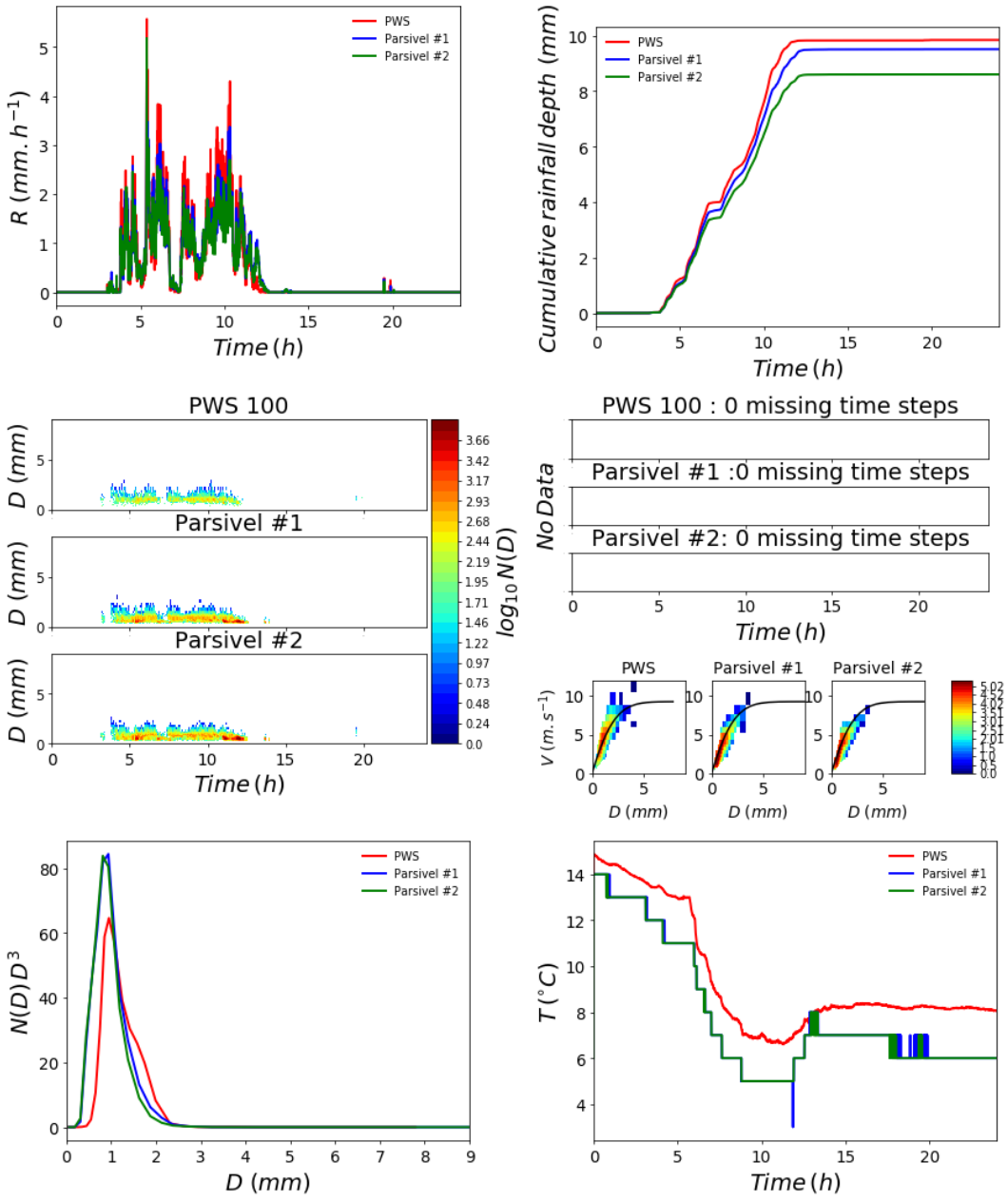

Figure 1.4: Quicklook of the disdrometer data available on 27 October 2019 (description of the plot can be found in the text)

1.1.1.3 Measurement campaigns

Though the data is being constantly measured at TARANIS (made available to public through daily quicklooks in the link mentioned before), for the scope of studies presented, Table 2.4 gives a brief outline of measurement campaign used in section 2.1. From November 2016 to September 2017 the instruments were moved to École Polytechnique (EP) on SIRTA (Site Instrumenté de

Recherche par Télédétection Atmosphérique) for a joint intensive measurement campaign over the Ile-de-France region. The aforementioned location is about 38 km away from ENPC towards south west of Paris. To summarise the data used from TARANIS (for section 2.1), the measurement campaigns involved two different types of optical disdrometers and data collected from two different locations of Paris region.

location	**start time**	**end time**
ENPC (1)	18 Jun 2013	10 Nov 2016
EP SIRTA	14 Nov 2016	20 Sep 2017
ENPC (2)	27 Dec 2017	31 Dec 2019

Table 1.1: Short description of the precipitation measurement campaign selected for section 2.1

Along with this, the data from TARANIS was also used to studying extinction coefficient in section 2.2, using the visibility sensor in PWS 100. The real condition measurements from the observatory was also utilized in simulating days inside the climate chamber, sense-city, in section 3.2.2. Same instruments were briefly moved inside sense-city to study the efficiency of simulated rain showers in the climate chamber; this is discussed in section 3.2.1.

1.1.2. Sense-city climate chamber

Sense-city is a climate chamber, funded by French Research Agency (ANR) and now managed by University Gustave Eiffel, which is designed for simulating specific weather conditions over fixed periods (*https://sense-city.ifsttar.fr/*). It spans over two separate territories of size 400 m^2 each (called mini-city or mini-ville: MV1 and MV2) with a vast array of micro - nano sensors and rainfall simulator available; this provides a unique opportunity to study preferred atmospheric conditions including solar conditions and rainfall. The mini-cities are engineered to monitor and study air, water, and soil pollution, and to test the performance of facilities and urban materials. Sense-city is easily visible as the 8 m height blue cube in Cité Descartes, inside ENPC campus (Fig. 1.5). The chamber was designed by IFSTTAR, L'Institut français des sciences et technologies de transports (*https://www.ifsttar.fr/*), which is now part of Gustave Eiffel University (*https://www.univ-gustave-eiffel.fr/*).

Figure 1.5: Sense-city chamber as viewed from the base of ENPC radar tower, Coriolis building can be seen in the background; a closer view of the chamber from parking lot is given in the inset (pictures: ©Jerry Jose). The location of ENPC is given in Fig. 1.2.

Sense-city houses an array of sensors and facilities for various applications mentioned before. Within the operational limit of sense-city, it is possible to simulate rainfall in two modes (so called 'light' $\approx$ 15-20 $\mathrm{mm\,h^{-1}}$ and 'heavy' $\approx$ 25-45 $\mathrm{mm\,h^{-1}}$), and to have desired atmospheric conditions including temperature (T, -10 °C to +40 °C) and relative humidity (RH, 30 % to 98 %) among other things. Inside the sense-city, the rainfall simulator covers an area of 25 $\mathrm{m^2}$, and the two rainfall modes are achieved (within a variation of 2 %) through 12 nozzles each located 8 m above chamber floor. In addition to these, sense-city also has provisions to simulate sun (with 30 laps of 2000), regulate the roof temperature of chamber, regulate rain temperature (+ 5 °C and 30 °C), and measure pollutants such as SO_2, CO_2 and NO_2. These were not used for the analysis presented here, which mainly consisted on simulation of rain, and T/RH evolution (see joint analysis in section 3.2). The sense-city facilities and sensors used in this thesis mainly involves the rain showers, temperature and humidity sensors. The sensors used here can be grouped into three sets according to their measuring frequency (ref Tab. 1.2). The meteo station at MV1 provides temperature, pressure, humidity, pressure, wind speed and direction, and rain rate at a measurement time step of 60 s. Along with this, chamber also houses separate sensors for chamber temperature (1 primary and 5 secondary), roof temperature (1 primary and 12 secondary), rain temperature (1 sensor), sun (1

sensor), and humidity (1 sensor), all at a finer measurement time step of 10 s. It also has 16 more temperature sensors (on 8 meteorological masts at two different heights - 0.5 m and 3 m) which monitors the temperature at 15 min frequency. However, not all of these selected sensors were used in the analysis; this is discussed in section 3.2.2.

No.	Sensor name	Measured field(s)	# sensors	unit	resolution
1	Rain flow	discharge	1	$mm\,h^{-1}$	10 s
2	Rain Temperature	T	5	°C	10 s
3	BIA_Humidity (primary)	RH	1	%	10 s
4	BIA_Temperature Chambre (one 1°, five 2°)	T	6	°C	10 s
5	Roof Temperature (one 1°, twelve 2°)	T	13	°C	10 s
7	Station-Meteo-MV1	T, P, RH, v	1	Pa, °C, %, $m\,s^{-1}$	60 s
8	Temperature-pt100 (on mast)	T	16	°C	15 min

Table 1.2: List of sense-city sensors that were used for simulations in section 3.2. T - temperature, P - pressure, RH - relative humidity, v - wind velocity, 1° - primary, 2° - secondary.

More information on operation of rain and sense-city's ability to simulate actual rainfall can be found in Gires et al. (2020a), where the simulated rain is examined drop size wise using disdrometers. For simulating T and RH, there exists a working window (the extend of values chamber can safely reproduce) which needs to be respected while programming the simulation time steps or 'ramps'. The programmable gradient of T and RH in 24 hours are $\pm$ 5°C and 5% respectively and while providing parameters to simulate, care should be taken for respecting the previously mentioned T/RH operational range. While simulating a known climatic situation, achieving the desired end values of T/RH in sense-city might take longer time than actual data as the chamber is limited by its smaller size, programming restrictions as well as the time required by soil and other inside components to dry/humidify or heat/cool. Hence, selecting the parameters for simulation is a trade off between time available and parameter values desired; this is discussed in more detail in section 3.2.2.

Three days were simulated inside sense-city following temperature and pressure measured from TARANIS observatory. The results are discussed in section 3.2.2 where the ability of sense-city to reproduce real conditions are evaluated using joint multifrctal framework. Previously, Gires et al. (2020a) used sense-city for measuring the simulated rainfall; this data was examined with intention for account for under reporting of rain drop kinetic energy in section 3.2.1.

1.1.3. RW - Turb project

1.1.3.1 Positioning and main objectives of the project

The effect of rainfall on wind and then in turn on wind turbine power production is not very well known; and in the ever growing economical shift towards renewable sources, understanding

the small scale spatio-temporal interactions between rainfall and wind is important for improving power production as well as their deployment. Rainfall Wind Turbine or Turbulence project (RW-Turb), a joint project involving University and industrial collaboration - École des Ponts (ENPC) and Boralex, a wind power producer, is designed towards tackling this lesser known issue. The project is funded by the French National Research Agency (ANR in French) and consists of high-resolution in-situ real time measurement of various hydro meteorological parameters along side produced power in a operational wind farm (through devices installed on a meteorological mast, Fig. 1.6 and Fig. 1.7). RW-Turb has a two fold approach - high resolution measurement campaign and joint multifractal analysis of associated fields (Gires et al., 2022), and numerical simulations of space time wind and torque using three modelling chains (Gago et al., 2022). Work presented here deals with the first part. More context on wind production and rainfall interactions, and complexity in their analysis are provided in section 3.1. The information provided below on instrumentation and data-set of RW-Turb are adapted from Gires et al. (2022), the data paper (that I co-authored) that details the project's measurement campaign along with required tools of analysis and 3 months of data that has been made publicly accessible.

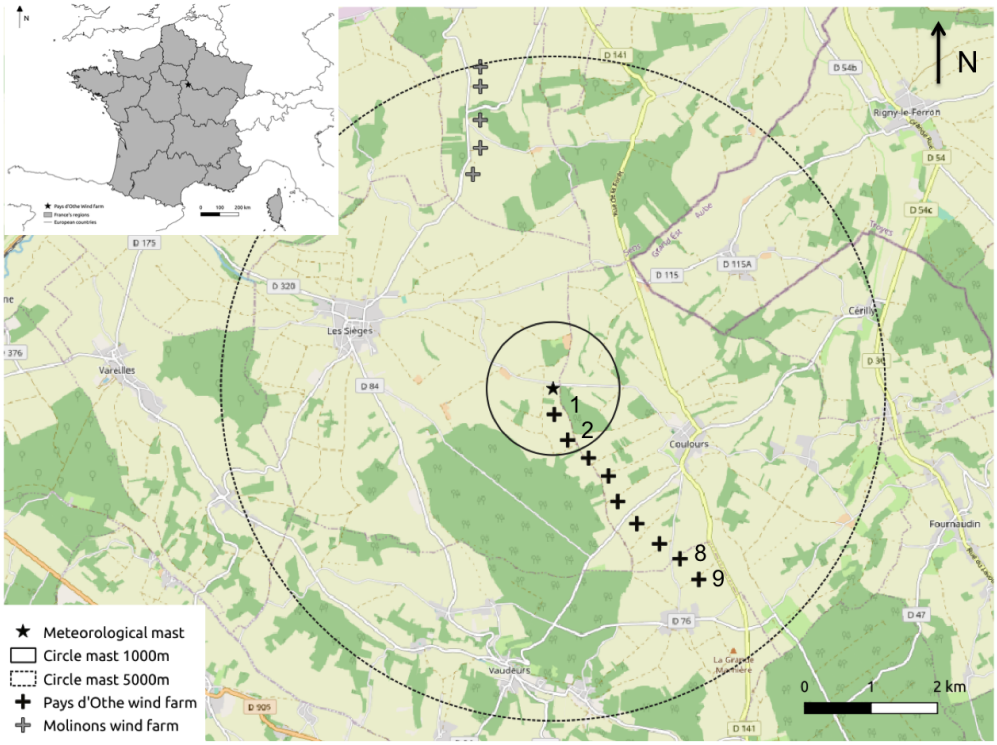

Figure 1.6: Location of the meteorological mast along with wind turbines at Pays d'Othe wind farm, adapted from Gires et al. (2022). Turbines managed by Boralex, the ones which were studied, are shown by their numbers - 1, 2, 8 and 9. Location of the wind farm with respect to France in inset.

Figure 1.6 shows the location of the meteorological mast (star in the middle) along with the

nine wind turbines of the Pays d'Othe wind farm (aligned South-East of it and within a 4 km radius, black vertical crosses). This wind farm is made of 9 wind turbines and is jointly operated by Boralex (*https://www.boralex.com/our-projects-and-sites/*) and JP Énergie Environnement (*https://pays-othe-89.parc-eolien-jpee.fr/*). The five turbines of the Molinons wind farm in the North are also visible within the 5 km radius (grey vertical crosses). It should also be noted that a small grove is located just South of the mast at roughly 160 m; a larger one is on the East at roughly 100 m. Nearby the mast (i.e. within the 1 km radius), there is a small slope in the North-South direction. The wind power data used for studies comes from four turbines by Boralex - 1 and 2 located closest to the mast, and 8 and 9 located at the farthest end. Fig. 1.6 shows a picture of the meteorological mast with various devices installed on it, the devices are managed by Hydrology, Meteorology, and Complexity laboratory of École des Ponts, HM&Co-ENPC). The mast consists of six high-resolution devices - two sets of 3D sonic anemometers (manufactured by Thies), disdrometers (OTT Parsivel^2, same as those in TARANIS) and two mini stations (manufactured by Thies) - at approximately 78 m (Location 1) and at 45 m (Location 2). Two raspberry pi computers, located in one of the boxes at roughly 10 m, collects data along with the 4G box enabling remote access (quicklooks made available in HM&Co website - *https://hmco.enpc.fr/calendars/Calendar_RW_Turb_wind_farm/Calendar_RW_Turb_wind_farm.html*). More photos of the mast and elevation map can be seen in Gires et al. (2022).

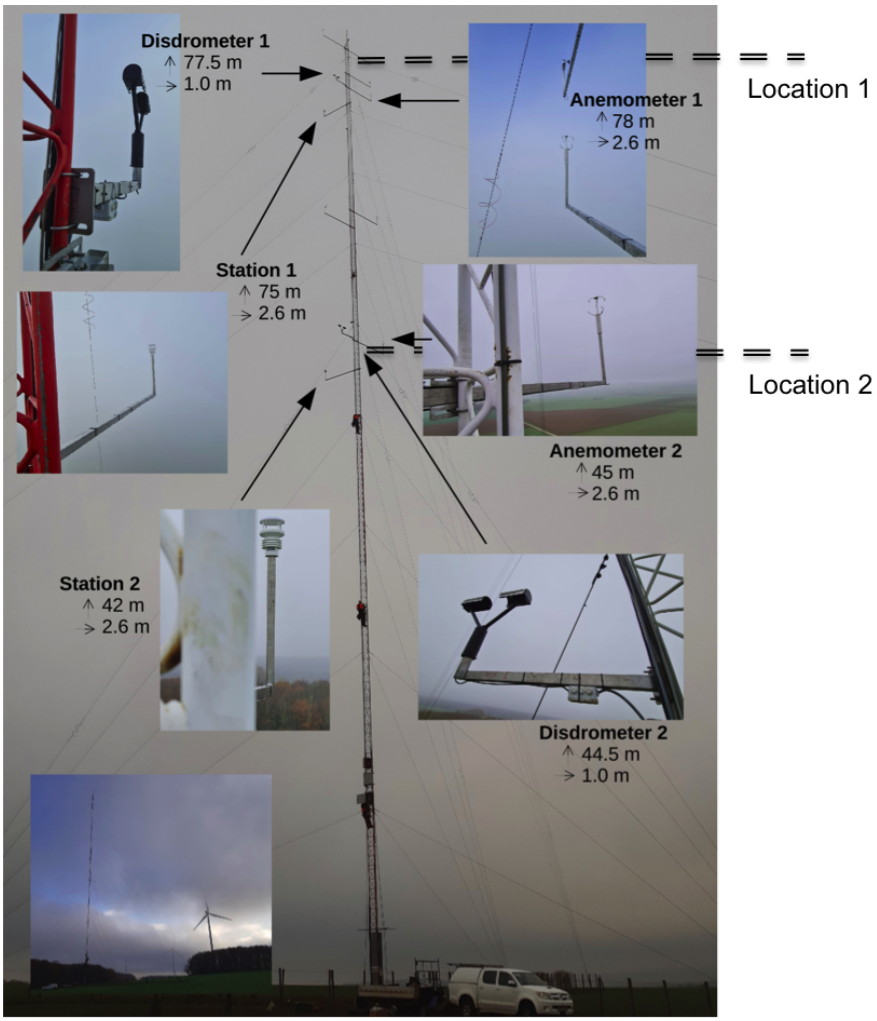

Figure 1.7: Summary of measurement devices on the meteorological mast, locations of set of devices are approximated as location 1 and location 2 for ease of discussion ; adapted from Gires et al. (2022). The position of the mast with respect to the closest turbine (Turbine 1) in inset.

1.1.3.2 Overview of instrument functioning and database

3D sonic anemometers and associated outputs

The 3D sonic anemometers used in this campaign are manufactured by ThiesCLIMA (ThiesCLIMA, 2013a). A 3D sonic anemometer is made of three pairs of transducers (acting as both transmitter and receiver) which measures the travel time of sound pulse between them. If L is the distance between two transducers, u_L the wind velocity along the corresponding axis, and travel times in either way is t_1 and t_2; we have $t_1 = L/(c+u_L)$ and $t_2 = L/(c-u_L)$, with c being the local speed of sound in the air; this yields:

$$u_L = \frac{L}{2}\left(\frac{1}{t_1} - \frac{1}{t_2}\right) \tag{4}$$

which does not depend on c. The wind velocity is assessed along the axis between each three pairs, enabling to reconstruct 3D wind.

It is also possible to estimate c from:

$$c = \frac{L}{2}\left(\frac{1}{t_1} + \frac{1}{t_2}\right) \tag{5}$$

Since c mainly depends on the local temperature T, the latter is derived using standard relationships assuming a dry air (virtual sonic temperature); with additional corrections, a corrected temperature accounting for relative humidity and pressure (see ThiesCLIMA, 2013a for more details) can be retrieved. The 3D anemometers in this campaign provides 3D wind measurement along with an estimate of temperature at a sampling rate of 100 Hz.

Meteorological stations and associated outputs

The two mini meteorological stations used here are from ThiesCLIMA (ThiesCLIMA, 2013b). They give access to the following meteorological parameters: wind velocity and direction, air temperature, relative humidity, precipitation and brightness. The wind information is obtained thanks to a 2D sonic anemometer made of two pairs of transducers positioned perpendicularly in relation to each other and functions similar to the 3D sonic anemometer explained before.

Built-in sensors are dedicated to measurement of air temperature and relative humidity, and measurement of pressure relies on a micro-electro-mechanical system; these are protected within a shelter. It also contains a doppler radar which measures the precipitation intensity; the rain rate is estimated from the signal reflected back by the hydrometeors while relying on strong assumptions of the DSD shape and the relation between size and velocity of drops. Station also has four photo sensors measuring brightness with spectral sensitivity curve tuned to the sensitivity of human eye, and a GPS sensor. The sampling rate for all the station parameters in this campaign is 1 Hz.

Disdrometers and associated outputs

The disdrometers used here are OTT Parsivel^2 disdrometers (OTT, 2014) whose functioning is already discussed with TARANIS dataset (section 1.1.1). The data functioning of OTT Parsivel^2 disdrometers and retrieval of data is discussed in more detail in Gires et al. (2018). The disdrometers provide data at a sampling rate of 30 s.

It is worth noting here this difference between rain rate provided by meteorological station, which is a single quantity, and the one obtained from disdrometer which integrated information

across an array of hydrometeors classes and their fall velocities. The difference in estimation of rain between disdrometers and station at RW-Turb is examined in detail at Appendix B.1. Among other comparisons, examples with rain gauges can be found in Miriovsky et al. (2004), Krajewski et al. (2006), Frasson et al. (2011) or Thurai et al. (2011), and many others.

Wind Turbines and associated outputs

Four Vestas V-90 (marked in Fig.1.6) are available in the framework of RW-Turb project from the Pays d'Othe wind farm, two are closer to the meteorological mat and two are farther from it ($\approx$ 3.5 km from mast). Technical and working information of the turbine can be found in Vestas Wind Systems A/S (2023).

The turbines have a rated power of 2.0 MW which is pitch regulated with variable speed. The hub height of the turbines is 80 m, this is closer to the vertical height of upper set of devices on the mast (location 1, $\approx$ 78 m). The turbines has a cut-in wind speed of $4\,\mathrm{m\,s^{-1}}$ and a rated wind speed of $12\,\mathrm{m\,s^{-1}}$; this can be see on power curves in quicklook (Fig. 1.8: last column, second and last row) where the turbine is seen to register power at cut-in speed and maintain the rated power of 2000 kW after rated wind speed. The cut out speed of Turbine is at $25\,\mathrm{m\,s^{-1}}$ (the extreme x axis point of power curves); this is the speed at which turbine stops registering power. Generally the turbines register positive values of wind power, however, when the power retrieved from wind is less than that is required for working of turbine it registers negative power. These can be seen in the power curves as clusters around 0. Along with the wind power, turbine also provides information of local velocity which is used for internal regulation; this is used for plotting power curves in Fig. 1.8. In this campaign the turbine data is available at a sampling frequency of 15 s.

Interested readers are directed to *https://zenodo.org/record/5801900* (doi: 10.5281/zenodo.5801900) where three month long data from RW-Turb is made available for public along with the raw files and scripts required for extracting the data (Gires et al., 2022, refer for detailed description of database). Daily overall information can be accessed through quicklooks at the project's web page as mentioned before, *https://hmco.enpc.fr/portfolio-archive/rw-turb/*. Quicklook for a rainy day (08/04/2022) is shown in Fig. 1.8; this day is also used as reference for testing joint multifractal framework in section 1.2.3). The quicklook here is similar to the one discussed at TARANIS with added information of wind and relative humidity, and pressure. Temporal evolution of rain rate, drop size, dropsize - velocity curve, and DSD curve highlighting influence of raindrop volume are shown in first column (in that order). Except for the first panel (Cumulative rainfall depth vs. time, as discussed for TARANIS), the second column deals with wind velocity. Total horizontal wind ($\sqrt{u_x^2+u_z^2}$ vs. time at one min time step) for anemometers and stations are shown in second panel of this column. The last two panels shows wind rose (using the horizontal wind measurements - u_x and u_y) and vertical wind (u_z at one min time step) from the anemometers. The missing time steps for all the devices for the day are shown in third column; the remaining panels of third column

consists of temporal evolution of temperature, pressure and relative humidity from station (also temperature from anemometer as discussed). The last column consists of temporal evolution and power curves (power vs. velocity, theoretical curve in red) for Turbine 1 and Turbine 9 (the closest and the farthest from the mast shown for illustration). The turbine data is not available in online quicklook or in datapaper since it is private information owned by Boralex; more on analysis of turbine data can be seen in section 3.1.

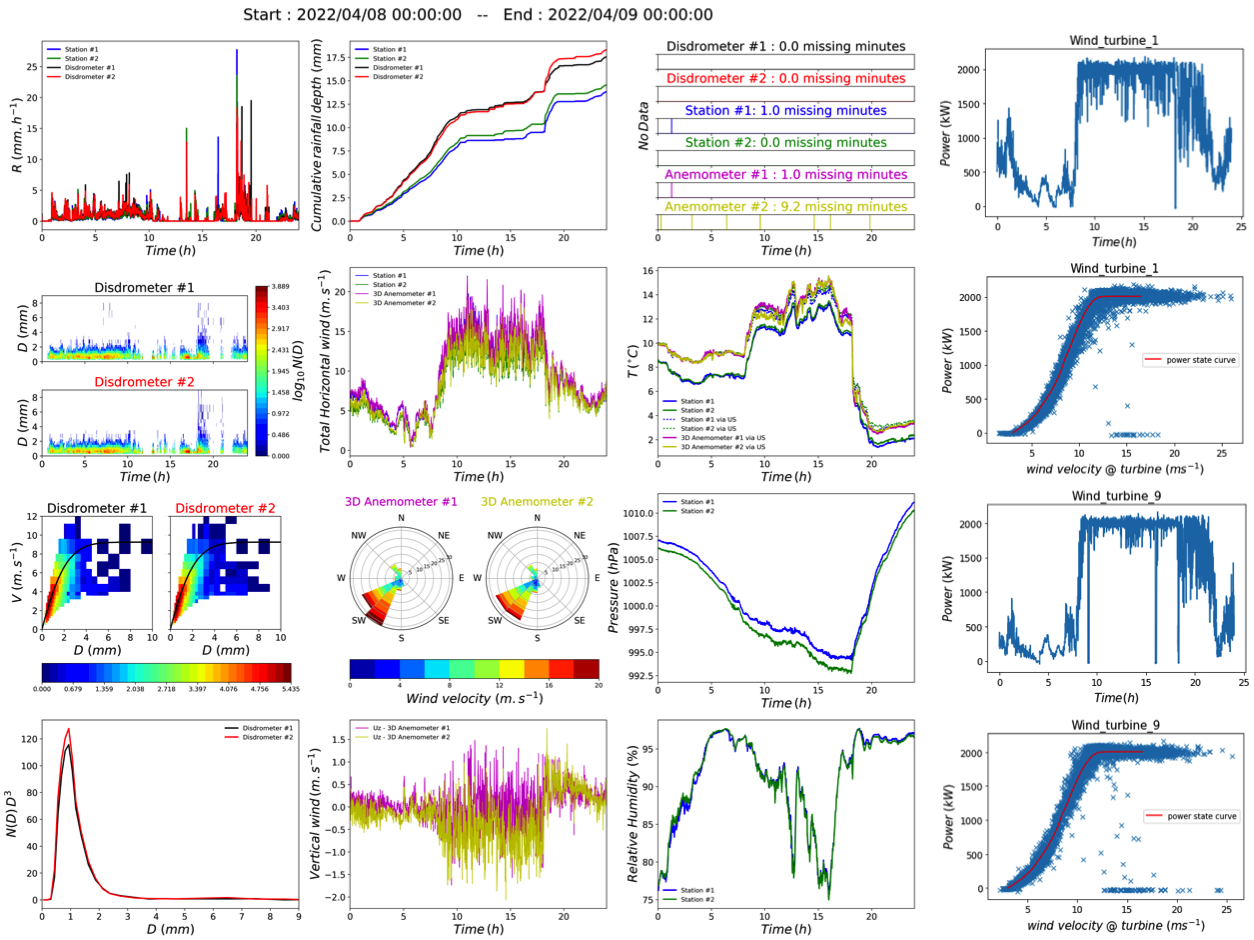

Figure 1.8: Quicklook of the RW-Turb data on 08 April 2022. Turbine power shown in right most column is proprietary of Boralex, this is not available in the public database of RW-Turb (online quicklook). Description of the plots can be found in the text.

The data from RW-Turb is used for joint analysis in section 3.1. Even though the instruments are ideally giving very high resolution data, the actual sampling resolution relevant for studying their variability seems to be a bit less; this is discussed using the framework of universal multifractals in section 1.2.2.4. As briefly mentioned previously, the data is also used for illustrating joint multifractal framework in section 1.2.3.1. A comparison study between rain measurement by disdrometers and stations at RW-Turb was co-supervised during PhD research, results from this

work is discussed in Appendix B.1.

1.1.4. Aerosol measurement campaign - IRSN database

1.1.4.1 Measurement campaign

Rain scavenging of below-cloud aerosol particles is known to be the most efficient pollutant sink in atmosphere. Since distribution of various aerosol species is a function of particle size, and as this interaction depends on particle size of scavenging rain drop, it is important to understand the microphysical interaction between both. Towards this, data was used from experimental station at the city of Cherbourg-Octeville, France (49°38.078'N, 1°38.757'W, 70 m above sea level) from 01/11/2010 to 12/03/2011. The station is managed by Institut de Radioprotection et de Sûreté Nucléaire (IRSN) and is part of INOGEV research program funded by French National Research Agency. The station provides data from simultaneous measurement of rainfall, aerosol particle concentration and distribution (in nanometer and micrometer size ranges) and wind velocity; this enables analysis on aerosol concentration variation during rain episodes.

Figure 1.9: a) Location of measurement campaign, b) disdrometer, c) Sonic anemometer and d) Scanning Mobility Particle Sizer (SMPS); images from (Laguionie et al., 2011)

1.1.4.2 Instruments and data set

The rainfall intensity was measured using OTT parsivel disdrometer and information on wind velocity and temperature was obtained using a sonic anemometer (Refer section 1.1.1 and section 1.1.3 for information on functioning of these devices). Information on rainfall drop size distribution was not available for this campaign. For measuring aerosol particle concentration and size distribution, a Scanning Mobility Particle Sizer (SMPS) coupled with Aerodynamic Particle Sizer (APS) was used. A general overview of campaign location and instrumentation is given in table 1.3 and Fig. 1.9. SMPS measures size particle size distribution in the range 1 nm to 1 µm using differential mobility analysis where basically particle size is obtained by drifting airborne particles according to their electrical mobility using an electric field (see brochure TSI-SMPS for more information). For particles above 1 µm, an Aerosol Particle Sizer (APS) was used which provides aerodynamic

measurements from 0.5 µm to 20 µm from particle light scattering (see brochure TSI-APS for more information).

Instruments	**data used**	**resolution**	**units**
Disdrometer	Rain rate	1 min	$\mathrm{mm.h^{-1}}$
Sonic anemometer	Wind velocity (U, V & W), Temperature	10 Hz	$\mathrm{m\,s^{-1}}$, °C
SMPS	Size distribution (14.6 nm to 478.3 nm in 98 granulometric classes), Total concentration	1 min	$\mathrm{d}N/\mathrm{d}\log D_p$, $\#\mathrm{cm^{-3}}$
APS	Size distribution (0.523 µm to 19.81 µm in 52 granulometric classes), Total concentration	1 min	$\mathrm{d}N/\mathrm{d}\log D_p$, $\#\mathrm{cm^{-3}}$

Table 1.3: Details of instruments and data used for analysis

This simultaneous measurement of aerosol concentration and rain is examined in section 3.3.1, to understand size resolved scavenging in dry and various rainy conditions.

1.2. Methodology: theoretical frameworks and illustrations

1.2.1. Need for multifractal framework

Atmospheric fields such as rainfall, wind velocity, temperature, humidity etc. exhibit extreme variability over a wide range of spatial and temporal scales. To give a quick example, the rainfall over a region and a time will not be similar to that at another time at the same location, nor to that at a different location during the same time. Further, the process exhibits strong intermittency; in the example of rainfall, it can be easily understood as the occurrence and non-occurrence of rain itself or very sharp local fluctuations. This behaviour is illustrated in Fig. 1.10 using precipitation data over 6 months recorded at 30 s; timeseries in Fig. 1.10a shows the intermittent behaviour where extreme rain rates are found to be existing non uniformly among time steps with smaller and no rain. In framework of UM, intermittency can be understood with a wider meaning, i.e. the idea that the activity of the field is more and more concentrated. The presence of extreme spatiotemporal variability and intermittency make the characterization of such fields difficult; this can be seen in Fig. 1.10b where corresponding Gaussian distribution is unable to capture the extremes in heavy tail.

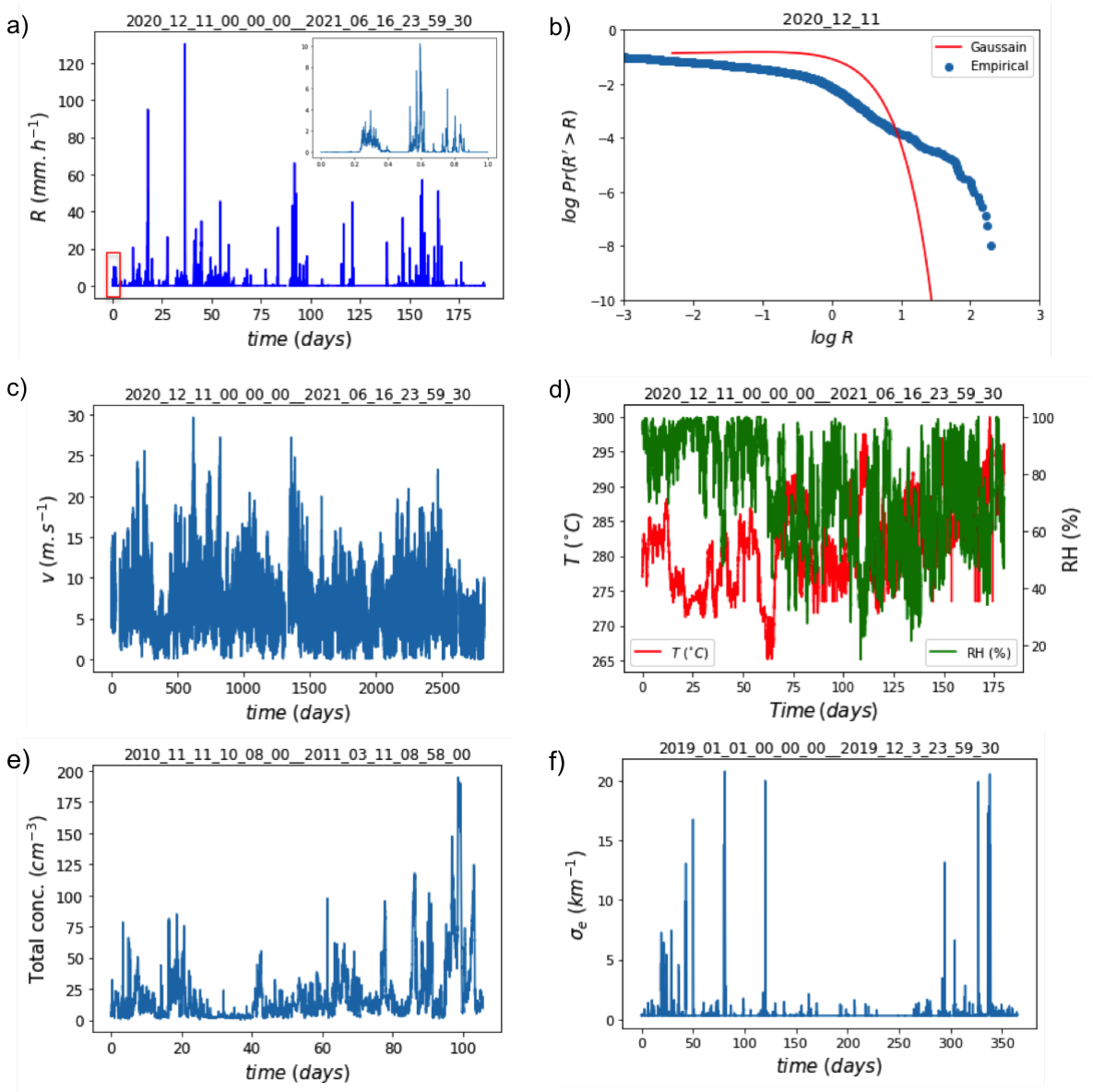

Figure 1.10: Illustration of intermittency and extreme variability in atmospheric fields.
Using precipitation as an example: a) Rain rate (mmh^{-1}) recorded at 30 s, a single day is shown in inset; b) Log-log plot of exceedance probability of precipitation intensity, $Pr(R' > R)$, during one day (12 Nov 2020) along with a gaussian distribution, the heavy tails corresponds to extreme values and shows the inadequacy of normal statistics.
Variability in wind velocity, temperature and humidity: c) Horizontal wind (at 1 Hz, ms^{-1}), d) Temperature (at 15 s, °C) and relative humidity (%); all fields from pays d'Othe wind farm
For row 1 and row 2, the data is from pays d'Othe wind farm, France (11 Dec 2020 to 16 June 2021, see section 1.1.3).
Variability in atmospheric aerosols: e) Aerosol particle concentration for particle size range 0.5 μm to 20 μm (1 min data from October 2010 to March 2011, $\#cm^{-1}$), section 1.1.4; f) light attenuation by particles (extinction coefficient, km^{-1}) estimated from visibility measurement at TARANIS observatory (15 s) during the year 2019, from section 2.2.

These heterogeneous properties of atmospheric fields come from the governing non-linear

equations of the atmosphere (Navier-Stokes) and this lets us to exploit a fundamental property of said non-linear equations - scale invariance.

$$\begin{gathered}\frac{\partial \underline{\mathrm{v}}}{\partial t}+(\underline{\mathrm{v}}\cdot\nabla)\underline{\mathrm{v}}=-\frac{\nabla p}{\rho_a}+\nu\nabla^2\underline{\mathrm{v}}+\underline{\mathrm{f}} \\ \nabla\cdot\underline{\mathrm{v}}=0\end{gathered} \tag{6}$$

where $\underline{\mathrm{v}}$, t, p, ρ_a, ν, and $\underline{\mathrm{f}}$ are velocity, time, pressure, fluid (air) density, kinematic viscosity, and body forces respectively (all parameters are non-dimensionalized).

Conservation of momentum and mass are expressed in first and second lines of the equation. If λ is the scale ratio (outer scale to observational scale) and H an arbitary scaling exponent, then under isotropic transformation, these equations are scale invariant: $\underline{\mathrm{x}}=\underline{\mathrm{x}}/\lambda$, as long as

$$\underline{\mathrm{v}}\to\underline{\mathrm{v}}/\lambda^H;\quad t\to t/\lambda^{1-H};\quad \nu\to\nu/\lambda^{1+H};\quad \underline{\mathrm{f}}\to\underline{\mathrm{f}}/\lambda^{2H-1} \tag{7}$$

This property of scale invariance should be valid for unknown partial differential equations that governs other atmospheric fields as well (Lovejoy and Schertzer, 1985; Brenier et al., 1991; Lovejoy and Schertzer, 1991; Tessier et al., 1993). For the rain time series shown above, this means that the variability in field intensities is statistically same at all scales, i.e. the same phenomenon is observed at each step of the process (no specific time scale exists for the process). This is in accordance with the fact that many physical processes in atmosphere are known to exhibit scaling behaviour (characterized by power law) in temporal and spatial domains between intensity and probability of occurrence despite the vast dynamic range of the process (Franzke et al., 2020). This includes turbulent eddies in few seconds of dissipation time in millimeter scale as well as coupled atmospheric-ocean systems spanning across the globe with centennial time scales and more (Mitchell, 1976; Williams et al., 2017). With the help of scaling exponents (introduced later), Lovejoy and Schertzer (2013) broadly classified the atmospheric spectrum into five regimes: weather, macroweather, climate, macroclimate and megaclimate (Lovejoy, 2015, Fig. 1.11). Granted, the scaling in atmospheric spectrum is anisotropic (multiple regimes and exponents), it still respect the causality principle; this corresponds to a cascade of structures at all scales and hence still valid in stochastic characterization and forecasts (Marsan et al., 1996; Lovejoy and Schertzer, 2007a).

By using multiplicative cascades (introduced later in section 1.2.1.2), it is possible to statistically reproduce the symmetries of Navier-Stokes equations for geophysical fields; and multifractal tools (introduced in section 1.2.2) expand upon this for characterizing the variability across scales by assuming same elementary process at each stage.

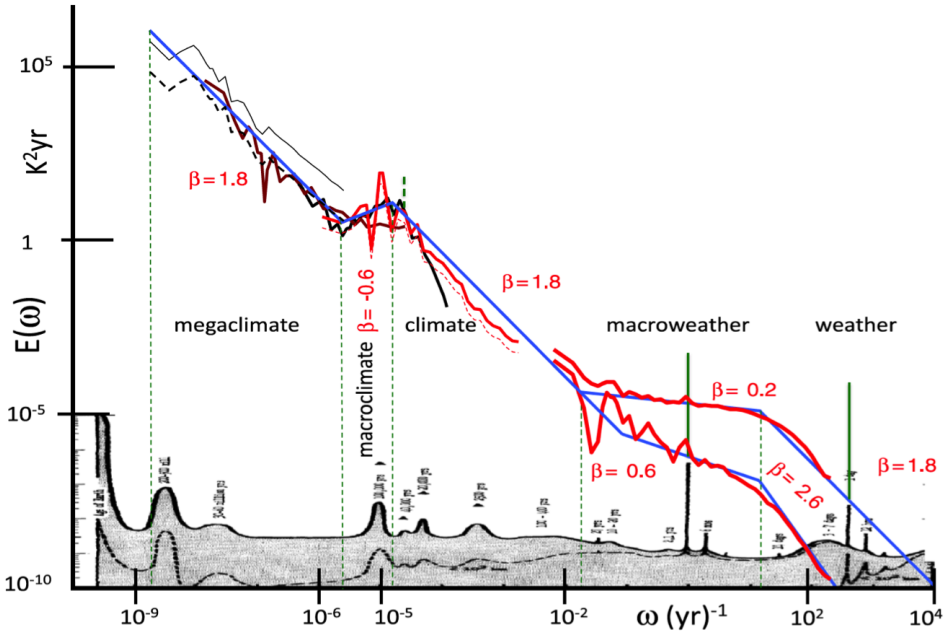

Figure 1.11: Spectral scaling ($E(\omega) \approx \omega^{-\beta}$, indicated in blue lines; same as Eq. 8) of a selection of series illustrating the various qualitatively different dynamic regimes in atmospheric spectrum, from Lovejoy (2015). The exponent values are from various sources reviewed in Lovejoy and Schertzer (2013).

1.2.1.1 Spectral analysis

Spectral analysis is a commonly used technique in turbulence (and signal processing) to estimate scaling behaviour using second-order statistics (the spectrum is obtained from Fourier transform of autocorrelation function) by transforming the field from time domain to frequency domain. In case of scaling behaviour, power spectrum $E(k)$ and frequency are power law related (Mandelbrot and Mandelbrot, 1982; Schertzer and Lovejoy, 1985):

$$E(k) \approx k^{-\beta} \tag{8}$$

where k is the corresponding frequency or wave number and β is the spectral exponent (slope in log-log plot, like in Fig. 1.11).

The spectrum is an ensemble statistical quantity which means that longer series are better for scaling estimation. The presence of a single power law suggests that there is no characteristic length of time scale to the process (scale invariant) and the presence of breaks shows different scaling regimes with different values of β. And peaks in the spectrum correspond to periodicities in the process (large amount of variance in those frequencies). For example, rainfall spectra are known to break around 2 weeks, which is considered to correspond with the 'synoptic maximum', the time scale associated with evolution of planetary scale atmospheric structures (Kolesnikova and

Monin, 1965; Tessier et al., 1993); and it is possible to observe sharp diurnal spikes in temperature spectra which corresponds to the day and night periodicity of the field (Lovejoy et al., 2012). This can be observed in the illustration of spectral analysis in section 1.2.2.4 and also in Fig. 1.11.

For fractal fields (mono-dimensional, introduced in the following section), the spectral slope with Fourier techniques is enough to characterize the complete scaling information but it falls short where there are multiple fractal dimensions involved. Also, power spectra being a second-order statistic doesn't capture information on higher (and lower) orders.

1.2.1.2 Cascades, fractals and multifractals

Cascade phenomenology

As briefly mentioned above, for fully characterizing the process, statistics at all orders should be considered and not just the second-order. The single spectral exponent (β) only corresponds to the fractal dimension (introduced later in this section) of the set of points exceeding a fixed threshold. Though, it gives some useful information, this is insufficient since fields in actuality are 'multiscaling', i.e. different moments of the field have different scaling behaviour with different characteristic exponents. One way to account for it is by considering the process as a multiplicative cascade, thereby incorporating intermittency as well (Lovejoy and Schertzer, 2007a).

Developments in cascades have a long history starting from Richardson's quatrain paraphrasing Jonathan Swift in 1920 (Richardson, 1920; Tamai, 2016):

> *"Big whorls have little whorls*
> *That feed on their velocity,*
> *And little whorls have lesser whorls*
> *And so on to viscosity."*
> – Lewis F. Richardson, 1920

Cascade phenomenology was intensively used to study atmospheric turbulence and has been extended to other atmospheric fields as well. Proposing local-similarity hypothesis (homogeneous and statistically isotropic turbulence in inertial range), Kolmogorov (1941) hypothesized that velocity fluctuations between two points rely only on average dissipation rate. In the power spectrum of wind fluctuations, this corresponds to an energy transfer from larger to smaller scales following a scaling law (Obukhov, 1941, $\beta = 5/3$), which was later verified many times (Gurvich, 1960; Pond et al., 1963, etc.). Since intermittency was not considered here, small deviations from '-5/3' law are expected and observed; leading to non-linear forms of (generalized) structure functions or moment of order q of fluctuations, $\zeta(q)$ (Oboukhov, 1962). The spectral exponent β is related to the second-order structure function: $\beta = 1 + \zeta(2)$.

For quantitatively describing cascade phenomenology with intermittency, various theoretical

formulations were introduced over the years, the first ones being Yaglom (1966) and Gurvich and Yaglom (1967). A cascade process can be considered as an ensemble of cells or structures, with a random variable (positive and independent) associated with each. Fig. 1.12 shows a discrete cascade model (in 1D and 2D) which is commonly used for pedagogical purposes. Its largest structure has a characteristic scale $L(\lambda = 1)$ with uniform energy ($\varepsilon_0 = 1$). This large structure is broken into smaller sub-structures of characteristic length defined by an elementary constant scale ratio λ_1 (usually taken as 2). The fraction of energy transferred is determined by the random variable. For an n^{th} cascade stage, the resolution of the process will be $\lambda = L/\lambda^n$ and energy $\varepsilon_n = \mu\varepsilon\ \varepsilon_{n-1}$. For this to work, the cascade phenomenology relies on three phenomenological assumptions: i) scale (the way structures are divided, i.e. probability distribution is the same at all scales), ii) conservation of flux (i.e. ensemble average is independent of scale, $\langle\varepsilon\rangle$ = 1), and iii) localized dynamics in Fourier space (the dynamics involve interactions between neighbouring structures). With these conditions respected, the generation of cascade processes primarily boils down to the division of substructures and probability distribution of random multiplicative increment. Gurvich and Yaglom (1967) considered a log-normal distribution for the random variable; some other important examples of discrete cascades are β-model, the simplest model with only two values for random variable: dead or 'active' and alive or 'inactive' (Frisch et al., 1978; Mandelbrot, 1974; Novikov and Stewart, 1964), and α-model by Schertzer and Lovejoy (1984) where the dichotomy in β-model is replaced by more realistic 'less active' or 'more active' sub-structures.

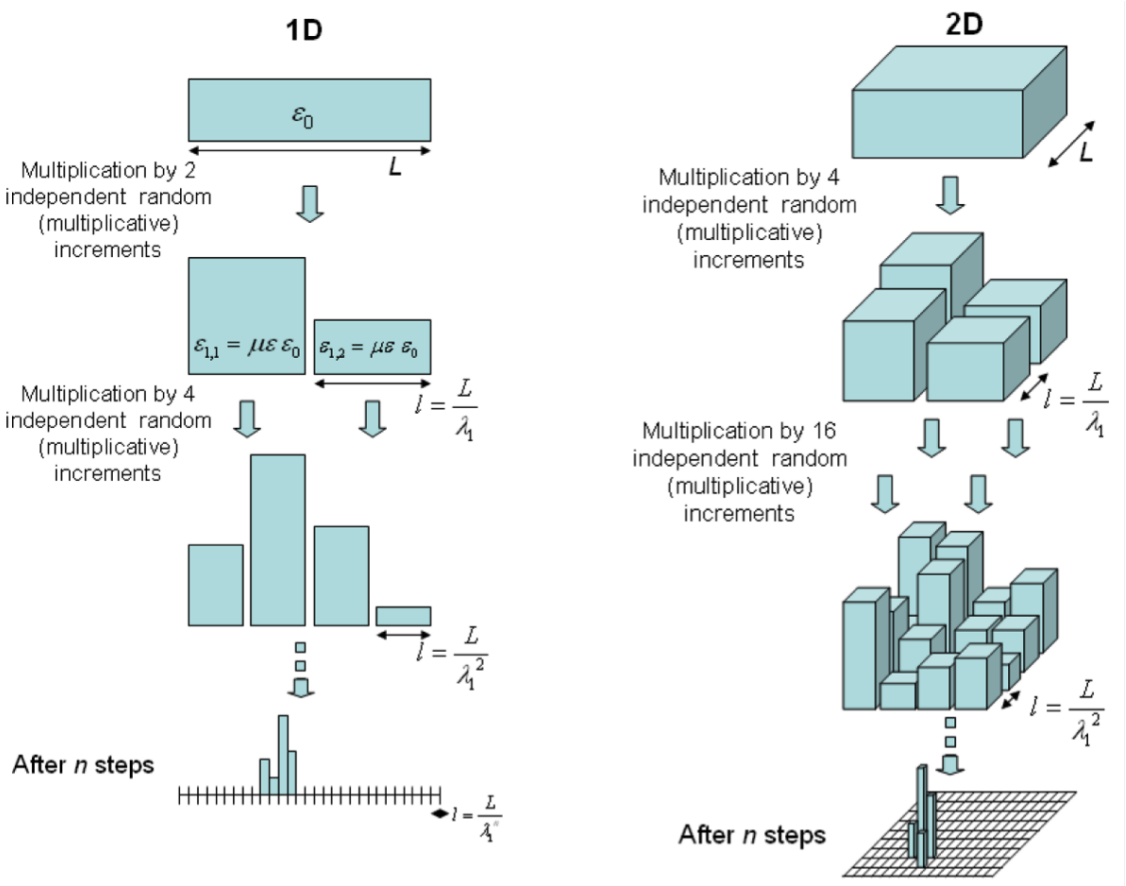

Figure 1.12: Schematic illustration of discrete cascade in 1D and 2D (scales are discretized), illustration from Gires (2012).

Outside of strictly turbulence studies, cascades are also being used in characterising various atmospheric fields and non-linear processes such as rain (Schertzer and Lovejoy, 1987), climate (Lovejoy and Schertzer, 2013), wind power output Calif and Schmitt (2014), astrophysics (Sylos Labini and Pietronero, 1996) etc. For reviews on cascades and scaling over the years, see Seuront et al. (2005) and (Schertzer and Tchiguirinskaia, 2020). Here, we use stochastic multiplicative cascades towards multifractal modelling of atmospheric fields.

Fractals and Multifractals

In multifractal formulation, it is possible to represent multiplicative cascade processes using the probability of a structure at a given observation scale and resolution exceeding a given scale invariant singularity using corresponding codimension. To understand this, the notion of fractal geometry needs to be introduced.

Fractal geometry (Mandelbrot, 1977) is the simplest form of scale invariance where self-similar

geometries (same features repeated at every scale) are characterized using their fractal sets. Developing on Richardson's previous observation in Richardson (1961), in the seminal paper 'How long is the coast of Britain', Mandelbrot (1967) illustrated the futility of classical geometry in characterizing geographical curves (exemplified by the titular coastline paradox which keeps on increasing as finer features are taken into account), and introduced the need for fractional dimensions for studying self-similar objects. Fractal objects are ubiquitous in nature in geophysical and non-geophysical senses, with clouds, snowflakes, leaf and tree structures, cauliflower, sponges etc. being some examples.

Fig. 1.13 illustrates this idea with the famous Sierpiński triangle: starting with an equilateral triangle and removing the central triangle leaving three (four counting the centre one) smaller congruent equilateral ones and then repeating the process to infinity. If the starting triangle is of area unity, the first iteration leaves an area of 3/4; at n^{th} step of iterations, the area will be $(3/4)^n$. And repeating the process ad infinitum will result in the area approaching zero (and perimeter approaching infinity!), while the shape remains conserved.

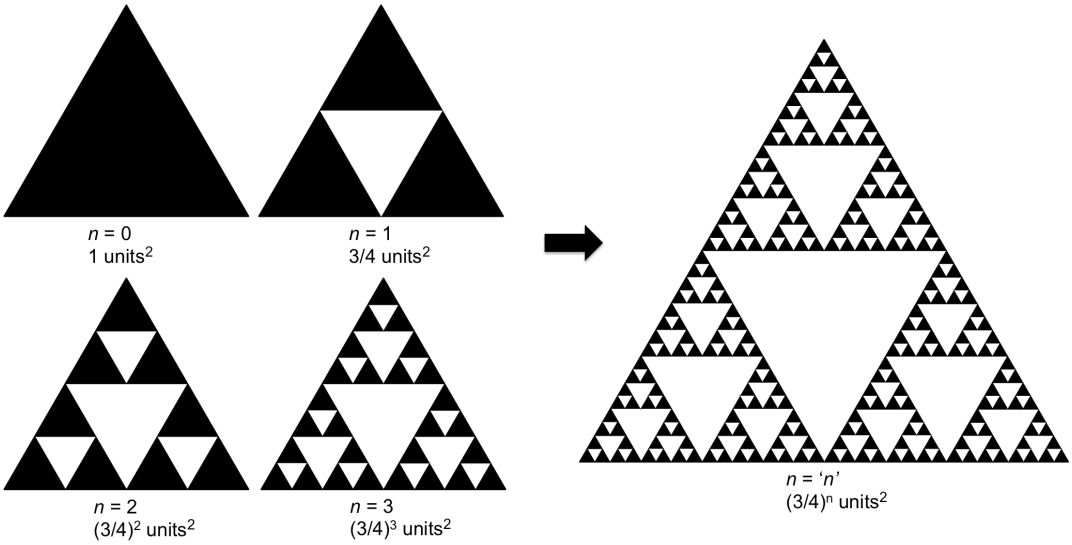

Figure 1.13: Example of fractal geometry: Sierpiński triangle till n^{th} iteration.

In classical geometry, dimensions are integers and refer to the embedding space of the geometry; for example, a point is 0 dimension (D), a line is $1D$, a plane (a square for ex.) is $2D$, and space is $3D$ (a cube for ex.). If we consider a cube of size l_0, the number of non overlapping smaller similar structures (cubes of size l) required to fill it can be obtained as $N(l) = \left[\frac{l_0}{l}\right]^D$ (D = 3 in this example): defining scale ratio or resolution λ ($\lambda = \frac{l_0}{l}$), this can be expressed in power law, $N_\lambda = \lambda^D$. For a fractal object, this scaling relationship doesn't follow a natural number like the topological dimension D, but, rather a non-integer value, the fractal dimension D_f. One standard

technique to estimate D_f is through box-counting where the number of non overlapping boxes N_λ (of size l approaching zero or $\lambda \to +\infty$) required to cover the structure at each iteration characterizes N_λ:

$$D_f = \lim_{\lambda \to +\infty} \frac{\ln(N_{\lambda,A})}{\ln(\lambda)} = \lim_{l \to 0} \frac{\ln(N_{\lambda,A})}{-\ln(l)}. \tag{9}$$

where A is the bounding set of size l_0 (outer scale) in an embedding space of dimension D.

For Sierpiński triangle, where each iteration scaled by a factor of 2 involves 3 copies of previous one, $D_f = \ln(3)/\ln(2) = 1.585$. In physical sense, $1 < D_f < 2$ here is in accordance with its properties, i.e. perimeter $\to +\infty$ (larger than 1D) and area $\to 0$ (smaller than 2D). Since D_f characterizes the sparseness of set A with respect to the embedding space, D_f can be estimated through probability. The probability of smaller structures of size l intersecting A in embedding space D, $Pr = N_{\lambda,A}/N_\lambda = \lambda^{D_f}/\lambda^D = \lambda^{-c_f}$. Here, c_f is the fractional codimension of the object:

$$c_f = D - D_f \tag{10}$$

Multifractals and Multiplicative cascades

The notion of fractal geometry can be extended to geophysical fields as well. For example, sticking to the example of rainfall, the relative occurrence of rain can be expressed as a fractal field (fractal set embedded in 1D space); and frequency of occurrence can be characterized using codimension (sparseness of said set in D, see Fig. 1.15). For such a mono fractal field, most of the scaling information can be obtained from second order moments (spectral analysis and β). However, this monofractal approach doesn't capture the extreme variability of the process over wide range of scales; this requires multiple set of fractal coefficients (hence multifractal, a term coined by Parisi et al.,1985).

Fig. 1.14a shows two year long time series of rain rate at ENPC (France) over various time scales (from measurement frequency of 30 s to 1 month, obtained by taking simple mean). The clustering of intensities (showing long range correlations) here is analogous to multiplicative cascade introduced before, and by using the notion of fractals and scale invaraiance it is possible to represent the probability of occurrence of structures at various intensities.

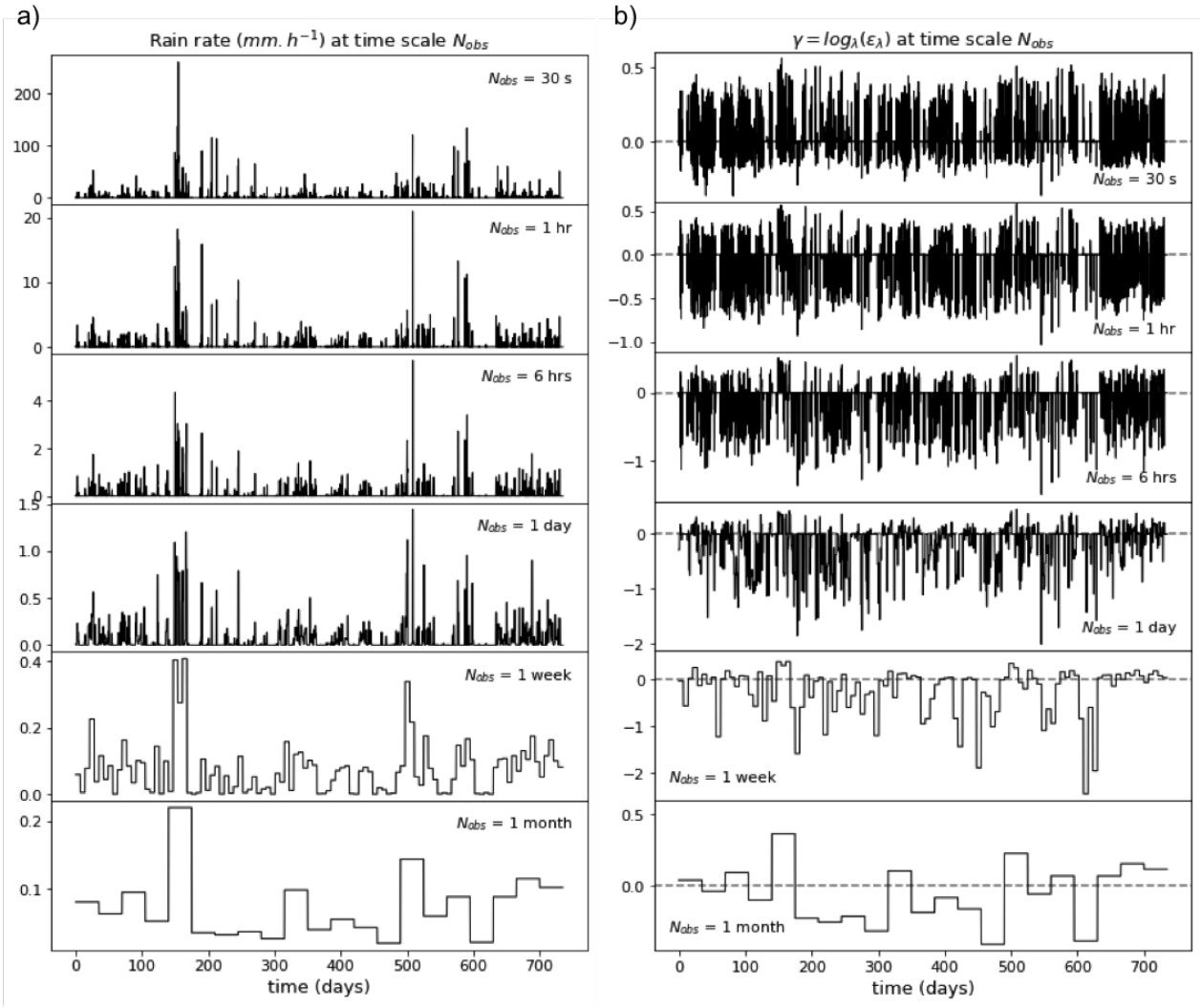

Figure 1.14: a) Variability in rain rate ($mm.h^{-1}$) at different time scales, from 30 s to 2 years (from Dec 2017 to Dec 2019), data from a disdrometer (Parsivel 1) at TARANIS observatory, ENPC; it can be seen that the intensities are clustering like in a multiplicative cascade in Fig. 1.12. b) variability in singularities, $\gamma = \log_\lambda(\varepsilon_\lambda)$, where ε_λ is the normalized rain rate; while rain rate is varying from 200 mm.h^{-1} to 0.2 mm.h^{-1} in intensity while averaging to larger scales, the singularities are rather stable over all scales. Refer Schertzer et al. (2010) for a cleaner presentation of singularities with a larger data set.

As mentioned before, for a multifractal process, to capture the variability in intensities, an infinite hierarchy of scaling exponents are required. In multifractal framework, this is done through the scale invariant concept of singularity (γ). Intensities at various scales can be made non dimensional by standardizing the process by mean, by averaging the observations at the finest scale before aggregating the densities to larger scales. If ${\varepsilon^*}_\lambda$ is the multifractal process, then $\varepsilon_\lambda = {\varepsilon^*}_\lambda / \langle \varepsilon_\lambda \rangle$ will be the renormalized field; his leaves $\langle \varepsilon_\lambda \rangle = 1$ independent of scales ($\langle\, \rangle$ means statistical averaging). Intensities of this normalized field ε_λ is approximated with the help if the singularity γ which is

independent of resolution as (Parisi and Frisch, 1985; Halsey et al., 1986; Schertzer and Lovejoy, 1987):

$$\varepsilon_\lambda \approx \lambda^\gamma \tag{11}$$

With the concept of singularity ($\gamma = \log_\lambda(\varepsilon_\lambda)$), information across all scales can be integrated using only one variable γ. This means that for an intensity in every scale, there exists a single singularity γ. Fig. 1.15 shows the relation between order of singularities of a multifractal process and various intensity levels. In simpler terms, the scale dependent intensities (decreasing intensities with scale in Fig. 1.14a and rather stable singularities with scale in Fig. 1.14b) are now made scale independent through singularities. This comes from long range correlations in the field; this can be illustrated easily by shuffling the intensities which cause degradation in singularities (see Lovejoy and Schertzer, 2013). For a multifractal field, this notion of singularity can be used for describing probability of the field exceeding a given intensity (or threshold) at every step of cascade (every scale). Mathematical formulation of this will be presented in next section.

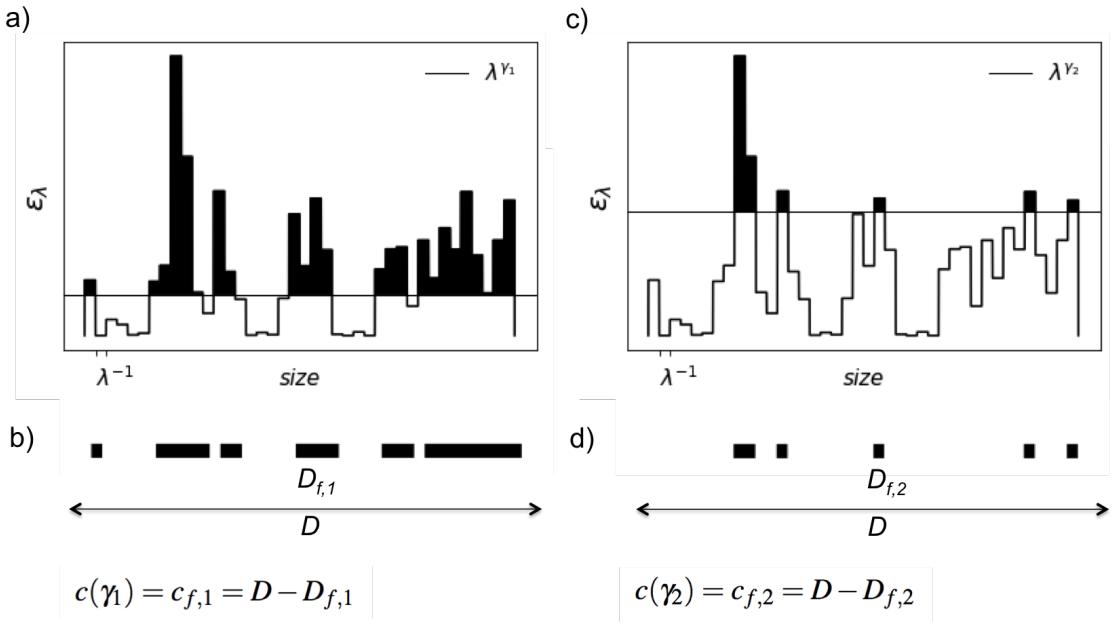

Figure 1.15: Schematic illustration of singularity and codimension at two different intensities (shown by horizontal line, λ^γ; $\gamma_2 > \gamma_1$). The shaded area (in a and c) and corresponding fractal set (in b and d) represents the probability of $\varepsilon_\lambda \geq$ the intensity or threshold, which can be estimated from codimension of the fractal set, $c(\gamma)$. Adapted from Schertzer and Lovejoy (1993).

This important information is exploited in following sections for introducing multifractal framework and its applications.

1.2.2. Universal Multifractal (UM) framework

1.2.2.1 Overview of the theoretical framework

The framework of Universal Multifractals (UM) enables to characterize the extreme variability of geophysical fields across scales, with the help of a limited number of parameters with physical meaning (Schertzer and Lovejoy, 1987). It relies on the assumption that these fields are generated through an underlying multiplicative cascade. As discussed before, such behaviour is assumed to be inherited from the scale invariant features of the Navier-Stokes equations, but has not yet been formally showed. Consequently, statistical properties of fields are conserved in all scales. Review by Schertzer and Lovejoy (2011) discusses the techniques and methodologies employed in more detail. The concepts discussed in previous section is applied here for introducing UM framework.

For analysis in UM framework, the field in consideration is normalized (divided by its mean value) and its total size in terms of numerical values is restricted to be a power of two. The field can be one or two dimensional; since current studies involve only time series we will be limiting our discussion to single dimension. Let us consider a normalized conservative field (an additional parameter for non-conservative fields is introduced later) ε_λ at resolution λ. Resolution λ is the ratio of L, the outer scale, to l, the observational scale. Let us first consider the occurrence pattern of the field, i.e. the same field with 1 for strictly positive values and 0 otherwise. If the field is fractal, then the probability p that a segment of length l intersects the field (p is the probability of occurrence of non zero elements in the total binary field) scales with resolution as follows:

$$p = \frac{\lambda^{D_f}}{\lambda^{D}} = \lambda^{-c_f} \tag{12}$$

where c_f is the fractal co-dimension of the field (Eq. 10). The fractal dimension D_f indicates how the binary field (rain and no rain if we take rainfall as an example field) fills the available space in a scale invariant way. As D is constant, in order to fully characterize the field a value of D_f for each threshold (same as intensity used in previous section) is required. This is the intuitive notion of multifractality. In order to be mathematically consistent, this characterization should actually be done with the help, not of a direct threshold at the maximum resolution, but with a scale-invariant threshold called singularity γ, and their corresponding codimension function $c(\gamma)$ as :

$$p\left(\varepsilon_\lambda \geq \lambda^{\gamma}\right) \approx \lambda^{-c(\gamma)} \tag{13}$$

where γ is the singularity ($\gamma = log_\lambda(\varepsilon_\lambda)$). $c(\gamma)$ can be geometrically interpreted as the fractal codimension of the portion of the field exceeding a given singularity γ. '$\approx$' shows statistical equivalence accounting the slowly varying and constant factors over operations across various λ. This relation implies that statistical moments q of the field scale with resolution (Schertzer and Lovejoy, 1987,

1988) with moment scaling funciton $K(q)$ as:

$$\langle {\varepsilon_\lambda}^q \rangle \approx \lambda^{K(q)} \tag{14}$$

$K(q)$ and $c(\gamma)$ are equivalent functions (via Mellin transformation that relates moment orders and probability density function) and fully characterize the variability of the process across all scales. For multifractals, both functions are related by a simple Legendre transform (Parisi and Frisch, 1985; Schertzer and Lovejoy, 1993):

$$\begin{aligned} K(q) &= \max_{\gamma}[q\gamma - c(\gamma)] \\ c(\gamma) &= \max_{q}[q\gamma - K(q)] \end{aligned} \tag{15}$$

Hence, for every singularity γ, there is a corresponding order of moment q associated with it and vice versa: $q = \frac{dc(\gamma)}{d\gamma}$ & $\gamma = \frac{dK(q)}{dq}$.

Though the determination of $K(q)$ (and $c(\gamma)$) ideally requires infinite number of parameters, it is possible to reduce them to a few parameters from local description of scaling functions around mean (q = 1) in UM framework. This is made possible by fixing the total range of scales of the multiplicative cascade processes (λ finite) and by the application of (generalized) central limit theorem (Schertzer and Lovejoy, 1997), causing all multiplicative processes to converge towards a universal behaviour. For a conservative field in UM framework, $K_c(q)$ can be fully determined with only two parameters, multi-fractality index α and mean intermittency codimension C_1.

$$K_c(q) = \begin{cases} \dfrac{C_1}{\alpha - 1}\left(q^\alpha - q\right) & \alpha \neq 1 \\ C_1 q \ln q & \alpha = 1 \end{cases} \tag{16}$$

C_1 measures clustering of average intensity across scales ($C_1 \in [0,1]$ for 1 dimensional fields); when $C_1 = 0$ the field is homogeneous with little variability. α measures how this clustering changes with respect to intensity levels ($\alpha \in [0,2]$); higher the value of α, higher the variability, with $\alpha = 0$ being a monofractal field where intermittency of extreme is same as that of mean. Larger values of both correspond to stronger extremes. Simulations of such fields can be obtained by generating a levy noise with parameter α, 'colouring' it to introduce C_1 and then taking the exponential which yields solely non-negative values.

If the UM parameters are known, co-dimension function of the conservative multifractal field, $c_c(\gamma)$ can also be obtained as

$$c_c(\gamma) = \begin{cases} C_1 \left(\dfrac{\gamma}{C_1 \alpha'} + \dfrac{1}{\alpha} \right)^{\alpha'} & \alpha \neq 1 \\ C_1 \exp\left(\dfrac{\gamma}{C_1} - 1 \right) & \alpha = 1 \end{cases} \tag{17}$$

where $\frac{1}{\alpha} + \frac{1}{\alpha'} = 1$. Fig. 1.16 shows the theoretical curves of scaling moment functions around various values of α and C_1..

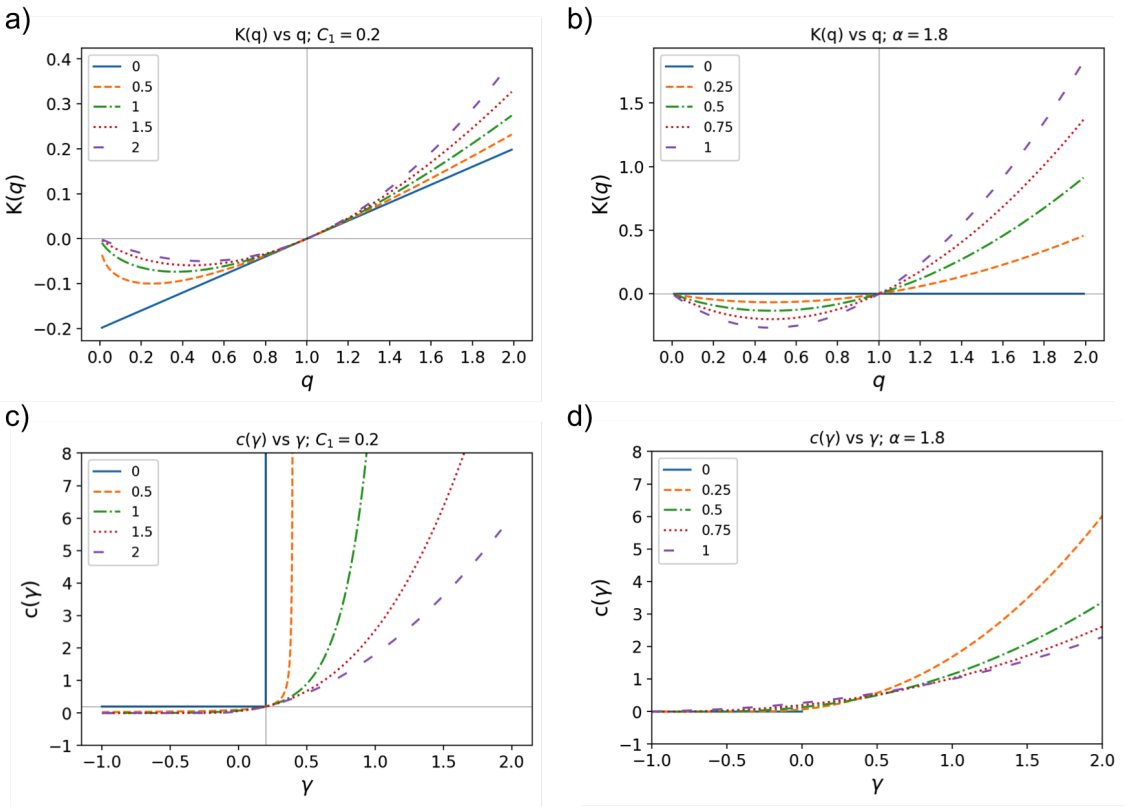

Figure 1.16: Illustration of the scaling moment functions in UM framework. a) $K(q)$ at various values of α at a fixed C_1; b) $K(q)$ at various values of C_1 at a fixed α. $q = 1$ corresponds to mean; c) & d) $c(\gamma)$ at similar conditions.

For a non conservative field ϕ_λ, i.e. a field whose average ($\langle \phi_\lambda \rangle$) changes with scales, a non-conservative parameter H is used in expression of scaling:

$$\phi_\lambda = \varepsilon_\lambda \lambda^{-H} \tag{18}$$

where ε is a conservative field characterized with C_1 and α.

H characterizes the variation in mean across all the scales ($\langle \phi_\lambda \rangle = \lambda^{-H}$); for a conservative field, H =0, in terms of Eq. 18, $\langle \varepsilon_\lambda \rangle$ = 1. Positive H represents a smoother field which needs to be fractionally differentiated for obtaining a conservative field. Conversely negative H represents a field in need of fractional integration for retrieving conservative field; which are equivalent to multiplication with k^H in Fourier space. H is related to the spectral slope β (Eq. 8), which gives a measurement of the correlation range. Larger β means higher contribution of large-scale phenomenon in variability of data.

$$\beta = 1 + 2H - K_c(2) \tag{19}$$

this comes from the previously mentioned relation between β and $\zeta(2)$ (section 1.2.1.2), and $H = \zeta(1)$.

With H added to moment scaling functions (replacing the conservative left hand side $K_c(q)$ with $K(q) - qH$ in Eq. 16 and $c_c(\gamma)$ with $c(\gamma + H)$ in Eq. 17), the model can be used for non-conservative fields as well.

1.2.2.2 Estimation of scaling behaviour and UM parameters

The scaling behaviour of conservative multifractal fields can be examined using trace moment (TM) where log-log plot of upscaled fields against resolution λ is taken for each moment q (Eq. 14). For multifractal fields, the plot is a straight line with moment scaling function $K(q)$ as slope. The quality of scaling is given by the estimate r^2 of the linear regression; the value for $q = 1.5$ is used as reference. From the $K(q)$ curve, α and C_1 are estimated from derivatives at $q = 1$ since in UM framework local.

$$\begin{aligned} K'(1) &= C_1 \\ K''(1) &= C_1 \alpha \end{aligned} \tag{20}$$

It should be mentioned that, in practise, local approximation of these derivatives are used, i.e. $K'(1) \approx \frac{K(1.05) - K(0.95)}{0.1}$.

Double trace moment (DTM) is a more robust version of TM tailored for UM fields where the moment scaling function $K(q, \eta)$ of the field ${\varepsilon_\lambda}^{(\eta)}$ (${\varepsilon_\lambda}^{(\eta)} = \frac{{\varepsilon_\lambda}^{\eta}}{\langle {\varepsilon_\lambda}^{\eta} \rangle}$, obtained in practice by raising ε to power η at the maximum resolution and then upscaling it) is expressed as a function of multifractality index α (Lavallée et al., 1993). For a multifractal field, $K(q, \eta)$ becomes

$$K(q, \eta) = K(\eta q) - qK(\eta) = \eta^{\alpha} K(q) \tag{21}$$

From this, it is possible to express the DTM relation as

$$\langle \left(\varepsilon_\lambda{}^{(\eta)}\right)^q \rangle \approx \lambda^{K(q,\eta)} = \lambda^{\eta^\alpha K(q)} \tag{22}$$

From the above equation, value of α can be obtained as the slope of the linear part when $K(q,\eta)$ is represented for a given q as a function of η in log-log plot. And C_1 from the intercept of the linear portion of the graph, using Eq. 16 ($K(q,\eta) = \eta^\alpha \frac{C_1}{\alpha-1}(q^\alpha - q)$). Both TM and DTM techniques give reliable estimates as long as the $H < 0.5$ for the conservative field analysed.

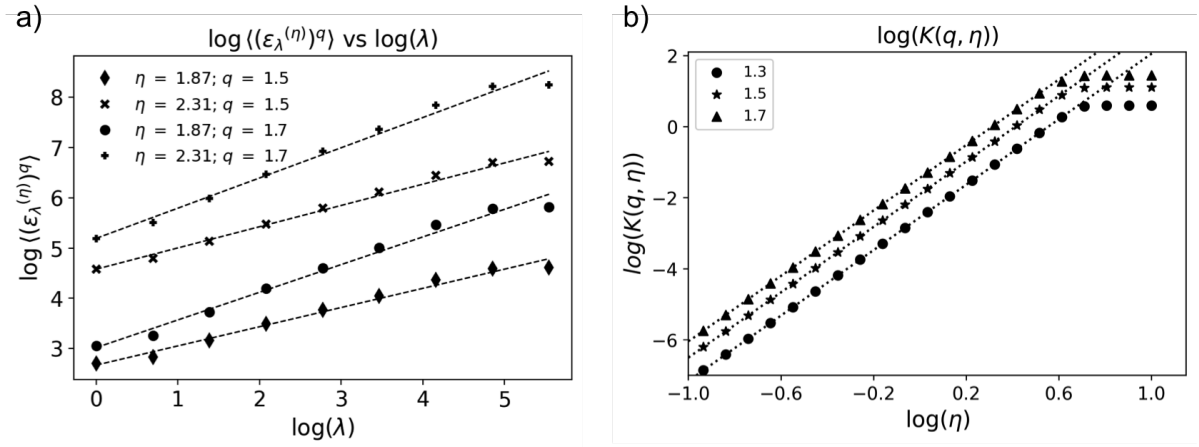

Figure 1.17: Illustration of DTM analysis (for a simulated field: $\alpha = 1.8$ & $C_1 = 0.2$): a) log-log plot of Eq. 14 for the renormalized η-power of the field ε_λ ($\varepsilon_\lambda^{(\eta)}$) at various values of q and η, slope of which gives $K(q,\eta)$; b) log-log plot of Eq. 21 for various q values, slope gives α and C_1 is calculated from the intercept.

Though $K(q)$ and $c(\gamma)$ are continuous convex curves in theory, in practice, the range of moments under which reliable estimates of UM parameters can be retrieved is limited by phase transitions (Schertzer and Lovejoy, 1987, 1992) due to the size of the sample analyzed as well as by the divergence of higher moments. There exists a single maximum value of the scale invariant threshold and hence of singularity γ_s (and of corresponding moment order q_s) at which the fractal codimension ($c(\gamma)$) becomes equal to the dimension of the embedding space (D). At this maximum point, the corresponding probability in Eq. 13 becomes 1 (the number of structures at or above the maximum singularity) divided by the total number of structures (λ^D). If the field consists of N_s independent samples ($N_s = \lambda_s^D$, where D_s is the sampling dimension), the maximum singularity can be obtained as $c(\gamma_s) = (D + D_s)$ ($Pr(\varepsilon \geq \lambda^{\gamma_s}) = \lambda^{-c(\gamma_s)} = \lambda^{-D_s}\lambda^{-D}$). In practice, the empirical $K(q)$ curve becomes linear at $q > q_s$, and trails below the theoretical curve (see sections 2.2 and 3.1.2.2 for this effect in practise and their consequences). Since multifractal processes are generated by cascade processes, the average values can get too concentrated over a certain area leading to spurious estimates of moments - divergence of moments. At the moment orders greater than

q_D (q above which divergence happens) $K(q) \approx +\infty$ giving unreliable estimates of UM parameters (there is no convergence, i.e. more the samples, greater the value). q_D can be estimated from power law fall off in probability distribution: $Pr(\varepsilon_\lambda \geq x) \approx x^{-q_D}$. For reliable statistical estimates of the moment scaling function and hence the UM parameters, the moment orders should not be exceeded beyond q_s or q_D.

For most fields studied here, positive H values were found; and when $H > 0$, a conservative field was obtained by the fractional differentiation implementing the commonly used approximation by Lavallée et al. (1993). Basically, the field ε at the maximum resolution ($\varepsilon_{\lambda_{max}}$) is estimated by renormalizing absolute fluctuations of the original field at maximum resolution ($\phi_{\lambda_{max}}$) is then upscaled at other resolutions λ in the estimation of UM parameters.

$$\varepsilon_{\lambda_{max}}(i) = \frac{|\phi_{\lambda_{max}}(i+1) - \phi_{\lambda_{max}}(i)|}{\langle|\phi_{\lambda_{max}}(i+1) - \phi_{\lambda_{max}}(i)|\rangle} \tag{23}$$

with i being the time step from 1 to length of the series, N (i = 1, 2, ..., N). UM gives reliable estimates for $H < 0.5$.

1.2.2.3 Power law relations in UM framework and practical implementation

If a field is UM, then a power law relation of it is also a UM field with coefficients depending upon initial UM parameters. The reasoning for power law comes from the DTM analysis in UM framework (Tessier et al., 1993; Lovejoy et al., 2008).

Consider two multifractal fields (ε_1 and ε_2) that are power law related by an exponent a and a prefactor b, as below :

$$\varepsilon_1 = b\varepsilon_2^a \tag{24}$$

From exponents in Eq. 22, $K(q)$ of ε_1 can be expressed as follows

$$\begin{array}{ccccc} <(\varepsilon_1)^q> & \approx & <(\varepsilon_2{}^{(a)})^q> & \approx & \lambda^{K_{\varepsilon_2}(q,a)} \\ K_{\varepsilon_1}(q) & = & K_{\varepsilon_2}(q,a) & = & a^{\alpha_{\varepsilon_2}} K_{\varepsilon_2}(q) \end{array} \tag{25}$$

Expanding $K(q)$ with UM parameters (as in Eq. 16)

$$\frac{C_{1,\varepsilon_1}}{\alpha_{\varepsilon_1} - 1}(q^{\alpha_{\varepsilon_1}} - q) = a^{\alpha_{\varepsilon_2}} \frac{C_{1,\varepsilon_2}}{\alpha_{\varepsilon_2} - 1}(q^{\alpha_{\varepsilon_2}} - q) \tag{26}$$

From the above equation, we can deduce that, if a power relation exists, the UM parameters

are related as follow :

$$\alpha_{\varepsilon_1} = \alpha_{\varepsilon_2} = \alpha$$
$$C_{1,\varepsilon_1} = a^{\alpha} C_{1,\varepsilon_2} \tag{27}$$

1.2.2.4 Illustration of scaling and UM analysis

Here, the relevance and one use case of UM analysis is briefly illustrated with a few real atmospheric fields, using the already discussed data from RW-Turb project (Section 1.1.3). This section is adapted from section 5 of the data paper (Gires et al., 2022) and uses framework along with spectral analysis for determining the quality of data.

It has been previously established that the RW-Turb project includes high-resolution simultaneous registration of data from 3D sonic anemometers (100 Hz) and meteorological stations (1 Hz) along with turbine power in a wind farm. While studying the small-scale space-time fluctuations, it is advantageous to use data at the finest available resolution. However, it is possible that the actual sampling resolution may be different due to quality problems in the series leaving spurious estimates at finer scales. To understand this, the finest available data from anemometers and meteorological stations were analysed using spectral analysis and the framework of Universal Multifractals (UM). A multifractal analysis of collected data is performed to check for the effective resolution of the data, i.e. to assess if measurements are affected or not by instrumental artifacts at small scales. Given the stated purpose, only small scales (i.e. from 16 s down to 0.01 s) are studied here.

Spectral estimates

Spectral analysis which consists of plotting Eq. 8 in log-log and trace moment (TM) analysis which consists of plotting Eq. 14 in log-log for various moments q enable to confirm scaling behaviour of studied fields. It is the case if straight lines are retrieved, potentially with several scaling regimes. The retrieved slopes give β for the spectral analysis and $K(q)$ in the TM analysis. In Fig. 1.18a, trace moment (TM) analysis, and spectral analysis for 100 Hz anemometer data is shown (ensemble analysis of 1 month long data - 01/03/2021 to 01/04/2021 - with a sample length of 40 minutes). If we use the terminology in section 1.2.2: anemometer data is the field, ε_λ, at various observational scales (0.01 s to 40 min here) with λ being the corresponding scale ratios (or resolutions in UM framework). The blue and red lines in TM and spectral plots correspond to two scaling regimes, both with separate scaling behaviour and estimates of β and UM parameters. In the spectral plot, a spectral spike is observed at frequency 0.0304 s^{-1} and spurious fluctuations are visible for small scales. The spike is due to the fact that at 100 Hz, same data is basically repeated over three successive time steps (revealed from manual checking). Data from other time periods were also tested and they yielded similar results.

UM estimates

Estimates of UM parameters, obtained with the help of DTM analysis (log-log plot of eq. 22) for the small scale regime (1 Hz - 100 Hz) yielded values of C_1 too low (2.80×10^{-5}) to consider any variation in the field. As the field is too smooth here (high value of β: 2.13 and 1.57), fluctuations were analysed by differentiating the field (eq. 23). This enables to study a approximation of the underlying conservative fields (hence the decrease in estimates of β and H). In fluctuations of same 100 Hz data, nearly 70% of the values are equal to zero, which results in strong bias for estimates with an artificial decrease of α ($= 0.31$ here) and an increase in C_1 ($= 0.21$ here), which is consistent with bias associated with numerous zeros (Gires et al. (2012). This further suggests the possibility of having instrumental noise in resolutions finer than 1 Hz. It is unclear where exactly the scaling break is (close to 1 Hz or 10 Hz) to consider instrumental noise, but for being on the safer side, we decided to take 1 Hz as the limiting value. Analysis of fluctuations of 1 Hz data (ensemble analysis of 1 month long data - 01/03/2021 to 01/04/2021 - with a sample length of 16 hours) is shown in fig. 1.18b. For the small scale regime (1 s - 16 s), we find $\alpha = 1.49$ and $C_1 = 0.09$ which is more consistent with estimates commonly retrieved for atmospheric fields.

Similar results (extremely small values of C_1 or β suggesting instrumental noise) are observed for other 1 Hz data available at meteorological stations - Temperature (T), Pressure (P), Humidity (RH) and air density (ρ, a function of T, P & RH) with 16 s being close to the actual effective sampling resolution. Fig. 1.18c shows the TM analysis for T; on the basis of spectra, the second scaling regime (16 s to 1 Hz) seems to suggest presence of instrumental artifacts (ensemble analysis of 1 month long data - 01/03/2021 to 01/04/2021 - with a sample length of 16 hours). For the 1 s - 16 s regime, we find $\alpha = 1.99$ and $C_1 = 1.61 \times 10^{-6}$; the low C_1 supports spectral observation. In 1 Hz station data, values of many data points were actually very close to each other resulting again in the presence of a lot of zeroes in fluctuations of the series (about 75% for T fluctuations). This in turn gave biased estimates of both α and C_1. Averaging data over time reduced this effect and by considering fluctuations of data at 15 s, realistic values of α and C_1 were retrieved (Fig. 1.18d; $\alpha = 1.12$ and $C_1 = 0.14$ for 15 s - 4 min scaling regime).

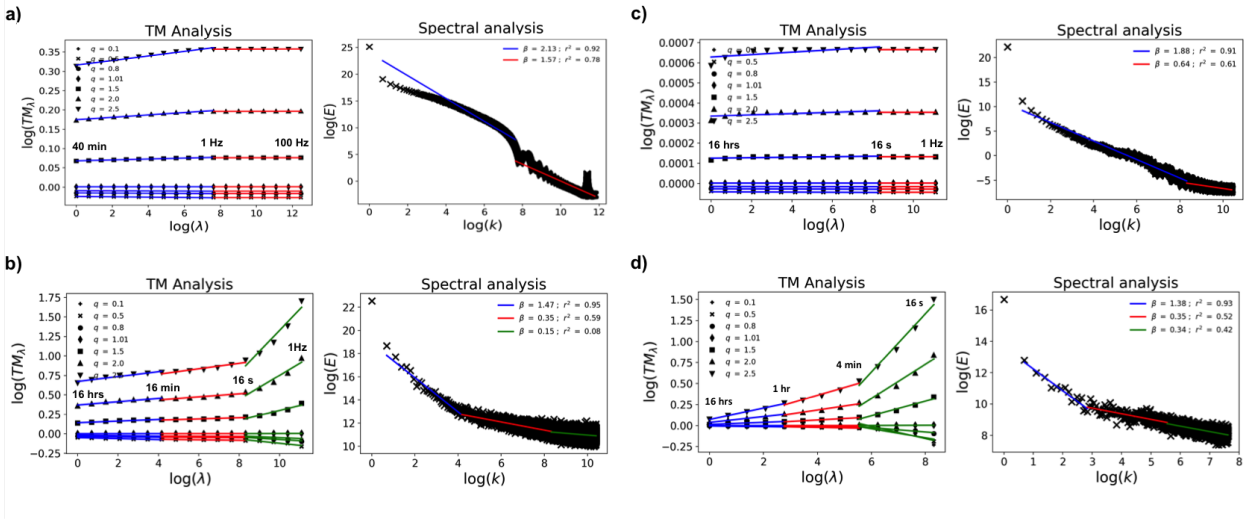

Figure 1.18: TM analysis (Eq. 14 in log-log plot), and spectral analysis (Eq. 8 in log-log plot) of 1 month long data (27/01/2021 to 27/02/2021) for a) anemometer data at 100 Hz (sample length of 40 min), b) fluctuations of anemometer data at 1 Hz (sample length of 16 hours), c) Temperature (T) at 1 Hz (sample length of 16 hours), d) fluctuations of Temperature (T) at 15 s (sample length of 16 hours)

For analysing the fields' variability, its worthwhile to note that the actual sampling resolution - resolution from which fields can be studied to obtain consistent UM parameters - is not necessarily the lowest resolution of instrumental data availability. Indeed, it could be affected by instrumental artifacts (white noise, repeated values). Here, it is more realistic to study anemometer as well as station data at a coarser resolution (1 Hz and 16 s respectively) where it is exhibiting clear scaling variability than at the finest available resolution of data recording (100 Hz and 1 Hz). Multifractal framework (UM) is thus a powerful tool to study this issue and assess the quality of the data.

1.2.3. Framework of joint multifractal analysis (JMF)

In previous section, UM framework was introduced which enables characterization of all the fluctuations of a field at all the scales, scaling behaviour with various regimes, degree of non-conservation, mean intermittency and variability of intermittency. Atmospheric fields are known to be inter related and understanding the complexity of a field also involve understanding its behaviour with correlated fields. Here, the framework of Joint Multifractals (JMF) is introduced which is designed for characterizing the correlation between two multifractal fields, relying on the already discussed framework of UM.

Though not extensive, various methodologies were suggested and used for studying coupling (across scales) between two simultaneously measured fields from their joint moments (like moments of individual fields mentioned before, but by multiplying both fields under consideration). Meneveau et al. (1990) used joint moment exponents to examine correlation between velocity and temperature fluctuations in the turbulent wake of a heated cylinder, and also between square of vor-

ticity fluctuations and dissipation of turbulent velocity component. Seuront and Schmitt (2005a,b) expanded upon this by introducing a 'generalized correlation function' (GCF, re-normalizing the joint moments) and argued the use case in effectively characterizing biological and physical coupling (using data on phytoplankton concentration, through fluorescence, and temperature at various turbulence intensities). Calif and Schmitt (2014) used GCFs to examine coupling between simultaneous data of wind speed and aggregate power output from a wind farm. Both cases used GCFs on log-normal cascades involving single parameter and linear correlation functions, and explored only two specific coupling cases between fields - a proportional or a power law relation. Between two fields, the GCF is symmetrical with respect to the moment between fields; this suggests the possibility of expressing the two quantities with a simple relation of proportionality. Relying on this, Gires et al. (2020b) expanded GCFs to UM providing a framework (JMF) where the related fields can be expressed as multiplicative power law combination of known UM fields. This framework not only retrieves the proportionality constants between fields but also provides an intuitive indicator that combines most of the information obtained from JMF.

Consider two simultaneously measured multifractal fields ε_λ and ϕ_λ of resolution λ, the correlation between them can be expressed using generalized correlation function (GCF) suggested by Seuront and Schmitt (2005a) as follows:

$$\frac{\langle {\varepsilon_\lambda}^q {\phi_\lambda}^h \rangle}{\langle {\varepsilon_\lambda}^q \rangle \langle {\phi_\lambda}^h \rangle} \approx \lambda^{S(q,h)-K_\varepsilon(q)-K_\phi(h)} \approx \lambda^{r(q,h)} \tag{28}$$

where $r(q,h)$ is the generalized scaling exponent (which is symmetrical: $r(q,h) = r(h,q)$) and $S(q,h)$ the scaling moment exponent of combined field $({\varepsilon_\lambda}^q {\phi_\lambda}^h)$. $K_\varepsilon(q)$ and $K_\phi(h)$ are scaling moment functions of ε_λ and ϕ_λ at moments q and h. For a log normal field ($\alpha = 2$), $r(q,h)$ is a linear function with regards to both h and q; and if the fields are independent, $r(q,h) = 0$.

In JMF, we can express ε_λ in terms of ϕ_λ and an independent multifractal field Y_λ with same C_1 as ϕ_λ. Below, both fields are correlated with a and b (relative weight in combination), and Y_λ (can be generated if we know its α and C_1). Note that ${\phi_\lambda}^a {Y_\lambda}^b$ is a single field expressed as a power law combination of ϕ and Y.

$$\varepsilon_\lambda = \frac{{\phi_\lambda}^a {Y_\lambda}^b}{\langle {\phi_\lambda}^a {Y_\lambda}^b \rangle} \tag{29}$$

Please note that numerator in Eq. 28 is average of the field and that in Eq. 29 is the field itself. Before proceeding further, it is important to state the meaning of a and b intuitively on correlation between fields. When $a = 1$ and $b = 0$, ε_λ is simply equal to ϕ_λ (maximum correlation) and during the converse, ε_λ is equal to Y_λ with no connection to ϕ_λ. Intermediate values of a ($1 > a > 0$) shows

progressive decorrelation between ε_λ and ϕ_λ.

Empirical technique for retrieving UM parameters of Y_λ and exponents a and b from JMF analysis starts with individual UM analysis of the fields to be correlated, ε_λ and ϕ_λ. For estimation of a, joint multifractal analysis is required: Eq. 28 is implemented with ϕ_λ and ε_λ (the order of fields are reversed here to follow the format in Gires et al. (2020b); this doesn't matter as the GCF is symmetrical, also in practical estimation in JMF both moment orders are kept same: $q = h = 0.7$). This can be reduced by introducing the independent multifractal field Y_λ. By substituting ε_λ (from Eq. 29) in above equation, and separating average of products to product of averages (as ϕ_λ and Y_λ are independent of each others) we are left with

$$\begin{aligned}\frac{\langle {\phi_\lambda}^q {\varepsilon_\lambda}^h\rangle}{\langle {\phi_\lambda}^q\rangle\langle {\varepsilon_\lambda}^h\rangle} = \frac{\langle {\phi_\lambda}^q \left(\frac{{\phi_\lambda}^a {Y_\lambda}^b}{\langle {\phi_\lambda}^a {Y_\lambda}^b\rangle}\right)^h\rangle}{\langle {\phi_\lambda}^q\rangle\langle \left(\frac{{\phi_\lambda}^a {Y_\lambda}^b}{\langle {\phi_\lambda}^a {Y_\lambda}^b\rangle}\right)^h\rangle} &= \frac{\langle \phi_\lambda^{q+ah} Y_\lambda^{bh}\rangle}{\langle \phi_\lambda^q\rangle\langle \phi_\lambda^{ah}\rangle\langle Y_\lambda^{bh}\rangle} \\ &= \frac{\langle \phi_\lambda^{q+ah}\rangle}{\langle \phi_\lambda^q\rangle\langle \phi_\lambda^{ah}\rangle}\end{aligned} \tag{30}$$

Here the ratio no longer depends on Y_λ which makes the joint scaling function $r(q,h)$ solely dependent on ϕ_λ. Following the generalized correlation in Eq. 28 and expressing scaling moment functions in UM framework (Eq. 16):

$$\begin{aligned} r(q,h) &= K_\phi(q+ah) - K_\phi(q) - K_\phi(ah) \\ &= \frac{C_{1,\phi}}{\alpha_\phi - 1}((ha+q)^{\alpha_\phi} - (ha)^{\alpha_\phi} - (q)^{\alpha_\phi}) \end{aligned} \tag{31}$$

Here, $r(q,h)$ is an increasing function of a for a given value of q and h; and this property is used for computing the values of a. One approach is to set q and h to known values (both at 0.7 for example) and compute the empirical value of $r_{emp}(q,h)$, and then find the value of a that yields this value. This technique works as long as the scaling moment functions remain stable, i.e. the exponents here ($ha+q$, ha, and q) are less than the critical moments (q_s and q_D) discussed in section 1.2.2.2.

Now remaining are the values UM parameters and exponent of independent field Y_λ: α_Y ($C_{1,Y} = C_{1,\phi}$) and b. They can be obtained by applying generalized correlation to ${\varepsilon_\lambda}^q$ following Eq. 29

$$\langle {\varepsilon_\lambda}^q\rangle = \frac{\langle \phi_\lambda^{aq}\rangle\langle Y_\lambda^{bq}\rangle}{\langle {\phi_\lambda}^a\rangle^q\langle {Y_\lambda}^b\rangle^q} = \lambda^{K_\varepsilon(q)} \tag{32}$$

$K_\varepsilon(q)$ can be expanded according to GCF (Eq. 28) and UM framework (Eq. 16) as

$$\begin{aligned} K_\varepsilon(q) &= K_\phi(qa) - qK_\phi(a) + K_Y(qb) - qK_Y(b) \\ &= \frac{C_{1,\phi}}{\alpha_\phi - 1}[(qa)^{\alpha_\phi} - qa) - q(a^{\alpha_\phi} - a)] + \frac{C_{1,Y}}{\alpha_Y - 1}[(qb)^{\alpha_Y} - qb) - q(b^{\alpha_\phi} - b)] \\ &= a^{\alpha_\phi} K_\phi(q) + b^{\alpha_Y} K_Y(q) \end{aligned} \tag{33}$$

Assuming ε_λ as a UM field, C_1 and α are obtained from derivatives of $K(q)$ around mean ($q = 1$) as per Eq. 20

$$\begin{aligned} C_{1,\varepsilon} &= K'_\varepsilon(1) = a^{\alpha_\phi} C_{1,\phi} + b^{\alpha_Y} C_{1,Y} \\ \alpha_\varepsilon &= \frac{K''_\varepsilon(1)}{C_{1,\varepsilon}} = \frac{C_{1,\phi} a^{\alpha_\phi} \alpha_\phi + C_{1,Y} b^{\alpha_Y} \alpha_Y}{C_{1,\varepsilon}} \end{aligned} \tag{34}$$

From above equations, both α_Y and b can be estimated. For α_Y estimation, replace $C_{1,Y} b^{\alpha_Y}$ as $C_{1,\varepsilon} - a^{\alpha_\phi} C_{1,\phi}$

$$\alpha_Y = \frac{\frac{C_{1,\varepsilon}}{C_{1,\phi}} \alpha_\varepsilon - a^{\alpha_\phi} \alpha_\phi}{\frac{C_{1,\varepsilon}}{C_{1,\phi}} - a^{\alpha_\phi}} \tag{35}$$

b can be obtained from $C_{1,Y} = C_{1,\phi}$ assumption

$$b = \left(\frac{C_{1,\varepsilon}}{C_{1,\phi}} - a^{\alpha_\phi} \right)^{1/\alpha_Y} \tag{36}$$

With a, b and Y_λ, it is possible to characterize the correlation between two multifractal fields. Along with these parameters, JMF framework also introduces a simplified indicator of correlation, $IC_{\varepsilon\phi}$ ($\approx IC_{\phi\varepsilon}$)

$$IC_{\varepsilon\phi} = \frac{C_{1,\phi} a^{\alpha_\phi}}{C_{1,\varepsilon}} \tag{37}$$

More information on the intuitive indicator and exponents can be found in Gires et al. (2020b) along with validation of the framework with real and simulated data. IC is reported to be relevant for values of α, typically greater than 0.8. Here, the usage of JMF is briefly illustrated using two fields whose correlations are known - available wind power and wind velocity ($P_a \propto v^3$).

1.2.3.1 Illustration of JMF analysis

Here, we illustrate for pedagocical purposes the estimation of coupling between two geophysical fields using JMF, using their real data measured simultaneously over a given period from the same location. The fields under discussion are wind velocity (v) measured by 3D sonic anemometer and wind power available ($P_a = \frac{1}{2}\rho A v^3 C_p$, from Eq. 64 in section 3.1) calculated from it. Here, P_a corresponds to the maximum power that can be extracted from wind at the point; C_p is Betz constant and corresponds to this retrievable limit, A is the area swept by turbine rotors, and ρ is the air density at the region. ρ is generally considered fixed at 1.225 kg.m^{-3}, the sea level value at 15 °C; here we use a dynamic value based on temperature, pressure and humidity of the location (Picard et al. (2008), see section 3.1). P_a is calculated by basing on the specifications of Vestas V90 installed at same location (section 1.1.3), and from horizontal wind (assuming cancellation of the vertical component by gravity, and predominant wind flow in the horizontal plane perpendicular to blades).

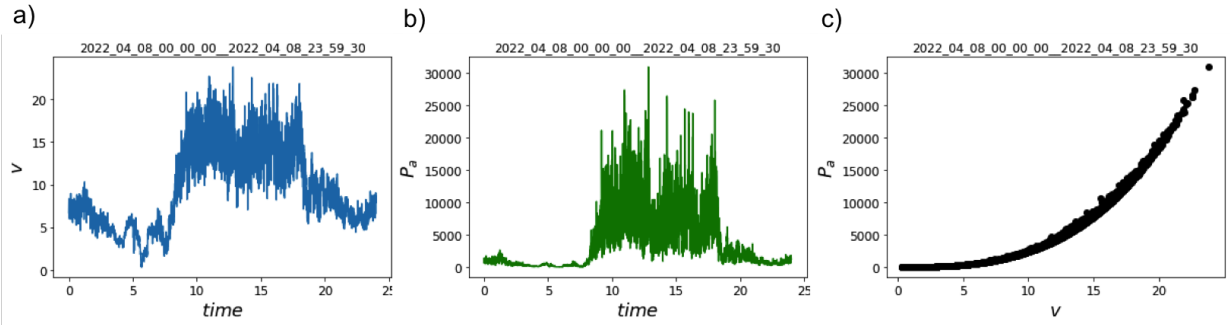

Figure 1.19: a) Time series of horizontal velocity (v), b) Time series of power available with varying air density (P_a), and c) Scatter plot of P_a and v (this is following the proportionality of $P_a \propto v^3$).

For estimating the coupling between two fields, it is important that the fields studied have physical significance to be correlated; and to study it in the framework of JMF, the fields should be multifractal. Fig. 1.20 shows the UM plots of $P_{a\lambda}$ and v_λ for the day 08 April 2022, from 3D anemometer on the meteorological mast (80m height, Location 1) at Pays d'Othe wind farm (quicklook of the day is shown in Fig. 1.8). An observational scale time step of 15 s (same as data obtained from Vestas V90) was used here for ease of illustration (see Fig. 1.19).

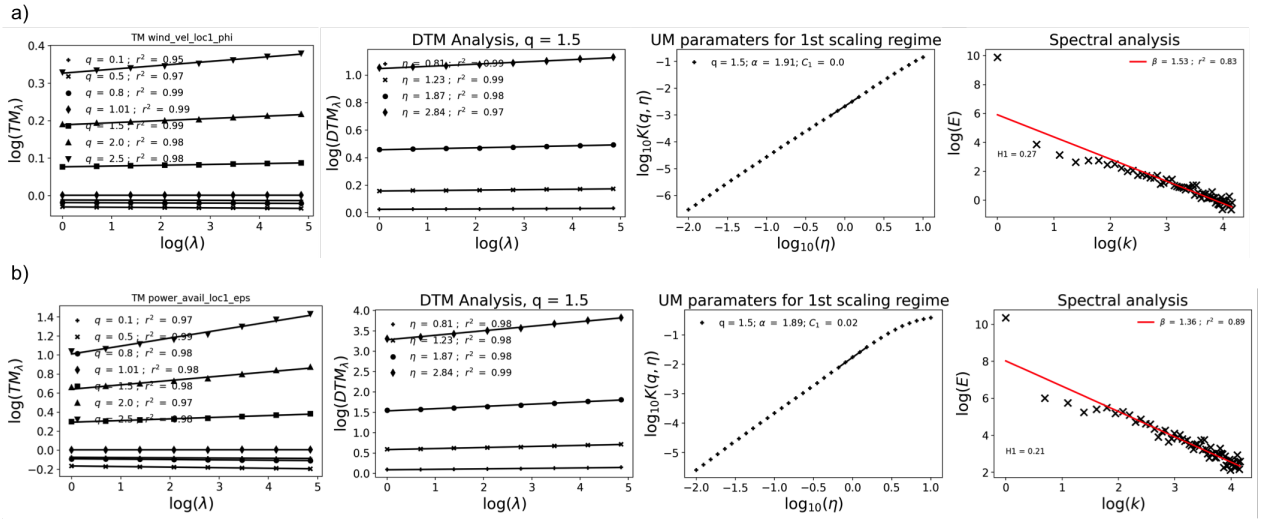

Figure 1.20: TM analysis (Eq. 14 in log-log plot), DTM analysis (Eq. 22 in log-log plot), DTM curve (Eq. 21 in log-log plot) and spectral analysis (Eq. 8 in log-log plot) of 1 day data (08/04/2022) for a) horizontal wind at 15 s, and b) available power (P_a) at 15 s (both as ensemble at a sample length of 30 min). $K(q)$ vs. q plots are shown in next figure.

Both of the fields show good scaling with UM values within the required limits and values of non-conservation parameter H below 0.5. Now, the framework of JMF is imposed for seeing the correlation between the fields; here, we are looking to confirm the known proportionality ($P_a \propto v^3$) with the value of JM exponent a when the fields are expressed as a mathematical combination of one another: $P_{a\lambda} = \frac{{v_\lambda}^a {Y_\lambda}^b}{({v_\lambda}^a {Y_\lambda}^b)}$ (as in Eq. 29).

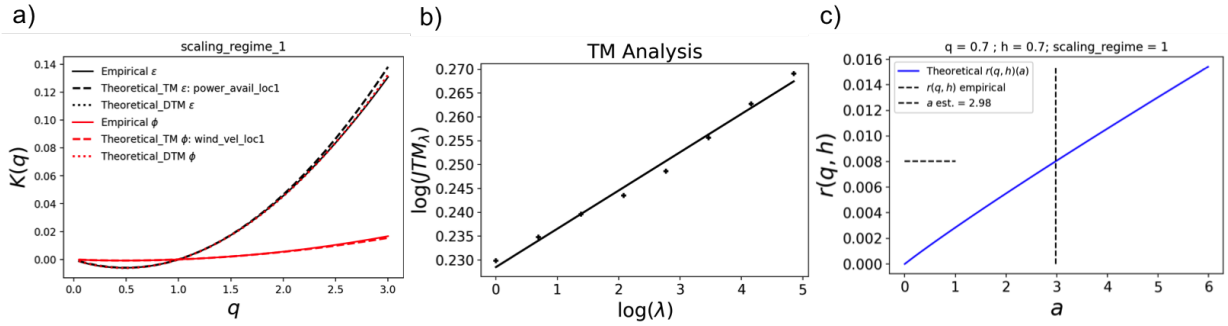

Figure 1.21: a) K(q) plots for $P_{a\lambda}$ and v_λ , (b) JTM plot for the joint field (Eq. 28 in log-log; the slope gives get r(0.7,0.7), and c) Estimation of JMF parameter a (Eq. 31). Samples are prepared as an ensemble of size 128 (30 minutes), for day 08/04/2022.

Fig. 1.21a shows the theoretical and empirical $K(q)$ of both fields (from individual UM) which are in good correspondence with each other; this shows that the UM estimates are good enough for being applied in JMF calculations. Fig. 1.21b shows the trace moment of joint multifractal field

(obtained from joint moments as in Eq. 28 for every resolution λ). From Fig. 1.21c, it can be seen that the value of a is estimated from $q = h = 0.7$ as mentioned previously. The retrieved value of 2.98 is in good agreement with the expected value of 3. The quality of scaling of the joint field is given by $r^2{}_{JMF}$, which is 0.989. It is also worth noting that the values of critical order of moments q_s and q_D here are well within the limits required for reliable estimation of JMF (q_s, $q_D > ha + q$, ha, and q).

1.3. Presentation of research outputs

As explained in this chapter, atmospheric fields inherit the scale invariant properties of governing Navier-Stokes equations and using the framework of universal multifractals, it is possible to quantify the small scale variability and intermittency across the scales using few parameters of physical meaning. The datasets introduced in this chapter are analysed in this line with the methodologies discussed. The results are presented in upcoming chapters, in two parts - individual UM analysis of various atmospheric multifractals and JMF analysis between various fields. Results presented involve statistical characterization of various stochastic fields across scales, and hence further validation of the scale invariant methodologies presented.

Chapter 2 deals with individual analysis of rainfall, kinetic energy and indirect analysis of particle concentration through extinction coefficient. In chapter 3, the fields are analysed jointly with emphasis on correlations between them. This chapter also includes the experimentation inside sense-city, and analysis of the scavenging coefficient of aerosol particles. Specifics of the result presentation in each chapter are briefly provided in corresponding introductions.

2. Independent multifractal analysis of atmospheric fields

In this chapter, various atmospheric fields are studied individually using UM analysis and examined for their small-scale variability, with the intention of understanding their scaling behaviour and characterizing it using UM parameters. This understanding is then applied to real-world applications and specific use cases are proposed. Section 2.1 is adapted from Jose et al. (2022) where a scale invariant relationship between rainfall intensity (often directly available) and rainfall kinetic energy (direct measurements are scarce), which has strong consequences on erosion in the soil as well as external structures such as wind turbine blades. For this purpose, directly measured data from three different disdrometers for around 7 years (at TARANIS observatory) were used (refer section 1.1.1). The results from UM analysis enabled development of a power law relationship between both fields (reinforced by previous results in literature and theoretical equations) without relying on any assumptions of drop size distributions.

In section 2.2, the parameter extinction coefficient which characterizes the light attenuation in the atmosphere is analyzed using UM framework. This coefficient is used in defining atmospheric visibility; here, we propose it as the actual field to be studied for characterizing the variability in visibility. Visibility is a subjective measurement whose values are adjusted to follow application-specific ranges. This notably results in the implementation of an upper threshold, which causes limitations in statistical analysis of the objectively measured extinction coefficient. This is identified and discussed in the framework of UM using real data and numerical simulations as well as theoretical computations.

2.1. Scale invariant relationship between kinetic energy (KE) and rainfall intensity (R)

2.1.1. Introduction

The importance of studying rainfall with its drop size distribution (DSD) and kinetic energy is examined here with its practical implications. And various commonly used formalisms of KE in literature are reviewed in the context of the current study.

2.1.1.1 On the importance of rainfall and kinetic energy

Understanding the relation between rainfall rate (R) and kinetic energy (KE) is essential for accurate determination of various rainfall parameters and understanding their after effects on surrounding ecosystem (Karlen et al., 2003). It has been well established that onsite erosion of soil - splash and runoff - depends on DSD and fall velocity of the spectrum (Ellison, 1944; Fernández-Raga et al., 2017). Hence, KE and R are primarily used to quantify rainfall erosivity and to estimate erosion rates in universal models towards sustainable land use planning (Angulo-Martínez et al., 2012; Shojaei et al., 2020; Mohamadi and Kavian, 2015). Erosion heavily affects agricultural sector: On on-site level, it impoverishes the top soil off nutrients and organic matter along with their

water holding capacity; this in turn increases the use of fertilizers and hence causes pollution at the recipient end of off-site erosion. Further, on off-site level, soil transport by erosion can trigger flood events through silting up of basins and rivers (Pimentel, 2006; Enne et al., 2000). Rainfall erosivity is a key parameter in various erosion models such as US based Universal Soil Loss Equation (USLE, Smith and Wischmeier, 1962) and its revised version (RUSLE, Renard et al., 1997), South Korean based SEMMA models for calculating soil loss (Deog Park et al., 2012), and in European models such as EUROSEM, WaTEM etc. that account for sediment transportation along soil loss (Morgan et al., 1998; Van Oost et al., 2000; Kirkby et al., 2008, an advance on USLE). Most of these frameworks use KE as the major quantifying factor for estimating erosivity at spatial scales as rainfall KE represents the total energy available for detachment and transport of soil on surface of impact. As direct measurement of KE is limited to specific geographical locations possessing required instrumental capabilities, understanding the relationship between KE and the more commonly available rainfall parameter, R, is important in estimating the former in more places.

Accurate estimation of rainfall KE is also important in understanding and mitigating leading-edge erosion (LEE) on wind turbine blades. Erosion damage reduces aerodynamic performance of blades resulting in reduced annual energy production and increased downtime (Keegan et al., 2013). Though LEE involves a multitude of atmospheric factors, impact velocity and amount of precipitation have been established as some of the major external factors in erosion (Herring et al., 2019). As in soil erosion, larger drops with greater mass and vertical terminal velocity causes a disproportionate amount of erosion in LEE also. Rainfall KE helps to quantify the impact of droplets hitting perpendicular to the surface and hence rainfall erosion on blades which is the accumulated aggregate of multiple impacts stochastically distributed over the surface of the coated laminate (Bech et al., 2018). In Whirling arm rain erosion test (WA-RET) (ASTM-G73-10, 2017; Liersch and Michael, 2014; DNVGL-RP-0171, 2014), the industrial standard for measuring durability of leading-edge structures, specimens are subjected in controlled velocity and rain conditions to assess the damage caused by droplet impacts (Bech et al., 2018). Considering the rapid growth of offshore wind industry as sustainable clean energy solution in the Americas and Asia with monsoon seasons, proper representation of KE and R is important in quantifying LEE in wind turbines.

2.1.1.2 Review of existing relations and need for a scale invariant representation

Application of erosion frameworks such as USLE or RUSLE poses uncertainties because of their empirical basis which has single or limited measurement locations and specific methods of data collection. These frameworks take KE as the major quantifying factor for erosivity, and employ various corrections to mitigate overestimation at low intensity rainfall as smaller droplets are less effective in soil detachment (van Dijk et al., 2002). Another commonly used erosivity index is rainfall momentum, but it has been shown that for natural rainfall they exhibit similar relationship with rainfall intensity (Hudson, 1971). These models are based on traditional two parameter exponential rain drop size distribution models developed from smaller sample collection methods such

as flour pellets or stain paper (Laws and Parsons, 1943; Marshall and Palmer, 1948). Later studies using multi parameter radiometry and disdrometers have shown improvements in measurement if DSD is assumed to be a three parameter gamma distribution (Ulbrich, 1983). Gamma distribution assumes fewer large drops in rain and represents a narrower DSD than the exponential one, and thereby reduces the overestimation of KE by the latter. For recording DSD and in turn obtaining empirical KE, disdrometers are commonly used in meteorological campaigns, where fall velocity is either directly measured or estimated from empirical relations (Gunn and Kinzer, 1949; Atlas et al., 1973).

There has been various studies towards accurate representation of $KE - R$ relationship. Fox (2004) demonstrates the impact of formulation of DSD in calculation of KE and hence on erosion. Smith and Wischmeier (1962) proposed a logarithmic function based on DSD formulation by Laws and Parsons (1943) and terminal velocity by Gunn and Kinzer (1949). It was used in modelling erosion in USLE, which was later replaced by continuous exponential functions in revised USLE approach (Renard et al., 1997; Brown and Foster, 1987). Other proposed forms of $KE - R$ equations were linear (Kinnell, 1981; Sempere-Torres et al., 1998), polynomial (Carter, 1979) and power-law (Park et al., 1982). Critical literature appraisal by van Dijk et al. (2002) on various $KE - R$ relations lists measurement techniques and procedures, sampling biases, interpretation methods and storm types as reasons for discrepancies and suggests another exponential based predictive equation. More recent reviews such as Angulo-Martínez and Barros (2015), Wilken et al. (2018), Mineo et al. (2019) shows lack of universality among various $KE - R$ relationships (logarithmic, linear, power law and exponential) using disdrometer measurements and modelling at different geographic stations, meteorologic conditions and time aggregation used for calibration.

Most of the empirical formulations express KE as volume specific - kinetic energy per unit area and mm of rainfall or KE_{mm} ($\mathrm{J\,m^{-2}\,mm^{-1}}$) due to prevalence of non automated measurements and lack of accuracy in determining exposure time. But expression of volume specific kinetic energy creates a statistical artefact (spurious ratio correlation) in $KE - R$ relationship due to the inclusion of R ($\mathrm{mm\,h^{-1}}$) in the KE_{mm} expression. Salles et al. (2002) suggests usage of more consistent time specific KE or KE_{time} ($\mathrm{J\,m^{-2}\,h^{-1}}$) that has been shown to produce less heteroscedasticity than corresponding $KE_{mm} - R$ scatter plots. For representing erosion, KE_{time} has been expressed as the rate of expenditure of rainfall kinetic energy (Kinnell, 1981), rainfall or kinetic power (Smith and De Veaux, 1992) and rainfall kinetic energy flux density (Steiner and Smith, 2000). The two expressions are related to each other through rain intensity and hydrological studies usually harmonize $KE - R$ relationships with KE_{time}.

$$KE_{time} = R \times KE_{mm} \tag{38}$$

In this section the expressions for KE are derived and analyzed in the form of KE_{time} unless other-

wise specified.

Due to variations in methodologies used and DSD characteristics during measurement, different functional forms show different behaviour towards $KE - R$ estimation. Though commonly preferred, exponential relations have been shown to underestimate KE_{time} for lower intensities of rainfall (Carollo and Ferro, 2015). Power-laws that predict kinetic energy well at lower intensities tend to overestimate the same for higher intensities. Logarithmic curves are limited in their usage though they fit low and high intensity KE rather decently (van Dijk et al., 2002). Further due to the empirical formulation, when it comes to expressing KE_{time} vs R, most of these mathematical equations fail to have much physical justification. Using generalized scaling formulation that expresses various existing DSD models as it's special cases (Torres et al., 1994; Sempere-Torres et al., 1998), Salles et al. (2002) found that power law is the most suitable function to relate KE_{time} and R from a microphysical point of view. The parameters (prefactor and exponent) of power law are related to rain type, geographical location and measuring technique. Shin et al. (2016) has proposed a representative power law based on the ideal assumption that the drop-size is uniformly distributed under the constant rainfall intensity.

2.1.1.3 Purpose of the study

Current literature on KE and R lacks a common consensus on the usage of expression that is valid across various scales of measurement, hydro-meteorological regimes or observation techniques. There is an increased focus on research characterizing rainfall microphysics at local and regional scales (Petan et al., 2010). Here we examine the variation of KE and R for over 7 years in Paris region using continuous data from three disdrometers from two different manufacturers. Using the framework of Universal Multifractal (UM) (Schertzer and Lovejoy, 1987), efforts were made to characterize the variability of KE_{time} and R on event based and year based analysis, and to formulate a scale invariant relation based on power law relationships. Multifractals allow characterization of complex geophysical fields with a limited number of scale invariant exponents (see Schertzer and Tchiguirinskaia, 2020, for a recent review). Multifractal behaviour of measured rainfall has been abundantly studied previously (see Gupta and Waymire, 1990; Kumar and Foufoula-Georgiou, 1993; Deidda et al., 1999; Olsson and Niemczynowicz, 1996; García-Marín et al., 2008; Langousis et al., 2009; Emmanouil et al., 2020, for some examples among others). Fractal tools and UM framework are used extensively in hydrology for modeling and analysis (Gires et al., 2017b). Wolfensberger et al. (2017) & Schertzer and Lovejoy (2011) used UM in climatological analysis of precipitation - modelled and actual - in relation to external geographical and meteorological descriptors. Checking the validity of UM framework on KE, which was never done to the knowledge of the authors, is a first goal of the section. The main goal of this section is to explore the possibility of establishing a physically based scale invariant power law relationship between KE and R using the UM framework, without having to rely on strong assumptions on DSD shape; and compare its performance with more classical approach.

This study is structured as follows. In section 2.1.2 the methodology used is detailed. First, the commonly used framework of gamma distributed DSD which yields a power-law relation is reminded along with the associated parameters' estimation techniques. Then, the process to identify power-law relation in the UM framework is explained after a required reminder on the theoretical underlying basis. Similarly, the associated parameters' estimation techniques, which will be implemented, are described. section 2.1.3 includes details of data collection and quality control. Results are discussed in section 2.1.4 where validity of formulated relation is tested and contrasted over different types of rain events. The final sub section, section 2.1.5, concludes the study and summarizes the main observations.

2.1.2. Methodology: Theoretical relation assuming gamma distributed DSD

2.1.2.1 Rainfall microstructure and commonly used gamma distribution

Rainfall is measured and represented as distribution of raindrops in different diameter classes or drop size distribution (DSD) and their corresponding terminal fall velocity in stable air. For meteorological purposes, size distribution of raindrops is represented as mean number of drops per unit volume in a particular diameter (more precisely equivolumic diameter, i.e. the diameter of a drop with the same volume but a spherical shape) range between D and $D+dD$, $N_v(D)$ (m^{-3} mm^{-1}). However, in hydrological studies, DSD measured by ground based devices such as disdrometers or optical spectrometers are represented as mean number of raindrops in a particular diameter range arriving at a surface per unit area per unit time, $N_A(D)$ (m^{-2} mm^{-1} s^{-1}). If effects of wind, turbulence and raindrop interactions are neglected, $N_v(D)$ and $N_A(D)$ are related as follows (Uijlenhoet and Stricker, 1999) :

$$N_A(D) = v(D)N_v(D) \tag{39}$$

where $v(D)$ represents the terminal fall velocity ($\mathrm{m\,s}^{-1}$) as a function of the equivalent spherical diameter of raindrop D (mm).

Traditional mathematical expressions describing $N_v(D)$ such as exponential (Marshall and Palmer, 1948), weibull (Best, 1950), gamma (Ulbrich, 1983) and lognormal (Feingold and Levin, 1986) can be expressed as particular case of general formulation proposed by Sempere-Torres et al. (1998). For the scope of this section, gamma distribution of DSD, which has been recognized to better represent natural rain, will be considered (Ulbrich, 1983). In this framework :

$$N_v(D) = N_0 D^{\mu} e^{-(\Lambda D)} \tag{40}$$

where $N_v(D)$ is in $\mathrm{m}^{-3}\,\mathrm{mm}^{-1}$, D in mm, N_0 (in $\mathrm{m}^{-3}\,\mathrm{mm}^{-1-\mu}$), μ and Λ (in mm^{-1}) are distribution parameters measuring raindrop concentration, mean size and shape of spectrum respectively. Λ is

usually expressed with the help of the median volume diameter D_0 as $\Lambda = (3.67 + \mu)/D_0$.

2.1.2.2 Theoretical power law relation between R and KE

Rainfall intensity or rain rate (R, in $\mathrm{mm\,h^{-1}}$) can be calculated from $N_A(D)$ using following expression (Steiner and Smith, 2000) :

$$R = 3.6 \times 10^{-3} \frac{\pi}{6} \int_0^\infty D^3 N_A(D) dD \tag{41}$$

Kinetic energy per unit area per unit time (KE_{time} in $\mathrm{J\,m^{-2}\,h^{-1}}$) of falling drops can also be expressed in terms of measured $N_A(D)$ as follows (Steiner and Smith, 2000) :

$$KE = 3.6 \times 10^{-6} \frac{\pi \rho}{12} \int_0^\infty D^3 v^2(D) N_A(D) dD \tag{42}$$

where ρ is density of water in standard conditions in ($\mathrm{kg\,m^{-3}}$).

Though there are more sophisticated equations proposed in the literature for $v(D)$, for simplicity in calculation, here we are following the widely used power law formulation by Atlas and Ulbrich (1977). Uijlenhoet (2001) demonstrated it has the only functional form consistent with power law relationship between rainfall related parameters :

$$v(D) = c D^g \tag{43}$$

$c = 3.78\,\mathrm{m\,s^{-1}mm^{-g}}$ and $g = 0.67$ (with v in $\mathrm{ms^{-1}}$ and D in mm).

Most of the rainfall parameters can be approximated as moments of the DSD; and when DSD follows gamma model, the n^{th} moment, M_n can be computed as (Atlas and Ulbrich, 1977) :

$$M_n = \int_0^\infty D^n N(D) d(D) = N_0 \Lambda^{-(\mu+n+1)} \Gamma(\mu + n + 1) \tag{44}$$

where $\Gamma(\alpha)$ is the complete gamma function

$$\Gamma(\alpha) = \int_0^\infty x^{\alpha-1} e^{-x} dx, \quad \text{where } \alpha > 0. \tag{45}$$

Substituting equations 39, 40, 43 and 44, and solving the integral gives reduced expressions for KE and R in terms of gamma function;

$$R = 6 \times 10^{-4} \pi c N_0 \frac{\Gamma(4+g+\mu)}{\Lambda^{(4+g+\mu)}} \tag{46}$$

$$KE = 3.6 \times 10^{-6} \frac{\rho \pi c^3}{12} N_0 \frac{\Gamma(4+3g+\mu)}{\Lambda^{(4+3g+\mu)}} \tag{47}$$

This reduction using gamma function enables representation of KE and R in the form of a power law as follows :

$$KE = bR^a \tag{48}$$

where

$$\begin{aligned} a &= \frac{4+3g+\mu}{4+g+\mu} \\ b &= 5 \times 10^{-4} \rho c^2 \left[6\pi c N_0 \times 10^{-4}\right]^{1-a} \frac{\Gamma(4+3g+\mu)}{(\Gamma(4+g+\mu))^a} \end{aligned} \tag{49}$$

The final expression follows the same pattern as that by Salles et al. (2002) based on generalized DSD and that of Uijlenhoet and Stricker (1999) based on exponential DSD. When $\mu = 0$ gamma distribution for DSD becomes a simple Marshall and Palmer negative exponential parameterization representation of DSD (Marshall and Palmer, 1948) with Eq. 48 becoming $KE = 8.539R^{1.287}$. Same values were obtained for exponent 'a' and pre-factor 'b' using the general function proposed by Salles et al. (2002) for Marshall and Palmer approximation. Closer value of exponential coefficient were also reported by Uijlenhoet and Stricker (1999) in a power law formulation based on Marshall and Palmer (1948) approximation of DSD and power law dependence of rain drop terminal velocity, Eq. 43 (Atlas and Ulbrich, 1977).

Many simplifications were followed in this formulation of KE-R relation as a power law (Eq. 48). Gamma DSD is notably assumed as well as a power law form for terminal fall velocity as function of diameter. This approximation shows limitations at higher values of diameter ($D > 5$ mm) and doesn't account for atmospheric turbulence or updrafts and downdrafts (Adirosi et al., 2016). Effect of truncation errors in measurement is not considered. The formulation also ignores the effect of horizontal wind velocity and surface impact angle of rain drops. Some authors tend to consider normalized spectra of DSD (Testud, 2001) that requires only two parameters to describe the DSD; it was also not considered here for the sake of simplicity in deriving a theoretical relation between KE and R. It should be noted that although widely accepted as the best representation of natural DSD, gamma function also has associated errors that exists outside experimental methodology and sampling (Adirosi et al., 2014).

2.1.2.3 Estimation of power law coefficients from gamma DSD parameters

As mentioned before, most rainfall parameters can be expressed as moments of the DSD according to Eq. 44. The right hand side of the equation is specific to the non normalized three parameter gamma distribution considered here, as shown in Eq. 40. In practice DSD is not measured continuously but for discrete diameters D_i. As a consequence, the estimated moments $\hat{M}_n$ of order n are computed thanks to the following discrete sum rather than previous integral :

$$\hat{M}_n = \sum_{i=1}^{N_{class}} D_i^n N_i(D_i) \Delta D_i \qquad [\mathrm{mm}^n \mathrm{m}^{-3}] \tag{50}$$

where D_i is the diameter of droplet in class i, $N_i(D_i)$ is the drop size distribution (estimation discussed in section 1.1.1), ΔD_i is the width of diameter class i and N_{class} the total number of diameter classes.

Investigation of various DSD parameter estimating methods by Cao and Zhang (2009) highlighted the risk in usage of maximum likelihood and L-moment estimators for processing data with truncation in lower end of DSD spectra. As all disdrometers are limited by some minimum value of measurable diameter D_{min} (> 0), it is advisable to use traditional method of moments (Brawn and Upton, 2008). Although the choice of moments for proper parameters estimation with the method of moments is a relevant topic, it is outside the scope of this analysis. Hence, authors relied on the existing literature. More precisely, although higher DSD moments are considered to be associated with higher errors, the tendency of lower errors with middle order moments was shown later in Smith et al. (2009) (using radar measurements) and Cao et al. (2008) (using joint disdrometer-radar observations). Cao and Zhang (2009) evaluated the performance of various moment estimators using simulations of gamma DSD (with a more realistic estimation of errors) and found that second, third and fourth moments (M234) as the best overall performer for estimating R. Konwar et al. (2014) (M234) and Huang et al. (2021) (even higher order moments - 2, 3 and 6) are some recent examples of using middle order moments while analysing data from same disdrometer make as the one in current study (OTT Parsivel^2). Hence, it was chosen to employ these moments for computing gamma DSD parameters: μ, N_0 and Λ (refer Eq. 44). Specific moment equations are provided in the appendix (Appendix A.1). These parameters are then introduced in Eq. 49 to derive the expected power law parameters assuming a gamma DSD.

Variation of a and b with DSD parameters is examined with the available data set in section 2.1.4 for different type of rainfall events.

In this study, both KE and R time series were analysed using UM framework introduced in section 1.2.2. An overview of the framework, estimation of scaling behaviour and UM parameters, and practical implementation of power law relationship between two multifractal fields are discussed

in detail there. As the UM model discussed here is solely non negative, it removes all possibility of having non-negative values for both fields in analysis. Using their UM parameters in Eq. 27, it is possible to formulate power law relationship in the format of Eq. 24. It has the same shape as the theoretical power law obtained using moments of the DSD in section 2.1.2, in Eq. 48. Details of disdrometer data collection and subsequent multifractal analysis are covered in upcoming sections.

2.1.3. Data collection and instrumentation

Details about the measurement campaigns, data and instrumentation are addressed in detail in section 1.1.1. To briefly recapitulate, continuously monitored data in natural conditions was obtained from three optical disdrometers operating with two different principles. The devices are part of the TARANIS observatory (exTreme and multi-scAle RAiNdrop parIS observatory, Gires et al., 2018) of the Fresnel Platform of École des Ponts ParisTech (*https://hmco.enpc.fr/Page/Fresnel-Platform/en*); and are operated on its campus by the Hydrology Meteorology and Complexity laboratory of École des Ponts ParisTech (HM&Co-ENPC) from 18 June 2013 to 27 Dec 2019, except during a national measurement campaign from November 2016 to September 2017 when the devices were located at École Polytechnique, EP, which is roughly 30 km South-East.

2.1.3.1 Data quality and filtering

For the data used in this part, filters suggested by various authors (Kruger and Krajewski, 2002; Thurai and Bringi, 2005; Jaffrain and Berne, 2012; Gires et al., 2018) were used to remove possible non-meteorological measurements (from environmental factors such as splashing, horizontal wind etc.) on the basis of size and velocity of drops. Using the disdrometer data set, two series of Multifractal analysis were performed - event based and year based. For event based analysis, individual rainfall events were identified with following criteria in rain intensity time series - rainfall events with a cumulative depth greater than 0.7 mm and separated by at least 15 minutes of dry weather before and after. From all measured events with this condition, rain rate (R), drop size distribution (DSD) and kinetic energy (KE) were calculated for the three disdrometers (denoted Pars 1, Pars 2 and PWS hereafter). From the results further filtering was done to remove events having a percentage of *nan* values (not a number - blank /missing data) $> 1\,\%$ and R^2 value $<$ 0.9, for both KE and R. Remaining *nan*s were then replaced with 0. In year based methodology, continuous time series from Jan 2016 to Dec 2019 - including rain and no rain conditions - were used for multifractal analysis, and results were compiled according to the year of measurement.

There were minor lapses in continuity of data measurement from Jun 2013 to Dec 2015; for that reason those time periods were not considered in continuous year based analysis to avoid possible measurement biases. However, since selection of individual events are not affected by that, event based analysis involves data from Jun 2013 to Dec 2019. Lesser number of events can be observed in the excluded years for year based analysis in Table 2.1. Between 2016 and 2019, there were also a few days of maintenance where data was not recorded - 27 Sep 2017 to 26 Dec 2017, 01 to 07

Jan 2018 and 12 to 14 Apr 2019. After quality control for each disdrometer, a total of 214,665 time steps were analysed in 556 rain events (total 1610 events counting all three disdrometers; data was not always available for all the disdrometers, hence the lesser number) from 2013 to 2019 for event based analysis. In year based analysis, a total of 3,919,680 time steps were considered from 2016 to 2019; percentages of rainy time steps were about 7 %, 6.6 % and 5.7 % for Pars 1, Pars 2 and PWS respectively.

2.1.4. Results and discussions

2.1.4.1 Overview of analysis

For analysing the KE and R time series using UM framework, as explained in previous sections, two strategies were followed - event based analysis and year based analysis. For event based analysis, we identified a total of 556 rainfall events between 28 Sep 2013 and 31 Dec 2019 of which 493 events were common among all three disdrometers. For UM analysis, each time series was resized to the highest power of two in such a way that the trimmed series accommodated maximum rainfall cumulative depth and then the field was normalized. After resizing for UM analysis, length of individual events ranged from 64 to 2048 time steps, where each time step corresponds to 30 s, i.e. the recording time step of disdrometers used. KE and R from each events were analyzed as separate fields in UM framework. For year based methodology, similar procedure was followed for UM analysis on year long continuous time series, for the years from 2016 to 2019.

In coming subsections, estimation of UM parameters and power law relations are illustrated using one event data for event based analysis and one year data for year based analysis. Power law coefficients were also estimated using theoretical framework with DSD parameters as mentioned in section 2.1.2. Variation and correspondence among coefficients determined by UM and DSD parameters are discussed thereafter and validated with data.

2.1.4.2 Multifractal analysis of events

For illustration of the analysis carried out, one event from 2017 for Pars 1 disdrometer, that occurred on 16 September between 11:35:00 and 13:00:00 (local time) is presented here. Fig. 2.1a displays the time series of R and KE for this event, as well as KE vs. R plots. The latter also shows power law fits with coefficients from UM analysis and DSD parameters (explained later in this section). For this event, 171 time steps were trimmed to 128 time steps along region of maximum rain occurrence of which 124 were rainy data points. Trimmed and normalized KE and R were then subjected to analysis using UM framework discussed in section 1.2.2. Initial analysis indicated values of non-conservative parameter H greater than 0.5 among many events. Hence to retrieve a conservative field on which the UM analysis can be implemented without bias, fluctuations of KE and R time series were used (Lavallée et al. 1993). Characterization of variability in KE field for the event considered here can be seen in Fig. 2.1b with TM (Eq. 14 in log-log plot), DTM graphs (Eq. 22 in log-log plot) and UM parameter values. As shown in TM and DTM graphs, the field exhibits

a very good multifractal behaviour with a single scaling regime from 30 s to 64 min. For example, TM coefficient of determination r^2 for $q = 1.5$ was greater than 0.99. Values of UM parameters α, C_1, and H for KE of this particular event were 1.820, 0.311 and 0.547 respectively. It should be mentioned that H computed on the fluctuations of KE was found to be equal to 0.189, meaning the taking the fluctuations indeed enabled retrieval of a conservative field from the original smoother field. R also exhibited excellent scaling behavior and corresponding values of UM parameters α, C_1, and H for this event were 1.655, 0.229, and 0.100 respectively.

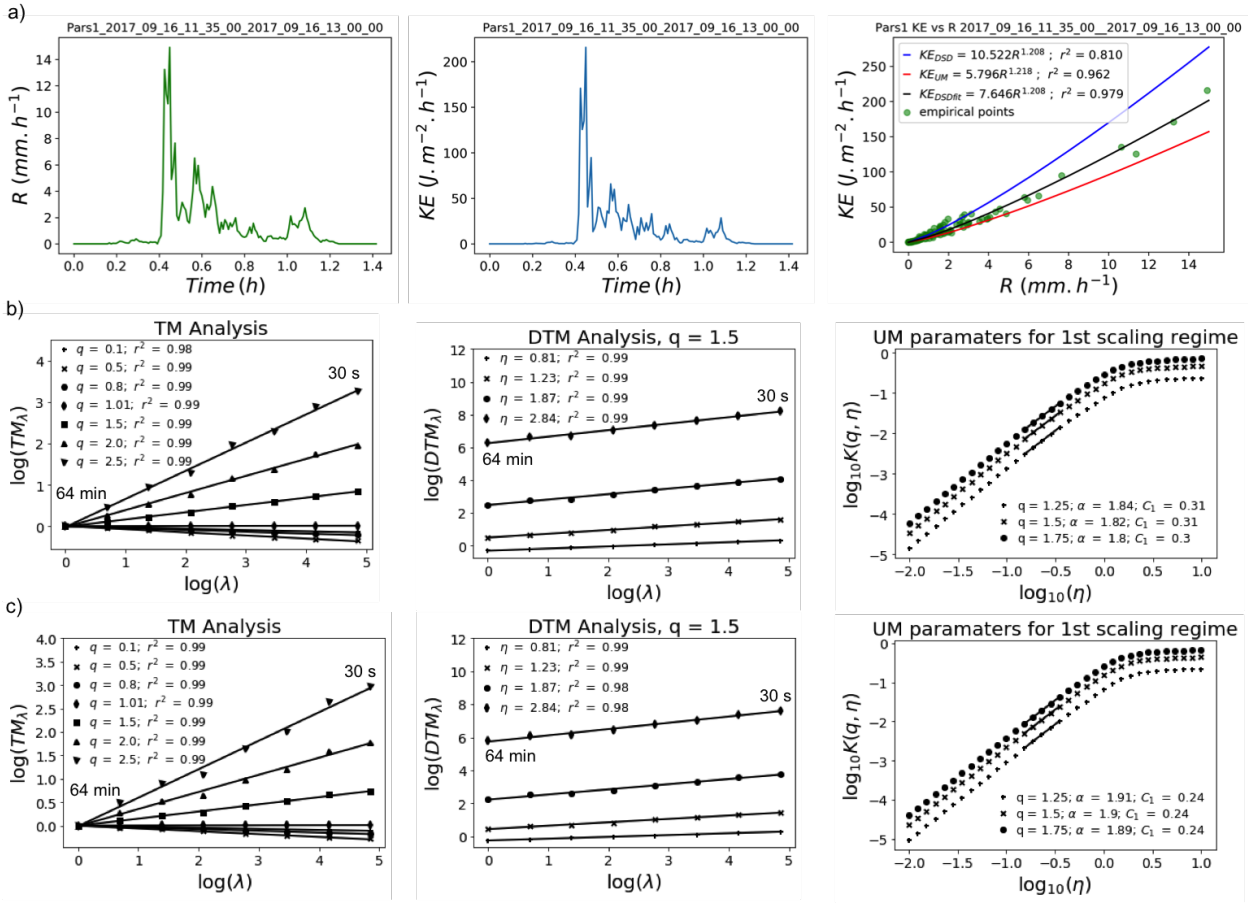

Figure 2.1: a) Time series of R, time series of KE, KE vs R graph b) and c) MF analysis graphs with KE and R (log-log plot of Eq. **??** and Eq. 22 for TM and DTM analysis respectively and log-log plot of exponents in Eq. 22 for UM parameters) for Pars 1 event 16 September 2017 11:35:00 to 13:00:00

KE and R analyzed from every event exhibited similar multifractal characteristics with a unique scaling regime. The quality of scaling was examined using coefficient of determination, R^2 for $q = 1.5$ in TM analysis, and as previously mentioned events with values < 0.9 were discarded. 9.8 % percentage of total events were rejected on this basis. For the events with good scaling behaviour, robust retrieval of multifractal parameters α, C_1, β and H was possible. For example, the assessed

values of α and C_1 for both KE and R time series, exhibited a maximum standard deviation (using various values of q in DTM analysis) of 0.0584 and 0.0670 for measurement at EP-SIRTA and 0.0446 and 0.0443 for measurements at ENPC.

Figure 2.2 displays the values of multifractality index α and mean intermittency C_1 for all the studied events for both fields. It appears that the values of α for KE and R are rather well distributed along the bisector. This pattern suggests a power law relation between these two quantities as discussed in section 2.1.2 (Eq. 24) where ε_1 and ε_2 are KE and R respectively (i.e. $KE = bR^a$ as in Eq. 48). The exponent of the power law a was deduced from corresponding α and C_1 values of UM fields (KE and R) for every event subjected to UM analysis, using the expected relations for power law related UM fields, i.e. Eq. 27. The α used is the average of α_{KE} and α_R (which were anyway similar). Value of prefactor b was estimated by fitting Eq. 48 at maximum resolution with estimated values of a on event's $KE - R$ graph. For the event used as illustration, we found a = 1.083 and b = 11.493. This power law fit from UM parameters is displayed in Figure. 2.1a as KE_{UM} in the KE vs. R graph.

Variation of computed power law exponent a and prefactor b are also shown in Fig. 2.2 as time series of events for each year. Graphs of remaining years are provided in Appendix A.2. For 3.5 % of total events filtered, estimates of α was found to be greater than the theoretical maximum (> 2); however a values for those events were found to be consistent with the overall average. Despite appreciable variability in UM parameters across events, values of a and b showed overall stability in the short range of values specified in graphs, suggesting robustness of the estimates. Year wise average values over the events for a and b, and number of events for all three disdrometers are given in Table 2.1. Average values of power law parameters from the events that were common between the three disdrometers are also shown in the same table. Comparable values of a and b were observed in both cases. A clear range of variation can be observed between the two types of disdrometers. For both Parsivel^2 the average a and b were similar and around 1.22 and 8.17 respectively, while for PWS100 a values were consistently lower than that of Parsivel^2 at around 1.17 and b values greater at 13.02. PWS generally registered slightly higher intensities than Pars 1 and Pars 2. It should be mentioned that a and b seem to show a very rough correlation where values of b decreases with increase in values of a. But between make of instruments, irrespective of the type and number of events, values of a remains rather constant. Differences in values obtained between Parsivel^2 and PWS is expected due to operational differences between disdrometers. Such effects are also reported in Johannsen et al. (2020) who showed biases in measurement and subsequent $R - KE$ relation due to difference in type of sensors used (three optical disdrometer were used). Angulo-Martínez and Barros (2015) also highlighted some differences among various Parsivel^2.

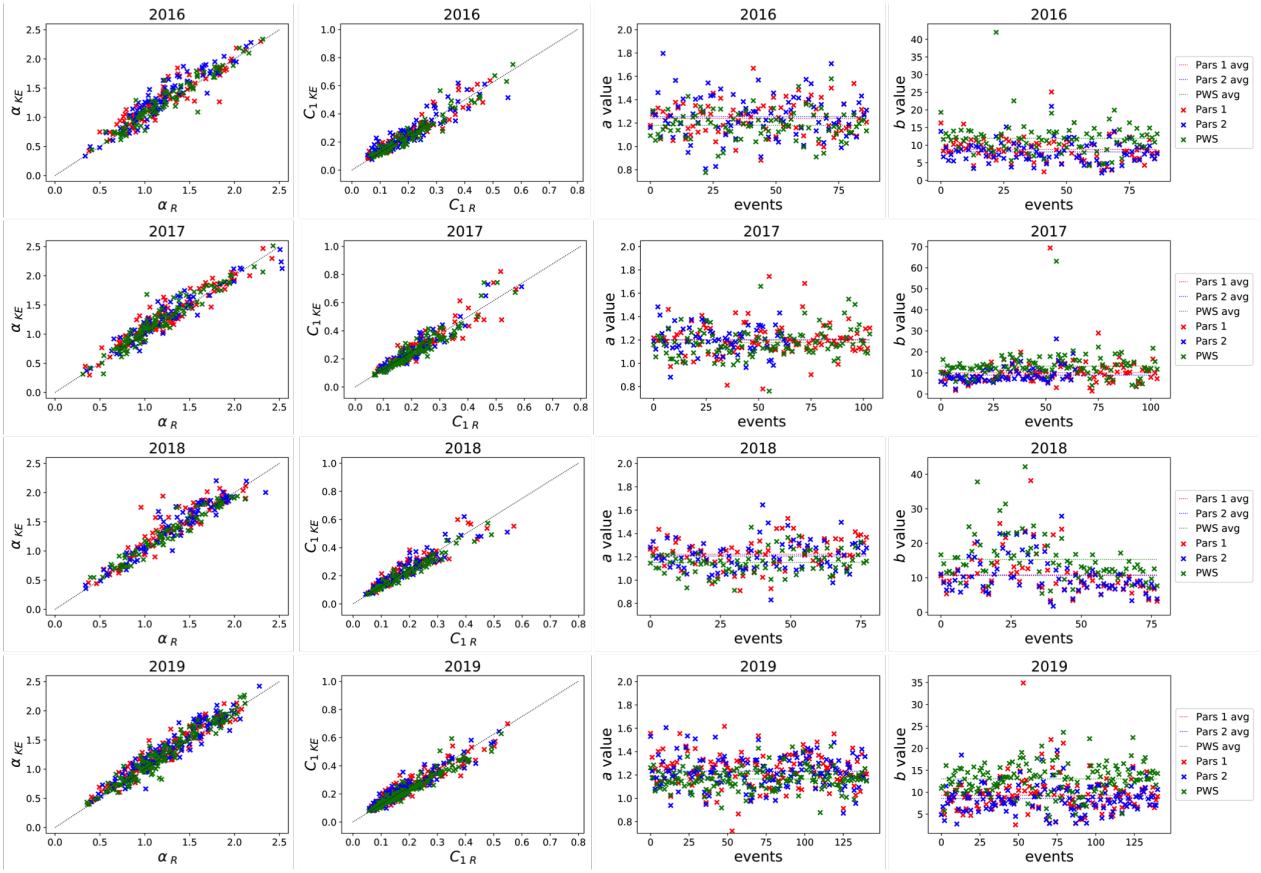

Figure 2.2: Year wise α and C_1 variation on event based analysis from 2016 to 2019 (remaining years are provided in Appendix A.2)

			total events			common events		
year	**location**	**disdrometer**	**# events**	**avg a**	**avg b**	**# events**	**avg a**	**avg b**
		Pars 1	29	1.248	9.224		1.246	9.224
2013	ENPC	Pars 2	11	1.254	9.093	11	1.254	9.093
		PWS	29	1.186	11.912		1.193	11.748
		Pars 1	84	1.207	11.548		1.207	11.548
2014	ENPC	Pars 2	84	1.186	11.065	84	1.186	11.065
		PWS	84	1.159	14.065		1.159	14.065
		Pars 1	38	1.235	9.459		1.235	9.459
2015	ENPC	Pars 2	38	1.207	8.532	38	1.207	8.532
		PWS	38	1.190	11.712		1.190	11.712
		Pars 1	87	1.238	8.802		1.238	8.802
2016	ENPC	Pars 2	87	1.253	8.069	87	1.253	8.069
		PWS	87	1.180	11.939		1.180	11.939
		Pars 1	102	1.197	10.126		1.193	10.013
2017	EP-SIRTA*	Pars 2	65	1.202	8.944	65	1.202	8.944
		PWS	104	1.176	13.238		1.151	15.282
		Pars 1	78	1.221	10.832		1.221	10.832
2018	ENPC	Pars 2	78	1.205	10.647	78	1.205	10.647
		PWS	78	1.151	15.282		1.151	15.282
		Pars 1	138	1.231	9.254		1.238	8.913
2019	ENPC	Pars 2	130	1.231	8.550	130	1.231	8.55
		PWS	141	1.165	13.024		1.649	12.960

Table 2.1: a, b and no. of events analysed between 2013 and 2019 according to location of measurement and disdrometer used.
* From Nov 2016 to Sep 2017 as shown in Table 2.4; preceding and succeeding years are adjusted accordingly, refer Table 2.4.

2.1.4.3 Multifractal analysis of continuous data (year based analysis)

To illustrate year based analysis, continuous time series and UM analysis for Pars 1 disdrometer for the year 2017 is shown in Fig. 2.3. Both KE and R fields showed similar multifractal features. Scaling behaviour of KE is shown in Fig. 2.3b. A unique scaling regime from 30 s to 311 days was considered.

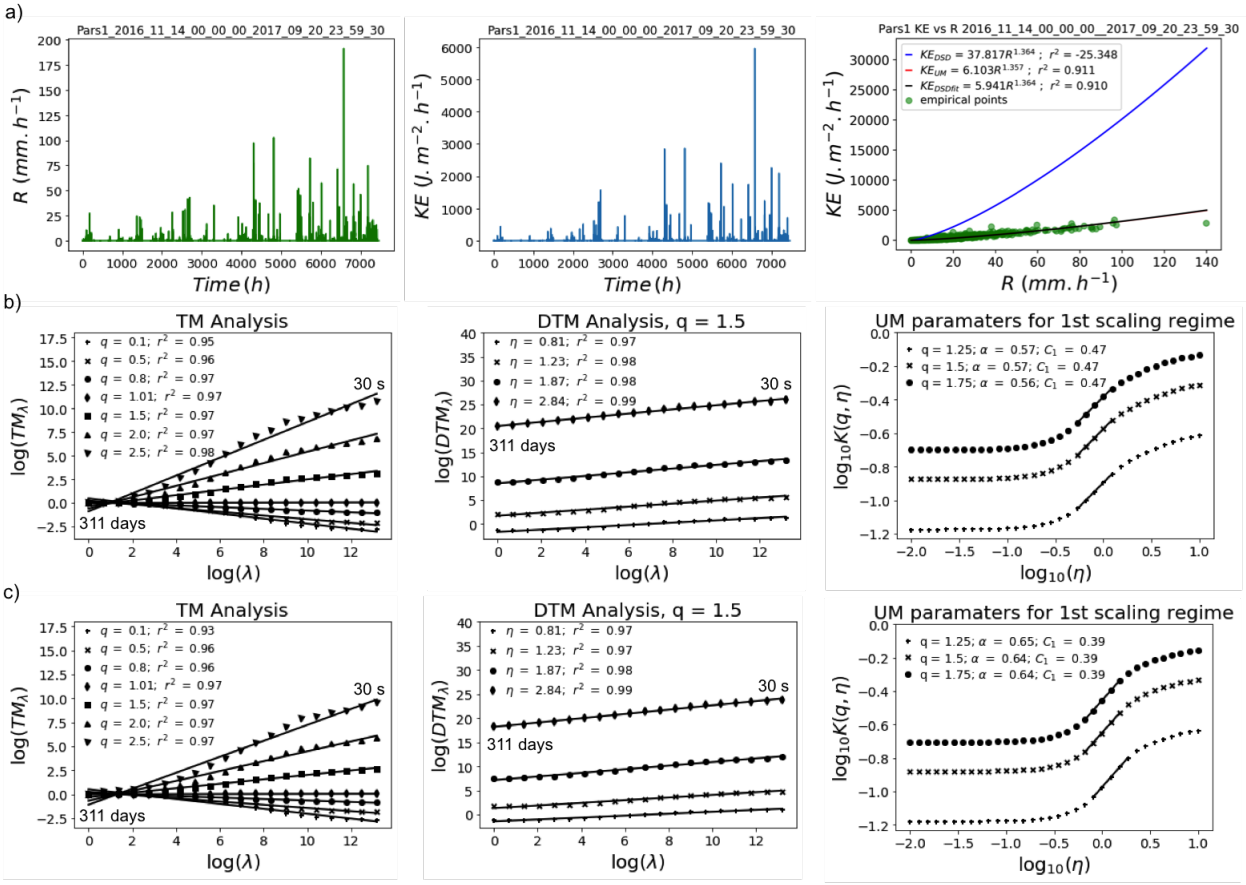

Figure 2.3: a) Time series of R, time series of KE, KE vs R graph b) and c) Multifractal analysis graphs with KE and R (log-log plot of Eq. 14 and Eq. 22 for TM and DTM analysis respectively and log-log plot of exponents in Eq. 22 for UM parameters) using the year based analysis, for Pars 1, for 2017

Variation of UM parameters α and C_1 between KE and R fields as well as values of power law exponent a and prefactor b (computed by fitting the relation at maximum resolution) are displayed in Fig. 2.4. Precise values of a and b according to the year of measurement are given in Table 2.2 in annexes. The curve KE_{UM} in the KE vs R graph of Fig. 2.3a, shows the power law fit using UM parameters for continuous data of 2016, for Pars 1. Values and trend of variation are similar to that observed for the event based analysis. This confirms the robustness of the discussed power law, which is valid and retrieved not only at the event scale, but also at the year scale.

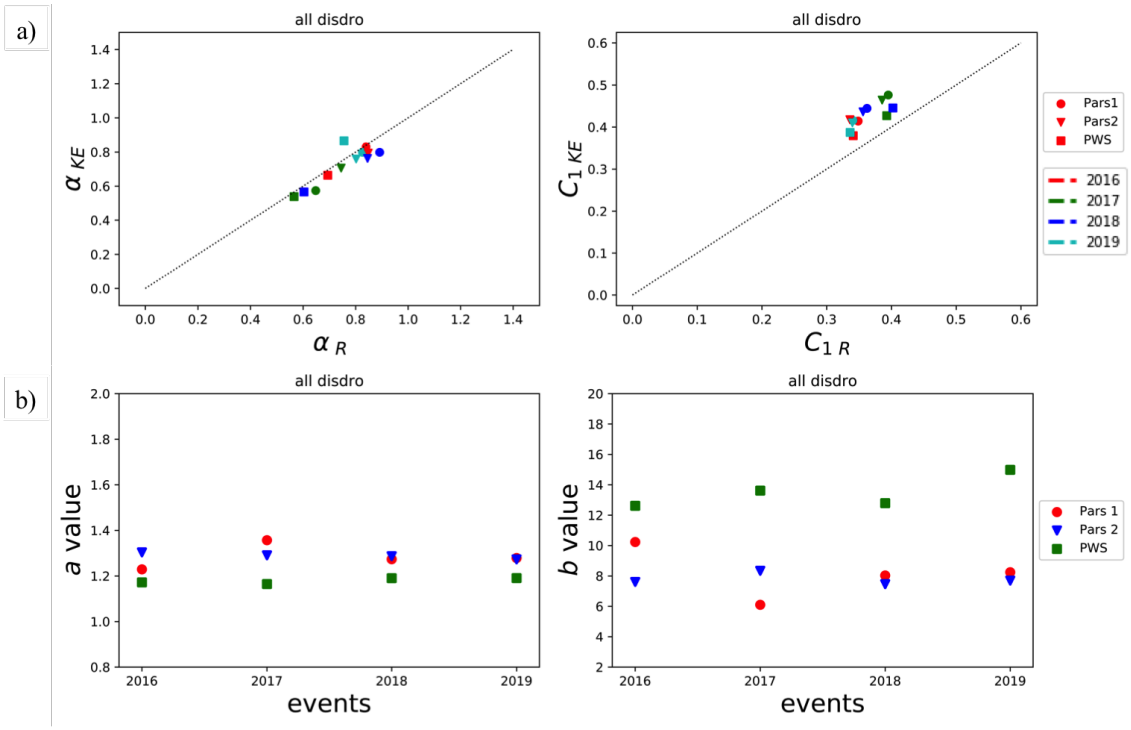

Figure 2.4: a) Results from multifractal analysis on continuous year wise data set: a) α and C_1 (DTM); b) a and b values

Disdrometer	coefficient	2016	2017*	2018	2019
Pars 1	a	1.229	1.356	1.273	1.278
	b	10.232	6.102	8.033	8.247
Pars 2	a	1.303	1.290	1.286	1.273
	b	7.605	8.338	7.463	7.695
PWS	a	1.171	1.164	1.190	1.190
	b	12.616	13.614	12.792	14.981

Table 2.2: a and b from year based analysis, from 2014 to 2019 according to disdrometer used for measurement.
* From Nov 2016 to Sep 2017 as shown in Table 2.4; preceding and succeeding years are adjusted accordingly

2.1.4.4 Power law coefficients from DSD parameters

To understand previous findings further, values of a and b were computed from theoretical framework discussed in section 2.1.2. Rainfall DSD was assumed to follow gamma distribution (Eq. 40) and theoretical values of a and b (denoted as a_{DSD} and b_{DSD} from here on for clarity) were computed as per Eq. 49 after estimating values of gamma DSD parameters (μ, N_0 and Λ) with the help of method of moments. The variation of rain rate R was accurately reproduced using M234 moment estimators (Fig. 2.7d for example). Theoretical power law relation ($KE_{DSD} = b_{DSD}R^{a_{DSD}}$) was then compared with the one estimated using UM analysis (represented from here on as KE_{UM}

with coefficients a_{UM} and b_{UM} for clarity) for every events. Average values of DSD parameters, estimation error and corresponding a_{DSD} and b_{DSD} for Pars 1 events are given in Tab. 2.3 according to event's rain type (definition introduced later). $RMSE_{DSD}$ is the root mean square error (RMSE) between empirical DSD and theoretical gamma DSD with fitted parameters (using the value for the center of each diameter class D_i). It is used here as an indicator of the quality of fit of the assumed gamma DSD distribution and the empirical one. For $RMSE$ estimation only the portion of DSD above 0.5 mm diameter class was considered as smaller drops have lesser contribution in overall KE and R, and are associated with greater uncertainties in measurement. Also, higher size drops (above 9 mm diameter class) were not observed during the events and are hence not shown in DSD figures discussed after (Fig. 2.5 and Fig. 2.7).

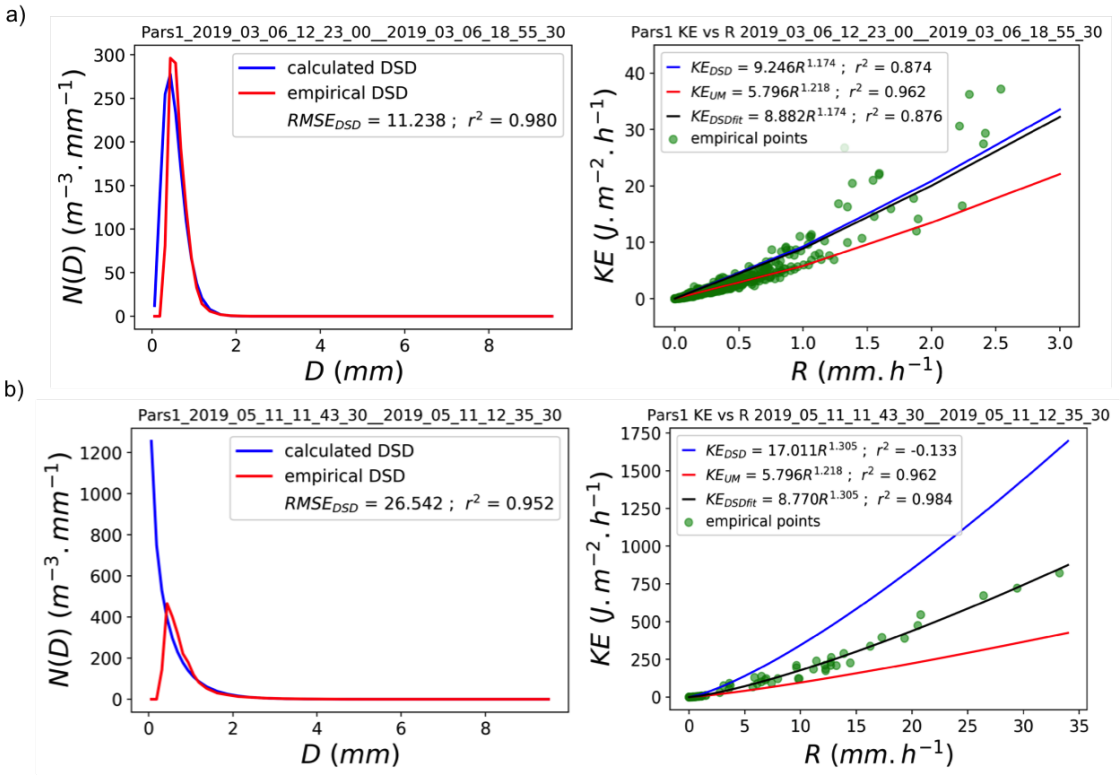

Figure 2.5: a) 2019 Pars 1 event where empirical DSD corresponds with gamma distribution and b) where it doesn't follow gamma distribution (DSD displayed only till diameter class around 9 mm as higher drops were not observed during the events)

Figure 2.5 represents two extremes cases among events from year 2019 for Pars 1: one event (Fig. 2.5a) where empirical DSD corresponds with a gamma distribution and one event (Fig. 2.5b) where it does not. The DSD fitting as well as the KE vs. R plots (fitted with power law relation from UM analysis and DSD extraction) are also displayed. For the event with empirical DSD closer to estimated gamma DSD, both power law relations (KE_{UM} & KE_{DSD}) are similar and show good

fit. For the other event, power law relation from DSD approach shows a considerable deviation from actual values of KE, with a strong overestimation. Power law from UM analysis on the other hand still provides a close fit. To see if there is such a trend through all the events, coefficient of determination of both $KE - R$ fits were plotted against each other (r^2_{UM} vs r^2_{DSD}) and compared using corresponding values of $RMSE_{DSD}$ (Fig. 2.6a). Negative value of coefficient of determination for DSD ($r^2_{DSD)}$) is due to the high difference between KE_{DSD} and empirical KE in certain events. From the plot it is evident that a generalized conclusion - theoretical values of a and b (a_{DSD} & b_{DSD}) works well in cases where empirical DSD coincides with gamma DSD - is not possible. However, there were many events with good DSD correspondence with gamma, where KE_{DSD} fitted data better.

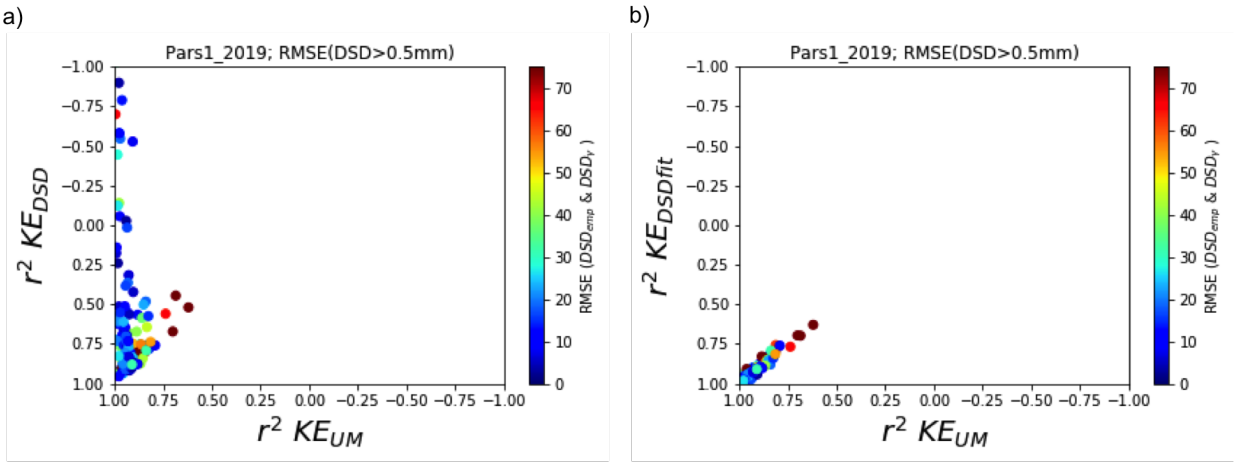

Figure 2.6: a) r^2 values between KE_{UM} and KE_{DSD} for Pars1, 2019; b) r^2 values between KE_{UM} and KE_{DSDfit} (b from fitting of data) for Pars1, 2019 (RMSE calculated by considering only parts of DSD where drop diameter > 0.5 mm)

To investigate further this issue and given that the DSD is available for all time steps, a_{DSD} and b_{DSD} were computed for each time step to study their variations within a rainfall event. Figure 2.7 displays their temporal evolution for the event in Fig. 2.1. Values of parameters, especially b_{DSD}, shows considerable variation within an event. These variations basically come from variations in DSD parameters μ an N_0 as it can be seen on Fig. 2.7c and 2.7f (also evident from Eq. 49), which are reflecting physical variations in the rainfall process. It should be mentioned that during this event (and other events), gamma DSD parameters were able to properly reproduce observed rain rate (Fig. 2.7d), meaning that the assumption of gamma DSD distribution and the M234 moment estimator approach remains valid throughout the event(s). This suggests that the variability of a_{DSD} and b_{DSD} observed at event scale is also valid within events at much smaller scales. This could explain some of the bias previously observed with DSD approach developed in this analysis.

As there were still considerable variation in r^2 values of $r^2_{KE_{DSD}}$ (Fig. 2.6a), especially if we compare with KE_{UM} which shows better $r^2_{KE_{UM}}$ regardless the type of event, a question of possible

bias arises due to difference in methods of estimation of power law coefficients. Unlike KE_{DSD} for which both coefficients are obtained from theoretical relation involving DSD parameters, for KE_{UM} only coefficient a is fully estimated from UM analysis. Prefactor b_{UM} is obtained by fitting the data at highest available resolution (30 s) using UM estimated a_{UM}. Such discrepency may introduce a bias in the comparison between DSD and UM approach to retrieving a power law. Hence, to understand this further and to make a fair comparison, a new power law was considered where only a_{DSD} is obtained using Eq. 49 while b_{DSD} is calculated from fitting of data (denoted hereafter b_{DSDfit}) - KE_{DSDfit}. Figure 2.6b shows r^2 between KE_{DSDfit} and KE_{UM}; and it can be seen that comparable fits are obtained between UM and DSD power laws regardless the nature of DSD, thus illustrating the presence of bias. This can also be observed in previous $KE - R$ plots - Fig. 2.1a, Fig. 2.3a, Fig. 2.5a and Fig. 2.5b.

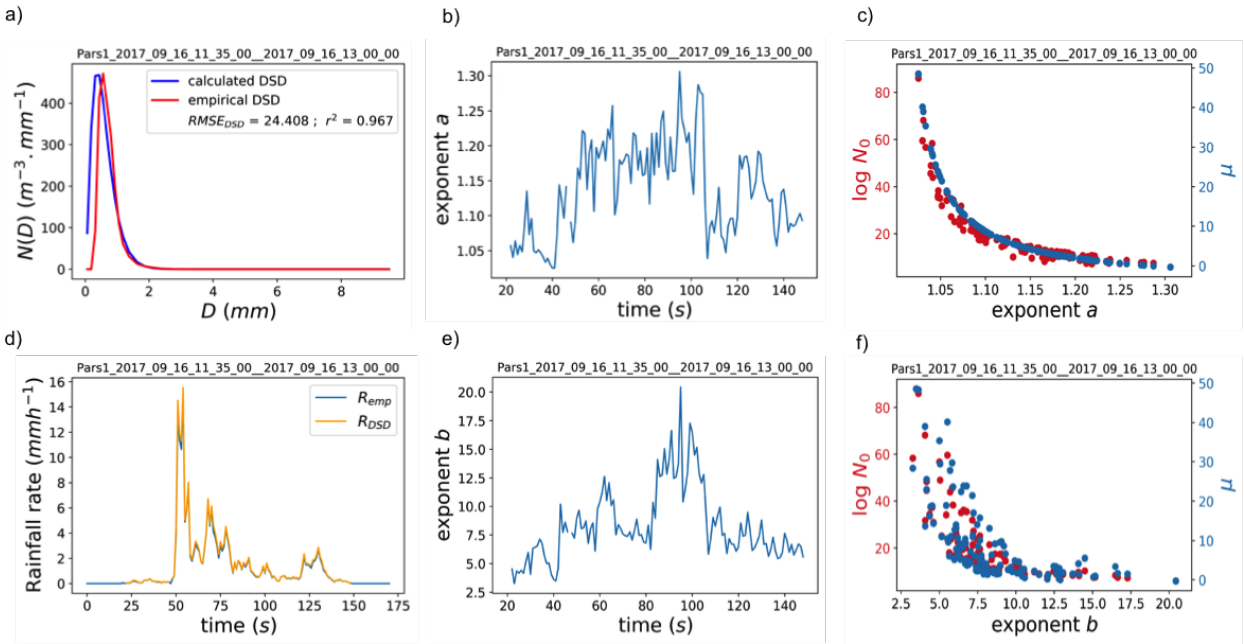

Figure 2.7: Variation of a_{DSD} and b_{DSD} for each time steps in an event (same event discussed in Fig. 2.1)
a) Correspondence between empirical DSD (red) and calculated DSD (blue); d) Correspondence between empirical rainfall rate (R_{emp}) and that calculated from DSD moments (R_{DSD})
b) & e) Variation of a_{DSD} and b_{DSD} within the event
c) & f) Variation of a_{DSD} and b_{DSD} with DSD parameters N_0 and μ

2.1.4.5 Comparison between $KE - R$ relations

Though the power law obtained is similar from UM and DSD analysis, they fit the data differently due to difference in values of corresponding parameters. KE_{DSD} in KE vs. R graph of Fig. 2.1a and Fig. 2.3a shows the power law fit using theoretical a and b (a_{DSD} & b_{DSD}), from DSD parameters for illustrated examples in event based and year based analysis analysis. The difference

in fit between two calculations of power law, KE_{UM} and KE_{DSD} can be observed there. It can be seen from Fig. 2.6a that KE_{UM} gives rather good fit regardless the event specific DSD shape, while r^2 value of KE_{DSD} fluctuates. However, there is a limited tendency for good fit towards empirical DSD following gamma distribution (for few events like Fig. 2.5). Figure 2.8 shows variation of a and b estimates from DSD and UM for Pars 1, Pars 2 and PWS for all events in year 2019. Values of a_{UM} and a_{DSD} are mostly clustered around the approx. 1.2 for all three disdrometers with no clear relation between them. On the other hand, values of b_{UM} and b_{DSD} are more spread out, ranging approximately from 2 to 25. Such spreading for b_{DSD} is not caused by the computation issues previously mentioned since it is visible on both b_{DSD} and b_{DSDfit}. This observed scattering, which is comparable regardless the estimation techniques and device, suggests that even if the power relation between KE and R remains relevant for all events, its parameters exhibit strong variability between events.

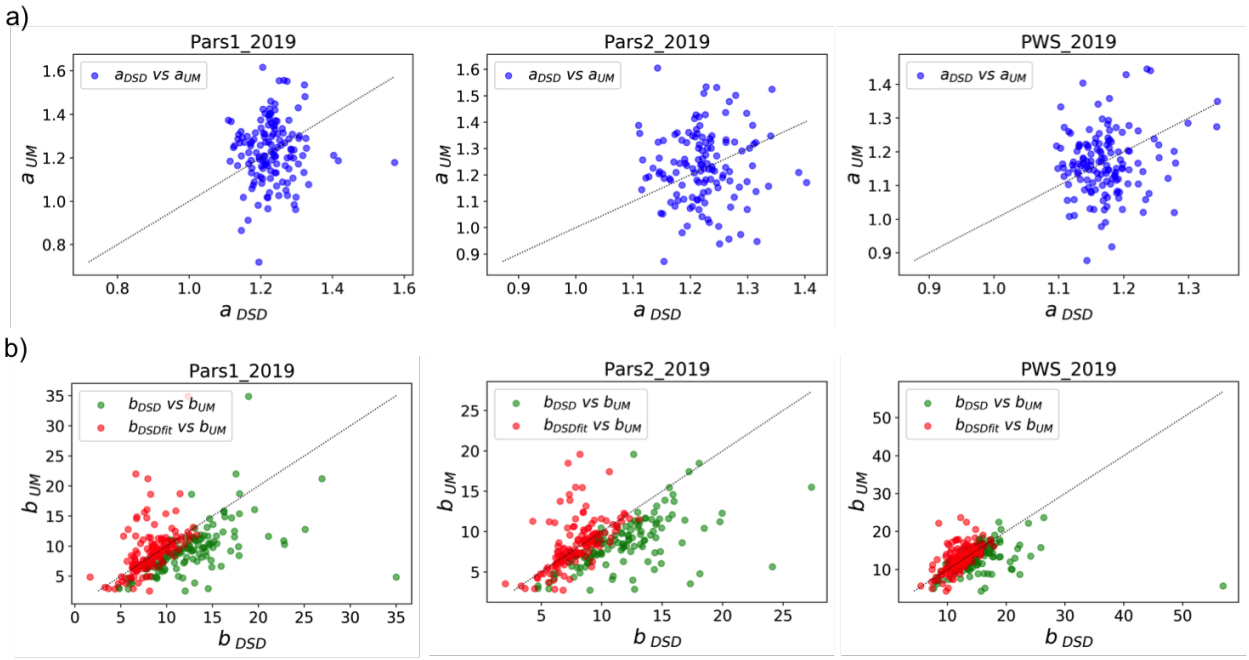

Figure 2.8: Variation of power law coefficients from UM and DSD calculation, for events in year 2019 (similar variation for other years also)

The constants of the power law relations (in literature) between KE and R are not universal in application and need tweaking as per the rainfall type, measurement location as well as techniques. Based on assumed dependence between DSD parameters and rain rate in formulation exponents; Salles et al. (2002) suggest four range of values for exponent values of the universal power law, and Uijlenhoet and Stricker (1999) propose six different relationships in their research. Hence, in order to refine the analysis of this observed variability between events and to examine possible dependence of a and b on type of rain, events were sorted according to rain types. Table 2.3 shows,

for Pars 1, averaged values of gamma DSD parameters, indicator of the quality of the fitting, and power law coefficients from both DSD and UM estimations across events sorted according to type of rainfall. Tables for Pars 2 and PWS are given in Appendix A.2 - (Table A1). For defining types of rainfall from light to extreme, a classification based on intensity (Tokay and Short, 1996) was employed. μ, λ and N_0 tend to decrease with heavier events, with a stronger trend for N_0. It should be mentioned that an opposite trend is reported in reference used; this could be due to instrumental bias in DSD measurement as the impact disdrometer used in reference is known to under-represents smaller drops in intense rainfall. It should also be noticed that the capacity of the gamma distribution to model observed DSD diminishes with heavier rainfall (this is more visible on RMSE estimation over whole range of DSD and less prominent in displayed estimate here involving only higher drop sizes), suggesting a limit in validity for gamma distribution assumption. Also, an increase in mean diameter is noticed (not shown here). These findings are in agreement with previous studies reported in literature (Carollo and Ferro, 2015). When it comes to power law coefficients, both a_{DSD} and b_{DSD} show increase with increasing rain rate, and this is more pronounced for b_{DSD}. Given the observed decrease in validity of gamma distribution of DSD, these trends should be taken carefully because they are likely to be mere artifacts and not representative of the actual process at stake. In the case of UM estimated parameters, b_{UM} follows similar trend with stronger magnitude (going from 8 to 33) while a_{UM} shows slight reduction in value with increasing rain rate (from 1.25 to 1.05). Since the average rainfall criteria used for classification here is a somehow arbitrary and more biased towards lesser rainfalls, another classification relying on the maximum of 10 minute moving average was also employed. The results are tabulated in Table A2 (Appendix A.2). With this criteria which is more biased towards larger rainfall events, consistent and similar results are retrieved when it comes to values and variation of power law coefficients a and b, from DSD as well as UM, suggesting robustness of obtained trends.

			from DSD moments						**from UM**	
		# events	μ	N_0	Λ	**RMSE**$_{DSD}$	a_{DSD}	b_{DSD}	a_{UM}	b_{UM}
				$(m^{-3}mm^{-1-\mu})$	(mm^{-1})	$(m^{-3}mm^{-1})$		$(Jm^{-2}mm^{-a}h^{a-1})$		$(Jm^{-2}mm^{-a}h^{a-1})$
very light	$R<1$	188	2.53	1.05×10^{7}	6.34	19.32	1.196	11.056	1.253	8.554
light	$1\leq R<2$	173	1.75	1.71×10^{9}	4.81	24.53	1.222	12.694	1.224	9.334
moderate	$2\leq R<5$	141	1.01	2.51×10^{7}	3.42	21.25	1.256	15.580	1.214	10.216
heavy	$5\leq R<10$	36	0.44	1.40×10^{4}	2.25	20.45	1.275	17.259	1.210	11.336
very heavy	$10\leq R<20$	14	-0.05	1.17×10^{3}	1.63	21.14	1.300	18.419	1.119	19.670
extreme	$R\geq20$	4	-0.85	5.48×10^{2}	1.04	44.82	1.353	44.82	1.052	33.250

Table 2.3: Variation of DSD parameters and power law coefficients according to the type of rainfall for Pars 1 (R = average rain rate for rainy time steps)

To evaluate the performance of established power law relationship across scales of measurement, KE was calculated from empirical R using $KE = bR^a$ with average values of a and b and compared with existing relations in literature. For this purpose, exponential equation used in RUSLE ($KE_{BF} = 29[1-0.72\exp(-0.05R)]$, Brown and Foster, 1987), exponential equation used

in RUSLE2 ($KE_{MG} = 29[1-0.72\exp(-0.082R)]$, C. McGregor et al., 1995), universal exponential law proposed by van Dijk et al. (2002) ($KE_{VD} = 28.3[1-0.52\exp(-0.0421R)]$) and ideal power law proposed by Shin et al. (2016) ($KE_{Shin} = 10.3R^{11/9}$) were used alongside KE_{UM} and KE_{DSD} derived here (power law where fitted values of b were used -KE_{DSDfit}- is also included). For UM and DSD power laws in this section, average values among all calculated events were used for representation according to make of disdrometers. Average values of coefficient a and prefactor b were close for both Pars 1 and Pars 2 disdrometers and were taken common for the Parsivel^2 make (for both UM and DSD). It is also logical to keep values of power law coefficients separate between different disdrometers as varying KE and R estimation has been reported across types of disdrometers used (Angulo-Martínez and Barros, 2015; Angulo-Martínez et al., 2018; Johannsen et al., 2020). Figure 2.9 shows KE and R variation fitted with above mentioned equations for maximum resolution, 30 s. As expected KE_{UM} provides better fit than KE_{DSD} (and KE_{DSDfit} shows closer fits). With respect to empirical data, UM power laws exhibit - for all three devices - slightly better or comparable coefficient of determination (r^2) with regards to commonly used relations. The exponential equations from literature appear very close to each other. The relatively lower values of coefficient of determination than that during event based fits are likely to be due to the effect of using average values instead of event specific values of a and b.

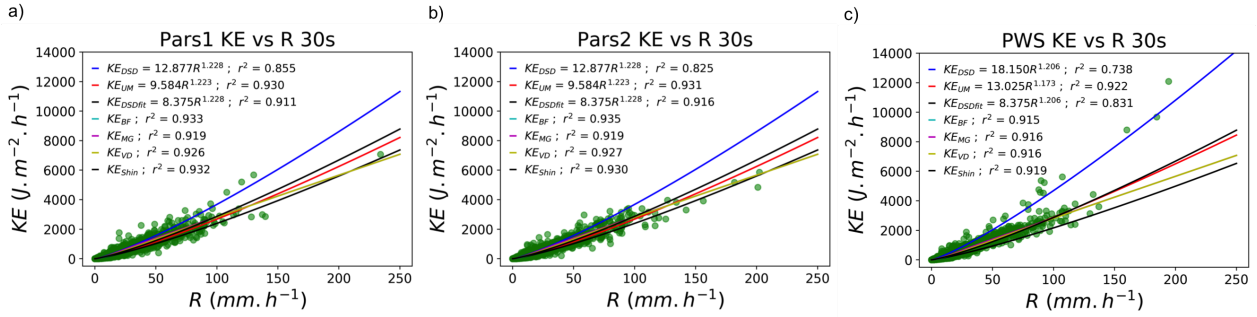

Figure 2.9: Fitting of empirical $KE-R$ using power laws from UM and DSD, and popular expressions from literature for a) and b) Parsivel^2, and c) PWS

To understand the performance of various equations further, r^2 was examined across various time periods and also across different type of rains. Results are displayed in Fig. 2.10. It appears that regardless of the duration as well as type of rainfall considered, tuned relations KE_{DSDfit} and KE_{UM} perform significantly better than the other fixed ones, yielding r^2 values greater than 0.9. In most cases, KE_{UM} exhibits slightly better performances with a difference not significant. The analysis also confirmed the poor performance of KE_{DSD}, i.e. the inability of the DSD approach to properly fit the prefactor 'b'. It should be stated that the power law obtained using UM analysis is not providing significant performance enhancement compared to that obtained from gamma DSD while the prefactor b is estimated from fitting of the data (KE_{DSDfit}). However, with UM analysis, it is possible to discard all assumptions of DSD following a gamma distribution thus eliminating the

known inadequacy of gamma model and its sensitivity to sampling resolution (Adirosi et al., 2013, 2014; Ignaccolo and De Michele, 2014; Adirosi et al., 2016; Gatidis et al., 2020). The inadequacy was observed in current analysis as well, as previously discussed and illustrated in Fig. 2.5 and Fig. 2.6.

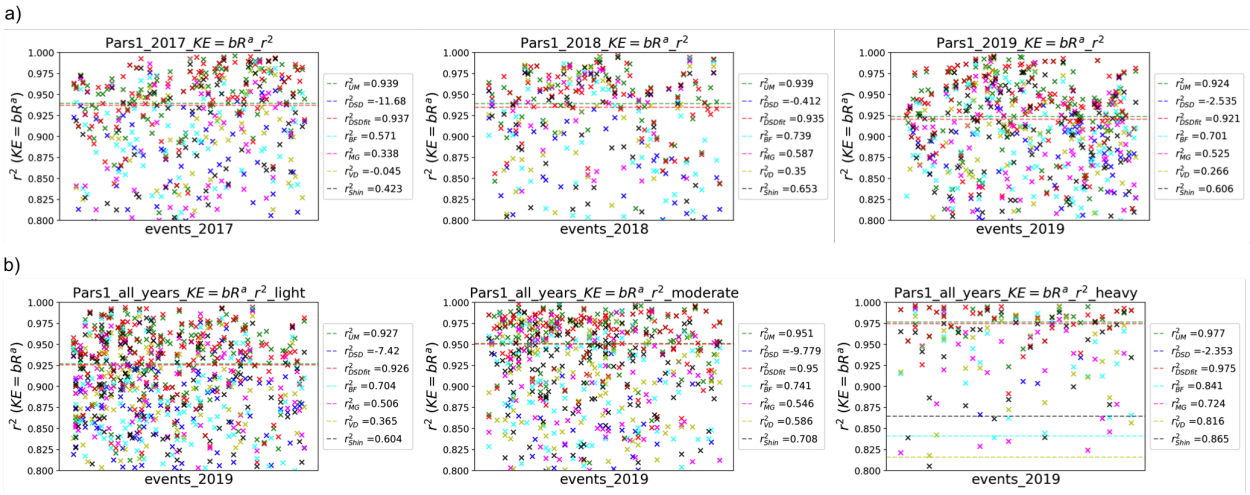

Figure 2.10: r^2 values of various KE-R relations discussed for a) events analysed in 2017, 2018 and 2019 (for Pars 1), b) all events grouped according to type of rain - light, moderate and heavy
Average value for each year is given in legends, with KE_{UM} and KE_{DSDfit} displayed in dotted lines

2.1.5. Main outcomes from UM analysis of KE and R

We examined the relationship between rainfall intensity R and time specific kinetic energy KE using high resolution (30 s) optical disdrometer data from the past 7 years in Paris region. The variability across scales of both parameters was characterized using the framework of Universal Multifractals. Analyzed KE and R times series were found to convey excellent multifractal behaviour (which is novel for KE), with multifractality index α and mean intermittency C_1 suggesting power law relation between them; it can be written as $KE = bR^a$. Such power law was found to be valid across analyzed data, i.e. independent of the event, on whether they are computed on event or yearly basis, and of the underlying corresponding drop size distribution. Some variability in the value of the exponent a and prefactor b is reported according the event and disdrometer type.

As shown by previous results, similar power-law can be theoretically obtained when relying on the common assumption of a gamma distribution for the DSD, and a power-law relation between fall velocity and equivolumic drop diameter. KE-R relation obtained through UM analysis was compared with results found using this common framework and biases were acknowledged. Despite some exceptions, in most cases when a gamma DSD approximation was relevant, estimations of power law parameters from the two approaches were found to be consistent. When not, UM approach provided slightly better fit in general but not in a significant manner, keeping in mind that the pre-factor needs to fitted to data in both cases to ensure a fair comparison. Thus, the newly

discussed power law relationship between KE and R retrieved with the help of UM framework generalizes previous results and theoretical formulations without having to rely on the ad-hoc assumption of a gamma DSD. The main underlying assumption of UM framework, i.e. that there is an underlying multiplicative process, is actually physically based in the sense that comes from the scale invariance features of the Navier-Stokes equations. Here, a UM analysis confirmed the validity of this assumption. Deriving the power-law relation in a multifractal framework opens the path to new approaches for simulating KE from simple R measurements. Given that complete KE measurement is much less available than R one, this impact will be investigated further in future work.

For the future, it would hence be interesting to expand the data set across geographical and meteorological conditions to reduce the biases that might have accumulated from region of measurement.

2.2. Multifractal analysis of extinction coefficient and its consequences in characterizing atmospheric visibility

2.2.1. Introduction

Visibility can be defined as a "a complex psycho-physical phenomenon, governed mainly by the atmospheric extinction coefficient associated with solid and liquid particles held in suspension in the atmosphere' (WMO-No. 8 (2018)). An accurate representation of visibility is required for safe functioning of transportation especially aviation (ICAO (2007)), free-space optic communications (Willebrand and Ghuman (2002)) as well as in understanding variations in air quality and climate (Hyslop (2009)). In meteorological context, visibility is a measurement of transparency of the atmosphere, which in turn is dependent on light attenuation property of gases and aerosols. Instrumental methods mainly involve measurement of extinction coefficient, σ_e from atmospheric attenuation and its conversion into a visual range as per requirement of application.

Most of the presently used instruments measure extinction coefficient, σ_e through either transmission factor or scattering coefficient using a light beam and an electronic detection mechanism. The instrument used in this study, forward scatter sensor, works on the assumption that scattering in forward direction is linearly related to the extinction coefficient at instrument angle and that the absorption factor is negligible for deducing visibility (Malm (2016), WMO-No. 8 (2018), Campbell-Scientific-Ltd (2012)). As extinction coefficient, σ_e directly corresponds to scattering and absorption by atmospheric particles, it is a more physically suited quantity over direct values of MOR for analysing visibility as a field. Mei et al. (2017) demonstrated good agreement between variation trends of averaged extinction coefficients retrieved from the Scheimpflug lidar technique and the PM10/PM2.5 concentrations with a correlation coefficient of 0.85. Since the governing non linear equations of atmosphere such as Navier-Stokes posses scale invariance, it is assumed that light attenuating particles should inherit scaling properties and exhibit associated features. Towards this, we extract σ_e from forward scattering visibility measurement of PWS 100 disdrometer (see Ellis et al. (2006) or device documentation, Campbell-Scientific-Ltd (2012)) at École des Ponts ParisTech and analyze its behaviour across various scales of measurements using the framework of Universal Multifractals (UM). Such framework has been widely used to characterize and simulate geophysical fields exhibiting extreme variability over wide range of scales ((see Schertzer and Tchiguirinskaia (2020) for a recent review). Meteorological Observable Range (MOR) values from Paris-Charles de Gaulle (CDG) airport METAR (METeorological Aerodrome Reports) data for the same time period was used for comparison purpose, and corresponding σ_e field was subjected to similar multifractal analysis. Direct statistical analysis of σ_e was found to be not as straightforward as expected as the MOR data (and in turn σ_e) are affected by the instrumental or operational measurement range of visibility. This means that, in visibility measurements, majority of the values are capped by an upper threshold (equal to the maximum range of measurement) which introduces bias in implemented statistical analysis.

Here we try to mimic the measured extinction coefficient fields using multifractal simulations

and imposed thresholds to illustrate the biases introduced by nature of actual data in multifractal analysis. Details about nature and extraction of data, as well as devices are presented in Sect. 2. The framework of UM is briefly discussed in Sect. 3 along with initial analysis of data which exhibits strong biases. Sect. 4 follows with discussion on the effect of biases with respect to the underlying theory in UM framework and validation of same through numerical simulations. Finally, section 5 discusses how to reduce bias in the analysis.

2.2.2. Data and instrumentation

2.2.2.1 Measurement of visibility and extraction of σ_e

World Meteorological Organization (WMO) formally recognizes Meteorological Observable Range (MOR) as the measure of visibility for aeronautical as well as general purpose uses. Commission for Instruments and Methods of Observation (CIMO) guide defines MOR (in km) as follows - MOR is defined as the length of path in the atmosphere required to reduce the luminous flux in a collimated beam from an incandescent lamp at a color temperature of 2700 K, to 5 percent of its original value (WMO-No. 8 (2018)). For measurement of visibility or transparency of air, light attenuation by particles in ambient air is first estimated using Bouguer-Lambert law; and then converted to visual range using Koschmieder's theory assuming homogeneous atmosphere with negligible multiple scattering (Koschmieder (1924)). For MOR calculation, WMO definition uses contrast threshold of 0.05 instead of 0.02 in Koschmieder's relationship.

$$MOR = -\frac{ln(0.05)}{\sigma_e} \tag{51}$$

where σ_e is extinction coefficient, usually represented in km^{-1}.

By definition, 'the extinction coefficient σ_e is the proportion of luminous flux lost by a collimated beam, emitted by an incandescent source at a colour temperature of 2700 K, while travelling the length of a unit distance in the atmosphere. MOR is defined relative to 550 nm (green light) as human eye has maximum sensitivity to green light. When σ_e measured by instruments is an objective property of air, visibility is subjective according to the defining models and intended applications (Horvath and Noll (1969), Lee and Shang (2016), Kim (2018)) which adjusts the measured value in application specified ranges. Assuming spherical particle size, extinction coefficient can be derived from size distribution according to Mie theory as follows (Bohren and Huffman (2008))

$$\sigma_e = \sum_{D_{min}}^{D_{max}} \frac{\pi D^2}{4} \Delta n(D) Q_{ext}(m,D) \tag{52}$$

where $Q_{ext}(m,D)$ is the Mie extinction efficiency factor (a function of particle size D and refractive index m) and $n(D)$ is the aerosol number size distribution.

Though light attenuation involves both scattering and absorption, it is possible to approximate extinction coefficient to scatter coefficient due to the negligible contribution of latter to total attenuation in the laser transmission window (Weichel (1990)). In such cases, reduction in visibility from scattering is compensated by assuming some constant ratio between absorption and scattering or constant scattering albedo (fraction of total extinction that is due to scattering: $\omega = \frac{\varepsilon_{scat}}{\varepsilon_{scat}+\varepsilon_{abs}}$). σ_e also depends on internal or instrumental factors such as wavelength of light source, forward scattering angle, location of measurement, sampling volume, spherical size assumption for particle etc. (Sheng-Jie and Da-Ren, Kim et al. (2001), Shah et al. (2015), Charlson (1969)) and on external factors such as density of sampled medium, meteorology, influence from regional sources, particle size distribution and species specific properties etc (Loveland and Lindberg (1988), Duthon et al. (2019), Grabner and Kvicera (2011), Nebuloni (2005), Tang (1996), Majewski et al. (2015), Uhlig and von Hoyningen-Huene (1993), Elias et al. (2009), Zieger et al. (2013), Sabetghadam et al. (2017)).

2.2.2.2 Available instruments

PWS100 (Campbell-Scientific-Ltd (2012)) is an optical present weather sensor which measures visibility using forward scatter technique (0 to 20 km with an accuracy of $\pm$ 10 %) with a laser diode of wavelength 830 nm. Visibility data for the year 2019, from Jan 01 to Dec 31, was taken from instrument operated by Hydrology Meteorology and Complexity laboratory of École des Ponts ParisTech (HM&Co-ENPC) at TARANIS observatory (exTreme and multi-scAle RAiN-drop parIS observatory (Gires et al. (2018)) of the Fresnel Platform of École des Ponts ParisTech (HM&Co, ENPC). The instrument provides an estimate of MOR from the amount of scatter generated particles in its sampling volume (projected area of approx. 40 cm^2). ICAO (International Civil Aviation Organization) and field tests recommends forward scatter sensors as a less expensive, less maintenance technically capable alternative to transmissiometers, which measures both absorption and scattering, for measuring MOR (ICAO (2007), Waas (2008)). For the purpose of this analysis, the value of σ_e was obtained from visibility data of PWS100 (referred to as ENPC after location of measurement) using Eq. 51. For simplicity same relation was used for the whole data set, regardless day and night. As the instrument follows WMO guidelines, σ_e estimated at near IR (830 nm) is assumed to be corrected for 550 nm as per MOR definitions. PWS100 reduces some of the previously mentioned uncertainties with visibility range correction (by calibrating amount of particle scatter against obscuring type for drizzle, snow and other large particles) and through averaging of visibility measurements to reduce noise levels (Campbell-Scientific-Ltd (2012)).

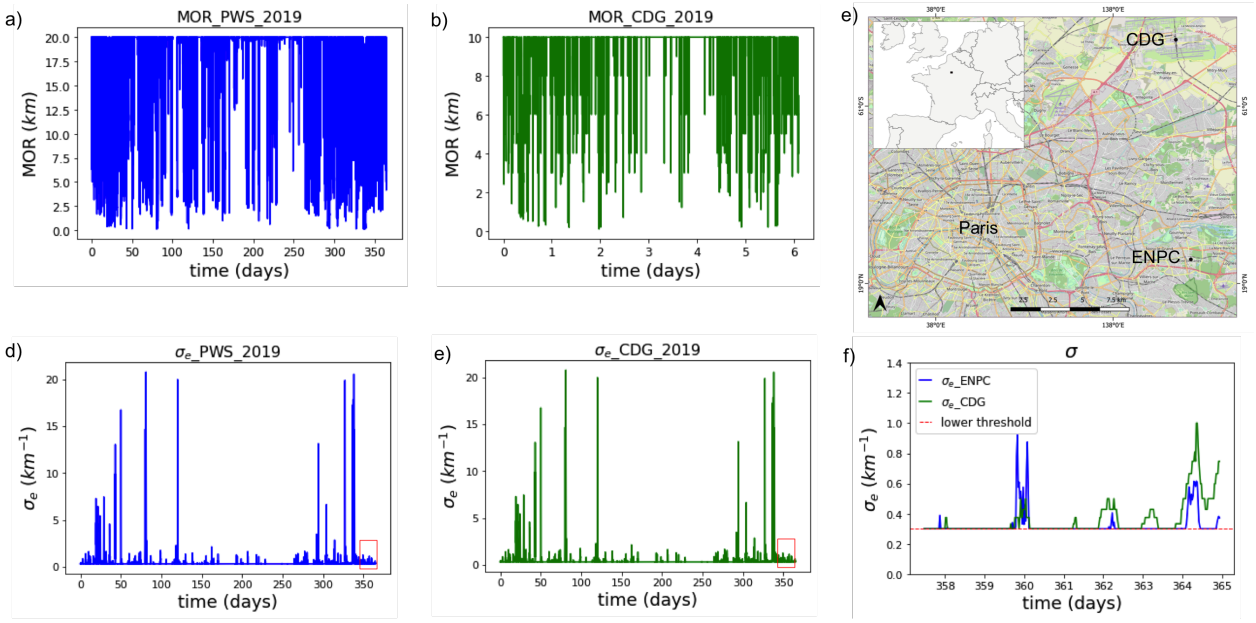

Figure 2.11: Variation of MOR and σ_e for the year 2019 at locations ENPC (a & b) and CDG (c & d), e) location of measurements (from google maps) f) zoomed version of Fig. 1c and fig. 1d to show the presence of lower threshold in σ_e.

location	data collection time	resolution	data range
ENPC	Jan 2019 – Dec 2019	30 s	0- 20 km
CDG	Jan 2019 – Dec 2019	30 min	0.1 - 10 km

Table 2.4: location and time of data collection

Paris Charles-de-Gaulle Airport (CDG) is 32 km away from ENPC, the site of present weather sensor, and is at the north east of Paris (Figure 2.11e). Visibility data was obtained from METAR data archive of Iowa Environmental Mesonet (IEM) for the same time period as forward scatter meter data under discussion. Extinction coefficient was extracted using equation 51 for CDG with same assumptions as that for ENPC.

2.2.2.3 Data and treatment

Table. 2.4 gives a brief outline of data collected and measurement period. It should be noted that the data used here corresponds to an average visibility and does not enable to distinguish the nuances of involved atmospheric particles and notably their species, time evolution, or seasonal variation etc. External factors such as relative humidity, scavenging by rainfall, wind, fog/haze episodes etc. are also not specifically accounted for in the analysis. Time series of MOR and

corresponding σ_e are shown in Fig. 2.11 for both data sets used along with a zoom during a short period.

Before extraction of σ_e, missing values of visibility (1.8 % for ENPC and 0 % for CDG) were set to maximum value of respective data sets (20 km for ENPC and 10 km for CDG) since majority of data points had values at upper instrumental threshold (83 % for ENPC and 89 % for CDG; see Fig. 2.11a and Fig. 2.11b). This decision was made on the basis of some preliminary UM analysis on direct MOR data; largest continuous portion of MOR provided similar results as that of data set where missing data points were replaced with upper threshold. Hence, it was decided to use the whole data set with substituted missing data for current analysis. However, it should be noted that the upper threshold translates to lower threshold while analysing σ_e (see Fig. 2.11f) and that replacing missing data with zeroes and lower threshold yielded similar results there. Unless explicitly stated, in order to limit bias in comparison of the field, ENPC data was set to same conditions as that of CDG (30 min resolution and 10 km upper MOR limit) before UM analysis.

2.2.3. Analysis: Direct Multifractal analysis of σ_e

2.2.3.1 Theoretical framework

Here we use the framework of Universal Multifractals (UM) to examine variations across scales of extinction coefficient, which has been covered in detail in section 1.2.2. The scaling of σ_e is explored using spectral analysis and UM analysis, and results are discussed in following sub sections.

2.2.3.2 Direct analysis of raw σ_e field

σ_e extracted from both location were subjected to UM analysis. Details of TM analysis, spectral exponent β, $K(q)$ and DTM curves are shown in Fig. 2.12 and Table 2.5 for both data sets at similar conditions (at the 30 min resolution and data range of CDG, effect of using a coarser resolution for ENPC is discussed in next paragraph). It can be observed that the σ_e extracted from MOR gives non realistic values of α and C_1 despite an acceptable scaling. Indeed, estimates of α greater than 3 are found. As σ_e measures extinction from atmospheric particles, and is related to the concentration of particles, it is expected to inherit scale invariant features of Navier-Stokes equations that governs atmospheric flow, and therefore to exhibit appropriate multifractal behaviour. There is hence a need to explore this unusual behaviour and determine, if possible, the real underlying multifractal properties. As mentioned before, this might have to do with the fact that majority of points (83% for ENPC and 89% for CDG) in the data analysed are set to lower threshold in σ_e (from upper threshold of 10km in MOR).

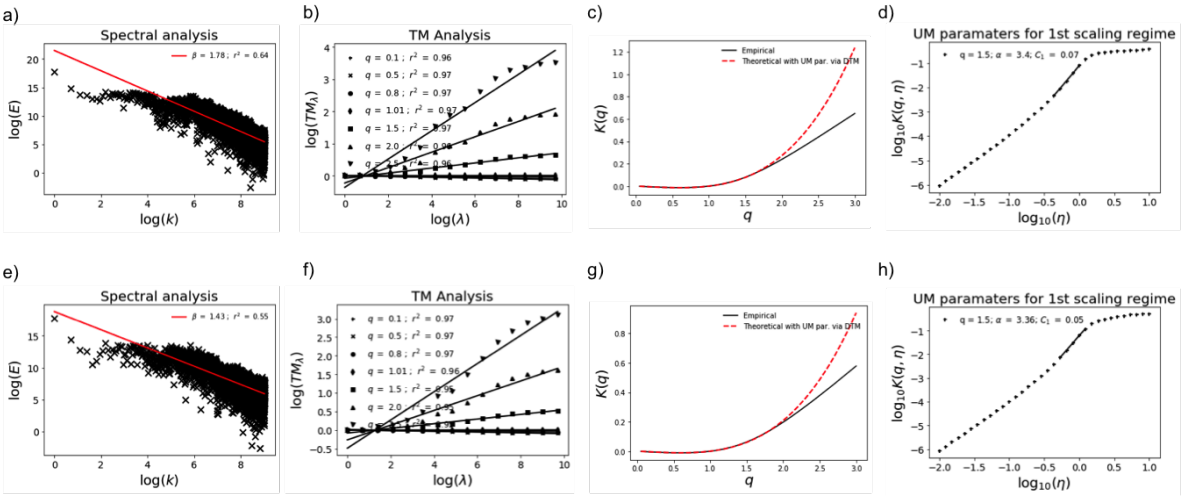

Figure 2.12: Direct UM analysis of raw σ_e yielding non realistic values. a) spectral slope (Eq. 19 in log-log), b) TM analysis (log-log plot of Eq. 14), c) scaling coefficient function $K(q)$ (Eq. 16) and d) DTM curve of σ_e (log-log plot of Eq. 22) at ENPC; similar results at CDG are shown in e, f, g and h. Both data set are studied at 30 min resolution with 10 km upper limit in MOR data.

		UM parameters				
Location	**% at threshold**	R^2_{TM}	α_{DTM}	$C_{1,DTM}$	β	H^*
ENPC	83%	0.990	3.402	0.076	1.782	0.391
CDG	89%	0.986	3.368	0.059	1.430	0.214

Table 2.5: Values of UM parameters for σ_e for ENPC and CDG (at 30 min resolution and 10 km upper threshold in MOR).
* Values of H presented here do not account for the correction with $K(2)$ in Eq. 18 as UM estimates are heavily biased already, hence H is simply estimated as $= \frac{(\beta-1)}{2}$.

To check possible influence of wavelength of measurement on estimation of σ_e, available MOR values were taken as reference and sensitivity analysis was performed at multiple wavelengths at visible and near IR range (from 350 - 1550 nm) with wavelength correction factor (Kim et al. (2001)). σ_e was found to preserve similar scaling behaviour for the various tested wavelengths for both visibility data sets; however, there was a slight reduction in value of α and slight increase in value of C_1 with increase in wavelength. As forward scatter meter sample obscurants over a small range, time averaging of data is recommended to avoid variable output (Campbell-Scientific-Ltd (2012)). Towards this, analysis was done by averaging ENPC data for a range of resolutions from 30 s to 1 hr. In general, sensitivity analysis on various resolution showed a small reduction in value of α (by 19%) and very slight increase in C_1 (by 7 %) till 1 min resolution, from where on the values seemed to be saturating with lower resolutions. As can been see in Tab. 2.5, at 30 min resolution, the values of α and C_1 from ENPC were roughly corresponding with those from CDG.

Averaging values of ENPC data to lower resolution (30 min) also reduced the poor scaling observed at finer scales through flattening of TM curves (figures 2.12b and 2.12f). This is consistent with the recommendation to smooth values of visibility over time periods to avoid dispersion in measurement due to rapid and random fluctuation of the volume of the atmosphere over where forward scattering measurement is based on (WMO-No. 8 (2018)).

2.2.4. Quantification of biases on UM estimates due to lower threshold

2.2.4.1 Effect of lower threshold in the theoretical framework of UM

In this section we examine what are the expected effects in UM framework of setting the fields values below a lower threshold to that threshold, in order to explain the observed behaviour of σ_e with lower thresholds in Fig. 2.12 (notably the sharp increase of α). Before going on, it should be reminded that the related issue of setting the values below a threshold to zeros has been widely studied and triggers a multifractal phase transition with a bias in UM parameter estimates (decrease in α and increase in C_1). This effect is detailed in Gires et al. (2012) and references therein.

As established earlier upper threshold in measuring instrument (MOR) becomes lower threshold in extinction coefficient (σ_e). We aim at exploring the theoretical consequences of implementing such threshold. Let us consider ε_λ a UM field. the field with lower threshold.

Let's take lower threshold T and consider its corresponding singularity γ_T, with Λ the maximum possible resolution

$$T = \Lambda^{\gamma_T} \tag{53}$$

Imposing the threshold corresponds to setting all values below singularity γ_T to zero. It means that $Pr(\varepsilon_\lambda \geq \lambda^\gamma) = 1$ for any singularity $\gamma \leq \gamma_T$. From Eq. 13, this makes the value of $c(\gamma)$ zero for singularities below γ_T (for $-\infty < \gamma < \gamma_T$, $c(\gamma) = 0$). Hence, here $c(\gamma_T)$ is the limiting non-zero value below which $c(\gamma)$ becomes zero. $c(\gamma)$ becoming constant (zero in our case) below a particular $c(\gamma_T)$ due to threshold is very similar to the already known influence due to the presence of zero on assessment of multifractal parameters mentioned before. If we set values of the field below the threshold to zero (imposition of threshold is notated as following in the section $\{\varepsilon_\lambda\}_{\varepsilon_\lambda \leq T} = 0$), then codimension function becomes bounded by a minimum value C_{min} corresponding to the singularity associated with the threshold γ_{min}. In our case, this minimum singularity $\gamma_{min} = \gamma_T$ and $C_{min} = c(\gamma_T)$.

When we set values below a threshold to zero in data ($\{\varepsilon_\lambda\}_{\varepsilon_\lambda \leq T} = 0$), $c(\gamma)$ (notated $c_0(\gamma)$ for clarity) is known to vary as below

$$c_0(\gamma) = \left\{ \begin{array}{lll} C_{min} & for & \gamma \leq \gamma_{min} \\ c(\gamma) & for & \gamma > \gamma_{min} \end{array} \right\} \tag{54}$$

In the case under study, when we set values below a threshold to threshold in data ($\{\varepsilon_\lambda\}_{\varepsilon_\lambda \leq T} =$

T), $c(\gamma)$ (notated $c_T(\gamma)$ for clarity) will vary as

$$c_T(\gamma) = \left\{ \begin{array}{cc} 0 & for \quad \gamma < \gamma_T \\ c(\gamma) & for \quad \gamma \geq \gamma_T \end{array} \right\} \tag{55}$$

In both cases, $c(\gamma)$ reaches the limiting value ($c(\gamma_T) = C_{min}$) at $\gamma = \gamma_T$. But when values below threshold are set to threshold, $c(\gamma)$ becomes zero for $\gamma < \gamma_T$. This behaviour can be observed more clearly on figure 2.13a. When $\{\varepsilon_\lambda\}_{\varepsilon_\lambda \leq T} = T$, $c(\gamma)$ drops to zero at γ_T immediately after reaching the limiting value C_{min}. The limit case value of γ ($\gamma_T = \gamma_{min}$) can be obtained from equation 17 in terms of C_{min}

$$\gamma_T = \gamma_{min} = \frac{C_1 \alpha}{\alpha - 1} \left(\frac{C_{min}}{C_1} \right)^{\frac{\alpha-1}{\alpha}} - \left(\frac{C_1}{\alpha - 1} \right) \tag{56}$$

Now we consider the behaviour of scaling moment function, $K(q)$ when lower threshold is present. Figure 2.13b illustrates $K(q)$ behaviour during lower threshold alongside the known influence due to the presence of zeroes.

In the case of zeroes, when $\{\varepsilon_\lambda\}_{\varepsilon_\lambda \leq T} = 0$, $K(q)$ (notated $K_0(q)$) becomes linear for moments $q \leq q_{min}$ where q_{min} is the critical order of statistical moment corresponding to γ_{min} (derived from Legendre transform)

$$K_0(q) = \left\{ \begin{array}{cc} q\gamma_{min} - C_{min} & for \quad q \leq q_{min} \\ K(q) & for \quad q > q_{min} \end{array} \right\} \tag{57}$$

For the case under study, i.e. where $\{\varepsilon_\lambda\}_{\varepsilon_\lambda \leq T} = T$, computing the Lengendre transform of $c_T(\gamma)$ enable to show that $K(q)$ (notated $K_T(q)$) becomes linear before q_{min} at an earlier value of moment, q_T.

$$K_T(q) = \left\{ \begin{array}{cc} q\gamma_T & for \quad q \leq q_T \\ K(q) & for \quad q > q_T \end{array} \right\} \tag{58}$$

It should be noted that corresponding critical order of statistical moments (from Legendre transform), q_T is not the same as q_{min} (which is why $_T$ and $_{min}$ indices are used)

$$q_{min} = c'(\gamma_{min}) = \left(\frac{C_{min}}{C_1} \right)^{\frac{1}{\alpha}} \neq q_T \tag{59}$$

Value of q_T can be derived from the limiting value of $K_T(q)$ at q_T below which $K(q)$ is linear. From Eq. 16 and Eq. 58 at $q = q_T$

$$\begin{aligned} K_T(q_T) = q_T\gamma_T &= \frac{C_1}{\alpha - 1}(q_T^\alpha - q_T) \\ q_T &= \left(\frac{\alpha - 1}{C_1}\gamma_T + 1 \right)^{\frac{1}{\alpha - 1}} \end{aligned} \tag{60}$$

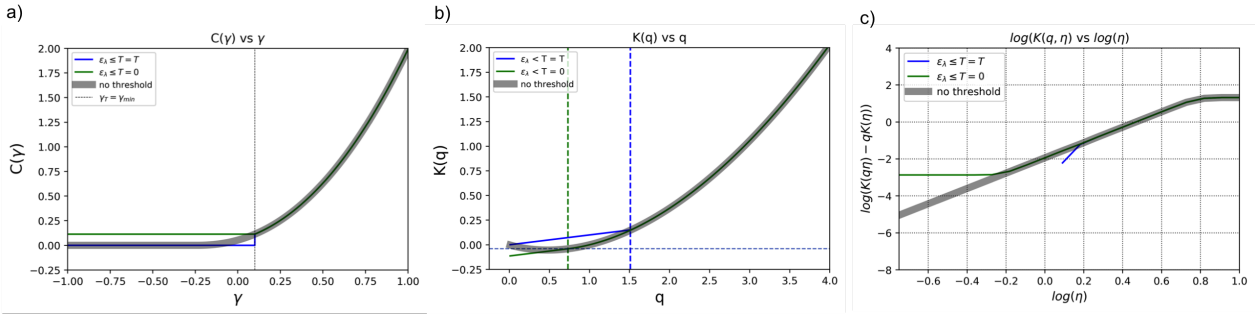

Figure 2.13: Influence of threshold on estimation of UM parameters: a) on codimension function $c(\gamma)$, b) on moment scaling function $K(q)$, c) on DTM curve. Figures were plotted with $\alpha = 1.8$ and $C_1 = 0.2$.

This behaviour of $K(q)$ is reflected in Double Trace Moment (DTM), the technique used for estimating values of UM parameters (illustrated in Fig. 2.13c). For a given q: $K(q,\eta) = K(\eta q) - qK(\eta)$, which for multifractal fields = $\eta^{\alpha}K(q)$. The known behaviour due to presence of zeroes in data ($\{\varepsilon_\lambda\}_{\varepsilon_\lambda \leq T} = 0$) in $K(q,\eta)$ is as follows

$$K_0(\eta,q) = \left\{ \begin{array}{ccc} (q-1)C_{min} & for & \eta \leq \eta_-(q) \\ \eta^{\alpha}K(q) & for & \eta_-(q) < \eta_+(q) \\ (q-1)(d+d_s) & for & \eta \geq \eta_+(q) \end{array} \right\} \tag{61}$$

where $\eta_-(q)$ and $\eta_+(q)$ corresponds to values of η where DTM curve becomes plateau like. Lower plateau starts at $\eta_-(q) = q_{min}$ and corresponds to presence of zeroes in the data and upper plateau starts at $\eta_+(q)$ is equal to the moment above which $K(q)$ becomes linear due to sampling limitation (Schertzer and Lovejoy (1989)), Hubert et al. (1993), Lovejoy and Schertzer (2007b)). $q_s = ((D+D_s)/C_1)^{1/\alpha}$ where D is the dimension of space ($D = 1$ for a one dimensional sample) and D_s is the sampling dimension (fractal dimension corresponding to the number of samples, $D_s = 0$ for a single sample).

Influence of threshold on DTM for the case under study ($\{\varepsilon_\lambda\}_{\varepsilon_\lambda \leq T} = T$) is as follows:

$$K_T(\eta,q) = \left\{ \begin{array}{ccc} 0 & for & \eta \leq q_T/q \\ K(\eta q) - q\eta\gamma_T & for & q_T/q < \eta \leq q_T \\ \eta^{\alpha}K(q) & for & \eta > q_T \\ (q-1)(d+d_s) & for & \eta \geq \eta_+(q) \end{array} \right\} \tag{62}$$

above equation is on the assumption that both q_T and q are greater than 1. When $q < 1$

$$K_T(\eta,q) = \left\{ \begin{array}{ccc} 0 & for & \eta \leq q_T \\ q\eta\gamma_T - qK(\eta) & for & q_T < \eta \leq q_T/q \\ \eta^{\alpha}K(q) & for & \eta > q_T \\ (q-1)(d+d_s) & for & \eta \geq \eta_+(q) \end{array} \right\} \tag{63}$$

To understand this behavior more clearly, efforts were also done to simulate conservative multifractal fields with the intention of retrieving obtained values of α and C_1 for σ_e through application of thresholds (in next section).

2.2.4.2 Analysis: Numerical simulations

To retrieve the underlying multifractal estimates found in the direct analysis of raw σ_e and to understand the influence of lower threshold, conservative fields ($H = 0$) were simulated with various values of α and C_1. These simulated fields were subjected to progressive application of lower thresholds where values $\leq$ lower threshold were set to lower threshold. As percentage of values $\leq$ lower threshold is increased, the values of α are increasing and C_1 decreasing along with a decreasing quality of scaling (table 2.6). This process was repeated for various values of α and C_1 and at values of 1.8 for α and 0.2 for C_1 (Fig. 2.14), estimates similar to that of raw σ_e (Tab. 2.5) were obtained for similar thresholds. These values of UM parameters are particularly interesting as they correspond to the typical values for atmospheric fields.

DTM curves of raw σ_e at Fig. 2.12 and simulated fields in 2.14 are showing similar behaviour, with sharp slopes as theoretically illustrated in Fig. 2.13c. Simulated behaviour is consistent with the biases induced by lower threshold on estimation of UM parameters as discussed in previous section. This numerically confirms theoretical expectations. It also illustrates that σ_e is indeed the underlying multifractal field of the studied process.

It should be noted that for both the simulations and the real data, the threshold is implemented only at the maximum resolution while in the theoretical analysis, it is done at all scales through a direct "truncation" of $c(\gamma)$. This explains why DTM diverges with strong slope with simulations while it goes to $-\infty$ theoretically. In real data (Tab. 2.5), the values of spectral slope β and correspondingly, value of H are greater that 0 while simulated fields are conservative. However, considering the value of H being less than 0.5 in real fields, TM and DTM are not much affected by this. Also the upper plateau in TM graph of real data is not visible in the simulations (more prominent on finer resolutions).

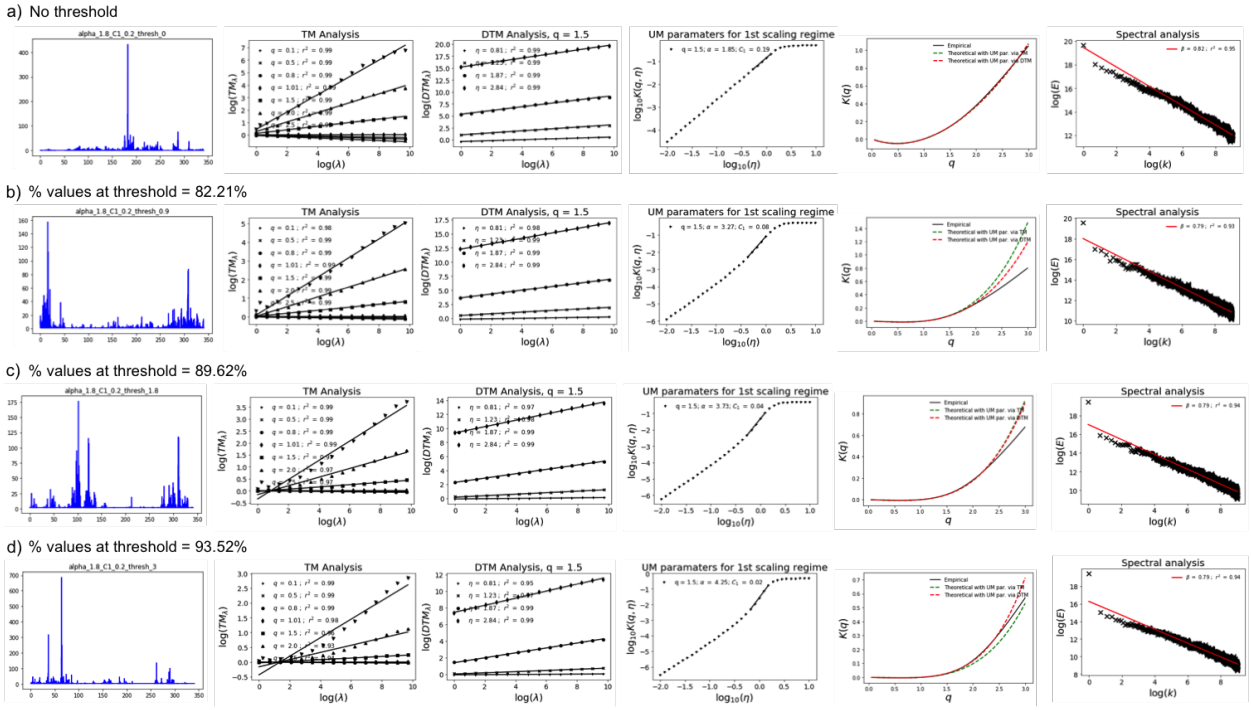

Figure 2.14: UM analysis of simulated MF fields at $\alpha = 1.8$ and $C_1 = 0.2$ at a) 0 % of values at lower threshold, b) 82.2 % of values at threshold, c) 89.6 % of values at threshold d) 93.5 % of values at threshold

	UM parameters				
% at threshold	$R2_{TM}$	α_{DTM}	C_{1DTM}	β	H
0 %	0.997	1.801	0.191	0.777	0.065
70.5 %	0.999	2.833	0.127	0.774	0.065
82.2 %	0.995	3.270	0.080	0.770	0.020
89.6 %	0.981	3.78	0.043	0.763	-0.028
93.5 %	0.963	4.267	0.022	0.754	-0.065

Table 2.6: Values of UM parameters for simulated fields with artificial imposition of lower thresholds.

2.2.4.3 Reducing the biases from lower threshold on σ_e

As illustrated through theoretical framework and numerical simulation, when values below a given lower threshold is set to lower threshold itself, $K(q)$ becomes zero below a value of η as defined by equation 62 or 63. This causes divergence in the logarithmic curve (Fig. 2.13c) leaving lesser space for accurate estimation of α (slope of the linear portion of the curve unaffected by threshold), even lesser than that available during presence of zeroes. This means that the estimate of α is highly biased by the presence of thresholds. This divergence in DTM curve can be observed

for σ_e (real and simulated) in Fig. 2.11 and 2.14 when data is imposed with lower threshold. Though not a solution, if data has a lower threshold, it is better to set values below threshold to zero than threshold itself. In Fig. 2.15 the reduction in bias can be seen when values $\{\varepsilon_\lambda\}_{\varepsilon_\lambda \leq T} = 0$ with respect to the case where $\{\varepsilon_\lambda\}_{\varepsilon_\lambda \leq T} = T$ (figure 2.12). The DTM curves (Fig. 2.15d and 2.15h) shows the presence of lower plateau due to presence of zeroes reducing the slope thereby giving a slightly better estimate of α. It should be noted that these estimates are still biased; Tab. 2.7 shows the effect of both thresholds on real as well as simulated σ_e data. Simulating fields will still require additional fractional integration to reproduce σ_e as the values of H employed are different from that in real data. For exact analysis, new approaches are needed that can account for the missing values that are replaced with lower threshold.

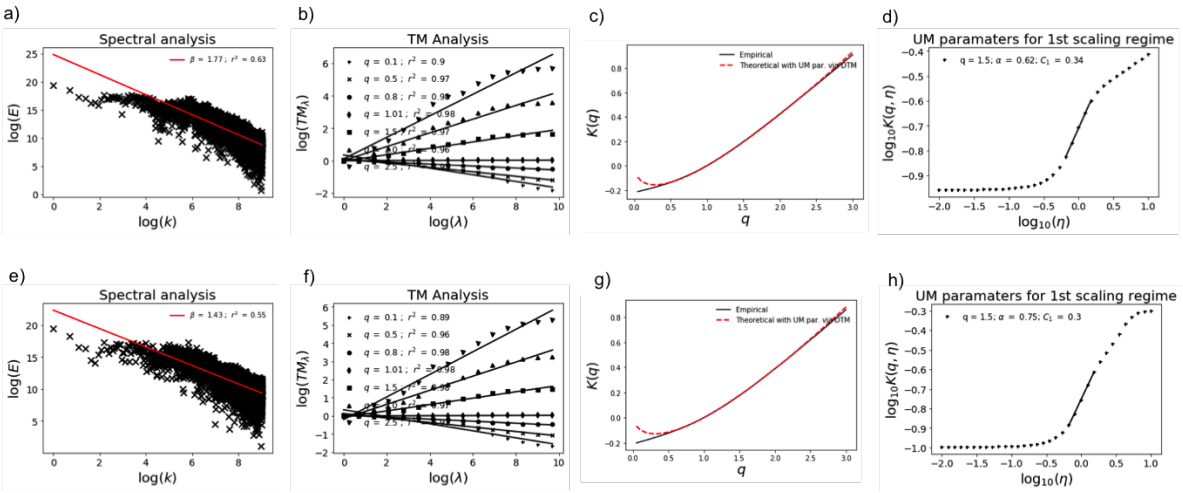

Figure 2.15: UM estimates of σ_e after setting values less than threshold to zero ($\{\varepsilon_\lambda\}_{\varepsilon_\lambda \leq T} = 0$); ENPC (a-d) and CDG (e-h) respectively.

	σ_e				$\alpha = 1.8;\ C_1 = 0.2$				
threshold	$\{\varepsilon_\lambda\}_{\varepsilon_\lambda \leq T} = T$		$\{\varepsilon_\lambda\}_{\varepsilon_\lambda \leq T} = 0$		$\{\varepsilon_\lambda\}_{\varepsilon_\lambda \leq T} = T$			$\{\varepsilon_\lambda\}_{\varepsilon_\lambda \leq T} = 0$	
% at threshold	83.2	89.07	85.8	83.17	0	82.2	89.6	82.2	89.6
$R2_{TM}$	0,971	0,957	0.971	0.98	0,997	0,995	0,981	0,995	0.9941
α_{DTM}	3,402	3,368	0,627	0.752	1,801	3,27	3,78	1.232	1.055
C_{1DTM}	0,076	0,059	0,344	0.305	0,191	0,08	0,043	1.243	0.263
β	1,782	1,43	1,778	1.437	0,777	0,77	0,763	0.783	0,78
H	0,527	0,32	0.599	0.413	0,065	0,02	-0,028	0.07	0.077

Table 2.7: Values of UM parameters for various threshold conditions for real and simulated data of σ_e.

Since atmospheric extinction depends on the presence of particles (ref equation 52), average

concentration of particulate matter (PM10) from the nearest available station (location: Lognes, data in μgm^{-3} at 1hr resolution by Airparif) was subjected to UM analysis. Good statistical correlation between extinction coefficients retrieved form lidar systems and conventional PM10/PM25 concentration was reported in Mei et al. (2017). Its worth noting that except for α, the values of UM parameters are comparable with that of σ_e (0.021, 1.674, 0.354 for C_1, β and H respectively). And that the value of α (1.811) is close to that of simulated σ_e (1.8) before application of threshold. This suggests that the expected correlation between particle concentration and scattering coefficient is masked by the presence of threshold in data set. However this is also a reduced take as concentration of aerosols are more complex than what one can infer from only PM10 values.

2.2.5. Main outcomes from UM analysis of σ_e

Temporal variation of σ_e values were extracted from MOR data from a present weather sensor and airport data here, and analysed in a Universal Multifractal framework. While the fields exhibited scaling behaviour, unrealistically elevated values of α and reduced values of C_1 were obtained from raw data. The bias is more visible in shape of $K(q, \eta)$, in DTM curve, the slope of which is used for calculating α. This behaviour was found to arise from the presence of a lower threshold in data due to artificially set measurement range in MOR as per application requirements. Using UM analysis, the influence of instrumental threshold in statistical estimates is illustrated here (with σ_e as the field) relying on both theoretical formulation and numerical simulations that confirm them. Basically imposing a lower thresholds sets $c(\gamma)$ to zero below a critical singularity. This in turns results in a linear portion for $K(q)$ below a critical moments which yields a divergence for $K(q, \eta)$ in log-log plot. As thresholds imposed by instruments or application exists in many geophysical measurements, these understanding will help in retrieving the actual underlying field as well as in modelling them.

Characterizing visibility poses a challenge as the field is inherently biased by the measurement range used for defining it from the objective measurements made in the atmosphere. Using multifractal analysis, we propose here the suitability of extinction coefficient for studying visibility or MOR because of its direct physical connection with atmospheric particles that acts as obscurants for visibility, and which should hence inherit scale invariant properties of Navier-Stokes equation. Analysis and simulation confirms this. However, the estimation of extinction coefficient can also create some biases from instrument corrections and varying interactions of different particle types with atmospheric parameters. This section only aim to account for the bias by virtue of range of measurement. In the specific analysis of σ_e, if computed with instrumental measurement thresholds, it is better suited to replace lower threshold with zero than value at lower threshold itself. There is a need to further examine σ_e using simulations involving fractional integration (to account for non conservative fields) and to link the same with associated atmospheric fields (pollutant concentration for example). This could further open new paths for more accurate numerical simulation and forecast of atmospheric visibility and tailoring it as per application requirements.

2.3. Towards joint multifractal analyses

In this chapter, individual multifractal analyses of various atmospheric fields were discussed, namely, R, KE and σ_e. The intention here, as illustrated in respective sections, is mainly to understand various fields in their real conditions so that this can be used for future simulations as well as experiments. Using the UM parameters, the fluctuations and intermittency across all scales were analyzed. Though not directly through the framework, the coupling between two fields (KE and R) was examined in line with existing understanding and theoretical backing. The correlation between the same fields (along with some others) are discussed in the next chapter. The need for selecting the appropriate field (the field with physical meaning and encompassing the variability in the process) was emphasised along with the need to be vigilant about the biases in data and their effect on statistical estimates. Specific conclusions and perspectives of the two studies on this topic are mentioned in their respective sessions.

In chapter 3, we continue the discussions with more emphasis on the coupling between various fields (RW-Turb and sense-city, sections 3.1 and **??**) in real as well as controlled environments.

3. Joint multifractal analysis of different atmospheric fields

The major focus of this chapter is the joint analysis of various fields for finding out the relative correlation between them in JMF. Towards this, the fields are first analysed individually using UM and based on the scaling behaviour observed they are subjected to joint analysis. The chapter is presented in three sub sections; data analysis from pays d'Othe windfarm, data analysis inside sense-city climate chamber, and analysis of rainfall and particles.

In section 3.1, various fields from the meteorological mast in section 1.1.3 are analysed alongside the turbine wind power following the sampling resolutions identified in section 1.2.2.4. Direct analysis of turbine power comes with a bias since the rated power acts as an upper threshold in time series. This is identified through comparison with total available power, and explained in the framework of UM. Using JMF, the correlations between the power available, wind velocity, and air density among each other and also with temperature, pressure, and relative humidity are explored during rain and dry conditions, and at various rain rates. Section 3.2 deals with two set of experiments performed inside sense-city for assessing its ability to reproduce small scale variability of rain and temperature - humidity. Using JMF tools, and the power law in section 2.1, the underreporting of rainfall kinetic energy by sense-city is identified and partially accounted for. This section also includes a joint analysis of temperature and humidity during a few real and simulated days inside sense-city. In the last section, 3.3.1, the scavenging efficiency of rain is examined using simultaneously measured aerosol particle concentration and precipitation. The biases encountered in JMF when the fields are non-conservative is also identified and commented on.

3.1. RW-Turb and fields studied

Modern wind turbines extract power from wind in the atmosphere and convert it into electricity that can be stored as well as distributed to locations of use via power grids. Popularly known term 'wind mill' refers to the historic usage where wind power was converted to mechanical energy at the location of usage (Manwell et al., 2010). In increasing global transition towards renewable and carbon neutral energy, wind power is extremely attractive as they have some of the lowest carbon emission in life cycle assessment (Li et al., 2020; Guezuraga et al., 2012; Wiser et al., 2011). The levelized cost of energy (LCOE, cost including building and operation) has also decreased drastically in past decades for both offshore and onshore wind power (80 % since early 1980, and further 30 % in past 5 years) giving it better economic value (Beiter et al., 2021).

Wind power production also plays an important role in achieving UN's (United nations) Sustainable development goal (SDG) 7 - affordable and clean energy for all. According to the IEA 2020 wind overview, global wind power capacity has increased by 14 %, with annual installations increasing by 54 % or 60 GW (IEA, 2020). This is projected to increase as UN high-level dialogue on Energy in 2021 (UN, 2022) has called for global doubling of annual investment in renewable

energy and energy efficiency by 2025 (triple by 2030 creating 60 million jobs worldwide). According to WindEurope (EWEA previously), an average offshore wind turbine (of capacity 2.5-3 MW, Vestas V90 used in this study falls under this category) can produce more than 6 million kWh a year which is enough for 1,500 average EU households. As per their estimation, by 2050, wind power production is expected to meet 50% of EU's energy demands (EWEA, 2012). In the context of France, wind alone accounts for one third of total renewable power production in 2021 (Jørgensen and Holttinen, 2022) which is set to increase as the country targets to have 50 offshore wind farms by 2050 through simplified legislation (Engie, 2022). One of the results from Cai and Bréon (2021)'s evaluation of wind power potential in France is that climate change will not significantly impact the statistical properties of mean load factor, thus making wind a reliable energy source in these changing times.

3.1.1. Importance of RW-Turb campaign and need for UM

Wind is a fluctuating field and owes its generation mainly to uneven heating of earth's surface by solar radiation and the pressure gradients generated from it. There are various other factors involved such as earth's gravitational and rotational forces, inertia of air, frictional forces on surface etc. resulting in atmospheric turbulence which makes characterization of the field a difficult task (with governing Navier-Stokes equations still remaining unsolvable, see section 1.2.1). This complexity is in turn transferred into extracted energy from the field - wind energy, as well as torque available at the turbine end, is proportional to the power of the instantaneous wind speed (introduced later in Eq. 64).

When it comes to power production by wind turbines, another complex effect is the influence of rainfall, which only a limited number of studies have tried to address so far. An earlier study by Corrigan and Demiglio (1985) reported a reduction in power production (20 % to 30 %, using a 38 m diameter two-blade turbine); this was later confirmed experimentally (Al et al., 1986). Cohan and Arastoopour (2016) (improving upon Cai et al. (2013)) examined the effect of rain on wind turbine blade aerofoil using multiphase (air as volatile and rain as liquid) computational fluid dynamics (CFD) and reported high sensitivity to performance in lower rain rates till rain rate is high enough to immerse most of the aerofoil surface underwater. Some positive influence of rain was also reported such as cleaning of blades (Corten and Veldkamp, 2001) increasing power production. Rain can also have long-term effects (mentioned previously in section 2.1) as the kinetic energy of impacting raindrops can cause leading-edge erosion (LEE) on turbine blades reducing their aerodynamic performance; this in turn results in lower annual energy and increased downtime (Keegan et al., 2013).

3.1.1.1 Importance of RW-Turb project

Understanding the long-term and short-term effect of rainfall on wind power production is hence important and the Rainfall Wind Turbine or Turbulence project (RW-Turb, *https://hmco*

.enpc.fr/portfolio-archive/rw-turb/), supported by Agence Nationale de la Recherche (ANR, French National research agency in English) is designed towards addressing this with simultaneous real-time in-situ measurement of rain and wind at turbine location. Details about the location and instrumentation of the meteorological mast and wind farm were already discussed in section 1.1.3. The main interest of the project as well as this section is twofold - the effect of rainfall on available energy and the effect on power extracted at turbine end. Towards this, like TARANIS observatory of section 1.1.1, RW-Turb is also equipped with measurement of drop sizes distribution (DSD) along with commonly examined rainfall rate (mmh^{-1}). As mentioned before, the small-scale fluctuations in wind are transferred to power produced; this is further complicated by the fact that wind turbine hubs are located in the atmospheric boundary layer. In addition, improved understanding of turbulence is identified as one of the leading challenges in the field of wind power by experts (van Kuik et al., 2016). Towards this, RW-Turb provides high-resolution (100 Hz) measurement of 3D wind velocity along with other atmospheric fields at the turbine location (see Fig. 1.7).

3.1.1.2 Need for UM analysis

When it comes to the working of modern turbines, one way to account for wind variations is through variable speed turbines and adaptive torque control enabling maximum power capture. However, the commonly used parameter for control, 'turbulence intensity' (standard deviation of wind speed divided by mean wind speed over 10 min) cannot fully capture the behaviour (see non-Gaussian behaviour of wind velocity in in Fig. 3.1), and is too coarse to represent the variability (active torque controls should responsive down to a few seconds). Further, this doesn't consider any effect of rain that could get transferred to loads on turbine (Johnson, 2004). To understand the complex effect of rain and turbulence on power production, with given access to high-resolution data, an appropriate theoretical framework is required to characterize intermittency at all scales of measurement. As introduced in section 1.2.1 and illustrated throughout this thesis, multifractal tools (UM and JMF) can be used for characterizing this complexity. Using the framework of UM, Fitton et al. (2011, 2014) studied scaling behaviour and multifractal properties of wind velocity and torque fluctuations in wind farm test sites (in Germany and Corsica), and made a case for multifractal modelling of atmospheric turbulence. Calif and Schmitt (2014) also illustrated the intermittent and multifractal nature of turbulent wind speed and aggregate power from a wind farm over a wide range of scales and showed a coupling between using generalized correlation function (GCF) based joint multifractal description.

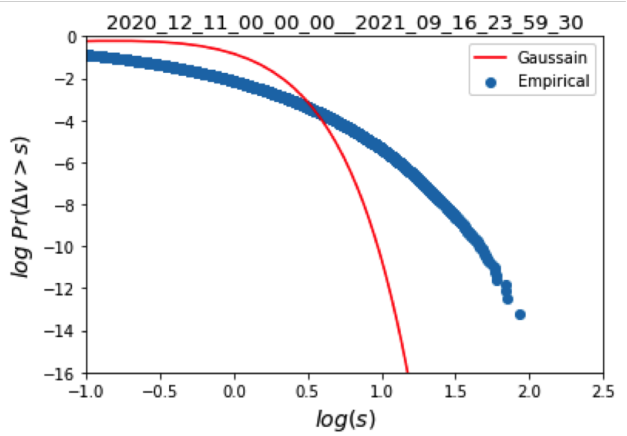

Figure 3.1: Log-log plot of exceedance probability, $Pr(\Delta v > s)$, of positive horizontal velocity increments, $\Delta v(\tau) = v(t+\tau) - v(t)$, in Fig. 1.10b (Dec 2020 to July 2021, at 1 Hz from location 1 of RW-Turb meteorological mast) along with a Gaussian distribution to illustrate latter's inadequacy. s is a threshold of intensity and τ here is 15 s.

In light of the scientific perspectives (and opportunities) mentioned so far, the main objectives of this subsection are - to characterize the small-scale fluctuations in wind and associated fields (using UM, refer section 1.2.2), and to explore correlations between them in various meteorological conditions (using JMF, refer section 1.2.3).

3.1.2. Data and availability

An overview of the campaign with data and instrumentation is provided in section 1.1.3. To recap, RW-Turb measurement campaign (Pay d'Othe, 110 km southeast of Paris, France) consists of a meteorological mast in a wind farm (jointly operated by Boralex and JP Énergie Environnement) with two sets of optical disdrometers (OTT Parsivel[2]), 3D sonic anemometers (ThiesCLIMA) and mini meteorological station at heights roughly 45 m and 80 m. The finest time-step of measurement available are 30 s, 0.01 s, and 1 s respectively. 3 months of continuous data from RW-Turb is made available for open access in Gires et al. (2022); for more details on campaign and instrumentation, readers are directed to the paper and section 3.1.

3.1.2.1 Wind power available and air density

Power production from turbines are analyzed at the lowest available time-step, 15 s, here (4 Vestas V90 - 2MW managed by Boralex, see Fig. 1.7 for location from the meteorological mast). Power available at the turbine for extraction is given by

$$P_a = \frac{1}{2}\rho A v^3 C_p \tag{64}$$

where ρ is the air density at wind turbine height (h_{hub})., A is the swept area of turbine rotor

, v the wind velocity (ms^{-1}) approximated at turbine height and C_p the power coefficient or Betz coefficient (for Vestas-90 examined here, h_{hub} = 80 m; A = 6,362 m^2, and rated power is 2 MW).

Aerodynamic losses prevent the turbine from extracting the maximum available wind power and this limiting factor is given by Betz coefficient ($C_{P,Betz} = \frac{16}{27}$). The value of air density is often approximated as $1.255\,kgm^{-3}$ (standard value at sea level, 15 °C). However, it is known to show fluctuations and reported to have an effect on power generation in varying levels (Jung and Schindler, 2019; Ulazia et al., 2018). It is possible to calculate air density by extrapolating ideal gas law: $\rho = P_h/G.T_h$, where P_h and T_h are the pressure and temperature at h_{hub}, and G the atmospheric gas constant ($287.058\,Jkg^{-1}K$ for dry air). For the purpose of this analysis, air density was considered as a varying quantity and estimated using the current official formula of the International Committee for Weights and Measures (CIPM), referred to as CIPM-2007 equation which accounts for humidity (Picard et al., 2008):

$$\rho(T,P,H_r) = \frac{PM_a}{Z(T,P,H_r)RT(K)} \left\{ 1 - x_v(T,P,H_r) \left[1 - \frac{M_v}{M_a} \right] \right\} \tag{65}$$

where T (°C), P (Pa) and H_r ($0 \leq H_r \leq 1$) are temperature, pressure and humidity from Meteorological station at h_{hub}. Other derived parameters are
$T(K)$, air temperature (in K; from T)
Z, compressibility factor (a function of T and P)
R, molar gas constant ($Jmol^{-1}.K^{-1}$)
x_v, mole fraction of water vapour
M_a, molar mass of dry air ($gmol^{-1}$)
M_v, molar mass of water ($gmol^{-1}$)

3.1.2.2 Turbine power and associated issues in data analysis

For Vestas V-90, the rated power is 2 MW; this means that the maximum power turbine can produce is 2000 kW. However, if we calculate the available power as per Eq. 64, there are many instances where it can go beyond the rated value. While analysing the variability of field using statistical methods, the presence of instrumental limits (here an upper limit) can introduce biases. For example, the effect of instrumental lower threshold was discussed in section 2.2 within the framework of UM analysis using extinction coefficient (σ_e) as the field. In addition to this, sometimes power "produced" was reported with negative values. This indicates that the turbine failed to produce any power during that time period and that energy was consumed in its basic operation. Fig 3.2 shows the real and theoretical turbine power state curve along with the bias it poses in statistical analysis.

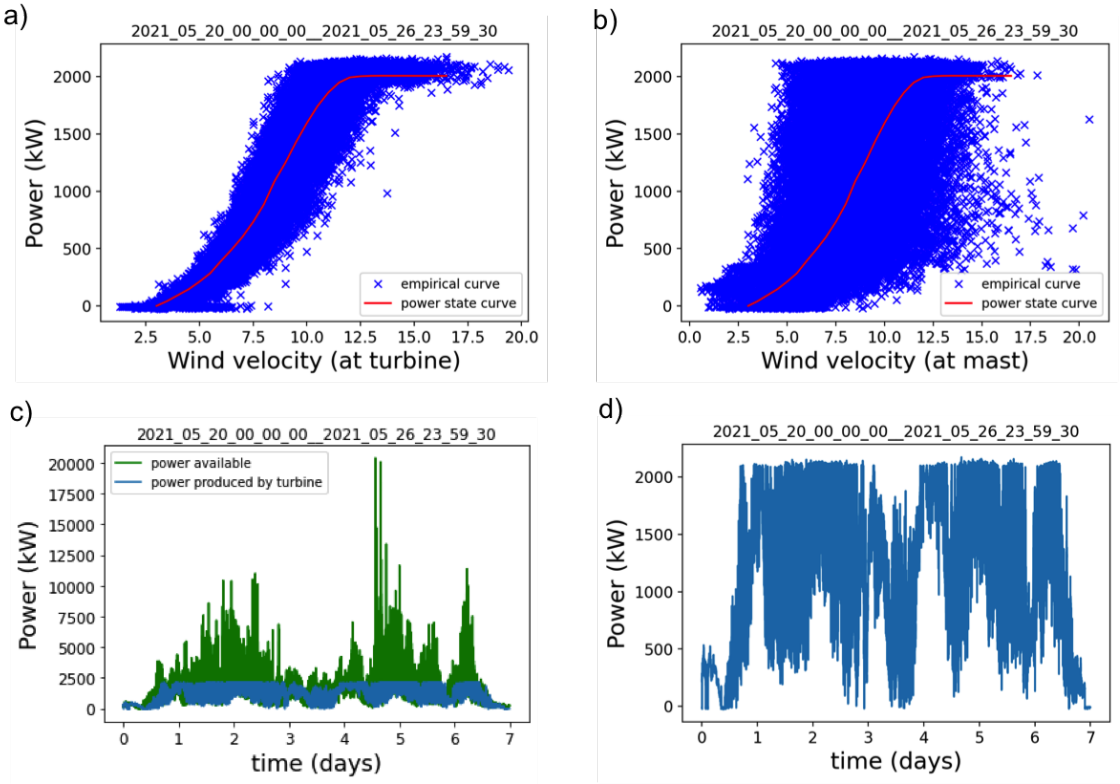

Figure 3.2: Illustration upper threshold (by virtue of rated power of 2000 kW) in power produced by turbine: a) Empirical and theoretical power state curve of turbine 1 with wind velocity from the turbine and b) Wind velocity from location 1 on the mast, c) Power produced by the turbine (P_t) and actual wind power available P_a, and d) Effect of rated power as threshold in time series and effect of negative values in P_t for 1 week long data - 20 May 2021 to 26 May 2021

Along with power produced, turbine data also provides wind velocity at the location (from a basic sensor installed on the hub), which is used for its internal monitoring; this also gave less scatter in the empirical state curve of turbine (Fig. 3.2a). But, for research purposes, 3D anemometer at the mast offers more reliable measurement (on almost same horizontal plane as turbine hub) and only this was data considered for analysis purposes (Fig. 3.2b). However, it should be noted that turbines are not in the exact location of mast (Turbine 8 and 9 are ≈ 3.5 km away) and hence approximation of wind velocity from mast comes with some biases. From Fig. 3.2c and Fig. 3.2d, it can be clearly seen that the rated power imposes an upper threshold on turbine power (P_t) while power available (P_a) is the actual field. For this week long series of P_t, 21.7 % of data was at upper threshold and 2.9 % were either zero or negative (taken as zeroes in analysis); this percentage was found to change according to data selected. Effect of these limits in UM analysis is shown in Fig. 3.3 where the data in Fig. 3.2 is treated as an ensemble of 32 minutes. UM analysis was performed on direct fields as values of H were within the acceptable limits ($H < 0.3$). Presence of rated power clips the values of field, and results in a reduced value of α for P_t (Fig. 3.3a: $\alpha = 1.36$, $C_1 =$

0.00715) from that of P_a (Fig. 3.3b: α = 1.93, C_1 = 0.01753). Imposition of a similar threshold ($P_a <= 200 = 200$) on P_a was found to artificially reducing the estimates (α from 1.93 to 1.39, C_1 from 0.10753 to 0.0076) in Fig. 3.3c, bringing them closer to that of biased turbine power, P_t (Fig. 3.3a).

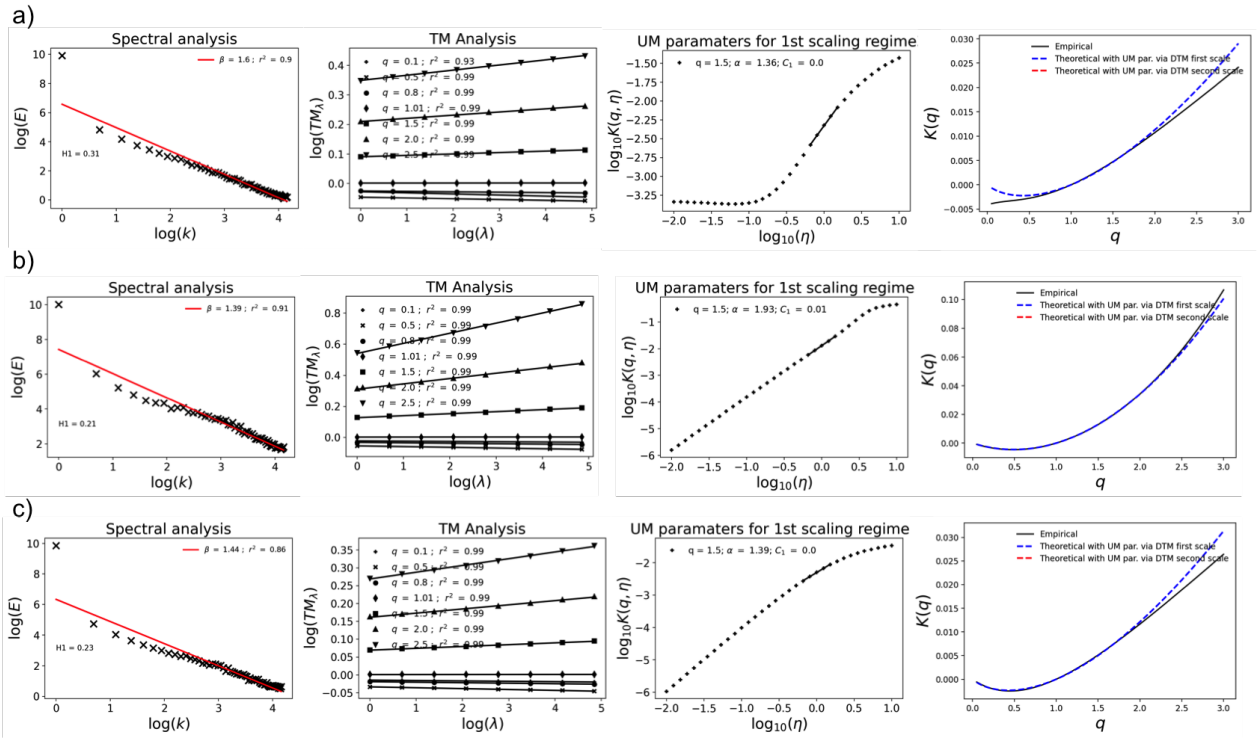

Figure 3.3: Spectral analysis (Eq. 8), TM analysis (Eq. 14), DTM curve (Eq. 21) and K(q) for a) power produced by turbine (P_t) which has intrinsic threshold because to rated power, b) power available (P_a) which is the actual field, and c) P_a where upper threshold is imposed at rated power of turbine. Data used: time series from 20 May 2021 to 26 May 2021 with lowest time step of 15 s.

It should be noted that the effect of threshold could be different according to size of sample and scaling regimes studied; for example for the same data, the difference in α was found to be greater (α_{P_a} = 1.59, α_{P_t} = 0.92 on fluctuations) when analyzed for scales greater than 4 min. In the same spirit as σ_e in section 2.2, the effect of rated power as upper threshold in P_t is explored here in the theoretical framework of UM. For simplicity, effect on different scaling regimes as well as the additional complexity from the known effect of zeroes (Gires et al., 2012) are not considered.

3.1.2.3 Testing the effect of upper threshold on UM analysis

Let's take the upper threshold (rated power in this case) at the largest possible scale ratio as

$$T = \Lambda^{\gamma_T} \tag{66}$$

where γ_T is the singularity corresponding to threshold T, and Λ the maximum resolution (length of time series).

For multifractal fields, the probabilities of exceeding scale independent thresholds, λ^{γ}, scale with resolution, λ (see Eq. 13). At the upper threshold T

$$Pr(\varepsilon_\lambda \geq T) \approx \lambda^{-c(\gamma_T)} \tag{67}$$

If we set the upper threshold i.e. setting all the values of the field greater than T equal to T (represented here by this expression: $\varepsilon_\lambda \geq T = T$), the probability of having values greater than T, $Pr(\varepsilon_\lambda > T)$, becomes 0 reducing the above relation into $Pr(\varepsilon_\lambda = T) \approx \lambda^{-c(\gamma_T)}$. This leaves the value of $c(\gamma)$ equal to $+\infty$ for singularities above γ_T (for $\gamma > \gamma_T$, $c(\gamma) = +\infty$). Here $c(\gamma_T)$ is the limiting non-zero value above which $c(\gamma)$ becomes $+\infty$. This effect of upper threshold ($c(\gamma) \to +\infty$ for $\gamma > \gamma_T$) is similar to the effect of sampling dimension (D_s) in UM framework. The maximum observable singularity can be defined by taking probability at corresponding threshold as in eq.67.

$$Pr(\varepsilon_\lambda \geq \lambda^{\gamma_S}) \approx \frac{1}{N_s \lambda^D} \tag{68}$$

where $N_s = \lambda^{D_s}$ (D_s being the sampling dimension: fractal dimension corresponding to the number of independent samples with resolution λ in a D dimensional space). λ^D is the number of values per sample. Using the notions of D_s and D, γ corresponding to sampling resolution, γ_s can be estimated from $c(\gamma_s)$, $c(\gamma_s) = (D + D_s)$

To recap, in the framework of UM, codimension function $c(\gamma)$ and scaling moment function $K(q)$ are (refer section 1.2.2, Eqs. 17 qnd 16)

$$\begin{aligned} c(\gamma) &= C_1 \left(\frac{\gamma}{C_1 \alpha'} + \frac{1}{\alpha} \right)^{\alpha'} \\ K(q) &= \frac{C_1}{\alpha - 1}(q^\alpha - q) \end{aligned} \tag{69}$$

When $\gamma > \gamma_s$, $c(\gamma) = +\infty$; by Legendre transform $K(q)$ becomes linear from $q > q_s = c'(\gamma_s)$

$$\gamma_s = \alpha' C_1 \left(\frac{D+D_s}{C_1}\right)^{\frac{1}{\alpha'}} - \frac{C_1}{\alpha-1}$$
$$q_s = \left(\frac{D+D_s}{C_1}\right)^{\frac{1}{\alpha}} \tag{70}$$

In the case of sampling dimension, $c(\gamma)$ varies as follows

$$c(\gamma) = \left\{ \begin{array}{ccc} +\infty & for & \gamma > \gamma_s \\ D+D_s & for & \gamma = \gamma_s \\ c(\gamma) & for & \gamma < \gamma_s \end{array} \right\} \tag{71}$$

Similarly, at the presence of upper threshold here ($\varepsilon_\lambda \geq T = T$), $c(\gamma)$ reaches $+\infty$ at an earlier limiting value value $c(\gamma_T)$ where $\gamma_T < \gamma_s$ (Fig. 3.4a)

$$c_T(\gamma) = \left\{ \begin{array}{ccc} +\infty & for & \gamma > \gamma_T \\ c(\gamma_T) & for & \gamma = \gamma_T \\ c(\gamma) & for & \gamma < \gamma_T \end{array} \right\} \tag{72}$$

In UM framework, the limit case $\gamma_T = \gamma_{min}$ can be obtained as eq.70 from eq.69

$$\gamma_T = \alpha' C_1 \left(\frac{c(\gamma_T)}{C_1}\right)^{\frac{1}{\alpha'}} - \frac{C_1}{\alpha-1}$$
$$q_T = \left(\frac{c(\gamma_T)}{C_1}\right)^{\frac{1}{\alpha}} \tag{73}$$

To summarize, in normal data analysis, $c(\gamma)$ is bounded by a maximum value $c(\gamma_s)$ above which it becomes infinite. $K(q)$ which is connected to $c(\gamma)$ through Legendre transform ($K(q) = \max_\gamma\{q\gamma - c(\gamma)\}$) becomes linear beyond this q ($q \geq q_s$) value ($K(q) = (q-q_s)\gamma_s + K(q_s)$). When an upper threshold is imposed ($\varepsilon_\lambda \geq T = T$), $K(q)$ becomes linear at an earlier value of q ($q_T < q_s$) defined by γ_T ($\gamma_T < \gamma_s$) at $c(\gamma_T)$ (Fig. 3.4b).

$$K_T(q) = \left\{ \begin{array}{ccc} \gamma_T(q-q_T) + K(q_T) & for & q > q_T \\ K(q_T) = q_T\gamma_T - c(\gamma_T) & for & q = q_T \\ K(q) & for & q < q_T \end{array} \right\} \tag{74}$$

In Double Trace Moment (DTM) technique, for a given q: $K(q,\eta) = K(q\eta) - qK(\eta)$, which for UM fields = $\eta^\alpha K(q)$. When no thresholds are applied $K(q,\eta)$ varies as

$$K(q,\eta) = \left\{ \begin{array}{cc} (q-1)(D+D_s) & for \quad \eta \geq \eta_+(q) = q_s \\ \eta^{\alpha} K(q) & for \quad \eta < \eta_+(q) = q_s \end{array} \right\} \tag{75}$$

where $\eta_+(q)$ corresponds to values of η where upper portion of DTM curve becomes plateau due to sampling limitation ($q_s = c'(\gamma_s) = ((D+D_s)/C_1)^{1/\alpha}$). It starts at $\eta_+(q)$, the moment above which $K(q)$ becomes linear (which is q_s). In the presence of an upper threshold ($\varepsilon_\lambda \geq T = T$), DTM curve will be (Fig. 3.4c)

$$K_T(q,\eta) = \left\{ \begin{array}{cc} (q-1)c(\gamma_T) & for \quad \eta \geq \eta_+(q) = q_T \\ \eta^{\alpha} K(q) & for \quad < \eta_+(q) = q_T \end{array} \right\} \tag{76}$$

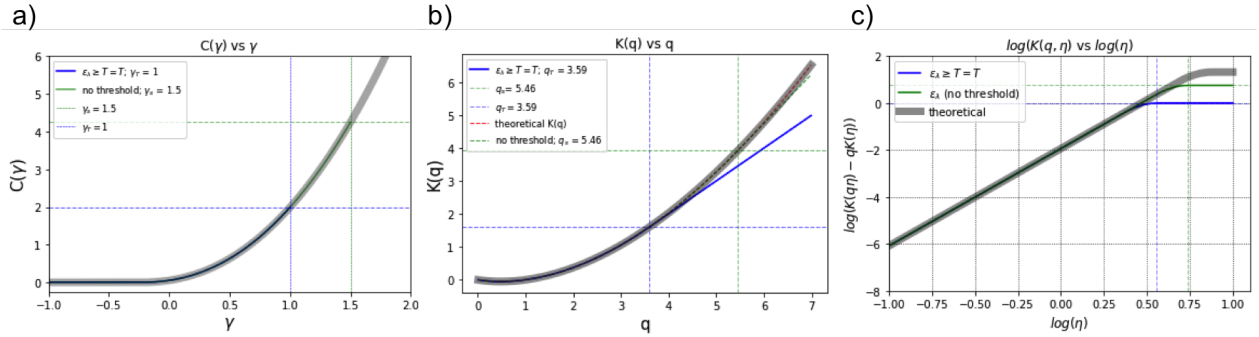

Figure 3.4: Influence of threshold on a) $c(\gamma)$ vs γ curve: $c(\gamma)$ reaching $+\infty$ at γ_T than γ_s, b) on DTM curve: $K(q)$ becoming linear at q_T than q_s), and c) on $K(q)$ vs q curve: $K(q,\eta)$ reaching upper plateau early. Arbitrary values were used for γ_s and γ_T; UM parameter values of fields were taken as $\alpha = 1.8$ and $C_1 = 0.2$.

It is important to note here that the value of $K(q,\eta)$ doesn't reach the upper plateau abruptly at q_T or q_s, rather, it flattens gradually starting from a value of $\eta = q_s/q$ or q_T/q (as per value of $q\eta$ in $K(q,\eta)$). Presence of upper threshold shifts this starting point and decreases the range of possible values for estimation of α (slope of DTM curve), hence, presence of plateau will result in biased (reduced) estimates.

Under estimation in values of α due to application of upper threshold was already observed Fig. 3.3c. To understand this further, numerical simulations ($\alpha = 1.2$; $C_1 = 0.2$ - ensemble of sample size 128 and number of samples 100) are shown in Fig. 3.5 with gradual application of upper threshold (effect of zeroes not considered). $K(q)$ becoming linear at earlier and earlier values of q (after respective q_T) with threshold can be seen in third column (like in Fig. 3.4b). The DTM curve in second column shows that both α and C_1 are decreasing with progressive application of thresholds (From 0 to 30%, α decreased from 1.8 to 1.56 while C_1 decreased from 0.17 to 0.05). While explaining this bias in framework before, the upper threshold was introduced at the maximum

resolution (Eq. 66, Λ^{γ_T}). Since in practice, the lower scales in UM are obtained from averaging the outer scale (at maximum resolution), the threshold values (and hence γ_T) at each stage doesn't exactly correspond to the originally defined one. Effect of this is the reason for increased 'transition part' (straight line slope to upper plateau) of the curve in simulations here (more than that in Fig. 3.4c). When the slope calculation was forced at $\eta = 1$ (so that TM and DTM estimates are same), the bias in values of α increased (for example the already biased value of α at 30 % threshold, 1.58, got further reduced to 0.95; C_1 remained moreover similar at all thresholds) as the slope estimation moved to 'transition part'. It is interesting to note that the trend here (only for α) is the opposite of what was observed during numerical simulations with lower threshold in section 2.2 (refer Fig. 2.14). However, unlike σ_e which only had a lower threshold, P_t (Fig. 3.3a), has a combination of upper threshold from rated power and lower threshold (zeroes) from negative power. This further reduces the range of available η for estimation of α by imposing a lower plateau as well (see Fig. 3.3, third column). There could also be additional complexity from the fact that conservative part of fields P_t and P_a were retrieved by fluctuations while the simulated fields are conservative by default.

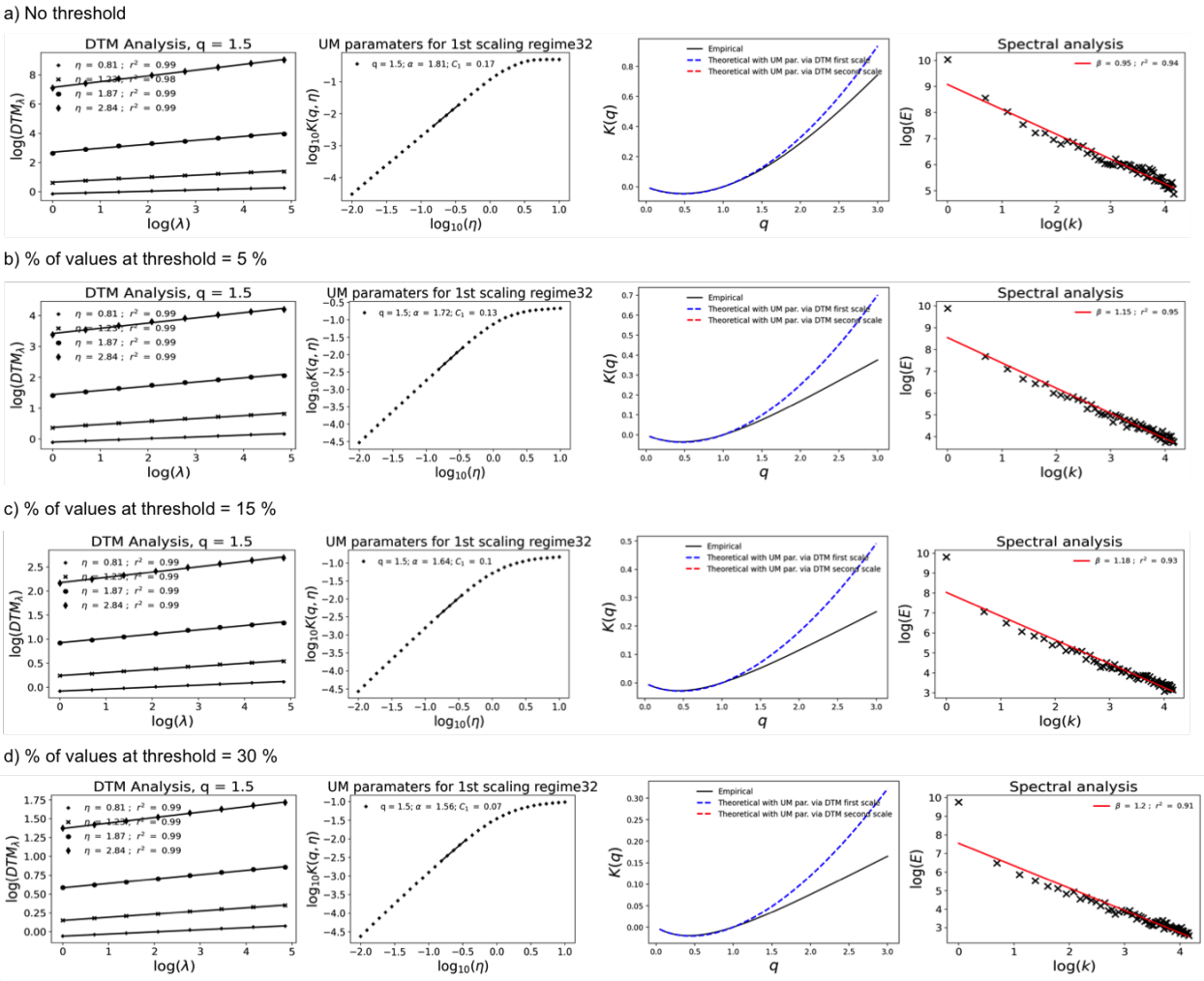

Figure 3.5: Effect of upper threshold illustrated using numerical simulations - discrete cascades of size 128 with 100 samples: $\alpha = 1.8$ and $C_1 = 0.2$. Decrease in α and increase in C_1 with threshold can be seen from sub figures a to d.

Actual sampling resolution and filtering of data

Other than this bias from rated power in turbine, there were few more concerns regarding the quality of remaining data. On the basis of data presented in Gires et al. (2022), UM analysis of the fields revealed that even though data is recorded at finer resolution, the actual sampling resolution for studying variability may be coarser. The analysis is reproduced in the section 1.2.2.4 and the potential of UM in detecting instrumental white noise is commented on. Based on this insight, the fields are analyzed here at lower resolutions than manufacturer claims (which are still high-resolution as far as data is concerned). Table 3.1 summarizes the fields studied and their actual sampling resolution. This is applicable for instruments at location 1 as well as location 2 on the mast (refer Fig. 1.7).

Field	**Data source**	**measured/derived**	**recording resoltion**	**actual sampling resolution**
Temperature (T)	Meteorological station	measured	1 Hz	15 s
Pressure (P)		measured	1 Hz	15 s
RH (RH)		measured	1 Hz	15 s
Air density (ρ)		derived, CIPM-2007	1 Hz	15 s
Power available (P_a)		derived (ρ, v)	1 Hz	15 s
Wind velocity (v)	3D sonic anemometer	measured	100 Hz	1 Hz
Power produced (P_t)	Wind turbine	measured	15 s	15 s
wind velocity (v_t)		measured	15 s	15 s
rainfall(R)	Disdrometer	measured	30 s	30 s

Table 3.1: Details of fields studied, their source and actual sampling resolution at which they were studied (based on results from UM analysis in 1.2.2.4). Station parameters were taken at 15 s (instead of 16 s) to match wind turbine power measurements.

Before proceeding to analysis, the whole data set was validated (Nov 2020 to May 2022) by checking for unusual entries and instrument downtimes at both locations on the mast as well as 4 turbines. Time steps were not considered for all fields if any one of the devices was not working. This included 5 months when Anemometer (17 June 2021 to 29 Nov 2021) and Station (17 June 2021 to 11 Nov 2021) at location 1 on the mast were struck by lightning and had to be replaced, and some time steps of turbine downtime (which were given as interpolation in unfiltered data) during March and June 2021. There were few time steps where abnormal values were recorded for T, P and RH; these were removed by a simple filter that replaced values of station parameters with 'nan' (not a number) whenever pressure was shown below 800 hPa. If 'nan' were isolated, they were replaced by the average of preceding and succeeding entries.

For studying the effect of rain specifically, dry and rain events were selected from 9 months of RW-Turb data (12 Nov 2020 to 16 Sep 2021). An event was considered strictly rain, if there was a cumulative depth greater than 0.5 mm and separated by at least 15 minutes of dry condition before and after. The converse of this criteria was employed for getting dry events; events smaller than 5 min were discarded as well as events where any of the devices (including turbines) are giving more than 30 % 'nan' or 50 % zeroes. This methodology identified a total of 431 rain events (and 592 dry events); further removal of events was performed in subsequent UM analyses to accommodate event size to the closest power of 2.

3.1.3. Joint analysis of RW-Turb fields

The primary interest in having a campaign where simultaneous measurement of wind and rain is to study the correlations between them. In this section, the results obtained from this endeavor are presented; previously discussed framework of joint multifractals (JMF) was used in joint char-

acterization (see section 1.2.3).

3.1.3.1 Dry and rain events

Before performing joint analysis, the fields were individually studied for possible differences in behaviour during rain and dry conditions using UM analysis. Rain and dry events were selected following the criteria mentioned in previous section, and each of the fields in Tab. 3.1 were subjected to multifractal analysis for the selected events separately as well as as an ensemble (rain ensemble and dry ensemble). After data filtering, a total of 213 rain (and 393 dry) events were identified from 6 month-long data (12 Dec 2020 to 03 June 2021). For UM analysis, a sample size (N_{sam}) of 128 (32 min) was used for fields at 15 s and 2048 ($\approx$ 32 min) for fields at 1 Hz. If an event was larger than the sample size (powers of 2 greater than N_{sam}), it was split into ensembles of length N_{sam}. For example, it the length of event is 300 (75 min), it was trimmed to nearest power of 2 (256, 64 min) and made into an ensemble of size 128 (32 min) with 2 columns. To maximize the number of events included in the analysis events with length greater $\geq$ 80% of N_{sam} (or powers of $2 > N_{sam}$) were included in the analysis by extending the event length in data set to N_{sam} (or powers of $2 > N_{sam}$).

Results of an ensemble analysis of all rain events are shown in Fig. 3.6 (fields at 15 s) and Fig. 3.7 (fields at 1 Hz). Wind velocity (v) was estimated as the horizontal resultant from U_x and U_y provided by 3D sonic anemometer; Power available P_a was derived from this using Eq. 64. Both quantities were initially estimated at an instrument resolution of 1 Hz (Fig.3.6) and also averaged to 15 s (Fig. 3.7). Since air density (ρ) involves station parameters (at 15 s), the finest time step was limited by them to 15 s. For illustration purposes only Turbine 1 (turbine closest to the mast, Fig. 1.6) is shown; other turbines gave similar estimates. The rest of the fields were taken from instruments at location 1 of the mast ($\approx$ 80 m height) which is on a similar horizontal plane as turbines.

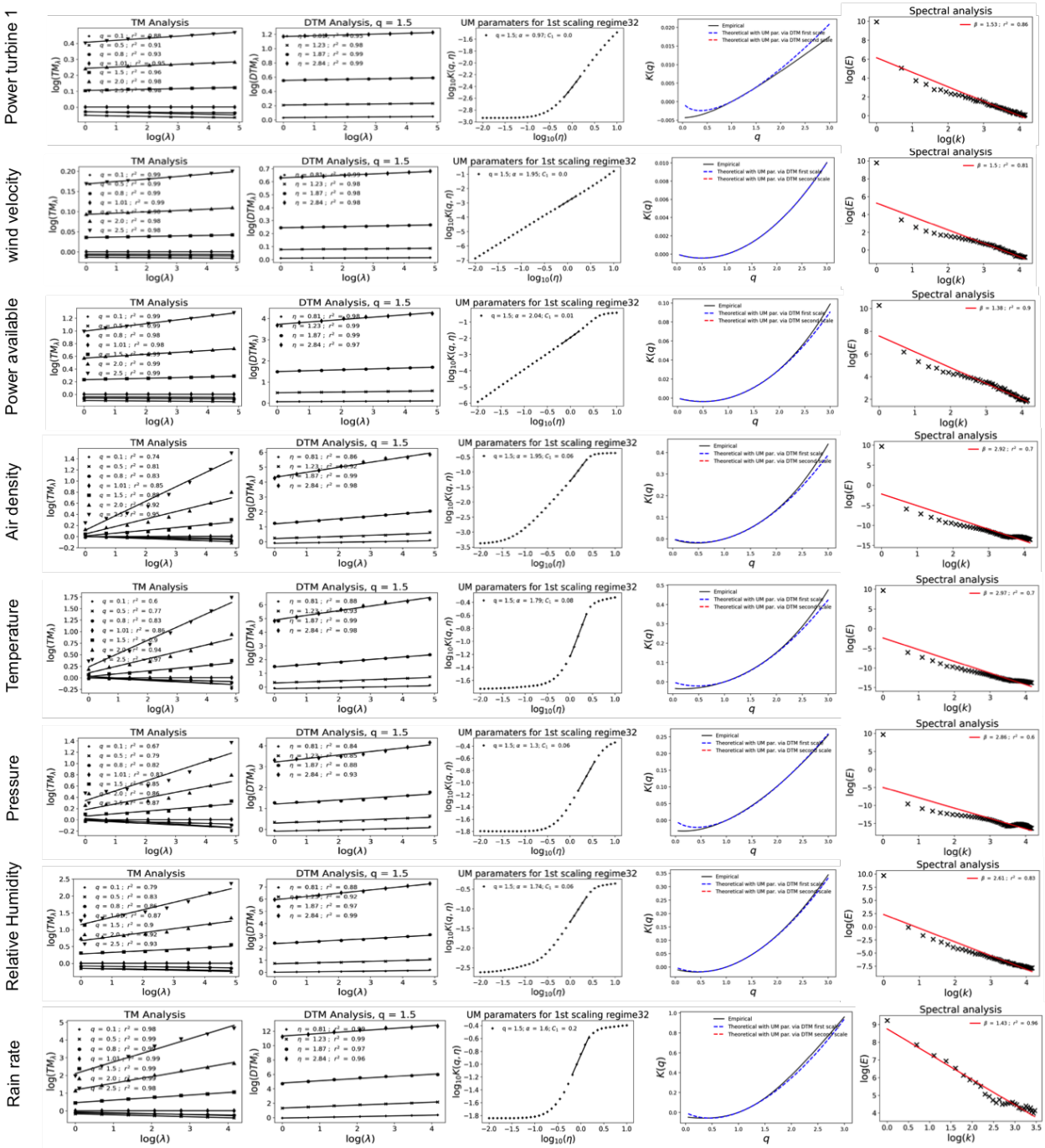

Figure 3.6: UM plots of rain events from 11 Dec 2020 to 03 June 2021 (6 months) for all fields studied at the lowest instrumental resolution of 15 s (except for Rain rate at 30 s). Ensemble of 213 events at a sample size of 128 (32 min), fluctuations of the field were used for station fields while direct field for rest; spectral plots here are from direct data.

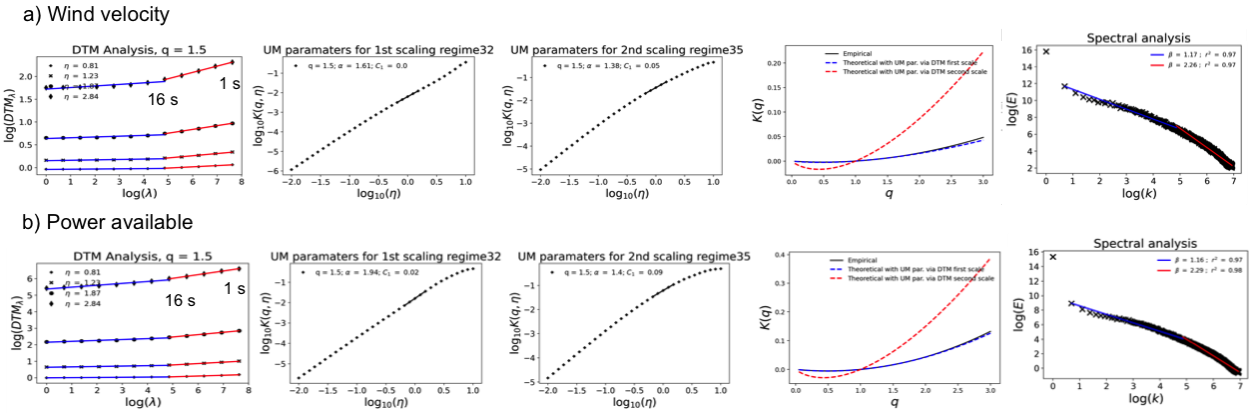

Figure 3.7: UM plots of rain events from 11 Dec 2020 to 03 June 2021 (6 months) for a) wind velocity and b) power available studied at the lowest instrumental resolution of 1 Hz. Ensemble of 213 events at a sample size of 2048 ($\approx$ 32 min); α was estimated from the slope of DTM curve at $\eta = 0$. FIF of the field was used; spectral plots here are from direct data.

UM plots for each field as an ensemble of all rain events are given in Fig. 3.6 and Fig. 3.7 for the time period considered. The value of the non-conservation parameter H was too high for UM analysis of station fields directly - T, P, RH, and ρ - ($H \sim 0.9$ and $\beta \sim 2.8$); this was reduced along with spectral slope to conservative values by fluctuations ($H \sim 0$ and $\beta < 1$). They all gave similar C_1 values (~ 0.06); T and RH gave similar α values (~ 1.75) as well while P and ρ gave values of 1.3 and 1.95. For P_a and v, the 1 Hz data, two scaling regimes were observed with a break closer to 15 s (16 s in actuality, Fig. 3.7). Direct data gave estimates of H acceptable ($H < 0.5$) for performing UM analysis when 15 s was used as the finest time step (Fig. 3.6: $H \sim 0.2$ and $\beta \sim 1.4$), while the smaller scale (1 Hz to 15 s) gave very non-conservative values ($H \sim 0.6$ and $\beta \sim 0.6$). For P_a and v at 1 Hz (1 Hz to 15 s), taking the fluctuations reduced H too much ($\sim$ -0.4). In examining these smaller scale variations, fractionally integrated flux (FIF) is recommended for retrieving the conservative part, this gave $H \sim 0$ (Fitton, 2013; Gago et al., 2022). For P_a and v, the values of α & C_1 were 2.04 & 0.014, and 1.95 and 0.0017 for larger scales (from 15 s); for finer scales (1 Hz to 15 s) α values were smaller while C_1 larger : 1.40 & 0.09, and 1.38 & 0.05. The possibility of 2 scaling regimes for 15 s fields is not considered here (Fig. 3.7) as it was convenient to compare rain and dry conditions in a single regime.

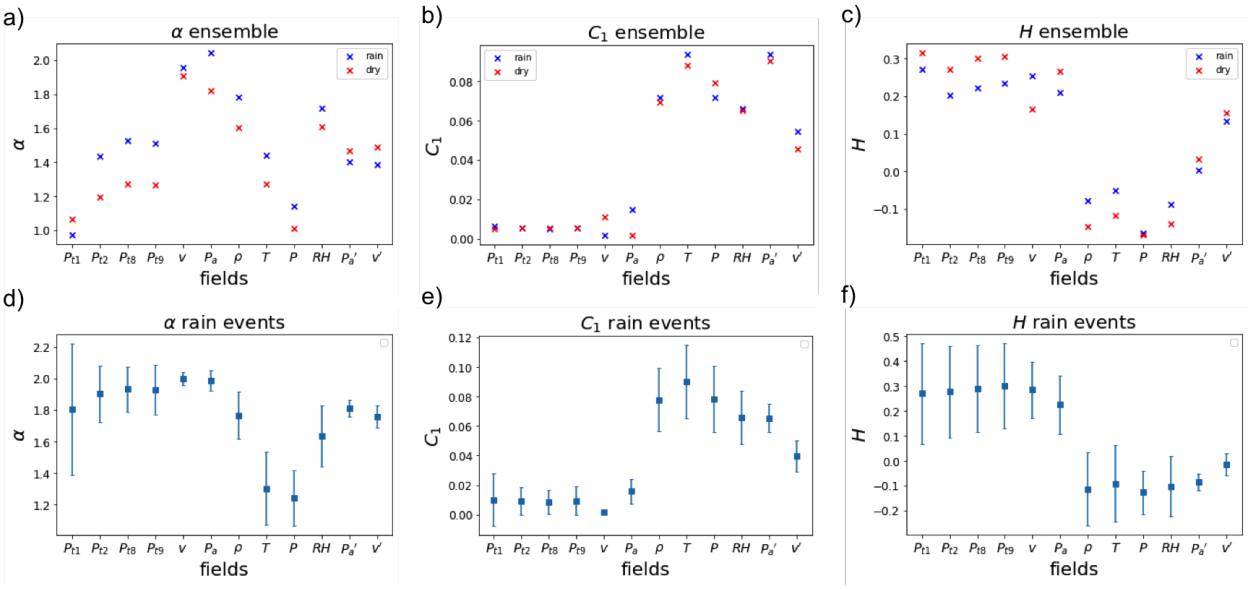

Figure 3.8: Comparison between UM parameters of rain and dry events ensemble: a) α, b) C_1, and c) H. Mean and standard deviation of d) α, e) C_1, and f) H for individual rain events. All fields were analyzed at 15 s resolution except those with $'$ (P_a and v, $'$ for 1 Hz to 15 s) at the end. Data from 12 Dec 2020 to 03 June 2021, the subscript of P_t shows the turbine number. The uncertainty range is different among fields, with v and P_a giving similar parameters for all events while the values are much fluctuating between events for rest.

From ensemble analysis, slightly increased values of α were observed for the rain ensemble in comparison to the dry ensemble (plots shown in Appendix A.3) for all fields. Since C_1 is rather similar, it can be inferred that the fields exhibit more variability when rain is present (Fig. 3.8a and Fig. 3.8b). With this insight, rain events are analyzed in detail individually. Mean and std dev of UM parameters considering all individual rain events used in the ensemble are given in Fig. 3.8.

3.1.3.2 Joint analysis of fields according to rain

The scaling and multifractal properties of fields were examined for rain (and dry) events individually and as an ensemble previously. The inter influence of some of these fields are obvious by virtue of definition: available wind (and hence power extracted by turbines, P_t) and air density (ρ) are derived from wind velocity (v) and station fields (T, P, and RH) respectively. For understanding the influence of rain on wind power, it is essential to understand its natural correlation with wind (and hence power available, P_a). Using the previously defined framework of joint multifractals (JMF, section 1.2.3), it is possible to analyze two conservative fields together and to estimate the correlation exponent between each other when one is expressed as a multiplicative combination of the other with an independent multifractal field. For example, the correlation of P_a with v can be explored by expressing them as $P_{a\lambda} = \frac{v_\lambda{}^a Y_\lambda{}^b}{(v_\lambda{}^a Y_\lambda{}^b)}$, where λ is the resolution of the field,, Y_λ another UM field and a and b are the exponents of correlation between them. (Gires et al., 2020b).

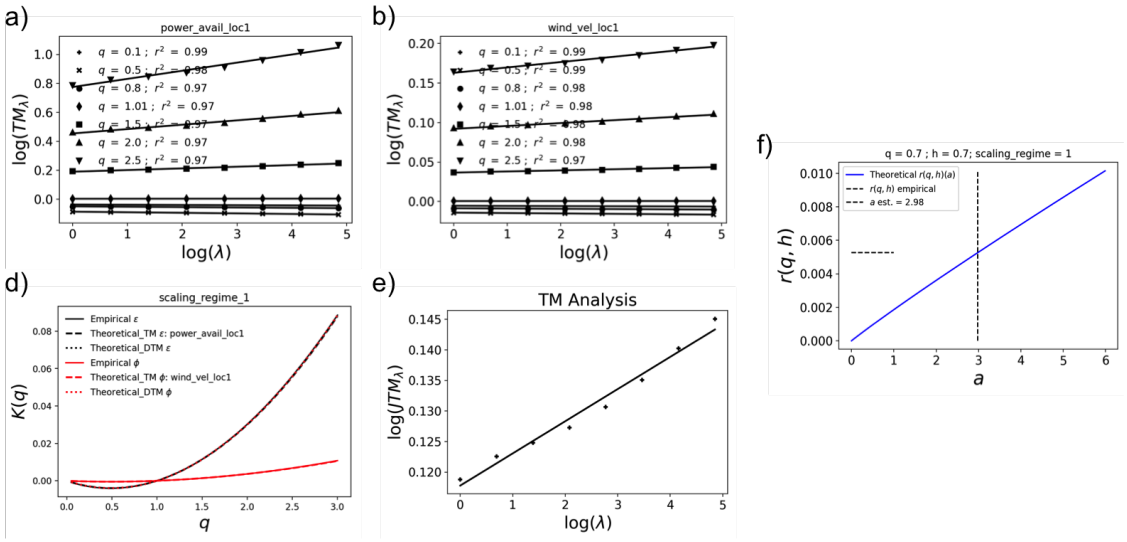

Figure 3.9: a) TM plots of P_a , b) TM plots of v (log - log plots of Eq. 14), c) K(q) plots for both fields, d) TM plot for the joint field (log - log plots of Eq. 28), e) estimation of JMF parameter a (Eq. 31); for an ensemble of all moderate rain events at location 1. Rain events were analyzed as an ensemble of size 128, from 12 Nov 2020 to 16 Sep 2021 (9 months).

With this framework, the correlation of P_t, P_a, v, and ρ with each other (and with station fields) are explored here according to rain rates. For this purpose, the rain events from 9 months (12 Nov 2020 to 16 Sep 2021) were classified into 6 groups based on the rain rate (same as in section 2.1 but with 5 min moving average for increasing number of events in higher rain rate groups) and analyzed as an ensemble of N_{sam} 128 or 32 minutes. Since JMF involves expressing fields as a combination of each other, the finest resolution of fields were limited by the highest actual sampling resolution (15 s, Table 3.1). JMF plots of P_a and v for an ensemble of all moderate rain events at location 1 are shown in Fig. 3.9 as a sample. Value of a closer to 3 was obtained (as expected from Eq. 64) and good scaling was observed with r^2_{JMF} value of 0.98. The variation of JMF parameters a and IC are given in Fig. 3.10 for location 1; similar estimates were obtained for location 2 as well. Overall, a very small increase in values of IC and a were observed with an increase in rain rate (5 min moving average) when correlations of P_a against v and station fields were considered (Fig. 3.10a). A similar trend was observed when v was analyzed against P_a and station fields (Fig. 3.10b), and also when ρ was analyzed against the rest of the station fields (Fig. 3.10c). Quality of scaling r^2_{JMF} didn't show any trend like the values of a or IC. The effect of the previously mentioned upper threshold in turbine power (due to rated power) seems to have a stronger bias in JMF; JMF of P_t with every field across various rain types gave estimates of a close to 0 (not shown in figure). P_t also gave inconsistent values of r^2_{JMF} with values going lower than 0.1 in some cases. This behaviour was consistent across all four turbines.

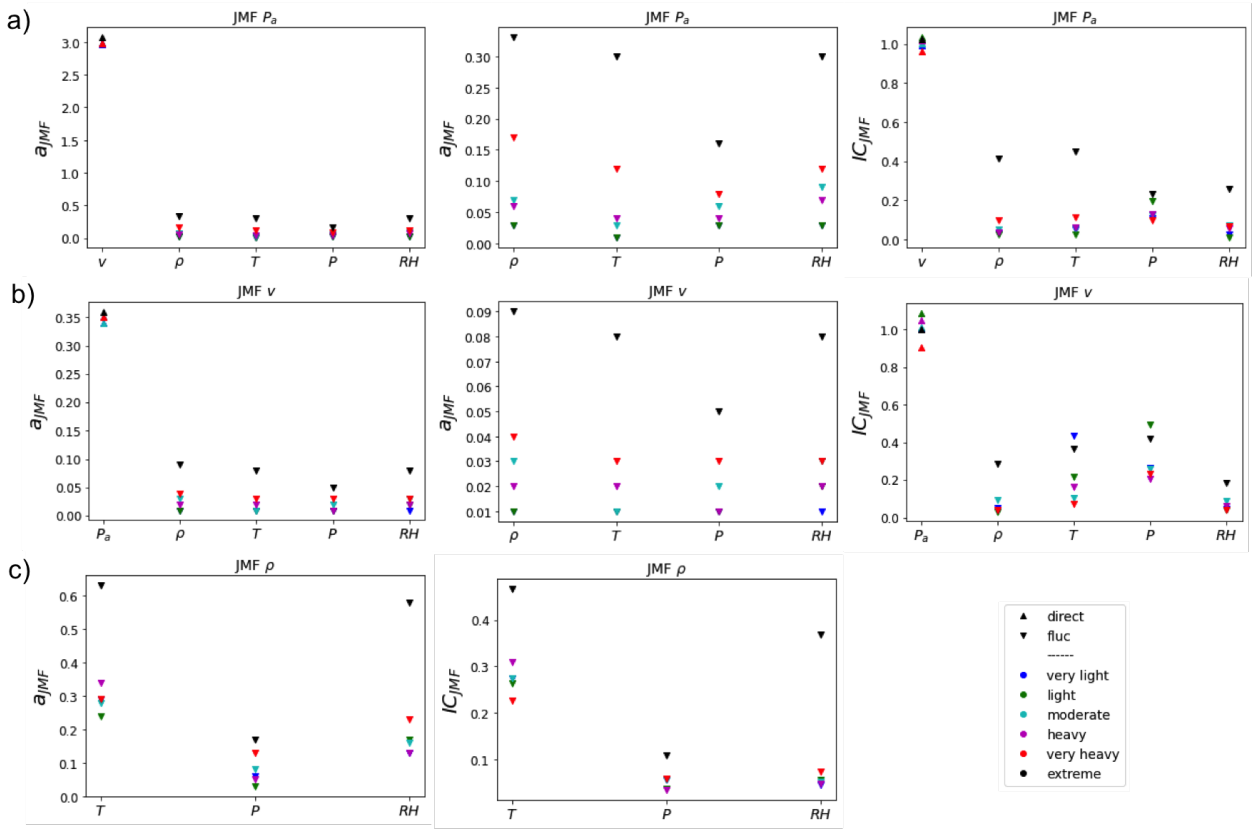

Figure 3.10: Variation of JMF parameters a and indicator of correlation IC between a) P_a, b) v, and c) ρ and other fields according to type of rain (on the basis of 5 min moving average of rain rate with criteria in Tokay and Short, 1996). The second column of a) and b) are zooms of first column removing the direct field for visual clarity. Rain events of each class were analyzed as an ensemble of size 128, from 12 Nov 2020 to 16 Sep 2021 (9 months).

From early UM analysis, it was decided that for fields at 15 s resolution, all station fields need to be analyzed as fluctuations while wind (v) and wind-derived fields (P_a and P_t) can be studied directly. Though the desired conservative field is retrieved by this choice, this could cause issues in JMF as it could be a combination of a direct field and an indirect field (fluctuations or FIF). For example, in Fig. 3.10a, P_a is a direct field while the fields its correlations are analyzed (ρ, T, P, and RH) are fluctuations. Consider a non conservative field $\varepsilon_\lambda{}'$ (i.e. $\langle\varepsilon_\lambda{}'\rangle \neq 1$); in UM, this can be expressed with the underlying conservative field as (ε_λ retrieved through fluctuations or FIF, $\langle\varepsilon_\lambda\rangle$ = 1) as

$$\varepsilon_\lambda{}' \approx \varepsilon_\lambda \lambda^{-H_\varepsilon} \tag{77}$$

where H_ε is the non-conservation parameter that characterizes the variation of mean across resolutions λ and ε_λ. The conservative part that is characterized by UM parameters (see section 1.2.2). When two fields $\varepsilon_\lambda{}'$ and $\phi_\lambda{}'$ are analyzed as a multiplicative combination in JMF, only their

respective conservative parts can be used ($\varepsilon_\lambda = \frac{\phi_\lambda{}^a Y_\lambda{}^b}{(\phi_\lambda{}^a Y_\lambda{}^b)}$). Hence, the estimated JMF parameter a doesn't correspond to the full field. If one field is direct and the other is a retrieved conservative part (fluctuations or FIF), values of a could be be biased as underlying H (H_ε and H_ϕ) is not considered in its estimation.

To assess the possible influences of this, a sensitivity analysis was performed using two known fields: P_a (ε_λ) and the field it is derived from v (ϕ_λ): $P_a \propto v^3$ (Eq. 64). The previously used dataset - respective ensembles of rain events from 12 Dec 2020 to 03 June 2021 (6 months, with N_{sam} 128) - was used for this purpose; the results are displayed in Table. 3.2. While using P_a and v as direct fields, a in JMF analysis retrieved the exponent value in Eq.64 (Table.3.2) with good joint scaling (r^2_{JMF}) and indicator value (IC). Though H isn't non-zero for either of the fields, they being similar gave a difference close to zero (H_ε - H_ϕ). Similarly, a closer value of a (a = 2.75) was obtained when both fields were taken as FIF. From the samples in Fig. 3.11a and Fig. 3.11b, it can be seen that the fields follow the same pattern when both fields are direct or FIF (Fig. 3.11b follows the same pattern as direct field in Fig. 3.11a while fluctuations in Fig. 3.11c does not) with the difference in amplitude from the mean line following the proportionality exponent in Eq. 64. When both fields were taken as fluctuations, values of a closer to 1 were obtained. This is rather consistent as fluctuations take the difference between time steps and are expected to show a proportional relationship as the fields are already related. However, this also puts the analysis at an apparent disadvantage as using JMF on fluctuations only retains the proportionality but not its order. This can be observed in the sample in Fig. 3.11c, where both fields appear moreover similar (following $P \propto v$ than the original $P \propto v^3$). In the remaining cases, - when both fields were not having similar values of H - the estimates of a are decreased except when H_ε was significantly lesser than H_ϕ (FIF - P_a and direct - v). This might have to do with ε_λ (P_a) being the field estimated based on ϕ_λ or v ($P_a = \frac{v^a Y_\lambda{}^b}{(v^a Y_\lambda{}^b)}$) while the JMF analysis is trying to express it in terms of fluctuations of ϕ_λ which doesn't follow the same time step pattern as direct data or FIF (Fig. 3.11c).

ε_λ	ϕ_λ	H_ε	H_ϕ	H_ε - H_ϕ	a	b	IC	r^2_{JMF}
direct	direct	0,210	0,256	**-0,045**	**2,98**	0,823	0,993	0,994
	FIF	0,210	-0,026	0,237	1,62	0,696	0,895	0,953
	fluc	0,210	-0,253	0,464	0,02	0,537	0,012	0,430
FIF	direct	-0,004	0,256	-0,259	4,57	0,843	0,934	0,960
	FIF	-0,004	-0,026	**0,022**	**2,75**	1,179	0,990	0,888
	fluc	-0,004	-0,253	0,250	0,01	0,806	0,002	0,043
fluc	direct	-0,182	0,256	-0,438	1,7	9,965	0,082	0,956
	FIF	-0,182	-0,026	-0,156	0,73	4,729	0,049	0,973
	fluc	-0,182	-0,253	**0,071**	**1,01**	0,397	0,892	0,779

Table 3.2: Sensitivity analysis using power available, P_a, (ε_λ) and wind velocity, v (ϕ_λ) where JMF parameters are estimated for different combinations of data - direct (dir), fluctuations (fluc), and FIF (fractionally integrated flux). Data from 12 Dec 2020 to 03 June 2021 at 15 s, fields were renormalized for comparison.

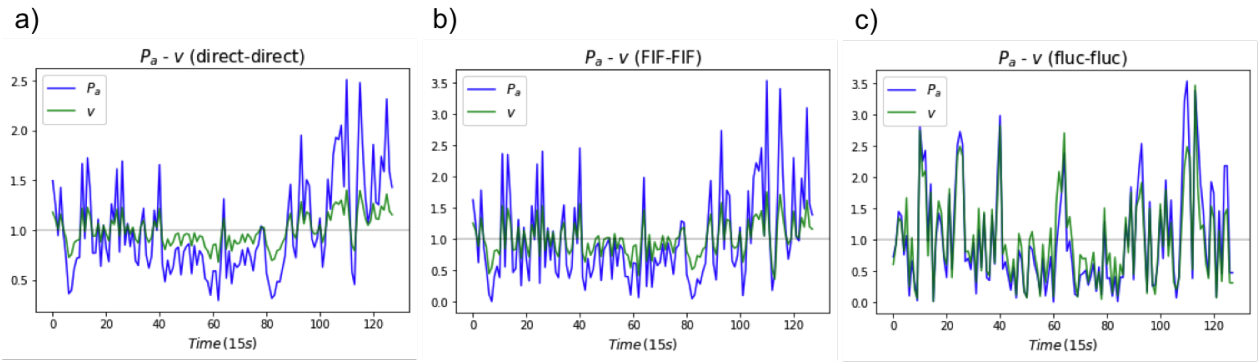

Figure 3.11: a) direct data of P_a and v b) FIF of P_a and v, and c) fluctuations of P_a and v for one sample ($N_{sam} = 128$) of the data analyzed (from 12 Dec 2020 to 03 June 2021 at 15 s, fields renormalized for comparison). Between plots, it can be seen that direct and FIF are following similar data pattern while fluctuations does not.

Though the biases from the analysis of JMF are acknowledged here, there is no correction available at this point. Among the results presented in Fig. 3.10, all JMF analysis except for P_a - v combinations are affected by this. More research is needed to account for this in the framework when accurate retrieval of correlation parameters is of interest. Even with biases, the values of a and IC are still strong indicators for comparing two multifractal fields, through various atmospheric conditions as illustrated in Fig. 3.11. The possibility of using JMF for retrieving an average field from a correlated known field using JMF is further explored in section 2.1 using KE and R.

3.1.3.3 Rain and power production - Possible influence from convective and stratiform rain

The yearly average cumulative depth of rain at the wind farm was found to be $\sim$ 600 mm and among the 6 months of rain events (213) studied, only 20 could be classified as heavier rain-

fall events (heavy, very heavy, and extreme). Because of this, it was speculated that the lack of a very strong correlation between rain and power produced could be due to rainfall events being not strong enough (apart from the known bias from threshold due to rated power). To test this hypothesis, efforts were made to identify the rain events as convective and stratiform. While convective rains have highly concentrated intensities, stratiform rains are more horizontally spread with lower intensities (Houze Jr, 2014; Marzano et al., 2010). Several criteria have been used for detecting this indirectly in literature; simple ones are the classification on the basis of rain rate exceeding a particular value. Popularly used criteria using rain rate is by Bringi et al. (2003) where convective rain samples are considered as those with rain rate, R, $\geq 5\,\mathrm{mmh}^{-1}$ and standard deviation (std dev) over 5 consecutive 2-minute samples $> 1.5\,\mathrm{mmh}^{-1}$ (mentioned as BR03 from here on). Tokay and Short (1996) proposed an empirical classification based on DSD parameters by identifying the shift from spectra dominated by small to medium drops (stratiform) to spectra dominated by large drops (convective) for similar rain rate (mentioned as TS96 from here on). Attributing temporal shift in DSD parameters (shape parameter Λ) to shifts in rainfall size distribution, they suggested a value of $\Lambda = 17R^{-0.37}$ above which precipitation can be considered as convective (stratiform if below).

To explore this, DSD parameters of rain events at the wind farm were estimated assuming a gamma distribution (following the method of moments in section 2.1). From the 6-month long data set in Fig. 3.8, about 32 events were found to be mostly convective using TS96 (out of 213, the rest being mostly stratiform). However, while using BR03 criteria, only 12 were found convective. Extending the data set to 9 months also didn't increase the number of convective events (42 - TS96 and 14 - BR03 from 12 Dec 2020 to 16 Sep 2021). 20 events were selected from both convective and stratifrom sides where at least 70 % of the time steps followed TS96 criteria. Two turbines were examined for these events - Turbine 1 and 8 (closest and farthest to the mast): any possible difference in turbine power between convective and stratiform events is not obvious from mean - std dev nor state curves (Fig. 3.12). This obviously comes with the disclaimer that it was a simple test using limited events without considering other complexities. However, considering the predominant stratiform nature of rain at the location studied, the hypothesis of needing stronger rainfall to see the proper correlation between power produced and rainfall is still worth exploring in the future.

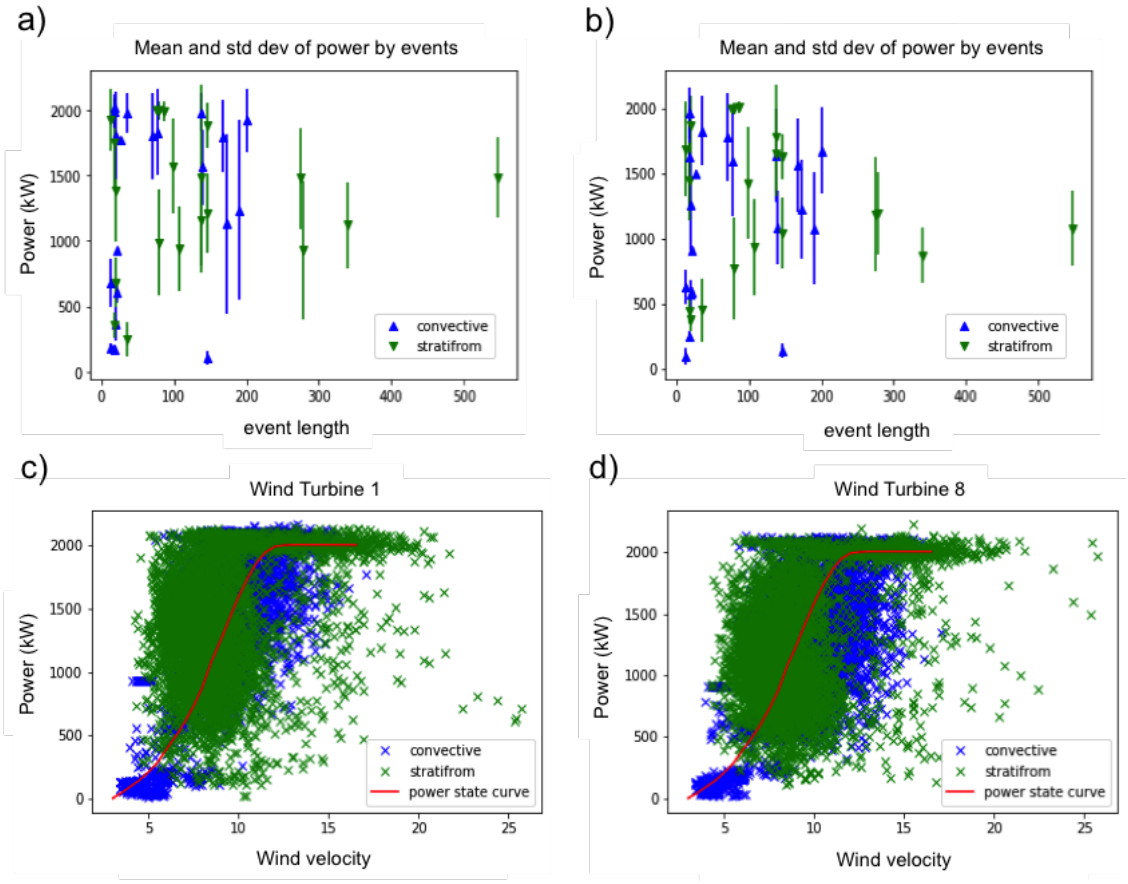

Figure 3.12: Mean and std dev of Power produced, P_t, for a) Turbine 1 (closest to the mast), and b) Turbine 8 (farthest from the mast). Power state curve during selected convective and stratifrom events for c) Turbine 1 (closest to the mast), and d) Turbine 8 (farthest from the mast).

3.1.3.4 Rain and power production - possible influence from wind direction

The turbines are aligned south east within a 4 km radius, and at the south of the mast a small groove is located at roughly 160 m, and a larger one in the east at around 100 m (Fig. 1.7). To see the effect of these topographical features and spread of vegetation around the mast, wind directions were identified as shown in Fig. 3.13 with mast as the centre. Based on this, average wind direction was calculated for all events (6-month events in Fig. 3.8 using U_x and U_y from 3D anemometer at location 1. Based on the position of immediate vegetation around the mast, the wind zones were grouped into three - least influenced (69), most influenced (60) and turbine direction (7 events).

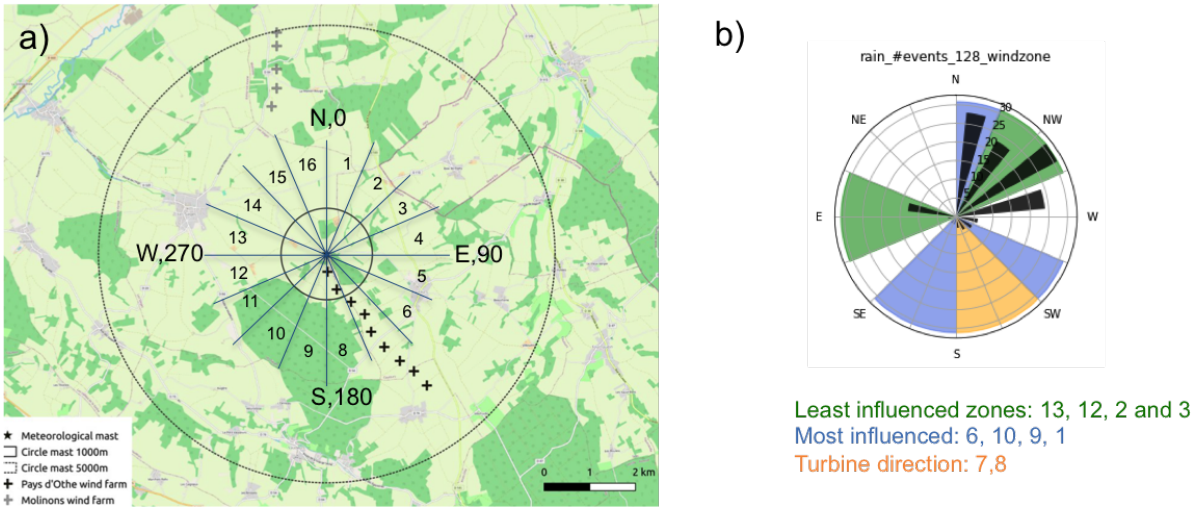

Figure 3.13: a) Location of wind farm and the wind directions identified, b) No. of events corresponding to the direction (colours show the direction classes, length of the black arcs corresponds to number of events while thickness to average magnitude) and the three groups considered

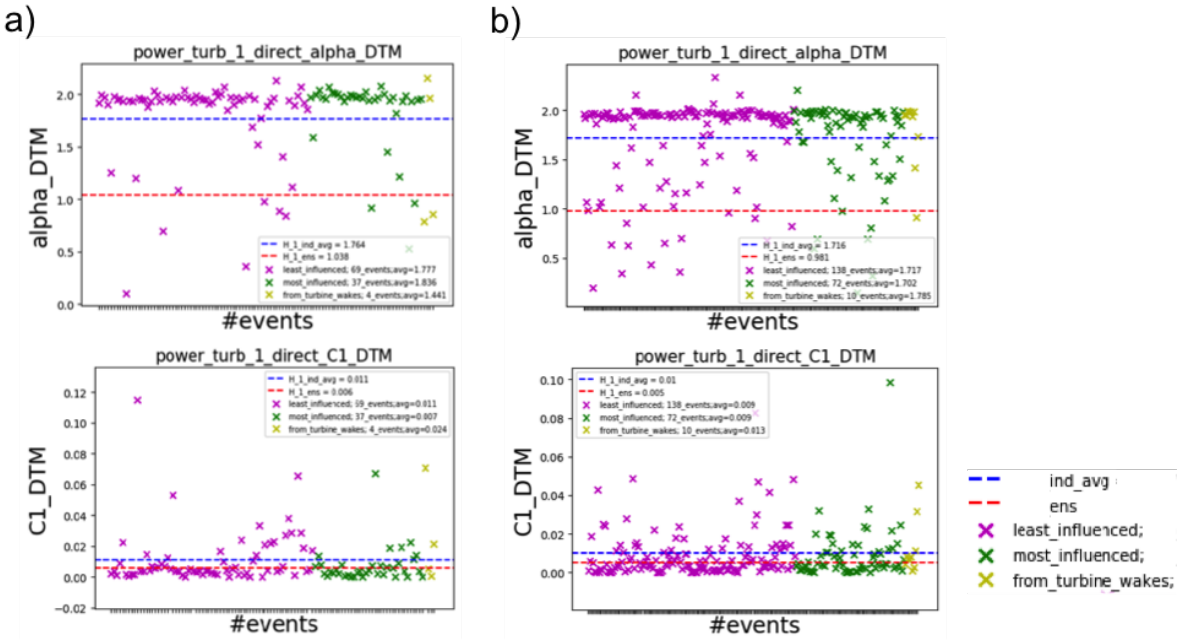

Figure 3.14: Variation of α and C_1 according to wind direction for a) rain events b) dry events. Values of ensemble and average value of individual events are shown using red and blue lines.

Variations of UM parameters of turbine power closest to the mast (Power turbine 1) according to wind classes are shown in Fig. 3.14 for rain and dry events. No obvious difference was observed, similar results were observed for rest of the turbines as well. Due to the previously identified bias from rated power in UM analysis, it is not possible to say exactly if this is the exact behaviour

or not. This was not explored further in this thesis. Factors known to affect power production at turbine wake, such as mixing of moist air Obligado et al. (2021), dynamic effects from inertial particles (Smith et al., 2021) etc. were also not considered here.

3.1.4. Main outcomes from UM and JMF analysis of RW-Turb data

From section 1.2.2.4, it was identified that the actual sampling resolution relevant for studying the variability of meteorological fields measured with the help of mini-station (temperature T, pressure P, humidity RH, and air density $\rho = f(T, P, RH)$) and that for 3D anemometer fields (wind velocity v, power available P_a) were 15 s and 1 s respectively (instead of 1 s and 0.01 s). Using the data averaged to these reliable frequencies, the main objective of this section is to analyze turbine power, P_t, as a temporal field and to gain insights into its correlation with rainfall, which is poorly understood, and also with other meteorological fields. However, the direct analysis of turbine power was found to be difficult since the output from wind turbines are limited by a maximum or rated power; in time series analysis this acts as an upper threshold resulting in reduced estimates of UM parameters. This bias is identified in section 3.1.2.2 in the theoretical framework of UM and is also illustrated using discrete cascades numerical simulations of conservative multifractal fields. Basically, the presence of an upper threshold introduces an upper plateau in DTM curve, similarly to the one due to the sampling dimension, but it begins at a lower value of η. This reduces the range of available η for estimation of the slope, and hence results in a biased value of α (reduced α and C_1). Since, UM in its usual form is not designed to handle negative values (time steps where power produced by turbine < energy consumed for its running), based on how these values are managed (taken as zero here), the values of α will be further biased due to the effect of lower threshold discussed in 2.2 (zeroes here, as negative values were set to zeroes). Due to the presence of these biases in P_t, the actual wind power available at the turbine hub for extraction ($P_a = f(v, \rho)$) was primarily used instead as the main field for joint analysis.

For UM analysis, fluctuations of the fields were required for station fields, for retrieving conservative fields so that estimates of TM and DTM are not biased. For anemometer fields, direct fields analysis were acceptable in large scale regimes (from 15 s) while small scales (0.01 s to 15 s) required retrieval of conservative fields through FIF. From UM analysis of rain and dry events as ensembles, it was found that almost all fields are showing a slight increase in variability with rain (larger α and similar C_1) in the scale range from 15 s to 32 min. An opposite trend was observed for finer scales of P_a and v (0.01 s to 15 s). Joint analysis of P_a, v and ρ against each other and with station meteorological fields (all fields at 15 s) revealed an increasing trend in the value of JMF correlation exponent a and IC with rain rate. However, this is not without biases since station fields were fluctuations while anemometer fields were direct in the analyzed scaling regime. The influence of this bias is identified and commented on. Also, detailed sensitivity analysis were made to identify the possible effects of wind direction and rainfall type on power production in turbines. No clear trends in the results were identified.

Future methodological developments in JMF framework are proposed here for handling the biases in analyzing direct and non direct fields. Though the effect of the upper threshold is identified in the framework, further work is required for precisely quantifying the bias. Also, considering the predominant stratiform nature of rain at the measurement location, studying the correlations under convective conditions is encouraged, for the future, for expanding the understanding on correlations between rainfall and wind power production.

3.2. Joint analysis using climate chamber (sense-city) data

For the joint analysis presented here, experimentation set up at sense-city (with the help of IFSTTAR, L'Institut français des sciences et technologies de transports, which is now part of Gustave Eiffel University) was used for studying kinetic energy (KE) and rainfall (R) as well as T and RH. Information on location, working and facilities inside sense-city are mentioned in section 1.1.2. For studying KE and R, data from a previous campaign inside sense-city (Gires et al., 2020a) involving two disdrometers was used. For joint analysis of T and RH, separate experiments were performed with IFSTTAR for recreating climatic conditions of a few selected days (see upcoming section 3.2.2 for a description of the designed measurement campaign).

3.2.1. Kinetic energy and rainfall

The importance of kinetic energy (KE) in understanding soil erosion, leading edge corrosion of wind turbine blade etc. are already discussed in section 2.1 along with the scale-invariant framework developed for estimating the same (Jose et al., 2022). The usability of sense-city as a rainfall simulator is already examined in Gires et al. (2020a) using disdrometers. Comparison with real rain revealed that even though the rainfall remain steady inside sense-city, the rain generated is thinner and centered on smaller drops (figure 3.16a). Further, the height of sprinklers (8 m) is not enough for larger drops (> 1 mm) to reach terminal velocity resulting in serious underestimation in KE.

In current analysis, disdrometer data set presented in Gires et al. (2020a) is used alongside real data for jointly analysing KE and R so that this under estimation can be accounted for. More information on the working of the disdrometers can be found in section 1.1.1 and in Gires et al. (2018). Figure 3.15 shows an overview of the campaign, along with positioning of devices inside the chamber. One rain event was recorded for each type of rain at 5 locations inside the simulator; Tab. 3.3 compiles the information about simulated events along with their gamma DSD parameters (using similar moment combination as in section 2.1, M234). As UM analysis requires the length of time series in powers of 2, only the portion of event that confirms to this (largest power of 2 < length of event) was used for current analysis. This also removed artefacts at the start and at the end of sense-city events since the sprinklers starts and stop abruptly unlike gradual progression in natural rain.

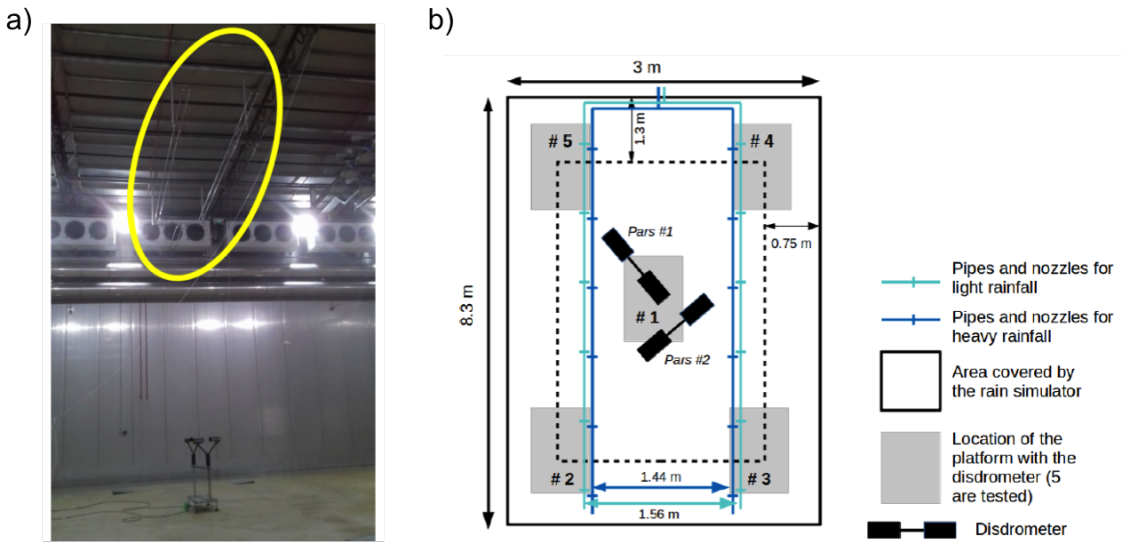

Figure 3.15: a) Overview of campaign highlighting sprinkler position and disdrometer positioning, b) Schematic representation of sense-city locations where rainfall was measured; figures reproduced from Gires et al. (2020a)

3.2.1.1 DSD analysis of sense-city rain

From Fig. 3.16a and Tab. 3.3, it can be seen that the drop size distribution (DSD) of sense-city events doesn't follow gamma distribution (higher values of root mean square error ($RMSE_{ND}$) between empirical DSD and gamma DSD). To compare sense-city events with real rain episodes, few similar rain events were selected (five for each rain types) from the data used in section 2.1 (Jose et al., 2022) following the classification in Tokay and Short (1996) (mentioned as sample-event(s) from here on). It was found that, while using this criterion (mainly average rain rate), the sense-city events fit into very heavy and extreme than the default so-called 'light' and 'heavy' classification of the chamber. It was also observed that though sense-city events didn't follow gamma distribution, the retrieved DSD parameters (N_0, μ, Λ) were closer to the reported values in Tokay and Short (1996); this was not the case for real events analysed in section 2.1 (Jose et al., 2022). Regardless, sense-city produced a lesser rain rate than that is expected from gamma distribution (further confirming the inappropriateness of gamma DSD here), and DSD was found to be thinner than gamma. Furthermore, a very less percentage of drops greater than 1 mm reached terminal velocity (Fig. 3.16a, second and third graphs). Resulting under reporting in KE can be seen in KE vs R graph, where real data (right extreme, Fig. 3.16b) shows good correlation with commonly used equations in literature as well as those obtained from UM and theoretical DSD while sense-city events fail to reach expected values (right extreme, Fig. 3.16a). Few other obvious differences were also observed: simulated rain events were smaller in length, more continuous and didn't have any zeroes in the data-set. They also produced poor scaling in comparison, with biased α and C_1; this in turn resulted in very low value of exponent a in both double trace moment (DTM) and joint multifractal (JMF) analysis (discussed in upcoming sections).

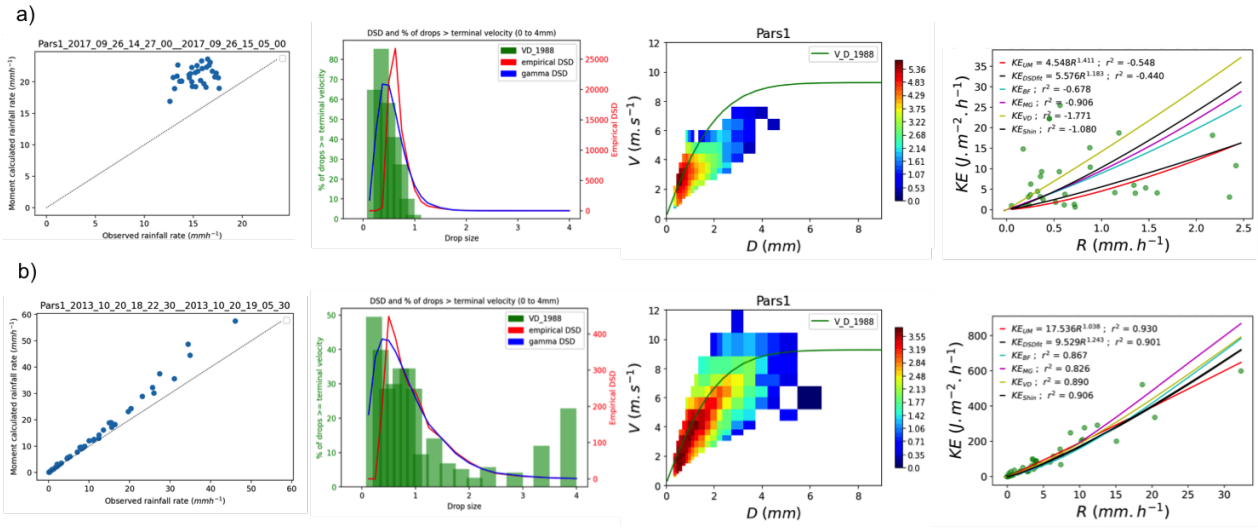

Figure 3.16: First column: Empirical rain rate vs. rain rate calculated from DSD moments with assumption of gamma distribution; Second column: DSD and % of drops reaching terminal velocity in each diameter class of disdrometer, velocity; Third column: diameter plot of rain drops, KE vs. R plot illustrating underestimation of KE (similar to plots in section 2.1, Fig. 2.9) for a) a heavy rain event in sense-city 26 September 2017 14:27:00 to 15:05:00 b) a sample-event from real conditions at ENPC location 20 October 2013 18:22:30 to 19:05:30; for Parsivel 1.

event time	location	length	rain type	$RMSE_{ND}$	D_0	μ_g	N_0	D_m	Λ
28 Sept 2017 13:22:00 to 14:07:00	1	64		1,84E+03	0,687	9,426	3,75E+10	0,844	15,91
28 Sept 2017 14:12:00 to 14:33:00	2	16		2,26E+03	0,562	5,89	6,03E+08	0,799	12,37
28 Sept 2017 14:34:00 to 14:54:00	3	16	light	1,07E+03	0,687	18,76	8,92E+15	0,796	28,605
28 Sept 2017 14:55:00 to 15:15:00	4	16		2,13E+03	0,562	11,92	2,34E+13	0,655	24,29
28 Sept 2017 15:16:00 to 15:34:00	5	16		5,09E+03	0,562	2,197	1,98E+06	0,915	6,773
26 Sept 2017 14:27:00 to 15:05:00	1	32		4,71E+03	0,562	2,663	4,49E+06	0,917	7,265
27 Sept 2017 15:10:00 to 15:43:00	2	32		1,87E+03	0,687	5,882	1,24E+08	0,998	9,893
26 Sept 2017 15:49:00 to 16:26:00	3	64	heavy	1,65E+03	0,687	4,725	2,57E+07	1,045	8,35
26 Sept 2017 08:21:00 to 09:05:00	4	32		2,34E+03	0,687	2,887	2,61E+06	1,068	6,451
27 Sept 2017 09:07:00 to 09:40:00	5	32		3,56E+03	0,562	4,394	5,05E+07	0,851	9,864

Table 3.3: Overview of rain events in sense-city along with their DSD parameters, for Parsivel 1

In terms of DSD parameters as well as UM values (discussed later) of sense-city events, no significant difference was found between the devices (Parsivel 1 or Parsivel 2) or location beneath the rain simulator (Tab. 3.3 and Fig. 3.17). Hence, it was decided to analyse them as an ensemble; this also increased the number of data points available for analysis. In the upcoming subsections, KE and R (sense-city as well as real data) are subjected to UM analysis using two approaches - the previously discussed DTM methodology discussed in section 1.2.2 and JMF discussed in section 1.2.3. Since the produced rainfall cannot be changed for sense-city, efforts were made to retrieve realistic values of KE using the measured rain data.

3.2.1.2 DTM methodology

It has already been established through gamma DSD and from DTM relations in UM analysis that KE and R follow a power law relation between each other, $KE = bR^a$ (KE_{UM}). The exponent a and pre-factor b were determined individually for each sense-city events through UM analysis (refer section 1.2.2). The differences in values of α, C_1, quality of scaling (r^2_{TM}) and also between the exponent a and pre-factor b of power-law estimated from UM methodology can be seen in Fig. 3.17; classification of rain mentioned here is on the basis of rain rates in Tokay and Short (1996) for sample-events. Variation of parameters for sense-city is also plotted along with; here sense-city events are still following the nomenclature defined from chamber modes ('light' and 'heavy', Tab. 3.3). For the real events selected here (sample-events: very heavy and extreme), the values of α and C_1 are on the extreme sides in section 2.1 (Fig. 2.2) than it is usually for rain events, but, the decent scaling (Fig. 3.17a, third column) shows that they are relevant for comparison. The difference in UM parameters and hence, the values of a and b are reflected in the r^2 values in Fig. 3.17b, where sense-city events have considerably bad scaling. However, within the events, no trends were observed for UM parameters according to the rain type. It should be noted that a variation in b was observed with rain rate while analyzing larger data-set (refer Fig. 2.2 and Tab. 2.3 from section 2.1), however, since the rain type distinction was found to be not valid in the case of sense-city (albeit the number of events is limited) and also for simplicity of analysis, distinction in rain types is ignored in upcoming analysis.

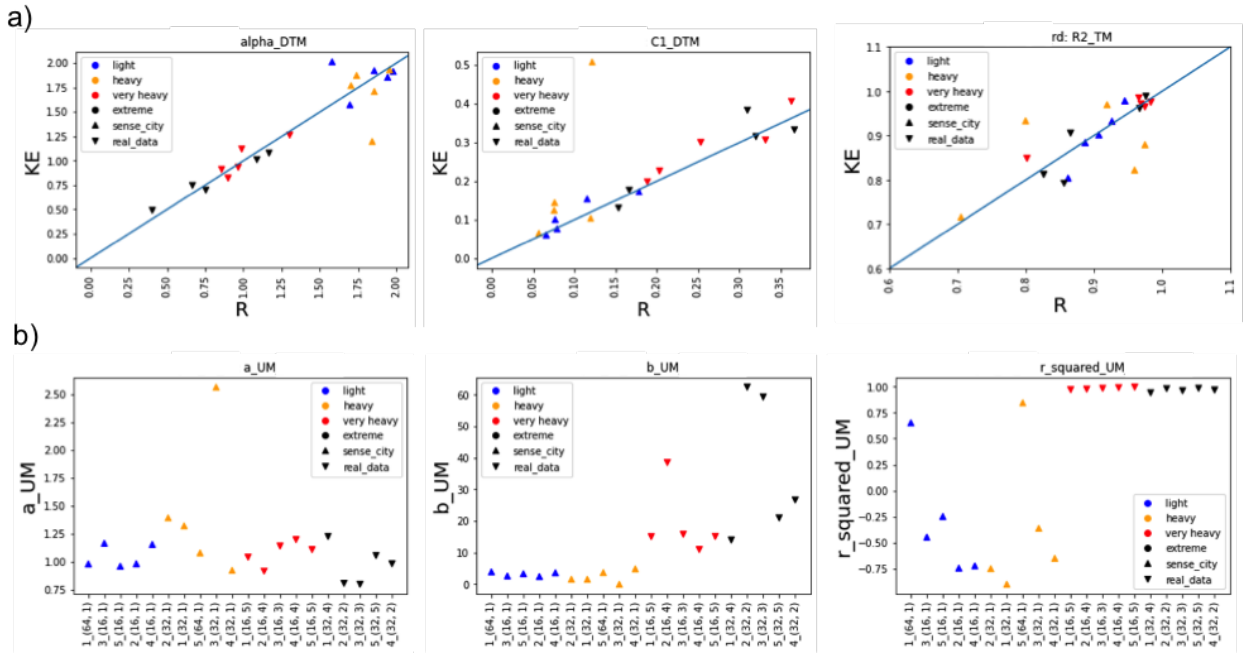

Figure 3.17: a) Variation of α, C_1, quality of scaling (r^2_{TM} for $q = 1.5$) between KE and R for sense-city rain events and similar real events (sample-events). b) Variation of exponent a, pre-factor b, and quality of fit between KE and R (r^2); both for fluctuations of the corresponding fields measured by Parsivel 1.

For convenience of analysis, all sense-city events were considered as an ensemble and were subjected to UM analysis for estimating the power law relation (KE_{ss}). While taking the ensemble, the event 27 September 2017 08:21:00 to 09:05:00 was not considered to avoid probable bias, as it provided unusual UM values compared to rest of the events. The sample size for sense-city was limited by the shortest event to 16 (8 min); the smaller size is justified to some extend by the fact that there are only two fixed modes of rain in chamber, and hence not possible to create variability in rain by design. For ensemble analysis of real events (all events from data-set used in section 2.1), the sample size was fixed at 64 (32 min) to be more consistent with real world conditions in characterizing variability (KE_{rd}). The performance was similar to the one obtained earlier in section 2.1 while using the power-law derived by averaging a values of individual events (KE_{UM} for Parsivel 1); to distinguish from the ensemble of same events (KE_{rd}), the averaged equation is mentioned from here on as $KE_{\overline{rd}}$). The under reporting of KE in sense-city can be seen more clearly in Fig. 3.18a, where except KE_{UM} (which corresponds to KE_{ss} here), every other equations (most commonly used ones in literature, see section 2.1.4.5) predicted an estimate higher than that detected by disdrometers in sense-city. The r^2_{ss} from KE_{UM} here is biased as b was estimated from fitting the already under estimated data.

$$\begin{aligned} KE_{ss} &= 2.601{R_{ss}}^{1.172} \quad ; r^2_{ss} = 0.896 \\ KE_{rd} &= 14.595R_{rd}^{1.132} \quad ; r^2_{rd} = 0.966 \\ KE_{\overline{rd}} &= 9.583R_{\overline{rd}}^{1.223} \quad ; r^2_{\overline{rd}} = 0.970 \end{aligned} \tag{78}$$

Using KE_{rd} or $KE_{\overline{rd}}$ as the target, it is possible to devise a generalized form of correction for underestimation of KE in sense-city ($KE_{ss} = bR^a_{ss}$).

$$\begin{aligned} R_{ss} &= \left[\frac{KE_{ss}}{b}\right]^{\frac{1}{a}} \\ KE_{rd/\overline{rd}} &= dR^c_{rd/\overline{rd}} \\ KE_{exp} &= d\left[\frac{KE_{ss}}{b}\right]^{\frac{c}{a}} \end{aligned} \tag{79}$$

where KE_{exp} is the 'corrected' value that corresponds to those expected from rain rate measured inside the chamber.

Fig. 3.18a and 3.18b shows the KE vs. R plots for all events in sense-city and sample-events; the under reporting of KE can be seen more clearly here as we get to compare performance of similar events side by side (similar plot involving all events from 6 years can be seen in Fig. 2.8, section 2.1). The corrections applied are shown in Fig. 3.18c and 3.18d with KE_{rd} as target (since sense-city events were also analysed as an ensemble). The r^2 values for both KE_{rd} and $KE_{\overline{rd}}$ in KE

vs. R graphs appear higher here since they were obtained from R_{ss}. In KE_{UM} vs. KE_{emp} graph, it can be observed that the applied correction elevates the values of KE to a more realistic KE_{exp} which is consistent with the rainfall rate.

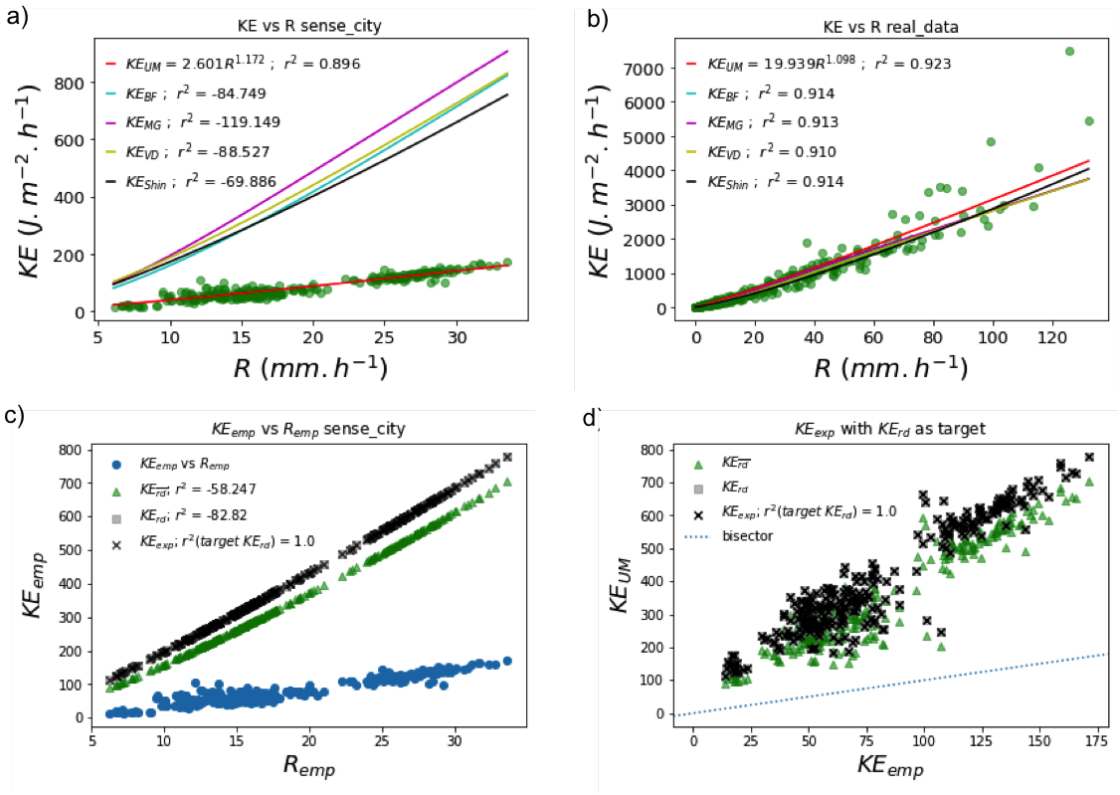

Figure 3.18: Illustration of under reporting of KE in sense-city: Fitting of empirical KE - R using power law from UM (KE_{UM}, on ensemble of all events) and popular expressions from literature for a) sense-city events, and b) sample-events.
Correction of KE_{emp} to KE_{exp} using KE_{rd} as target: a) KE vs R plot for empirical values alongside KE_{rd} and $KE_{\overline{rd}}$ (r^2 between KE_{emp} and fitted $KE-R$ equations), b) KE_{UM} vs KE_{emp} plot with correction (r^2 between KE_{emp} and KE from Eq. 78).

3.2.1.3 JMF approach

As multifractal and scaling properties of KE and R are known at this point, it is worth exploring the use case of joint multifractal analysis (JMF, section 1.2.3) for first quantifying correlations between these two fields and then explore the possibility to address the already known under reporting of KE in sense-city. Towards this, fluctuations of KE (fluctuations to retrieve conservative fields) was expressed as combination of fluctuation of R and an independent multifractal field Y_λ with exponents a and b characterizing their relative weight - $KE_\lambda = \frac{{R_\lambda}^a {Y_\lambda}^b}{({R_\lambda}^a {Y_\lambda}^b)}$, where λ is the resolution of the field (Gires et al., 2020b). Here, Y_λ is an independent multifractal field with same C_1 assumed as KE_λ; value of a quantifies the correlation between KE_λ and R_λ.

Like in DTM methodology, KE and R were subjected to JMF for each individual events as well as for an ensemble, for sense-city events, sample-events and all real events used in section 2.1. The variation of JMF parameters (a, b, indicator of correlation IC, quality of joint scaling (r^2_{JTM}) among sense-city and sample-events are shown in Fig. 3.19a. As it could be expected from previous analysis, Sense-city events exhibited very bad scaling and reduced estimates of exponent a (to be taken with caution given the bad scaling), suggesting a much lower correlation accross scales. Similar to the previous case, the events didn't show any notable difference according to the position of disdrometer or rain rate. Since, the behaviour of JMF parameters according to rain type is not known, all real events previously studied were subjected to JMF individually. Using the rain criteria in Tokay and Short (1996), no discernible behaviour changes were observed across types of rain events (Fig. 3.19b). With this reassurance, and also with the intention to improve statistics, ensemble analysis was performed like before - with sense-city at a sample size of 16 (8 min, $KE_{\lambda,ss}$), and real data at a sample size of 64 (32 min, $KE_{\lambda,rd}$) excluding the anomaly event 27 September 2017 08:21:00 to 09:05:00. In the framework of JMF, estimation of a can be obtained by using different values of the exponent h and q in the analysis (see section 1.2.3, Gires et al. (2020b)). Here, values were estimated at $q = h = 0.7$ based on sensitivity analysis around various q/h options (for both individual and ensemble analysis). Values of q_s and q_d (moment corresponding to sampling limitation and divergence respectively) were above $ha+q$, ha and q for all the cases analyzed here as desired, this is required for obtaining reliant values in JMF.

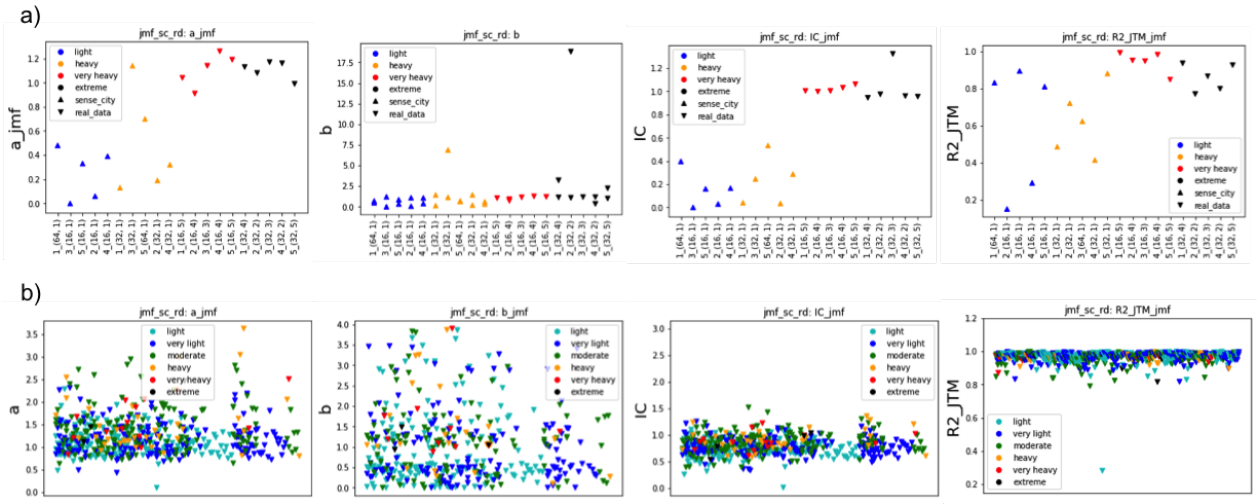

Figure 3.19: a) Variation of JMF parameters a, b, indicator of correlation IC, quality of joint scaling (r^2_{JTM}) between KE and R for sense-city rain events and sample-events b) same for all events; both for fluctuations of the corresponding fields measured by Parsivel 1 as an ensemble

Fig. 3.20 shows the TM, $K(q)$ and joint TM (JTM) plots for ensemble analysis of KE and R in JMF framework for sense-city and sample-events. The value of exponent a is much lower for sense-city ($KE_{\lambda,ss}$) in comparison with sample-events ($KE_{\lambda,se}$) - 0.4 vs 1.05. Values of a, b,

IC and r^2_{JTM} were 0.4, 0.955, 0.242 and 0.89 for sense-city and 1.05, 0.3740, 0.944 and 0.983 for sample-events. Ensemble of all events from section 2.1 were also considered at a sample size of 64 ($KE_{\lambda,rd}$). This suggests that the renormalized fields can be written as:

$$
\begin{aligned}
KE_{\lambda,ss} &\approx \frac{R_{\lambda,ss}{}^{0.4} Y_{\lambda,ss}{}^{0.955}}{(R_{\lambda,ss}{}^{0.4} Y_{\lambda,ss}{}^{0.955})}; \quad r^2_{JTM,ss} = 0.890 \\
KE_{\lambda,se} &\approx \frac{R_{\lambda,se}{}^{1.05} Y^{0.374}_{\lambda,se}}{(R_{\lambda,se}{}^{1.05} Y_{\lambda,se}{}^{0.374})}; \quad r^2_{JTM,se} = 0.983 \\
KE_{\lambda,rd} &\approx \frac{R_{\lambda,rd}{}^{1.01} Y^{0.232}_{\lambda,rd}}{(R_{\lambda,rd}{}^{1.01} Y_{\lambda,rd}{}^{0.232})}; \quad r^2_{JTM,rd} = 0.983
\end{aligned}
\tag{80}
$$

This opens the path to simulating KE fields from R ones and a Y_λ generated as a 1D discrete cascade fields (having same size as corresponding R_λ/KE_λ)

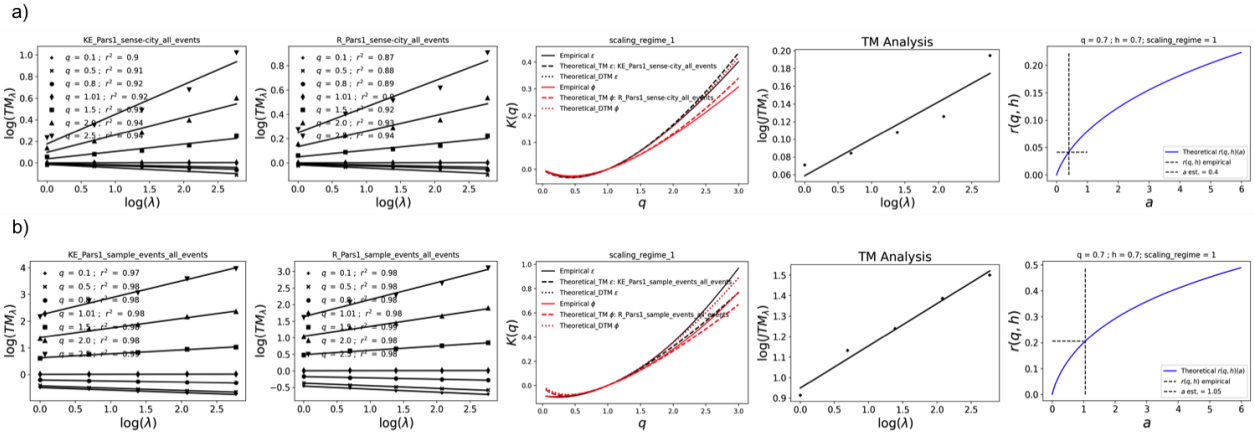

Figure 3.20: TM plots of KE, TM plots of R, $K(q)$ of both fields, Joint TM of KE and R, and estimation of JMF parameter a for a) ensemble of sense-city events; and b) ensemble of sample-events.

The increased correlation with R_λ (higher a) and hence, the reduced correlation with Y_λ (low b) in Eq. 80 for real rain estimates is obvious while comparing it with sense-city events (figure 3.20). However, unlike the DTM methodology, JMF approach isn't deterministic. Though the average properties are conserved in this approach, it falls short when the interest is in estimating exact values. In our specific use case, the estimates of KE_λ is dependent on a deterministic field R_λ and a stochastic field Y_λ. The exact values of KE_λ need not correspond to those of R_λ as the simulation of Y_λ is bound to slightly change every time. As a result, depending on the distribution of values inside Y_λ, estimated KE_λ could have values higher or lower than R_λ; and the position of this changes according to the Y_λ simulated as well. This behaviour can be seen clearly in Fig. 3.21 where, unlike DTM methodology (Fig. 3.18), the estimated KE (KE_{JMF}) doesn't follow the behaviour

of corresponding R (R_{emp}) values. Here, Y_λ of same shape was simulated using discrete cascades specifying α and C_1 ($C_{1,R} = C_{1,\phi}$); to account for the stochastic nature of actual UM estimates, a loop of 100 simulations were run and the field with lowest percentage error between values used for simulation and actual values was selected for this figure. Another caveat in this approach is the fact that the estimated UM field (KE_λ) is a normalized field and needs to be multiplied by average value of KE_{emp} for retrieving the expected field. It should also be mentioned that even though direct fields were used in estimating KE, JMF parameters were estimated by considering only their conservative portions (fluctuations of the field). Since one-to-one correspondence is mandatory in current study (KE being a field derived from R), it is not possible to suggest JMF approach for quantifying the under-reporting of KE in sense-city. As commented in previous section while discussing RW-Turb fields (section 3.1), further development of methodology is also needed to properly handle non-conservative fields.

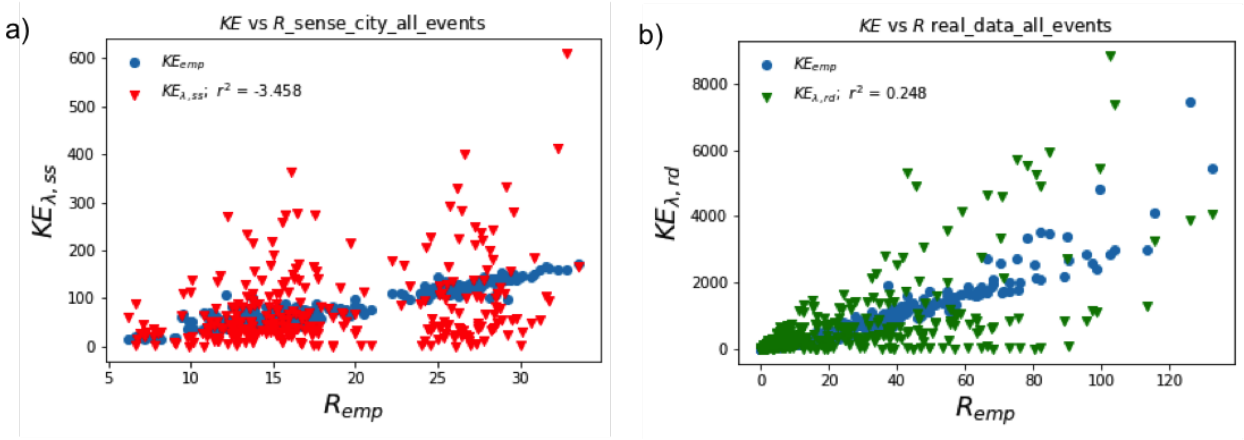

Figure 3.21: a) Estimate of KE alongside empirical values for sense-city (using parameters in $KE_{\lambda,ss}$) and for sample-events (using parameters in $KE_{\lambda,rd}$; eq. 80); Y_λ was simulated using discrete cascades

To illustrate the possibilities of JMF approach in estimating average properties, a sensitivity analysis was performed using a known rain event measured at ENPC (22 Nov 2016 23:02:30 to 23 Nov 2016 06:59:30, Fig. 3.22a). 100 realizations of 512 long 1D discrete cascades (Y_λ) were used and corresponding KE_λ were estimated. Fig. 3.22b shows the 10 and 90 percentile fields along with the empirical field. Despite having variations in amplitude, estimated KE_{JMF} seems to follow the actual field and reproduce the properties on average. The percentage error in α and C_1 of each realization of Y_λ is shown in Fig. 3.22c along with r^2_{JTM} values of JMF analysis for KE and R. Despite having a greater variation in percentage error of UM parameters, good joint multifractal scaling (r^2_{JTM}) was observed in most cases.

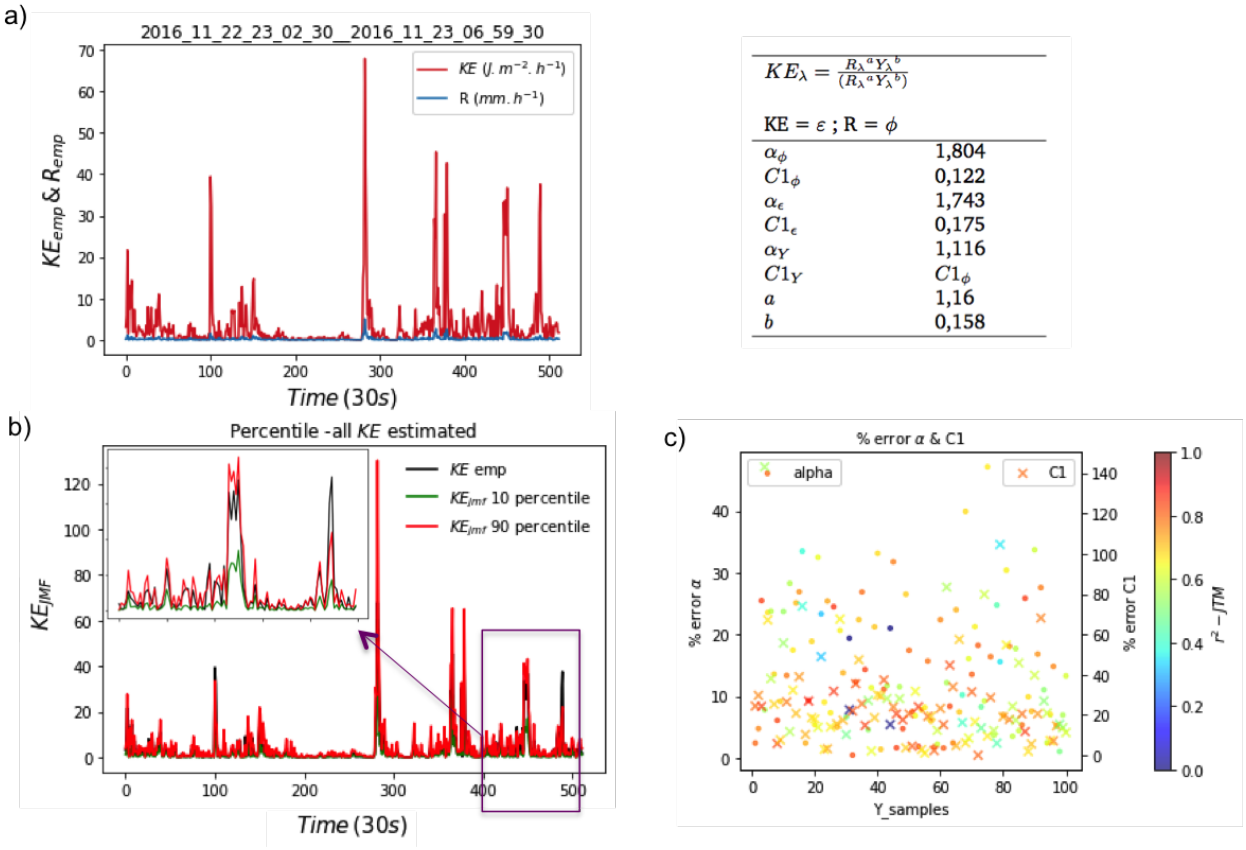

$KE_\lambda = \frac{R_\lambda{}^a Y_\lambda{}^b}{(R_\lambda{}^a Y_\lambda{}^b)}$

KE = ε ; R = ϕ

α_ϕ	1,804
$C1_\phi$	0,122
α_ε	1,743
$C1_\varepsilon$	0,175
α_Y	1,116
$C1_Y$	$C1_\phi$
a	1,16
b	0,158

Figure 3.22: a) R and KE for the event 22 Nov 2016 23:02:30 to 23 Nov 2016 06:59:30, b) empirical KE estimated using JMF approach (100 realizations of Y_λ) shown alongside empirical values, from overall KE_{JMF} obtained 10 and 90 percentile are shown, c) percentage error of α_{Y_λ} and C_{1,Y_λ} with colour plot of r^2_{JTM}

JMF methodology suffers from the obvious handicap of being a statistical approach and hence cannot be recommended for obtaining deterministic values like DTM process. However, as illustrated in Fig. 3.22b, JMF provides reliable statistical estimates in estimating average properties of a field if the correlated multifractal field is known.

3.2.2. Temperature and Humidity

Ariza-Villaverde et al. (2019) used joint multifractal algorithms (not JMF) to see the influence of T and RH on evapotranspiration by grouping cases according to fractal dimension values. In the previous section, JMF was used to study the already-known correlation between KE and R with the intention of quantifying discrepancies in KE produced by simulated rain in a climate chamber (sense-city). The under reporting of KE in simulated rain of sense-city is already noticed by Gires et al. (2020a) and referred. In a similar spirit, efforts were made to reproduce climatic conditions of a few days inside sense-city by focusing on mimicking T and RH of real measurements as well as their correlation. Such analysis could help understand the correlation between both fields and its expected impact on various domains such as the thermal balance of buildings, human comfort (Bensafi et al., 2021), agricultural yield (Chairani, 2022), air pollutants (Elminir, 2005) etc. Others have studied correlations between two fields using various approaches: such as detrended cross-correlation analysis or DCCA (Vassoler and Zebende, 2012; Zebende et al., 2018) which found positive as well as negative correlations depending on location and scale, Gao et al. (2018) explores the influence of wind on temperature-humidity similarity etc.

The main objective here is to evaluate the ability of sense-city in reproducing climatic conditions using scale invariant tools (UM and JMF). For this, a pilot study was done for simulating four days (one summer with rain, same day ignoring rain and two autumn days) inside sense-city chamber in ENPC campus. Information about location and working of chamber are already discussed in section 1.1.2; to quickly recap, sense-city is a climate chamber designed for simulating specific weather conditions for fixed time. Tab. 3.4 summarizes the days selected for mimicking the data inside sense-city, along with their UM parameters. Fig. 3.23 shows the variation of T, RH, and R for the selected days; data from the PWS100 (by Campbell Scientific) disdrometer located on the roof of École des Ponts building and part of the TARANIS observatory was used. It belongs to the same set of instruments that were used in studying rainfall throughout this thesis (along with OTT Parsivel[2]). In addition to rainfall measurements, this device also has precise T and RH sensors within a dedicated shelter. For the rainy day in autumn in Fig. 3.23a, a decrease in T during rainfall and slight increase afterwards can be observed. The summer days shows a more classical diurnal evolution of temperature with day 4 being extremely hot (Fig. 3.23d), and were selected for their difference in humidity.

No.	Day to mimic	season	rain condition	Fields
day 1	27/10/19	autumn	rain	T, RH, R
day 2	27/10/19	autumn	no rain	T, RH
day 3	27/06/19	summer	no rain	T, RH
day 4	25/07/19	summer	no rain	T, RH

Table 3.4: Days and conditions selected to mimic inside sense-city

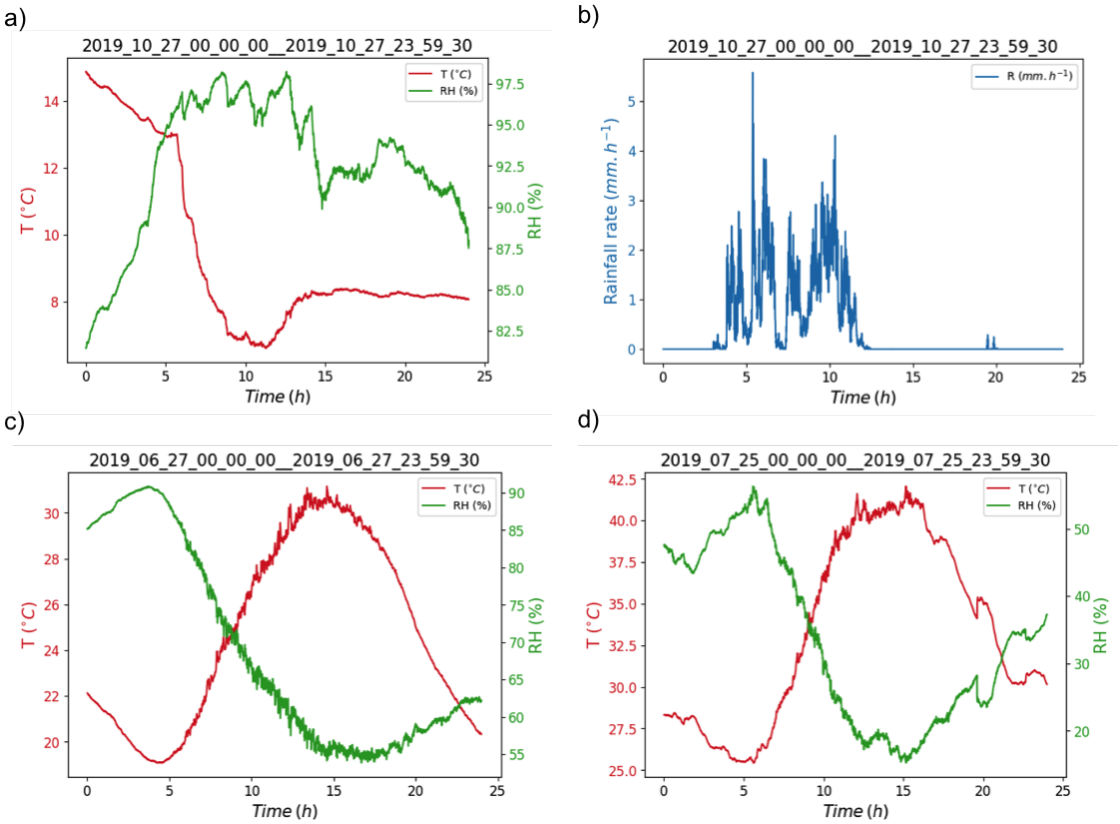

Figure 3.23: Real day conditions used for simulating conditions in sense-city: a) T and RH variation during the autumn day with rain - 27/10/2019, b) R during the autumn day with rain - 27/10/2019, c) T and RH variation during the summer day - 27/06/2019, d) T and RH variation during the summer day - 25/07/2019. Data from PWS disdrometer at TARANIS observatory, ENPC.

3.2.2.1 Experimentation inside sense-city

As briefly mentioned in section 1.1.2, selecting the values of parameters (T and RH here) for simulation is a trade off between time available and chamber limitation (T: -10 °C to +400 °C, gradient of ± 5°C in 240 hr; RH: 300 % to 98 %, gradient ± 50 % in 24 hr). To respect the programmable gradients and operational ranges of chamber, the values of T and RH (at 30 s instrumental resolution of disdrometer sensors) were discretized into various ramps ranging from 45 min to 10 hrs (from Fig. 3.24a to Fig. 3.24b) following directions of sense-city management at IFSTTAR (L'Institut français des sciences et technologies de transports, Gustave Eiffel University). Sense-city programming is to be designed for fixed time periods or ramps (can be set as per simulation requirements) during which the chamber is instructed to transition from initial to target values over a gradient; the length of ramps inside a cycle can be different. This involved cycle preparation time (for reaching initial conditions) as well as change over time while shifting between days. Since the duration of programmable test cycles were to be set fixed by design, the lengths were

selected manually to accommodate variations in both T and RH (Fig. 3.24b). In current experimentation, cycle preparation time and change over time between the 4 simulated days were 3, 3.5, 7 and 4 hours respectively (grey regions in Fig. 3.24b and c). It should be noted that sense-city might not always reach the targets in specified time (due to its limited size and inside components). As reproduction of real days was the focus here, fixed times of ramps were strictly followed regardless chamber achieving target values (Fig. 3.24c). The final program for four days included a total of 30 ramps including the change over time. Before starting the simulation, relevant sensors were selected beforehand and were calibrated by the operators; this mainly included various temperature, humidity and rain sensors inside the mini village (mini-ville 1, mv1) of sense-city. For rain, sense-city only has two modes (light and heavy) and the sprinklers do not cover whole area of the chamber; efficacy of this is already covered in section 3.2.1. For the simulations, rain was considered only for one day with both modes alternating during actual rain time (Fig. 3.24d-f). From Fig. 3.24c, it can be seen that sense-city reproduced conditions better at lower T and higher RH (day 27/10/19: rain and no rain) but not during days of higher T (days 27/06/19 & 25/07/19). For day 3, RH values did not start at required point (temperature as well to a lower extend) and for day 4, temperature failed to reach required targets. Since there were some operational issues with roof temperature during this period, it is not easy to comment whether last two days not reaching target curve being an intrinsic result of sense-city.

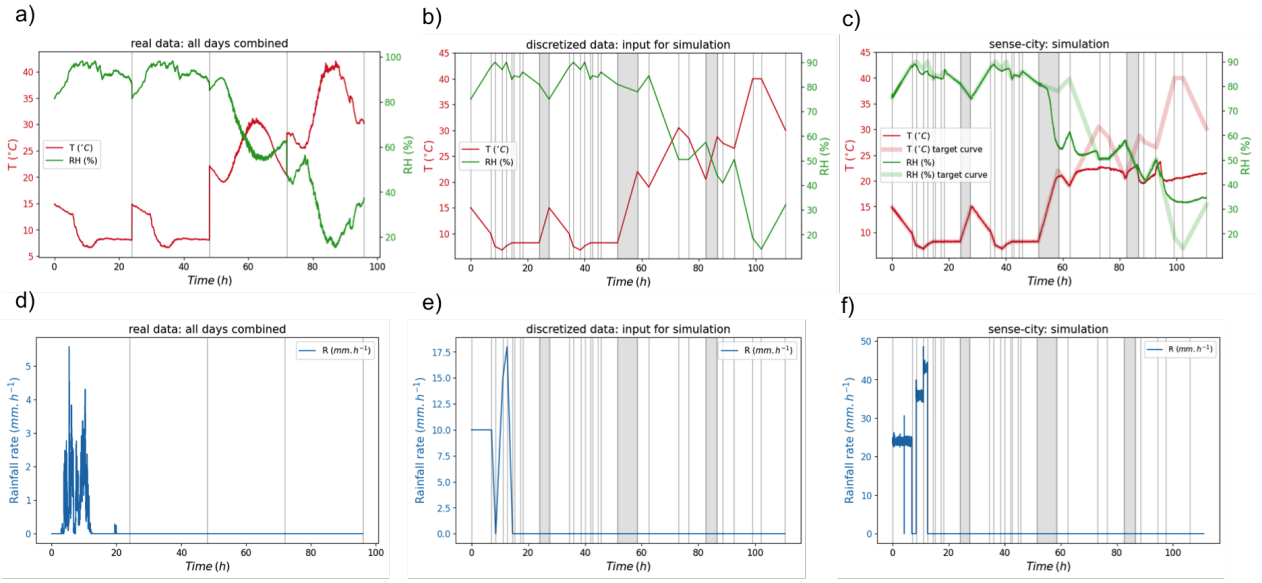

Figure 3.24: a) T and RH variation of all days as obtained from TARANIS observatory, b) discretized version of field as input to sense-city simulation, c) variation of simulated fields inside the chamber during experimentation; d), e) and f) are similar plots for rain.

Tab. 3.5 shows the list of sensors inside sense-city that were used for this study. Sensors dealing with air quality, discharge, roof temperature, rain temperature, wind, chamber position etc. are

No.	Sensor name	field	no. of sensors	resolution
1	BIA_Humidity (primary)	RH	1	10 s
2	BIA_Temperature Chambre (primary)	T	1	10 s
3	BIA_Temperature Chambre (secondary)	T	5	10 s
4	Station-Meteo-MV1	T, RH	1	60 s
6	Temperature-pt100 (on mast)	T	16	15 min

Table 3.5: List of sensors in sense-city that were used for this study

not considered. Studied sensors included two primary sensors measuring T and RH variation inside the chamber at 10 s time-step and two meteorological stations measuring at 60 s. Other secondary sensors included temperature sensors on masts (a set of two sensors on 7 masts at 0.5 m and 3 m height) at various locations inside the chamber; and also two sensors near roof height. Among the listed sensors, the higher resolution primary sensors were the ones used for comparing simulations inside sense-city with real data. For comparison purposes, UM analysis were performed by averaging the primary sensor data to 30 s, the lowest time-step at which real fields were measured at TARANIS. The issues encountered while using station data and temperature sensors on masts are discussed later.

3.2.2.2 UM analysis of sensor outputs and results

Primary sensor outputs

Figure 3.25 shows the UM plots for ensemble analysis of real and simulated data (using primary sensors) for day 1 with a sample size of 64 (32 min) for T and RH. For this day, sense-city basically reproduces the values at large scale (see Fig. 3.24c), but it is only able to partially mimic the scaling features. Indeed quality of scaling is is different between real fields and simulations (degraded for T and improved for RH, second column in Fig. 3.25, and Fig. 3.26c) and there are some noticeable differences for α (with different shape for DTM curves, third column of Fig. 3.25), while similar C_1 values are retrieved. Though the low values of r^2 suggest (Fig. 3.26c) the possibility of scale break, given the length of studied samples, it is not explored here.

Figure 3.26 shows the variation of UM parameters for real conditions and simulated fields inside sense-city. For real data, day 1 and day 2 are same since day 2 was designed to mimic day 1 in sense-city without the precondition of rain. For real as well as simulated fields, fluctuations were required for retrieving conservative fields (β value being higher than encompassing dimension (D = 1 for time series here) in spectral plots, hence higher value of H: $H > 0.5$) for both real and simulated fields. For example, T on day 1 gave an H value of 1.06 while β being 3.13; taking fluctuations reduced these to 0.03 and 0.912 respectively, meaning that TM and DTM are not expected to be biased. As seen in Fig. 3.26a and 3.26b, α shows differences in values while

C_1 remains more or less comparable. For T, α of simulations gave higher values (with a maximum difference of 0.43 for day 2) except for day 4; for RH, the trend was opposite (with a maximum difference of 0.507 for day 1) with real data giving higher estimates except for day 4. Secondary temperature sensors also gave similar results. It is interesting to note that for day 2 (same as day 1 but without rain), both T and RH simulations gave higher α suggesting increased variability in the field when rain showers are not operated. Given that rainfall is only "falling" on a very limited portion of the area in sense-city, it is difficult to interpret this any further. As seen from the behaviour of fields in Fig. 3.23, only day 1 and day 2 are reproducing the expected values; this further limits the interpretation of results.

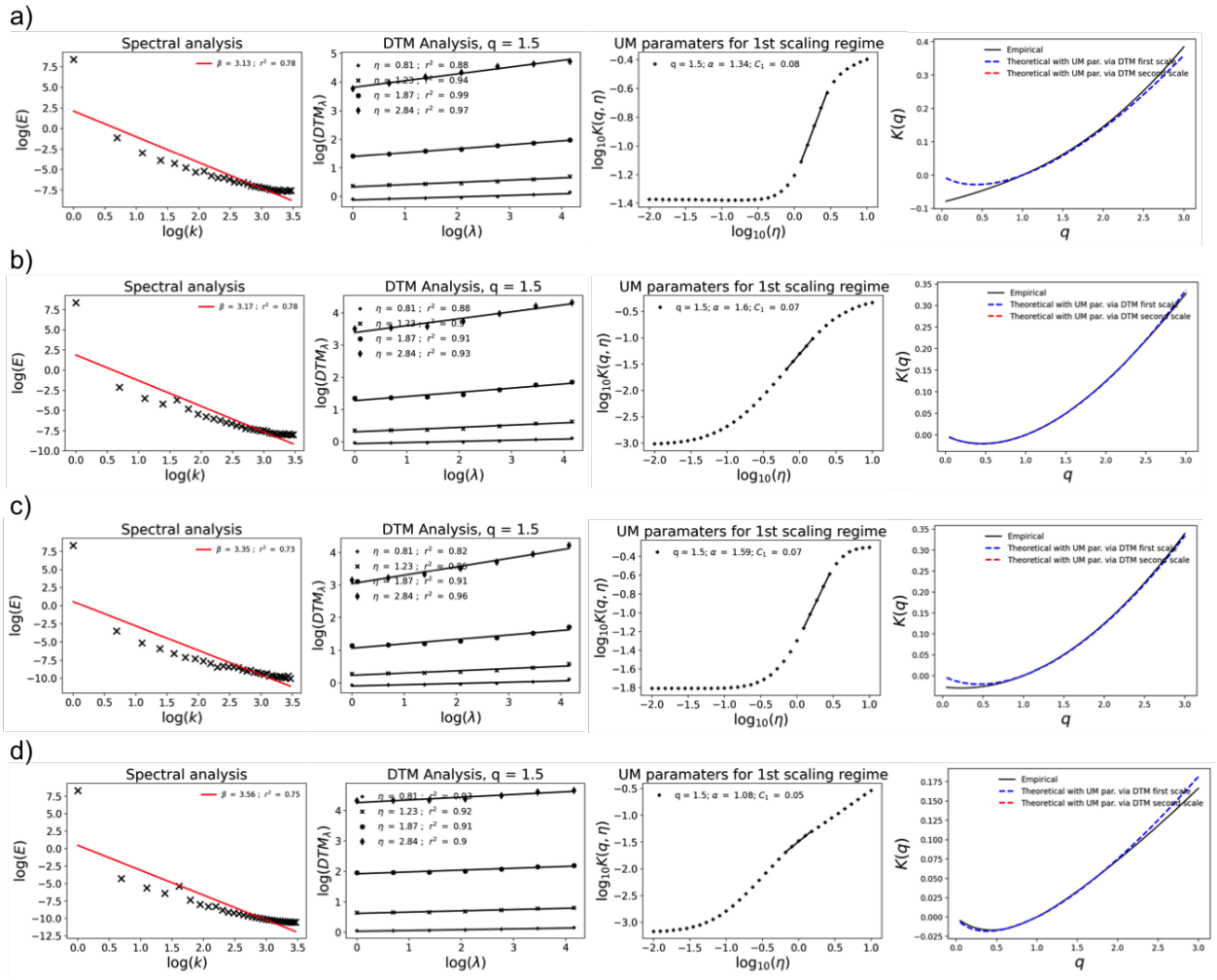

Figure 3.25: Spectral analysis (Eq. 8 in log-log form), DTM analysis (Eq. 22 in log-log form), DTM curve (Eq. 21 in log-log form) and $K(q)$ for day 1 (27/10/2019) a) real temperature (T), b) simulated T inside sense-city, c) real relative humidity (RH), and d) simulated RH inside sense-city. Fluctuations of data were analysed as an ensemble of size 64, corresponding to 32 minutes with 30 s being the lowest time step; spectral plots shown are on direct data.

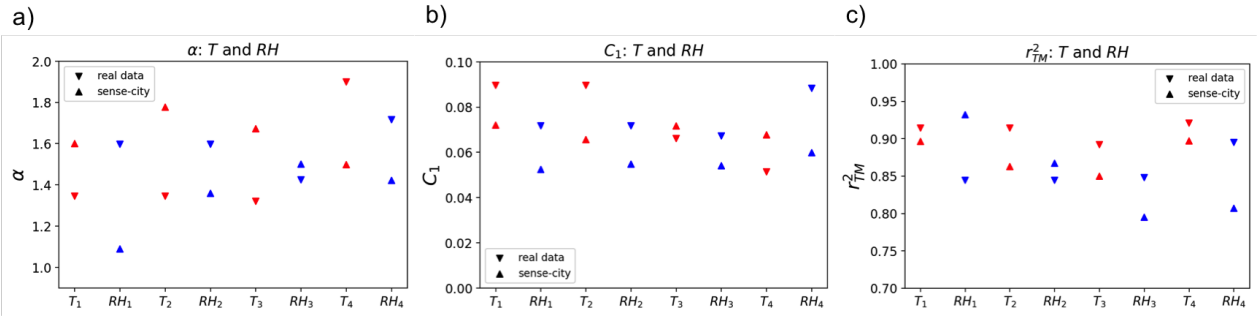

Figure 3.26: variation of UM parameters and quality of scaling for day 1 as an ensemble of 32 min, for both T and RH: a) α, b) C_1, and c) quality of scaling (r^2_{TM}).

Meteorological station and secondary sensor outputs

The meteorological station (Station-Meteo-MV1) gave measurements of T and RH at 60 s time-step inside the chamber. As established previously, both fields required fluctuations for retrieving conservative fields for UM analysis. However, fluctuations gave very low estimates of α (α = 0.0041, C_1 = 0.49 for an ensemble of 32 min for day 1) with a clear lower plateau on the DTM curve suggesting the presence of zeroes in the field. Indeed, 88 % of fluctuation data was zero suggesting repetition of data in direct field at 60 s. To identify the actual sampling resolution relevant for studying variability, a sensitivity analysis was performed by gradually increasing the initial observation scale of data by a factor of 1 (from 1 min resolution to 15 min resolution by averaging the data for each day as a single series). Using primary sensors as a reference, the differences in α and C_1 were examined for each case along with the presence of zeroes. As it could be expected, the percentage of zeroes was found to be decreasing on taking averaging, however, it was difficult to indentify a time-step below 15 min for which T started to exhibit a similar behaviour to the one found on the primary sensor. Except for day 3, T from the station was found to be giving reliable estimates from 6 min with the percentage of zeroes falling below 10 %. For RH, the field gave reliable estimates of UM from averaged data at 6 min (with % of zeroes $\sim$ 1 %). As 15 min is too coarse for studying small-scale variations (in which we are interested here), station data are not presented here. Among the secondary sensors on the masts, two sensors (9 and 13) were not working properly. Further, due to the coarser measuring resolution of 15 min, it was not possible to do any ensemble analysis. Analysing mast temperature as a series for individual days also seemed difficult since the retrieval of conservative fields was difficult with the available data. For example, direct analysis on the sensor (Temperature-pt100-bas-1) for day 1 gave H value of 0.76 (β = 2.5) suggesting a non-conservative field; and, taking fluctuations of the field only lowered this value to 0.5 (β = 1.94). Though acceptable values of α ($\alpha < 2$) and $C_1 \sim 0.05$) were obtained for all secondary temperature sensors, the data wasn't pursued further as higher values of H and β suggested a remaining bias in TM and DTM analysis.

Due to the issues explained above, the UM analysis here is limited to only primary sensors. These results are used below in JMF framework to see the extend to which the coupling between T and RH are retained in sense-city.

3.2.2.3 JMF and results

To understand the extent of coupled reproduction of T and RH inside the sense-city simulation, the framework of joint multifractal analysis (JMF) was used to quantify in a scale invariant way the correlation between both fields inside and outside the sense-city (Gires et al., 2020b). The framework of JMF was previously explored in sections 3.1 and 3.2.1 along with its associated biases. For this joint analysis, the underlying idea is to express mathematically the fluctuations of T as a combination of corresponding RH (conservative part of the field from fluctuations) and an independent multifractal field (Y_λ, λ being the resolution) with similar C_1: $T_\lambda = \frac{{RH_\lambda}^a {Y_\lambda}^b}{({RH_\lambda}^a {Y_\lambda}^b)}$. Values of a and b quantify the correlation between T_λ and RH_λ.

Figure 3.27a shows the joint TM plots and estimation of parameter a for real data in day 1, while the results of JMF for simulated fields inside chamber for the day are shown in Fig. 3.27b. The variation of JMF parameters (a, indicator of correlation IC, quality of joint scaling (r^2_{JTM}) between T and RH at real conditions and sense-city simulations are shown in Fig. 3.28. As seen in JMF plots (Fig. 3.27), correlation is stronger for real days than sense-city for all the days. From the limited real data, it appears that T and RH have a stronger correlation during rainy days than dry ones in sense-city; this need to be explored in detail along with the increased variability observed in dry days in UM analysis. In all the simulations, sense-city simulations gave reduced estimates of exponent a, correspondingly showing poor scaling and correlation. This seems consistent with the difference observed between α estimates of both fields in real and mimicked data.

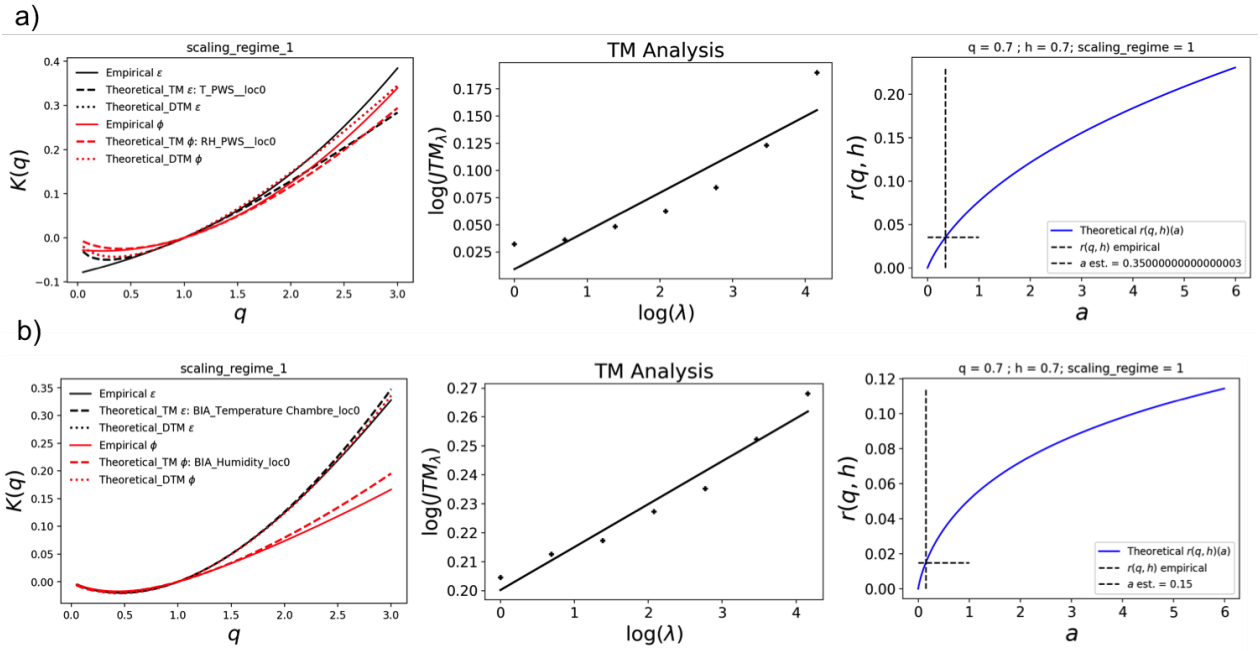

Figure 3.27: K(q) plots for T_λ and RH_λ (fluctuations of the field), TM plot for the joint field, and estimation of JMF parameter a for an ensemble of size 64 (32 minutes), for day 1: a) for real data, b) for sense-city simulation

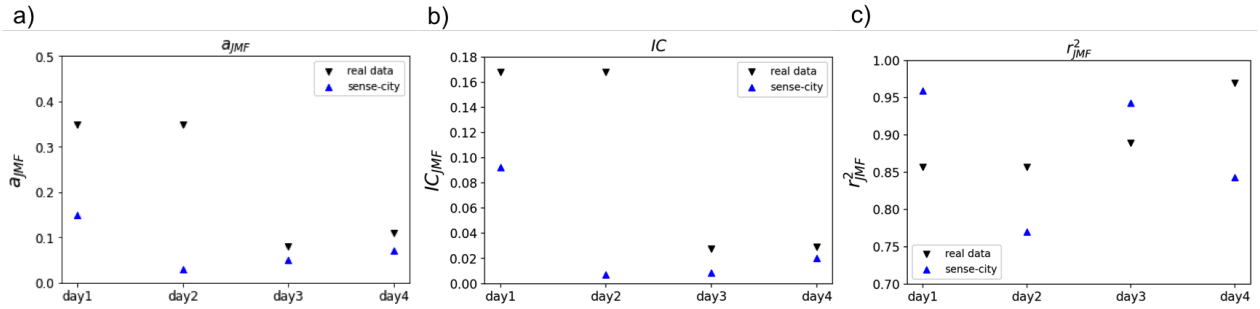

Figure 3.28: Variation of JMF parameters a, indicator of correlation IC and quality of scaling r^2_{JTM} between T and RH for real data and sense-city.

Regardless the differences observed and handicaps with inside sensors, from the results on days 1 and 2, it can be said that the sense-city was able to mimic the fields at larger scales more efficiently than finer scales (and partially recover the scaling properties) even when simulations were programmed in fixed time spans. However, the correlations between T and RH was not exactly reproduced within the chamber. As discussed in previous section (3.2.2, sense-city was also able to reproduce rain (albeit with under reporting of KE and limitations of only two modes) with similar DSD parameters observed in literature. It also goes without saying that more detailed and longer experimentation are required for properly assessing the chamber efficiency since the few days examined here are not sufficient.

3.2.3. Main outcomes from sense-city experiments' analyses

In this section, UM and JMF analysis are performed on simulations inside sense-city to see the extent of the chamber's ability to reproduce scaling and variability of geophysical fields.

In the first sub section, the DSD properties of artificial rain from the sprinklers at various locations were examined using disdrometer measurements (instruments moved from TARANIS observatory). As discussed in section 1.1.2, rain inside sense-city has only two modes - 'light' and 'heavy'. Though the rain, as expected, didn't have any variability within these modes, it managed to provide DSD values commonly observed for similar rain rates in the literature (Tokay and Short, 1996). However, if we follow that criterion, the sense-city rain rates are 'very heavy' and 'extreme' than the predefined modes. The under-reporting of KE by sense-city was previously detected by Gires et al. (2020a) during the experimentation using disdrometers. Here, efforts were made to quantify the same using similar real events from section 2.1 (sample-events). UM analysis of rain events in sense-city showed considerably bad scaling with widely different values of α and C_1 from those of the sample events. The power law exponents between KE and R were also obtained for sense-city and sample-events using the DTM methodology in section 2.1; values obtained illustrated the under reporting in KE even more. Since no obvious trends were observed in values of power law exponents nor UM parameters within events or among locations of disdrometer positioning inside sense-city, sense-city events were taken as an ensemble for improving the data. With this ensemble, corrections were proposed to the sense-city KE using the power law in section2.1 (obtained by averaging the value of exponents from individual rain events, $KE_{\overline{rd}}$) and also using power law corresponding to the ensemble of all rain events in section 2.1 (KE_{rd}); and the correction were made using KE_{rd} as target. The use case of JMF analysis for correcting KE is also explored in this section. Towards this, the possibility of variation in JMF exponent a across rain events was examined first using all rain events in section 2.1. With the reassurance of a lack of trend, JMF was used for extracting sense-city KE as a multiplication of R and an independent field. Though JMF retrieved average properties of the field, being a statistical approach, it cannot be used for obtaining a single deterministic values like DTM methodology. The effectiveness of JMF in the retrieving average field was further explored through a sensitivity analysis of one rain event using 100 realizations. Despite having a variation in percentage error of UM parameters, the analysis gave good joint multifractal scaling (r^2_{JTM}) and managed to retrieve a KE field that followed the properties of the average.

In the second sub section, UM and JMF tools were used to study temperature, T, and relative humidity, RH, of three real days (one day in autumn with, same day without rain, two dry days from summer) and their corresponding simulations inside sense-city. Programming of days inside the chamber consisted of fixed time ramps where a sets of T and RH were defined at the start and end of the ramp, as initial and targets values. The total program for four days included a total of 30 ramps. Though sense-city housed a wide array of temperature sensors and a meteorological station, only primary sensors (at 10 s, averaged to 30 s for comparing with real data of disdrometers) were used

here since the others were found to be too coarse to study variability. For UM analysis, fluctuations were required for both real and simulated fields as they were conservative by default similar to what was observed in section 3.1. From the average variation of values as well as UM analysis, sense-city was found to be able to reproduce only the first 2 days (autumn day with and without rain) properly. Those were also the days with larger number of ramps in programming. However, the data is not sufficient to make any comments on correlation between number of programming steps and output; there were issues with roof temperature during experimentation of later days. For the two days in sense-city, while comparing with real data, a general increase in values of α was observed for T with reduced scaling while RH showed an opposite trend. This result does not induce confidence in using RH as the actual underlying field to study humidity, this needs to be explored in future. Also, from UM values, day 2 (same as day 1 but without rain) seemed to have increased variability of T and RH during the absence of rain. However, it is not possible to make any conclusions due to lack of data and also due to the fact that 'falling rain' is not uniform and limited to specific areas of the chamber according to sprinkler position. JMF analysis of T and RH inside sense-city for days 1 and 2 revealed a considerable reduction in values of JMF coefficient a with those in real conditions. A larger correlation was also observed during dry days than rainy days; since higher variability was also observed for dry days in UM analysis, this is worth exploring in future with more data. From these limited results, sense-city seems to be able to reproduce the large scales more efficiently than smaller scales and recover some of the scaling properties of the field. Further experiments are required for deriving proper conclusions, and UM and JMF are strong tools for understanding this. The results here are also encouraging towards future exploration of atmospheric correlation between T and RH in UM framework.

3.3. Rainfall and particles

3.3.1. Below cloud scavenging of aerosol particles by rainfall

Atmospheric aerosol particles, both anthropogenic and natural, exhibit extreme spatio-temporal variability (McMurry, 2000). They also possess a wide range of lifetime from minutes to several months according to their size range and climatic conditions (Pruppacher and Klett, 1996). Understanding their source and sink is important due to their strong influence on climate, air quality and human health (Pöschl, 2005). One of the main removal mechanisms of aerosols in nature is precipitation-driven 'wet scavenging'. Understanding micro-physical interactions between rainfall and atmospheric particles is hence important to analyse this sink (Hou et al., 2018). This also has implications for atmospheric visibility and the safe functioning of various domains associated with it (see section 2.2).

Depending upon the relative position where aerosols enter the cloud or precipitation particles, the process of 'wet scavenging' can be in-cloud scavenging (ICS, also known as 'wash-out') and below-cloud scavenging (BCS, also known as 'rain-out'). In ICS, aerosols serve as cloud condensation nuclei and are incorporated in the drops, while in BCS, the particles between cloud base and ground are washed out by precipitation (Seinfeld and Pandis, 2016). The overall wet scavenging flux is the sum of the transfer of species from cloud to rain and BCS and both processes have different transfer rates (wash-out rate and rain-out rate). Though ICS is considered to be the main reason for finding aerosol particles in cloud, for scavenging process itself, these drops need to be removed from atmosphere to the ground. When it comes to pollution and air quality, BCS is of specific interest as it acts as a sink of pollution and source for ground ecosystem (Duhanyan and Roustan, 2011). It is important in long term issues such as chemical composition of precipitation and atmosphere (Celle-Jeanton et al., 2009; Roy et al., 2019; Connan et al., 2013; Laguionie et al., 2014) as well as in short term pollution events (Duhanyan and Roustan, 2011). The BCS part of the wet flux is known to be dependent on the aerosol and raindrop distribution (Andronache, 2003), and here we are studying BCS at various particle size ranges and rain conditions. While studying aerosol removal by raindrops, size-resolved analysis is necessary since different mechanisms are involved at different ranges: brownian diffusion and interception dominate sizes below 0.1 µm, while for particles larger than 2 µm, scavenging is through inertial impaction. Between 0.1 and 2 µm, the collection efficiency of aerosol particles are found to be rather minimum, and the size range is often termed as 'scavenging gap' or 'Greenfield gap' (Greenfield, 1957; Chate and Pranesha, 2004). Assuming a homogeneous below-cloud atmosphere before and during precipitation, and by assuming that the aerosol species is non-reacting during the process, it is possible to define BCS using a scavenging coefficient, λ^*. The evolution of aerosol concentration or fraction of aerosols collected by hydrometeors relative to initial concentration during BCS can be represented using as (Seinfeld and Pandis, 2016):

$$\left.\frac{\mathrm{d}c(d_p)}{\mathrm{d}t}\right|_{BCS} = -\lambda^*(d_p)c(d_p) \tag{81}$$

Here λ^* (s^{-1}) is the scavenging coefficient, $c(d_p)$ (in cm^{-3}) is the particle concentration for particle diameter d_p, and $\mathrm{d}c(d_p)$ is its change during the time $\mathrm{d}t$ (in s). The scavenging coefficient λ^* is size specific and depends on interaction between the particles and raindrops, as evident in theoretical expression below :

$$\lambda^*(d_p) = \int_0^\infty \frac{\pi}{4} {D_p}^2 v(D_p) E(D_p, d_p) N(D_p) dD_p \tag{82}$$

Here D_p and d_p are drop and particle diameters, $E(D_p, d_p)$ is the collision efficiency between them, $v(D_p)$ is the terminal velocity of drop of size D_p, and $N(D_p)$ is the drop size distribution of rain (DSD). The approximations made for terminal velocity (van Dijk et al., 2002), as well as DSD (see section 2.1), can influence the estimation of λ^*; complexity of microphysical interactions further complicates the chances of having a common consensus. Hence, a more empirical derivation of the scavenging coefficient is relevant for better analysing the process. However, this is also not without biases since dynamic effects often dominate when scavenging coefficients are obtained from pollution concentration alone (Quérel et al., 2014). $\lambda^*(d_p)$ is commonly calculated from particle concentration between two timesteps (1 and 2) (Laakso et al., 2003):

$$\lambda^*(d_p) = -\frac{1}{t_2 - t_1} \ln\left(\frac{c(d_p)_2}{c(d_p)_1}\right) \tag{83}$$

See Duhanyan and Roustan (2011) and Zhang et al. (2013) for a comprehensive review on BCS of aerosols and gases by rain and the associated uncertainties. Further, BCS can be expressed in terms of rainfall intensity as $\lambda^* = nR^m$ where n and m are coefficients that depend on aerosol characteristics; various variants of this relation have been reported in the literature on the basis of aerosol and rain type (Andronache, 2003; Duhanyan and Roustan, 2011).

Another commonly used parameter for characterizing BCS is scavenging efficiency where change in particle concentration before (index 1 in Eq. 84) and after (index 2 in Eq. 84) rain (30 min) is represented in percentage (Laakso et al., 2003):

$$\%\Delta C = -\frac{c_2 - c_1}{c_1} \cdot 100 \tag{84}$$

A positive value of λ^* and $\%\Delta C$ suggests reducing concentration with rain, and hence positive scavenging. For current study, simultaneously measured data of particle number concentration and

rainfall were used to study their variability. The assumptions used at section 2.2 for analysing σ_e in a scale invariant framework is valid here as particle number concentration follows the similar governing non-linear equations, and is hence also expected to inherit the scale invariance features of the Navier-Stokes equations that governs atmospheric behaviour. This hypothesis is tested in coming sections and some preliminary results from multifractal analysis of particle concentration is presented with its implications for future research.

3.3.2. Measurement campaign and data filtering.

Details of the location and duration of the measurement campaign, instruments used and parameters measured are already discussed in section 1.1.4. To quickly recap, the data was obtained from the experimental station of IRSN in the city of Cherbourg-Octeville, France. The campaign involved simultaneous measurement of rain (disdrometer; $\mathrm{mm\,h^{-1}}$), wind (sonic anemometer; $\mathrm{m\,s^{-1}}$), and aerosol particle concentration (SMPS - 14.6 nm to 478.3 nm in 98 granulometric classes APS (0.523 µm to 19.81 µm in 52 granulometric classes; $\mathrm{cm^{-1}}$) for a duration of about 3 months (01/11/2010 to 12/03/2011). Except for sonic anemometer (10 Hz), every instrument recorded data at a measurement frequency of 1 min.

Since, the intention of this study was to analyse aerosol particle concentration alongside rain, filtering was done in the data-set to obtain only those time steps that are common among the four instruments; this provided 77503 common data points in 1 min resolution (50.97 % of time steps were discarded using this). To select the rain events, the criteria followed in Blanco-Alegre et al. (2021) was adopted - in rain intensity time series, rain events were counted when mean intensity exceeded $0.2\,\mathrm{mm\,h^{-1}}$, cumulative rainfall depth was greater than 0.4 mm and when there was a minimum dry weather of 60 min before and after. In order to make sure that rainfall is the main meteorological parameter affecting aerosols, only those events were considered where variation in temperature (T) and wind velocity (U_{xy}) were within $\pm 3.5\,^{\circ}\mathrm{C}$ and $2\,\mathrm{m\,s^{-1}}$ respectively. Due to limitations in available data, the remaining restrictions in Blanco-Alegre et al. (2021) were not employed, namely relative humidity variation (RH) variation, New Particle Formation (NPF) bursts and mode based pollution burden. A total of 26 rain events were obtained this way, corresponding to a total duration of 149.76 hours.

3.3.3. Analysis of total aerosol concentration during rain and dry conditions

To see the overall behaviour of aerosol number concentration during rain and during dry conditions, ensemble UM analysis (see section 1.2.2) was performed on total particle concentration ($\mathrm{cm^{-3}}$) of the identified events, for both SMPS and APS. For this purpose, choice was made to analyse the rain events as a single ensemble at a sample length of 64 (approximately 1hr). From the previously identified 26 events, 17 were selected based on this size selection; and resulting ensemble contained 132 samples. A total of 81 dry events were also subjected to UM analysis with same size; ensemble of dry events contained 541 samples. Detailed information on how the data is prepared for ensemble analysis is given in section 1.2.3.

Total aerosol concentration showed similar good scaling behaviour over the range of scales studied (1 min to 64 min) for ensemble analysis of both rain and dry data-sets (for both SMPS and APS). Since the estimates of spectral slope exceeded field's embedding dimension (dimension = 1 for time series), conservative part of the fields were subject to TM and DTM analysis. As commonly done (see section 1.2.2 for more details), it was approximated by taking absolute values of the fluctuations. This reduced the values of non-conservation parameter H and spectral slope β (keeping under 1) while retaining the scaling properties (for SMPS, H was reduced from 0.64 to 0.08 for rain data, and from 0.58 to 0.05 for dry data; for APS, H was reduced from 0.82 to 0.02 for rain data, and from 0.83 to 0.04 for dry data). This means that TM and DTM will not be biased. Fig. 3.29 shows the TM, DTM (both on fluctuations) and spectral graphs (on direct data) for rain and dry events for both instruments. The high coefficient of determination for the linear regression illustrate the good scaling behaviour initially mentioned. It can be observed that, both rain and dry ensemble gave similar estimates of α and C_1 (α, C_1 for SMPS-dry: 1.96, 0.09; APS-dry: 1.83, 0.08; SMPS-rain: 1.96, 0.09; APS-rain: 1.72, 0.07) across respective devices. Values α and C_1 obtained here were consistent with the values commonly found for fields under the influence of atmospheric turbulence (α = 1.8 and C_1 = 0.2). Much like the ensemble analysis, no discernible differences were observed between UM parameters of individual events during rain and dry conditions as well.

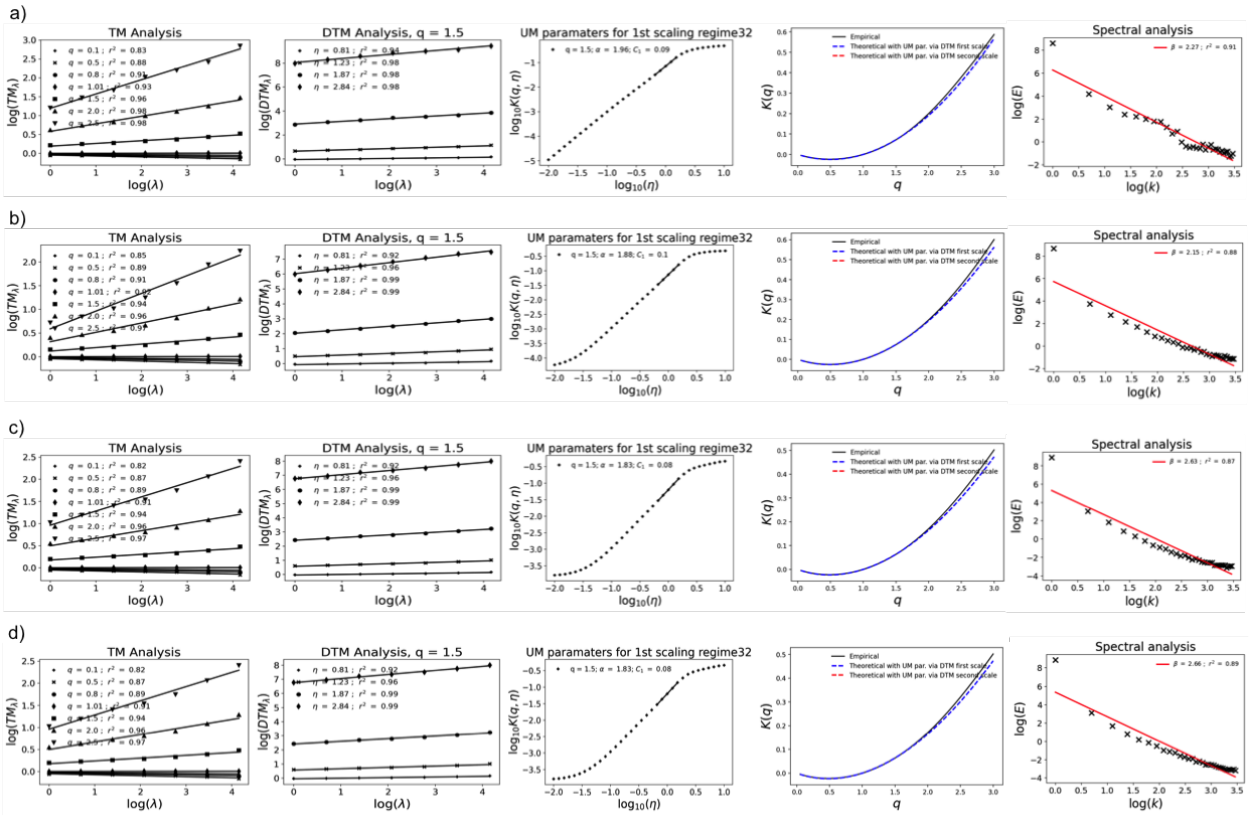

Figure 3.29: Multifractal and spectral graphs of total aerosol concentration as an ensemble for a) SMPS rain events, b) SMPS dry events, c) APS rain events and d) APS dry events. The graphs from left to right: Trace moment analysis (TM, Eq. 14 in log-log plot), Double trace moment analysis (DTM, Eq. 22 in log-log plot), DTM curve, Scaling moment function K(q) for $0 \leq q \leq 3$ and power spectra (Eq. 8). The spectra shown here is in direct data while multifractal graphs are using fluctuations

For understanding the behaviour of total aerosol concentration in rain, the events were categorized into 4 classes on the basis of 5 min moving average rain rate following the criteria in (Tokay and Short, 1996). In terms of UM parameters, it seems that in general more variability is found in nm range (SMPS) than μm range (APS) as the former exhibits higher α and C_1 (Fig. 3.30b). No obvious tendency with rain rate is noticed. In terms of scavenging efficiency, total concentration in nm range also showed relatively larger %ΔC (Eq. 84) in those events (Fig. 3.30a); they exhibited higher scavenging in moderate rain while lower in heavier events analyzed. Total concentration in μm range exhibited higher scavenging mostly in heavier rain events; this confirms to the known theory that bigger particles are scavenged more efficiently by larger drops. As the number of events available for study were limited, it is not possible to make any overarching conclusions from these results. Further, the value of mean scavenging coefficient being negative suggests that the filtering of rain events used here for isolating scavenging is not ideal as well. No matter how carefully selected the rain events are, it is difficult to avoid the other processes influencing the concentration change, such as advection, turbulent diffusion, coagulation, hygroscopic behaviour of various

aerosol species etc. (Laakso et al., 2003).

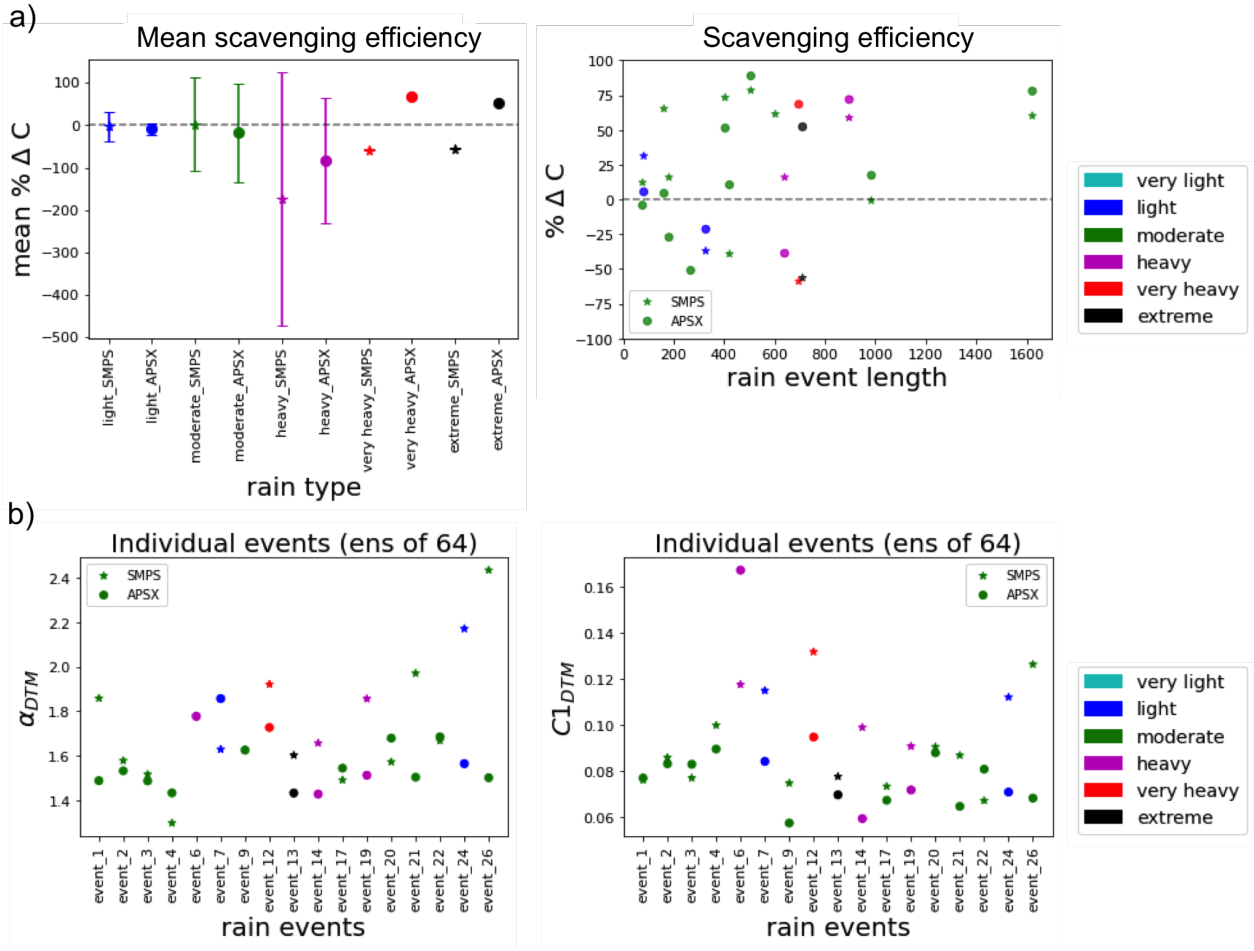

Figure 3.30: a) Mean and standard deviation of scavenging efficiency for all events in a particular rain class (Eq. 84), and scavenging efficiency of all events plotted against their length (Y axis is limited to a lower limit of -100 here for visibility) ; b) Variation of α and C_1 among rain events studied.

3.3.4. Analysis of individual aerosol concentration inside one rain event

To understand the variation of size resolved aerosol concentration, a single event was considered which exhibited positive scavenging (a moderate rain event from 18 Feb 2011 22:35:00 to 19 Feb 2011 07:00:00 with positive %ΔC for total concentration). Number concentration for individual classes were calculated from size distribution available using width of particle bins - values of dN from dN/dlogD_p (normalized concentration value independent of bin width) provided by instruments. From the Fig. 3.31a, consistent scavenging can be observed with rain for total concentration as well as in changes of particle size distribution before and after rain. It can be observed that most particle classes in nm range shows positive scavenging efficiency (%ΔC) during the event with an increasing trend in lower end (<100 nm roughly); for µm range, positive scavenging is limited only

around 1 µm with a decreasing trend (Fig. 3.31b). Median BCS coefficient λ^* (Eq. 83) on the other hand shows variation around 0 for both nm and µm range particles. This difference from overly positive %ΔC is from variations in particle concentration at lower frequencies since λ^* was computed between consecutive time steps (1 min), while the former used concentration difference 30 min before and after rain. This limits the use case of λ^* here as a UM field which is strictly positive in conventional analysis. As mentioned before, λ^* is known to follow a power law relation with rainfall rate ($\lambda^* = nR^m$) for a given size range. Such relation does not seem to remain valid at the high resolutions available in this study. Given these reported negative values, it's not possible to subject λ^* to UM analysis as a time series; hence, in this current form, possibility of obtaining the power law relation in a scale invariant manner (using DTM methodology covered in section 1.2.2) is also not possible. Presence of median zeroes in λ^* plot (Fig. 3.31.b, last column) corresponds to the size distribution, with larger drops having lesser presence in the rain event.

Time series of individual particle class concentration were subjected to UM analysis to understand aerosol variability across various sizes inside the event considered. Overall, they showed similar scaling behaviour as total concentration discussed before, with higher β and H suggesting the need for performing TM and DTM analysis on the fluctuations of the fields. Variation of UM parameters across particle sizes are given in Fig. 3.31 for both SMPS and APS. Values of fractal dimension (D_F) of the field is also plotted alongside to illustrate biases from presence of zeroes (D_F = 1 implies occurrence of particle in every time steps). For SMPS, till 23.2 nm and from 346 nm, α and C_1 are influenced by presence of zeroes in data (decrease in α and increase in C_1); for APS, this bias can be observed after 2.28 µm (Gires et al., 2012). This corresponds to mean particle size distribution in Fig. 3.31. Within the non biased regions, UM parameters appear stable providing reliable estimates of α and C_1; and meaning the consistent behaviour across particle size.

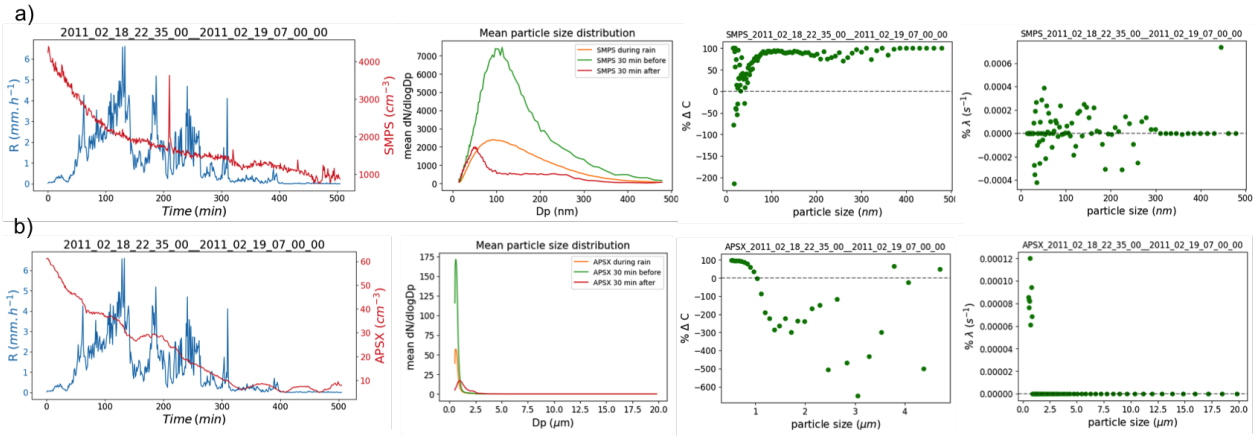

Figure 3.31: In column order: Total concentration variation and rain rate, mean particle size distribution, size resolved scavenging efficiency and median scavenging coefficient for rain event 2011_02_18_22_35_00 to 2011_02_9_7_00_00: a) for particles in nm range (SMPS), b) same information for particles in µm range (APS)

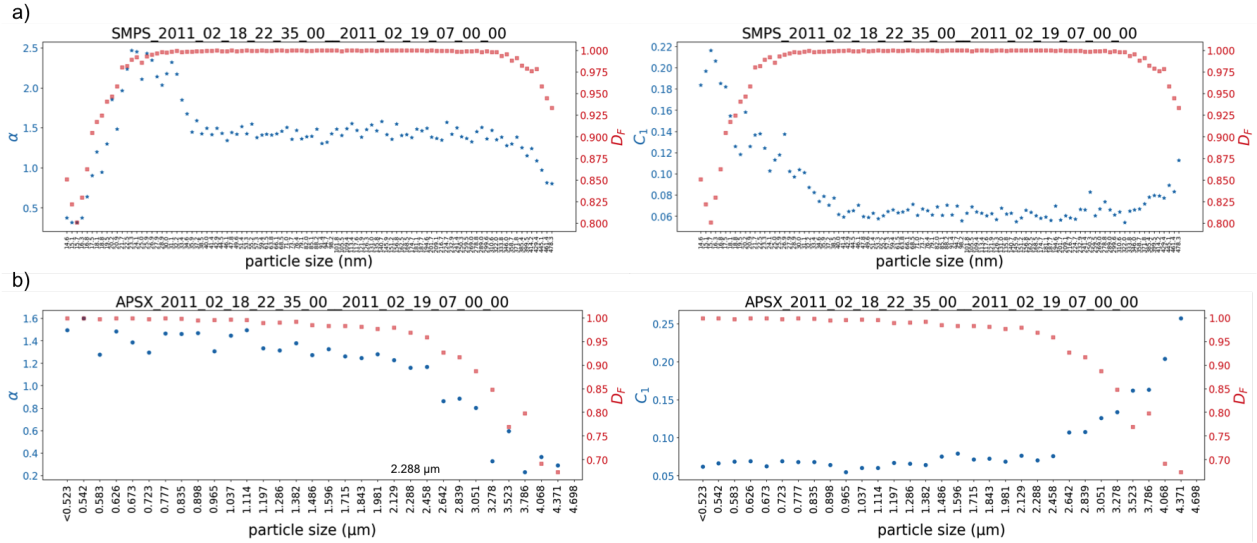

Figure 3.32: Variation of α and C_1 for a) for particles in nm range (SMPS), b) same information for particles in µm range (APS)

3.3.5. Analysis of individual aerosol concentration variation according to type of rain

The analysis in previous section was extended to every rain event studied in ensemble analysis. Efforts were done to organize the results to see if there is any observable difference between types of rain. Using the scavenging efficiency of total concentration (%ΔC) in Fig. 3.30a, events were classified into those with positive and negative scavenging. Similar trend was observed as that has been seen during the analysis of single event (Fig. 3.32). Outside the region of bias, UM parameters showed consistent estimates; values and pattern of estimates remained similar across positive and negative %ΔC. The results were also plotted according to the rain type in Fig. 3.33. Across all the rain types, a slight reduction in α is observed as size increases. However, as mentioned previously, since the number of rain events available in each class is limited here (only one each for heavy and extreme, and none for very light criteria), extended analysis over larger data set is recommended for making conclusive results. It is worth mentioning that this mild trend was observed while consolidating events on the basis of ±%ΔC as well as while considering all the events available.

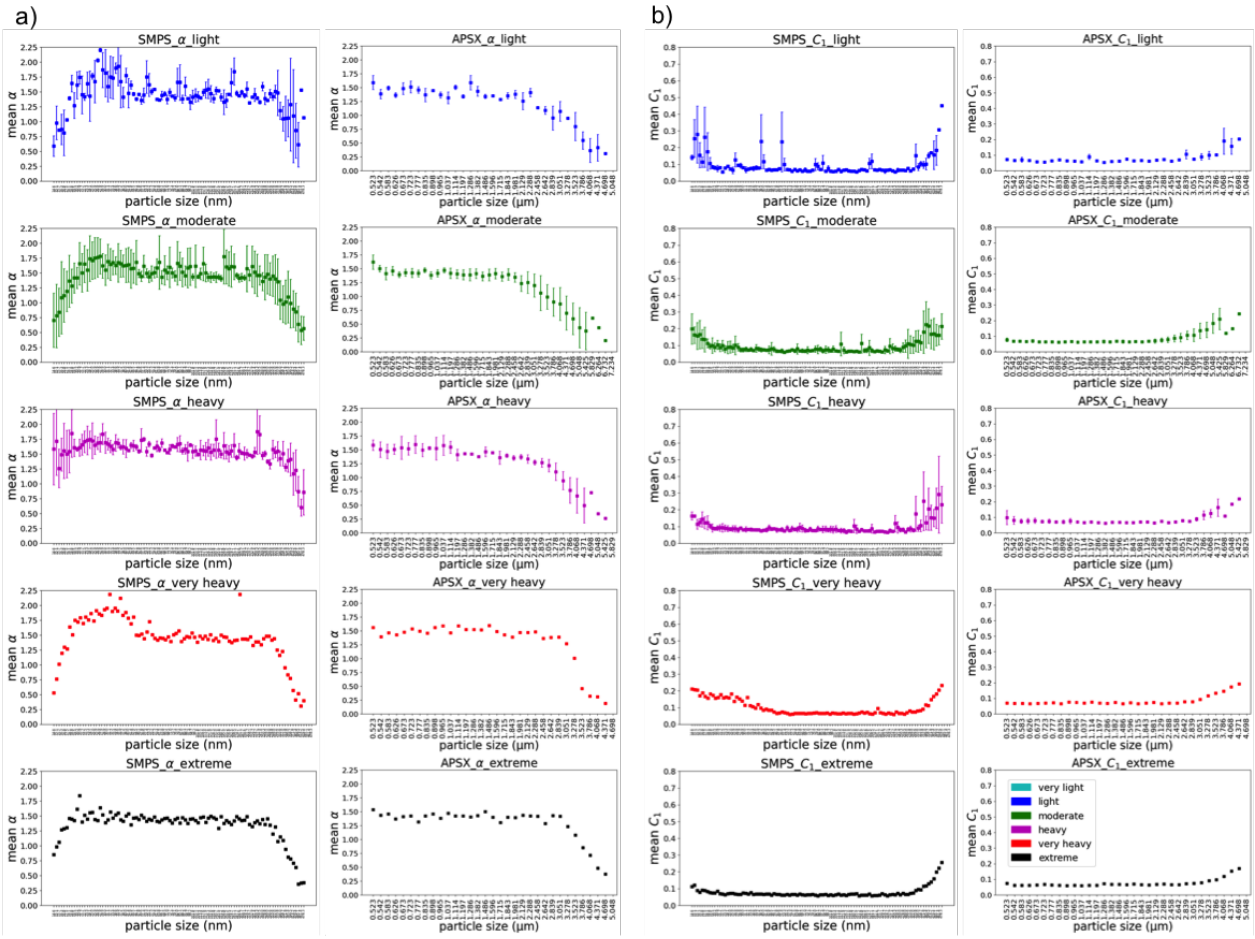

Figure 3.33: Mean and standard deviation of UM parameters of events according to rain type, for every particle class in nm (SMPS) and μm (APS) range

3.3.6. Recommendations for future research

It has been observed that various particles exhibit different scavenging behaviour in rain based on their size. Except for the tail ends, reliable estimates of UM parameters were obtained which suggests the possibility of using multifractal tools for studying particle size groups. This is of specific interest since evolution of concentration during scavenging is influenced by many different processes, and hence rather complex to analyse. The complexity is reflected in current analysis as well, where only considering rain wasn't enough to understand the process.

Since λ^* of various sizes are known to follow a power law with rain rate, simultaneous analysis of particles and raindrops is of interest in understanding the scavenging process better. The limitation in using λ^* as a UM field was briefly mentioned before. If enough data can be amassed from rain episodes long enough to have positive values of λ^*, this is a potential future research area for understanding scale invariant behaviour between aerosol concentration and rain rate. It will also

be interesting to expand this understanding using raindrop size distribution as aerosols of various sizes interact differently with raindrops of different sizes in the atmosphere in BCS.

3.4. Main outcomes of joint analyses

The scale invariant analyses in the previous chapter are continued here, but with a major focus on correlations between the fields in the framework of JMF. As in the previous chapter, the need for identifying the actual underlying field and detecting the resolution relevant for studying the variability of the process is encountered here as well. Similar was the case for instrumental threshold affecting UM analysis. The use case of JMF as a powerful tool for studying correlations between various fields is illustrated here while acknowledging the associated biases. The ability of controlled environments in reproducing real fields (sense-city and wind farm) is also investigated here with efforts to quantify the differences using UM and JMF parameters. Complementing the UM analysis on atmospheric particles in the previous chapter, here the size-resolved evolution of concentration, as well as their scavenging, are explored with comments on the future prospectus. Specific conclusions and perspectives of the studies are mentioned in their respective sessions

In the next chapter, the overall conclusions and future perspectives of the thesis are discussed.

Conclusions and perspectives.

The importance of studying small scale variability of atmospheric fields is illustrated throughout this thesis using various geophysical fields. Here, the results and perspectives are briefly summarized with respect to the SDG goals identified in the introduction (Sachs et al., 2022).

Towards climate action, the importance of studying rainfall with its full complexity involving drop size distribution is emphasized. Using UM, the microstructure of rain is studied through the commonly examined field, rainfall intensity R and also through the seldom explored, at least using multifractals, time specific kinetic energy KE (section 2.1). The newly postulated scale invariant power law relation between them is devoid of any assumptions of drop size distribution (DSD) and has the backing of theoretical relationships; it also provides comparable performance with existing relationships that are based on DSD assumptions. Considering the easy availability of rain measurement all over the world, such a relationship enables realistic retrieval of rainfall kinetic energy, which otherwise requires complex and expensive instrumentation. A better knowledge on kinetic energy space-time variability is needed to better understand and manage diseases spread in crop fields, erosion in rural and urban areas (including buildings and structures) or removal of pollutants deposited on the ground in urban areas. Since, DSD is known to be varying across the globe, in the future, the relationship and developed methodology needs to be expanded across geographical and meteorological conditions through its implementation on other data sets.

Towards sustainable cities and communities, the correlations between various geophysical fields were studied in real and controlled environments, notably temperature and humidity, and rainfall (section 3.2). Such understanding of correlations across scales is actually a much needed step for the large scale deployment of nature based solutions. Indeed it is required to properly evaluate their functioning which remains a challenge for the community. Efforts were made to simulate real-world conditions inside the climate chamber of sense-city. The efficiency of the chamber in reproducing small scale variability was examined using multifractal tools and efforts were made to quantify the differences. Since sense-city houses scaled models of urban areas with their features such as roads, houses, plants etc. reducing the uncertainties between real and simulated fields is important for future research in the development of sustainable urban environments. The analysis of aerosols here, through extinction coefficient and aerosol particle concentration, is also important since the proper functioning of urban communities needs proper knowledge of air quality (section 2.2 and 3.3.1). The scaling behaviour observed in the extinction coefficient as well as particle number concentration opens new pathways for studying aerosol distribution in the atmosphere and their scavenging using multifractal tools. More precisely, a clearer understanding of the correlation between rainfall and scavenging will enable a new kind of modelling for particle concentration in the atmosphere, opening up the path for innovative approaches for forecasting.

Towards the goal of clean and sustainable energy, the small scale variability in turbulent wind

power and their coupling with various atmospheric fields were examined using UM framework (section 3.1). Reported correlations between wind power available and rain open up new discussions on the effect of precipitation on wind turbulence and ultimately power production, which is not well understood in the scientific community. The use of multifractal tools enabled quantification of these correlations across scales and not only at a unique (usually low) resolution as commonly done. This enables to better account for the underlying complexity of the involved processes. The analysis also revealed various potential biases in joint analysis posed by the conservative and non conservative nature of different fields at various scaling regimes, and by the fact that actual power production is rated. The biases were studied and their basic effect was quantified. Further investigations to fully account for them in the JMF are needed. In future, joint analysis between wind power available and wind velocity, the effect of air density, wind direction, orography, location etc. which were not fully captured here, needs to be included and accounted for.

In addition to these goals, the dissertation also illustrates the use case of UM as a powerful tool for analysing the quality of data. Indeed, even though the instruments are providing high-resolution data, it is important to identify the sampling resolution valid for considering the variability in the field studied (section 1.2.2.4). The influence of upper and lower thresholds in recorded data, which is often encountered in analysis, and their consequences in UM analysis are also explored theoretically, and empirically with the help of wind turbine power and atmospheric visibility data as well as numerical simulations. Though these biases are explained using a theoretical framework, as of now, there is no solution to completely account for them. The same is the case for biases identified in JMF of various fields; future research is needed to improve reliable estimates of scaling regimes and UM parameters despite these effects. In addition to the relevant sampling resolution, the need for selecting the actual field relevant for characterizing variability, i.e. the one which exhibits the expected multifractal behaviour is also emphasized (section 2.2).

Thus, this research enabled to better understand the variability of various atmospheric fields in a scale invariant framework and to study their correlation across scales. This is seldom done and constitutes an innovative first step towards significant improvement in the understanding of the atmosphere as a complex system. Various hints for potential theoretical developments, notably with regards to inherent biases in data collection, have been identified and initial solutions are provided. Stochastic analysis and biases identified here provide new information in the application fields of SDG goals identified above as well as for future analysis in scaling and modelling of the atmosphere.

References

Adirosi, E., Baldini, L., Lombardo, F., Russo, F., Napolitano, F., 2013. Comparison of different fittings of experimental dsd. AIP Conference Proceedings 1558, 1669–1672. URL: *https://aip.scitation.org/doi/abs/10.1063/1.4825850*, doi:10.1063/1.4825850, arXiv:https://aip.scitation.org/doi/pdf/10.1063/1.4825850.

Adirosi, E., Gorgucci, E., Baldini, L., Tokay, A., 2014. Evaluation of Gamma Raindrop Size Distribution Assumption through Comparison of Rain Rates of Measured and Radar-Equivalent Gamma DSD. Journal of Applied Meteorology and Climatology 53, 1618–1635. URL: *http://journals.ametsoc.org/doi/10.1175/JAMC-D-13-0150.1*, doi:10.1175/JAMC-D-13-0150.1.

Adirosi, E., Volpi, E., Lombardo, F., Baldini, L., 2016. Raindrop size distribution: Fitting performance of common theoretical models. Advances in Water Resources 96, 290–305. URL: *http://www.sciencedirect.com/science/article/pii/S0309170816302639*, doi:10.1016/j.advwatres.2016.07.010.

Al, B., C., C.K., Hann, D., 1986. Effect of rain on vertical axis wind turbines, proceedings of the international conference on renewable energies and power quality, las palmas de gran canaria (spain), 13th to 15th april 2011. .

Andronache, C., 2003. Estimated variability of below-cloud aerosol removal by rainfall for observed aerosol size distributions. Atmospheric Chemistry and Physics 3, 131–143. URL: *https://acp.copernicus.org/articles/3/131/2003/*, doi:10.5194/acp-3-131-2003.

Angulo-Martínez, M., Beguería, S., Latorre, B., Fernández-Raga, M., 2018. Comparison of precipitation measurements by ott parsivel^2 and thies lpm optical disdrometers. Hydrology and Earth System Sciences 22, 2811–2837. URL: *https://www.hydrol-earth-syst-sci.net/22/2811/2018/*, doi:10.5194/hess-22-2811-2018.

Angulo-Martínez, M., Barros, A., 2015. Measurement uncertainty in rainfall kinetic energy and intensity relationships for soil erosion studies: An evaluation using PARSIVEL disdrometers in the Southern Appalachian Mountains. Geomorphology 228, 28–40. URL: *https://linkinghub.elsevier.com/retrieve/pii/S0169555X14004140*, doi:10.1016/j.geomorph.2014.07.036.

Angulo-Martínez, M., Beguería, S., Navas, A., Machín, J., 2012. Splash erosion under natural rainfall on three soil types in NE Spain. Geomorphology 175-176, 38–44. URL: *http://www.sciencedirect.com/science/article/pii/S0169555X12003005*, doi:10.1016/j.geomorph.2012.06.016.

Ariza-Villaverde, A., Pavón-Domínguez, P., Carmona-Cabezas, R., de Ravé, E.G., Jiménez-Hornero, F., 2019. Joint multifractal analysis of air temperature, relative humidity and reference evapotranspiration in the middle zone of the guadalquivir river valley. Agricultural and Forest Meteorology 278, 107657. URL: *https://www.sciencedirect.com/science/article/pii/S0168192319302655*, doi:https://doi.org/10.1016/j.agrformet.2019.107657.

ASTM-G73-10, 2017. Standard test method for liquid impingement erosion using rotating apparatus. Astm , 1 – 19doi:https://doi.org/10.1520/G0073-10R17.

Atlas, D., Srivastava, R.C., Sekhon, R.S., 1973. Doppler radar characteristics of precipitation at vertical incidence. Reviews of Geophysics 11, 1. URL: *http://doi.wiley.com/10.1029/RG011i001p00001*, doi:10.1029/RG011i001p00001.

Atlas, D., Ulbrich, C.W., 1977. Path- and Area-Integrated Rainfall Measurement by Microwave Attenuation in the 1–3 cm Band. Journal of Applied Meteorology 16, 1322–1331. URL: *https://journals.ametsoc.org/doi/abs/10.1175/1520-0450%281977%29016%3C1322%3APAAIRM%3E2.0.CO%3B2*, doi:10.1175/1520-0450(1977)016<1322:PAAIRM>2.0.CO;2.

Battaglia, A., Rustemeier, E., Tokay, A., Blahak, U., Simmer, C., 2010. PARSIVEL Snow Observations: A Critical Assessment. Journal of Atmospheric and Oceanic Technology 27, 333–344. URL: *https://journals.ametsoc.org/doi/10.1175/2009JTECHA1332.1*, doi:10.1175/2009JTECHA1332.1.

Bech, J.I., Hasager, C.B., Bak, C., 2018. Extending the life of wind turbine blade leading edges by reducing the tip speed during extreme precipitation events. Wind Energy Science 3, 729–748. URL: *https://www.wind-energ-sci.net/3/729/2018/*, doi:10.5194/wes-3-729-2018.

Beiter, P., Cooperman, A., Lantz, E., Stehly, T., Shields, M., Wiser, R., Telsnig, T., Kitzing, L., Berkhout, V., Kikuchi, Y., 2021. Wind power costs driven by innovation and experience with further reductions on the horizon. WIREs Energy and Environment 10, e398. URL: *https://wires.onlinelibrary.wiley.com/doi/abs/10.1002/wene.398*, doi:https://doi.org/10.1002/wene.398, arXiv:https://wires.onlinelibrary.wiley.com/doi/pdf/10.1002/wene.398.

Bensafi, M., Ameur, H., Kaid, N., Hoseinzadeh, S., Memon, S., Garcia, D.A., 2021. Thermophysics analysis of office buildings with a temperature–humidity coupling strategy under hot-arid climatic conditions. International Journal of Thermophysics 42, 1–20.

Best, A.C., 1950. The size distribution of raindrops. Quarterly Journal of the Royal Meteorological Society 76, 16–36. URL: *https://rmets.onlinelibrary.wiley.com/doi/abs/10.1002/qj.49707632704*, doi:10.1002/qj.49707632704.

Blanco-Alegre, C., Calvo, A., Castro, A., Oduber, F., Alonso-Blanco, E., Fraile, R., 2021. Scavenging of submicron aerosol particles in a suburban atmosphere: The raindrop size factor. Environmental Pollution 285, 117371. URL: *https://www.sciencedirect.com/science/article/pii/S0269749121009532*, doi:https://doi.org/10.1016/j.envpol.2021.117371.

Bohren, C.F., Huffman, D.R., 2008. Absorption and scattering of light by small particles. John Wiley & Sons.

Brawn, D., Upton, G., 2008. Estimation of an atmospheric gamma drop size distribution using disdrometer data. Atmospheric Research 87, 66–79. URL: *https://linkinghub.elsevier.com/retrieve/pii/S0169809507001238*, doi:10.1016/j.atmosres.2007.07.006.

Brenier, P., Schertzer, D., Davis, A., Lavalle, D., Lovejoy, S., Wilson, J., 1991. Multifractal dynamics. Video distributed by World Scientific, Singapore .

Bringi, V.N., Chandrasekar, V., Hubbert, J., Gorgucci, E., Randeu, W.L., Schoenhuber, M., 2003. Raindrop size distribution in different climatic regimes from disdrometer and dual-polarized radar analysis. Journal of the Atmospheric Sciences 60, 354 – 365. URL: *https://journals.ametsoc.org/view/journals/atsc/*

60/2/1520-0469_2003_060_0354_rsdidc_2.0.co_2.xml, doi:10.1175/1520-0469(2003)060<0354:RSDIDC>2.0.CO;2.

Brown, L., Foster, G., 1987. storm Erosivity Using Idealized Intensity Distributions. Transactions of the ASAE 30, 0379–0386. URL: *http://elibrary.asabe.org/abstract.asp??JID=3&AID=31957&CID=t1987&v=30&i=2&T=1*, doi:10.13031/2013.31957.

C. McGregor, K., L. Bingner, R., J. Bowie, A., R. Foster, G., 1995. Erosivity Index Values for Northern Mississippi. Transactions of the ASAE 38, 1039–1047. URL: *http://elibrary.asabe.org/abstract.asp?aid=27921&t=3*, doi:10.13031/2013.27921. place: St. Joseph, MI Publisher: ASAE.

Cai, M., Abbasi, E., Arastoopour, H., 2013. Analysis of the Performance of a Wind-Turbine Airfoil under Heavy-Rain Conditions Using a Multiphase Computational Fluid Dynamics Approach. Industrial & Engineering Chemistry Research 52, 3266–3275. URL: *http://dx.doi.org/10.1021/ie300877t*, doi:10.1021/ie300877t.

Cai, Y., Bréon, F.M., 2021. Wind power potential and intermittency issues in the context of climate change. Energy Conversion and Management 240, 114276. URL: *https://www.sciencedirect.com/science/article/pii/S0196890421004520*, doi:https://doi.org/10.1016/j.enconman.2021.114276.

Calif, R., Schmitt, F.G., 2014. Multiscaling and joint multiscaling description of the atmospheric wind speed and the aggregate power output from a wind farm. Nonlinear Processes in Geophysics 21, 379–392. URL: *https://npg.copernicus.org/articles/21/379/2014/*, doi:10.5194/npg-21-379-2014.

Campbell-Scientific-Ltd, 2012. Pws100 present weather sensor, user guide, 2012.

Cao, Q., Zhang, G., 2009. Errors in Estimating Raindrop Size Distribution Parameters Employing Disdrometer and Simulated Raindrop Spectra. Journal of Applied Meteorology and Climatology 48, 406–425. URL: *http://journals.ametsoc.org/doi/10.1175/2008JAMC2026.1*, doi:10.1175/2008JAMC2026.1.

Cao, Q., Zhang, G., Brandes, E., Schuur, T., Ryzhkov, A., Ikeda, K., 2008. Analysis of video disdrometer and polarimetric radar data to characterize rain microphysics in oklahoma. Journal of Applied Meteorology and Climatology 47, 2238 – 2255. URL: *https://journals.ametsoc.org/view/journals/apme/47/8/2008jamc1732.1.xml*, doi:10.1175/2008JAMC1732.1.

Carollo, F.G., Ferro, V., 2015. Modeling Rainfall Erosivity by Measured Drop-Size Distributions. Journal of Hydrologic Engineering 20. URL: *http://ascelibrary.org/doi/10.1061/%28ASCE%29HE.1943-5584.0001077*, doi:10.1061/(ASCE)HE.1943-5584.0001077.

Carter, C.A., 1979. Activation of reovirion-associated poly(A) polymerase and oligomer methylase by cofactor-dependent cleavage of polypeptides. Virology 94, 417–429. URL: *http://www.sciencedirect.com/science/article/pii/0042682279904720*, doi:10.1016/0042-6822(79)90472-0.

Celle-Jeanton, H., Travi, Y., LoÃ¿e-Pilot, M.D., Huneau, F., Bertrand, G., 2009. Rainwater chemistry at a mediterranean inland station (avignon, france): Local contribution versus long-range supply. Atmospheric Research 91, 118–126. URL: *https://www.sciencedirect.com/science/article/pii/S0169809508001634*, doi:https://doi.org/10.1016/j.atmosres.2008.06.003.

Chairani, S., 2022. The correlation between rainfall, temperature, relative humidity, and rice field productivity in aceh besar. IOP Conference Series: Earth and Environmental Science 1071, 012030. URL: *https://dx.doi.org/10.1088/1755-1315/1071/1/012030*, doi:10.1088/1755-1315/1071/1/012030.

Charlson, J., 1969. Atmospheric Visibility Related to Aerosol Mass Concentration A Review , 6.

Chate, D., Pranesha, T., 2004. Field studies of scavenging of aerosols by rain events. Journal of Aerosol Science 35, 695–706. URL: *https://www.sciencedirect.com/science/article/pii/S002185020300483X*, doi:https://doi.org/10.1016/j.jaerosci.2003.09.007.

Cohan, A.C., Arastoopour, H., 2016. Numerical simulation and analysis of the effect of rain and surface property on wind-turbine airfoil performance. International Journal of Multiphase Flow 81, 46–53. URL: *http://www.sciencedirect.com/science/article/pii/S0301932216000069*, doi:10.1016/j.ijmultiphaseflow.2016.01.006.

Connan, O., Maro, D., HÃ©bert, D., Roupsard, P., Goujon, R., Letellier, B., Le Cavelier, S., 2013. Wet and dry deposition of particles associated metals (cd, pb, zn, ni, hg) in a rural wetland site, marais vernier, france. Atmospheric Environment 67, 394–403. URL: *https://www.sciencedirect.com/science/article/pii/S1352231012010916*, doi:https://doi.org/10.1016/j.atmosenv.2012.11.029.

Corrigan, R., Demiglio, R., 1985. Effect of precipitation on wind turbine performance. nasa tm-86986 .

Corten, G.P., Veldkamp, H.F., 2001. Insects can halve wind-turbine power. Nature 412, 41–42. URL: *https://doi.org/10.1038/35083698*, doi:10.1038/35083698.

Cristiano, E., ten Veldhuis, M.c., Van De Giesen, N., 2017. Spatial and temporal variability of rainfall and their effects on hydrological response in urban areas–a review. Hydrology and Earth System Sciences 21, 3859–3878.

Deidda, R., Benzi, R., Siccardi, F., 1999. Multifractal modeling of anomalous scaling laws in rainfall. Water Resources Research 35, 1853–1867. URL: *https://agupubs.onlinelibrary.wiley.com/doi/abs/10.1029/1999WR900036*, doi:10.1029/1999WR900036.

Deog Park, S., Song Lee, K., Sook Shin, S., 2012. Statistical Soil Erosion Model for Burnt Mountain Areas in Korea—RUSLE Approach. Journal of Hydrologic Engineering 17, 292–304. URL: *http://ascelibrary.org/doi/10.1061/%28ASCE%29HE.1943-5584.0000441*, doi:10.1061/(ASCE)HE.1943-5584.0000441.

van Dijk, A., Bruijnzeel, L., Rosewell, C., 2002. Rainfall intensity–kinetic energy relationships: a critical literature appraisal. Journal of Hydrology 261, 1–23. URL: *https://linkinghub.elsevier.com/retrieve/pii/S0022169402000203*, doi:10.1016/S0022-1694(02)00020-3.

DNVGL-RP-0171, 2014. Recommended practice, testing of rotor blade erosion protection systems, edition 2018-02 URL: *http://www.dnvgl.com*.

Duhanyan, N., Roustan, Y., 2011. Below-cloud scavenging by rain of atmospheric gases and particulates. Atmospheric Environment 45, 7201–7217. URL: *https://www.sciencedirect.com/science/article/pii/S1352231011009344*, doi:https://doi.org/10.1016/j.atmosenv.2011.09.002.

Duthon, P., Colomb, M., Bernardin, F., 2019. Light Transmission in Fog: The Influence of Wavelength on the Extinction Coefficient. Applied Sciences 9, 2843. URL: *https://www.mdpi.com/2076-3417/9/14/2843*, doi:10.3390/app9142843.

Elias, T., Haeffelin, M., Drobinski, P., Gomes, L., Rangognio, J., Bergot, T., Chazette, P., Raut, J.C., Colomb, M., 2009. Particulate contribution to extinction of visible radiation: Pollution, haze, and fog. Atmospheric Research 92, 443–454. URL: *https://linkinghub.elsevier.com/retrieve/pii/S0169809509000192*, doi:10.1016/j.atmosres.2009.01.006.

Ellis, R.A., Sandford, A.P., Jones, G.E., Richards, J., Petzing, J., Coupland, J., 2006. New laser technology to determine present weather parameters URL: *https://repository.lboro.ac.uk/articles/New_laser_technology_to_determine_present_weather_parameters/9574658*.

Ellison, W.D., 1944. Ellison: Studies of raindrop erosion - Google Scholar. URL: *https://scholar.google.com/scholar_lookup?title=Studies%20of%20raindrop%20erosion&publication_year=1944&author=W.D.%20Ellison*.

Elminir, H.K., 2005. Dependence of urban air pollutants on meteorology. Science of The Total Environment 350, 225–237. URL: *https://www.sciencedirect.com/science/article/pii/S0048969705000732*, doi:https://doi.org/10.1016/j.scitotenv.2005.01.043.

Emmanouil, S., Langousis, A., Nikolopoulos, E.I., Anagnostou, E.N., 2020. Quantitative assessment of annual maxima, peaks-over-threshold and multifractal parametric approaches in estimating intensity-duration-frequency curves from short rainfall records. Journal of Hydrology 589, 125151. URL: *https://www.sciencedirect.com/science/article/pii/S0022169420306119*, doi:https://doi.org/10.1016/j.jhydrol.2020.125151.

Engie, S., 2022. Offshore wind power is on the rise in france. *https://www.engie.com/en/news/offshore-wind-france*. Accessed: 2023-02-14.

Enne, G., Zanolla, C., Peter, D., 2000. Desertification in europe: Mitigation strategies, land-use planning .

EWEA, 2012. Wind energy's frequently asked questions (faq). URL: *https://www.ewea.org/wind-energy-basics/faq/*.

Feingold, G., Levin, Z., 1986. The Lognormal Fit to Raindrop Spectra from Frontal Convective Clouds in Israel. Journal of Applied Meteorology 25, 1346–1364. URL: *http://adsabs.harvard.edu/abs/1986JApMe..25.1346F*, doi:10.1175/1520-0450(1986)025<1346:TLFTRS>2.0.CO;2.

Fernández-Raga, M., Palencia, C., Keesstra, S., Jordán, A., Fraile, R., Angulo-Martínez, M., Cerdà, A., 2017. Splash erosion: A review with unanswered questions. Earth-Science Reviews 171, 463–477. URL: *http://www.sciencedirect.com/science/article/pii/S0012825217301150*, doi:10.1016/j.earscirev.2017.06.009.

Fitton, G., 2013. Multifractal analysis and simulation of wind energy fluctuations. Theses. Université Paris-Est. URL: *https://pastel.archives-ouvertes.fr/tel-00962318*.

Fitton, G., Tchiguirinskaia, I., Schertzer, D., Lovejoy, S., 2011. Scaling of turbulence in the atmospheric surface-layer: Which anisotropy? Journal of Physics: Conference Series 318, 072008. URL: *https://doi.org/10.1088/1742-6596/318/7/072008*, doi:10.1088/1742-6596/318/7/072008.

Fitton, G., Tchiguirinskaia, I., Schertzer, D., Lovejoy, S., 2014. Torque fluctuations in the framework of a multifractal 23/9-dimensional turbulence model. Journal of Physics: Conference Series 555, 012038. URL: *https://doi.org/10.1088/1742-6596/555/1/012038*, doi:10.1088/1742-6596/555/1/012038.

Fox, N.I., 2004. TECHNICAL NOTE: The representation of rainfall drop-size distribution and kinetic energy. Hydrology and Earth System Sciences 8, 1001–1007. URL: *http://www.hydrol-earth-syst-sci.net/8/1001/2004/*, doi:10.5194/hess-8-1001-2004.

Franzke, C.L., Barbosa, S., Blender, R., Fredriksen, H.B., Laepple, T., Lambert, F., Nilsen, T., Rypdal, K., Rypdal, M., Scotto, M.G., et al., 2020. The structure of climate variability across scales. Reviews of Geophysics 58, e2019RG000657.

Frasson, R.P.d.M., da Cunha, L.K., Krajewski, W.F., 2011. Assessment of the Thies optical disdrometer performance. Atmospheric Research 101, 237–255. URL: *http://www.sciencedirect.com/science/article/pii/S0169809511000639*.

Frisch, U., Sulem, P.L., Nelkin, M., 1978. A simple dynamical model of intermittent fully developed turbulence. Journal of Fluid Mechanics 87, 719–736.

Gago, Á.G., Gires, A., Veers, P., Schertzer, D., Tchiguirinskaia, I., 2022. Transfer of small scales space-time fluctuations of wind fields to wind turbines torque computation. Technical Report. Copernicus Meetings.

Gao, Z., Liu, H., Li, D., Katul, G.G., Blanken, P.D., 2018. Enhanced temperature-humidity similarity caused by entrainment processes with increased wind shear. Journal of Geophysical Research: Atmospheres 123, 4110–4121. URL: *https://agupubs.onlinelibrary.wiley.com/doi/abs/10.1029/2017JD028195*, doi:https://doi.org/10.1029/2017JD028195, arXiv:https://agupubs.onlinelibrary.wiley.com/doi/pdf/10.1029/2017JD028195.

García-Marín, A.P., Jiménez-Hornero, F.J., Ayuso-Muñoz, J.L., 2008. Universal multifractal description of an hourly rainfall time series from a location in southern Spain. Atmósfera 21, 347–355. URL: *http://www.scielo.org.mx/scielo.php?script=sci_abstract&pid=S0187-62362008000400003&lng=es&nrm=iso&tlng=en*.

Gatidis, C., Schleiss, M., Unal, C., Russchenberg, H., 2020. A critical evaluation of the adequacy of the gamma model for representing raindrop size distributions. Journal of Atmospheric and Oceanic Technology 37, 1765 – 1779. URL: *https://journals.ametsoc.org/view/journals/atot/37/10/jtechD190106.xml*, doi:10.1175/JTECH-D-19-0106.1.

Gires, A., 2012. Analyses et simulations multifractales pour une meilleure gestion des eaux pluviales en milieu urbain et péri-urbain. Ph.D. thesis. Université Paris-Est.

Gires, A., Bruley, P., Ruas, A., Schertzer, D., Tchiguirinskaia, I., 2020a. Disdrometer measurements under sense-city rainfall simulator. Earth System Science Data 12, 835–845. URL: *https://essd.copernicus.org/articles/12/835/2020/*, doi:10.5194/essd-12-835-2020.

Gires, A., Jose, J., Tchiguirinskaia, I., Schertzer, D., 2022. Combined high-resolution rainfall and wind data collected for 3 months on a wind farm 110 km southeast of paris (france). Earth System Science Data 14, 3807–3819. URL: *https://essd.copernicus.org/articles/14/3807/2022/*, doi:10.5194/essd-14-3807-2022.

Gires, A., Tchiguirinskaia, I., Schertzer, D., 2017a. Method and device for measuring the equivalent diameter of a water drop. European Patent Office (Application nb. EP3246692) .

Gires, A., Tchiguirinskaia, I., Schertzer, D., 2018. Two months of disdrometer data in the paris area. Earth System Science Data 10, 941–950. URL: *https://www.earth-syst-sci-data.net/10/941/2018/*, doi:10.5194/essd-10-941-2018.

Gires, A., Tchiguirinskaia, I., Schertzer, D., 2020b. Approximate multifractal correlation and products of universal multifractal fields, with application to rainfall data. Nonlinear Processes in Geophysics 27, 133–145. URL: *https://npg.copernicus.org/articles/27/133/2020/*, doi:10.5194/npg-27-133-2020.

Gires, A., Tchiguirinskaia, I., Schertzer, D., Lovejoy, S., 2012. Influence of the zero-rainfall on the assessment of the multifractal parameters. Advances in Water Resources 45, 13–25. URL: *https://www.sciencedirect.com/science/article/pii/S0309170812000814*, doi:https://doi.org/10.1016/j.advwatres.2012.03.026. space-Time Precipitation from Urban Scale to Global Change.

Gires, A., Tchiguirinskaia, I., Schertzer, D., Ochoa-Rodriguez, S., Willems, P., Ichiba, A., Wang, L.P., Pina, R., Van Assel, J., Bruni, G., et al., 2017b. Fractal analysis of urban catchments and their representation in semi-distributed models: imperviousness and sewer system. Hydrology and Earth System Sciences 21, 2361–2375.

Grabner, M., Kvicera, V., 2011. The wavelength dependent model of extinction in fog and haze for free space optical communication. Optics Express 19, 3379. URL: *https://www.osapublishing.org/oe/abstract.cfm?uri=oe-19-4-3379*, doi:10.1364/OE.19.003379.

Greenfield, S.M., 1957. Rain scavenging of radioactive particulate matter from the atmosphere. Journal of Atmospheric Sciences 14, 115–125.

Guezuraga, B., Zauner, R., PÃ¶lz, W., 2012. Life cycle assessment of two different 2Â mw class wind turbines. Renewable Energy 37, 37–44. URL: *https://www.sciencedirect.com/science/article/pii/S0960148111002254*, doi:https://doi.org/10.1016/j.renene.2011.05.008.

Gunn, R., Kinzer, G.D., 1949. THE TERMINAL VELOCITY OF FALL FOR WATER DROPLETS IN STAGNANT AIR. Journal of Meteorology 6, 243–248. URL: *https://doi.org/10.1175/1520-0469(1949)006<0243:TTVOFF>2.0.CO;2*, doi:10.1175/1520-0469(1949)006<0243:TTVOFF>2.0.CO;2.

Gupta, V.K., Waymire, E., 1990. Multiscaling properties of spatial rainfall and river flow distributions. Journal of Geophysical Research: Atmospheres 95, 1999–2009. URL: *https://agupubs.onlinelibrary.wiley.com/doi/abs/10.1029/JD095iD03p01999*, doi:10.1029/JD095iD03p01999.

Gurvich, A., Yaglom, A., 1967. Breakdown of eddies and probability distributions for small-scale turbulence. The Physics of Fluids 10, S59–S65.

Gurvich, A.S., 1960. Measurement of the skewness coefficient for the velocity difference distribution in the bottom layer of the atmosphere, in: Doklady Akademii Nauk, Russian Academy of Sciences. pp. 1073–1075.

Halsey, T.C., Jensen, M.H., Kadanoff, L.P., Procaccia, I., Shraiman, B.I., 1986. Fractal measures and their singularities: The characterization of strange sets. Physical review A 33, 1141.

Hansen, J., Sato, M., Ruedy, R., Lo, K., Lea, D.W., Medina-Elizade, M., 2006. Global temperature change. Proceedings of the National Academy of Sciences 103, 14288–14293. URL: *https://www.pnas.org/doi/abs/10.1073/pnas.0606291103*, doi:10.1073/pnas.0606291103, arXiv:https://www.pnas.org/doi/pdf/10.1073/pnas.0606291103.

Herring, R., Dyer, K., Martin, F., Ward, C., 2019. The increasing importance of leading edge erosion and a review of existing protection solutions. Renewable and Sustainable Energy Reviews 115, 109382. URL: *http://www.sciencedirect.com/science/article/pii/S1364032119305908*, doi:10.1016/j.rser.2019.109382.

Holleman, C., Rembold, F., Crespo, O., Conti, V., 2020. The impact of climate variability and extremes on agriculture and food security-An analysis of the evidence and case studies. Technical Report.

Horvath, H., Noll, K.E., 1969. The relationship between atmospheric light scattering coefficient and visibility. Atmospheric Environment 3, 543–550. doi:10.1016/0004-6981(69)90044-4.

Hou, P., Wu, S., McCarty, J.L., Gao, Y., 2018. Sensitivity of atmospheric aerosol scavenging to precipitation intensity and frequency in the context of global climate change. Atmospheric Chemistry and Physics 18, 8173–8182. URL: *https://acp.copernicus.org/articles/18/8173/2018/*, doi:10.5194/acp-18-8173-2018.

Houze Jr, R.A., 2014. Cloud dynamics. Academic press.

Huang, C., Chen, S., Zhang, A., Pang, Y., 2021. Statistical characteristics of raindrop size distribution in monsoon season over south china sea. Remote Sensing 13. URL: *https://www.mdpi.com/2072-4292/13/15/2878*, doi:10.3390/rs13152878.

Hubert, P., Tessier, Y., Lovejoy, S., Schertzer, D., Schmitt, F., Ladoy, P., Carbonnel, J., Violette, S., Desurosne, I., 1993. Multifractals and extreme rainfall events. Geophysical Research Letters 20, 931–934. URL: *https://hal.inrae.fr/hal-02592049*.

Hudson, N.W., 1971. Soil conservation. Batsford, London.

Hyslop, N.P., 2009. Impaired visibility: the air pollution people see. Atmospheric Environment 43, 182–195. URL: *https://linkinghub.elsevier.com/retrieve/pii/S1352231008009217*, doi:10.1016/j.atmosenv.2008.09.067.

ICAO, 2007. Annex 3 - Meteorological Service for International Air Navigation. URL: *https://store.icao.int/en/annex-3-meteorological-service-for-international-air-navigation*.

IEA, P., 2020. Global energy review 2020. https://www.iea.org/reports/global-energy-review-2020, License: CC BY 4.0 .

Ignaccolo, M., De Michele, C., 2014. Phase space parameterization of rain: The inadequacy of gamma distribution. Journal of Applied Meteorology and Climatology 53, 548–562.

Jaffrain, J., Berne, A., 2012. Quantification of the Small-Scale Spatial Structure of the Raindrop Size Distribution from a Network of Disdrometers. Journal of Applied Meteorology and Climatology 51, 941–953. URL: *https://journals.ametsoc.org/doi/10.1175/JAMC-D-11-0136.1*, doi:10.1175/JAMC-D-11-0136.1.

Johannsen, L.L., Zambon, N., Strauss, P., Dostal, T., Neumann, M., Zumr, D., Cochrane, T.A., BlÃ¶schl, G., Klik, A., 2020. Comparison of three types of laser optical disdrometers under natural rainfall conditions. Hydrological Sciences Journal 65, 524–535. URL: *https://doi.org/10.1080/02626667.2019.1709641*, doi:10.1080/02626667.2019.1709641, arXiv:https://doi.org/10.1080/02626667.2019.1709641. pMID: 32257534.

Johnson, K.E., 2004. Adaptive torque control of variable speed wind turbines. NREL/TP-500-36265 .

Jørgensen, B.H., Holttinen, H., 2022. Iea wind tcp annual report 2021, IEA.

Jose, J., Gires, A., Tchiguirinskaia, I., Roustan, Y., Schertzer, D., 2022. Scale invariant relationship between rainfall kinetic energy and intensity in paris region: An evaluation using universal multifractal framework. Journal of Hydrology 609, 127715. URL: *https://www.sciencedirect.com/science/article/pii/S0022169422002906*, doi:https://doi.org/10.1016/j.jhydrol.2022.127715.

Jung, C., Schindler, D., 2019. The role of air density in wind energy assessment â a case study from germany. Energy 171, 385–392. URL: *https://www.sciencedirect.com/science/article/pii/S036054421930043X*, doi:https://doi.org/10.1016/j.energy.2019.01.041.

Karlen, D., Andrews, S., Weinhold, B., Doran, J., 2003. Soil quality: Humankind's foundation for survival. Journal of Soil and Water Conservation 58, 171–179.

Keegan, M.H., Nash, D.H., Stack, M.M., 2013. On erosion issues associated with the leading edge of wind turbine blades. Journal of Physics D: Applied Physics 46, 383001. URL: *http://stacks.iop.org/0022-3727/46/i=38/a=383001?key=crossref.b21f1d8515962c024d50ce37171c3281*, doi:10.1088/0022-3727/46/38/383001.

Kim, I.I., McArthur, B., Korevaar, E.J., 2001. Comparison of laser beam propagation at 785 nm and 1550 nm in fog and haze for optical wireless communications, Boston, MA. pp. 26–37. URL: *http://proceedings.spiedigitallibrary.org/proceeding.aspx?articleid=895905*, doi:10.1117/12.417512.

Kim, K.W., 2018. The comparison of visibility measurement between image-based visual range, human eye-based visual range, and meteorological optical range. Atmospheric Environment 190, 74–86. URL: *https://linkinghub.elsevier.com/retrieve/pii/S1352231018304679*, doi:10.1016/j.atmosenv.2018.07.020.

Kinnell, P., 1981. Rainfall Intensity-Kinetic Energy Relationships for Soil Loss Prediction1. Soil Science Society of America Journal 45, 153. URL: *https://www.soils.org/publications/sssaj/abstracts/45/1/SS0450010153*, doi:10.2136/sssaj1981.03615995004500010033x.

Kirkby, M.J., Irvine, B.J., Jones, R.J.A., Govers, G., team, P., 2008. The pesera coarse scale erosion model for europe. i. â model rationale and implementation. European Journal of Soil Science 59, 1293–1306. URL: *https://onlinelibrary.wiley.com/doi/abs/10.1111/j.1365-2389.2008.01072.x*, doi:https://doi.org/10.1111/j.1365-2389.2008.01072.x, arXiv:https://onlinelibrary.wiley.com/doi/pdf/10.1111/j.1365-2389.2008.01072.x.

Kolesnikova, V., Monin, A., 1965. Spectra of meteorological field fluctuations(time-space spectral analysis of meteorological fields based on time-dependent spectra of wind velocity, temperature, pressure and turbulent pulse and heat fluxes). ACADEMY OF SCIENCES, USSR, IZVESTIYA, ATMOSPHERIC AND OCEANIC PHYSICS 1, 377–386.

Kolmogorov, A.N., 1941. The local structure of turbulence in incompressible viscous fluid for very large reynolds number, in: Dokl. Akad. Nauk. SSSR, pp. 301–303.

Konwar, M., Das, S.K., Deshpande, S.M., Chakravarty, K., Goswami, B.N., 2014. Microphysics of clouds and rain over the western ghat. Journal of Geophysical Research: Atmospheres 119, 6140–6159. URL: *https://agupubs.onlinelibrary.wiley.com/doi/abs/10.1002/2014JD021606*, doi:https://doi.org/10.1002/2014JD021606, arXiv:https://agupubs.onlinelibrary.wiley.com/doi/pdf/10.1002/2014JD021606.

Koschmieder, H., 1924. Theorie der horizontalen sichtweite. Beitrage zur Physik der freien Atmosphare , 33–53.

Krajewski, W.F., Kruger, A., Caracciolo, C., GolÃ©, P., Barthes, L., Creutin, J.D., Delahaye, J.Y., Nikolopoulos, E.I., Ogden, F., Vinson, J.P., 2006. DEVEX-disdrometer evaluation experiment: Basic results and implications for hydrologic studies. Advances in Water Resources 29, 311–325. URL: *http://www.sciencedirect.com/science/article/pii/S0309170805001272*.

Kruger, A., Krajewski, W.F., 2002. Two-Dimensional Video Disdrometer: A Description. Journal of Atmospheric and Oceanic Technology 19, 602–617. URL: *https://journals.ametsoc.org/doi/full/10.1175/1520-0426%282002%29019%3C0602%3ATDVDAD%3E2.0.CO%3B2*, doi:10.1175/1520-0426(2002)019<0602:TDVDAD>2.0.CO;2.

van Kuik, G.A.M., Peinke, J., Nijssen, R., Lekou, D., Mann, J., Sørensen, J.N., Ferreira, C., van Wingerden, J.W., Schlipf, D., Gebraad, P., Polinder, H., Abrahamsen, A., van Bussel, G.J.W., Sørensen, J.D., Tavner, P., Bottasso, C.L., Muskulus, M., Matha, D., Lindeboom, H.J., Degraer, S., Kramer, O., Lehnhoff, S., Sonnenschein, M., Sørensen, P.E., Künneke, R.W., Morthorst, P.E., Skytte, K., 2016. Long-term research challenges in wind energy – a research agenda by the European Academy of Wind Energy. Wind Energ. Sci. 1, 1–39. URL: *http://www.wind-energ-sci.net/1/1/2016/*, doi:10.5194/wes-1-1-2016.

Kumar, P., Foufoula-Georgiou, E., 1993. A multicomponent decomposition of spatial rainfall fields: 2. Self-similarity in fluctuations. Water Resources Research 29, 2533–2544. URL: *https://agupubs.onlinelibrary.wiley.com/doi/abs/10.1029/93WR00549*, doi:10.1029/93WR00549.

Laakso, L., GrÃ¶nholm, T., Ãllar Rannik, Kosmale, M., Fiedler, V., VehkamÃ€ki, H., Kulmala, M., 2003. Ultrafine particle scavenging coefficients calculated from 6 years field measurements. Atmospheric Environment 37, 3605–3613. URL: *https://www.sciencedirect.com/science/article/pii/S1352231003003261*, doi:https://doi.org/10.1016/S1352-2310(03)00326-1.

Laguionie, P., Maro, D., Letellier, B., Cavelier, S., 2011. Rain scavenging of below-cloud aerosol particles: field measurements using disdrometer and smps; european aerosol conference, eac 2011.

Laguionie, P., Roupsard, P., Maro, D., Solier, L., Rozet, M., HÃ©bert, D., Connan, O., 2014. Simultaneous quantification of the contributions of dry, washout and rainout deposition to the total deposition of particle-bound 7be and 210pb on an urban catchment area on a monthly scale. Journal of Aerosol Science 77, 67–84. URL: *https://www.sciencedirect.com/science/article/pii/S0021850214001165*, doi:https://doi.org/10.1016/j.jaerosci.2014.07.008.

Langousis, A., Veneziano, D., Furcolo, P., Lepore, C., 2009. Multifractal rainfall extremes: Theoretical analysis and practical estimation. Chaos, Solitons Fractals 39, 1182–1194. URL: *https://www.sciencedirect.com/science/article/pii/S0960077907003700*, doi:https://doi.org/10.1016/j.chaos.2007.06.004.

Lavallée, D., Lovejoy, S., Schertzer, D., Ladoy, P., 1993. Nonlinear variability and landscape topography: analysis and simulation. Fractals in geography , 158–192.

Laws, J.O., Parsons, D.A., 1943. The relation of raindrop-size to intensity. Eos, Transactions American Geophysical Union 24, 452–460. URL: *https://agupubs.onlinelibrary.wiley.com/doi/abs/10.1029/TR024i002p00452*, doi:10.1029/TR024i002p00452.

Lee, Z., Shang, S., 2016. Visibility: How Applicable is the Century-Old Koschmieder Model? Journal of the Atmospheric Sciences 73, 4573–4581. URL: *https://journals.ametsoc.org/jas/article/73/11/4573/42768/Visibility-How-Applicable-is-the-CenturyOld*, doi:10.1175/JAS-D-16-0102.1.

Lhermitte, R.M., 1988. Cloud and precipitation remote sensing at 94 ghz. IEEE transactions on geoscience and remote sensing 26, 207–216.

Li, J., Li, S., Wu, F., 2020. Research on carbon emission reduction benefit of wind power project based on life cycle assessment theory. Renewable Energy 155, 456–468. URL: *https://www.sciencedirect.com/science/article/pii/S0960148120304651*, doi:https://doi.org/10.1016/j.renene.2020.03.133.

Liersch, J., Michael, J., 2014. Investigation of the impact of rain and particle erosion on rotor blade aerodynamics with an erosion test facility to enhancing the rotor blade performance and durability. Journal of Physics: Conference Series 524, 012023. URL: *http://stacks.iop.org/1742-6596/524/i=1/a=012023?key=crossref.010c71a204a1e683cb616b2c527d4c05*, doi:10.1088/1742-6596/524/1/012023.

Lovejoy, S., 2015. A voyage through scales, a missing quadrillion and why the climate is not what you expect. Climate Dynamics 44, 3187–3210. URL: *https://doi.org/10.1007/s00382-014-2324-0*, doi:10.1007/s00382-014-2324-0.

Lovejoy, S., Pinel, J., Schertzer, D., 2012. The global space–time cascade structure of precipitation: Satellites, gridded gauges and reanalyses. Advances in Water Resources 45, 37–50. URL: *https://www.sciencedirect.com/science/article/pii/S0309170812000796*, doi:https://doi.org/10.1016/j.advwatres.2012.03.024. space-Time Precipitation from Urban Scale to Global Change.

Lovejoy, S., Schertzer, D., 1985. Generalized scale invariance in the atmosphere and fractal models of rain. Water Resources Research 21, 1233–1250. URL: *https://agupubs.onlinelibrary.wiley.com/doi/abs/10.1029/WR021i008p01233*, doi:https://doi.org/10.1029/WR021i008p01233, arXiv:https://agupubs.onlinelibrary.wiley.com/doi/pdf/10.1029/WR021i008p01233.

Lovejoy, S., Schertzer, D., 1991. Multifractal Analysis Techniques and the Rain and Cloud Fields from 10â3 to 106m. Springer Netherlands, Dordrecht. pp. 111–144. URL: *https://doi.org/10.1007/978-94-009-2147-4_8*, doi:10.1007/978-94-009-2147-4_8.

Lovejoy, S., Schertzer, D., 2007a. Scale, scaling and multifractals in geophysics: twenty years on. Nonlinear dynamics in geosciences , 311–337.

Lovejoy, S., Schertzer, D., 2007b. Scaling and multifractal fields in the solid earth and topography. Nonlinear Processes in Geophysics 14, 465–502. URL: *https://npg.copernicus.org/articles/14/465/2007/*, doi:10.5194/npg-14-465-2007.

Lovejoy, S., Schertzer, D., 2013. The Weather and Climate: Emergent Laws and Multifractal Cascades. Cambridge University Press. doi:10.1017/CBO9781139093811.

Lovejoy, S., Schertzer, D., Allaire, V.C., 2008. The remarkable wide range spatial scaling of TRMM precipitation. Atmospheric Research 90, 10–32. URL: *https://hal-enpc.archives-ouvertes.fr/hal-00711539*, doi:10.1016/j.atmosres.2008.02.016.

Loveland, R.B., Lindberg, J.D., 1988. Problems in comparing particulate spectrometer and visibility meter data. Applied Optics 27, 4318. URL: *https://www.osapublishing.org/abstract.cfm?URI=ao-27-20-4318*, doi:10.1364/AO.27.004318.

Majewski, G., Rogula-Kozłowska, W., Czechowski, P., Badyda, A., Brandyk, A., 2015. The Impact of Selected Parameters on Visibility: First Results from a Long-Term Campaign in Warsaw, Poland. Atmosphere 6, 1154–1174. URL: *http://www.mdpi.com/2073-4433/6/8/1154*, doi:10.3390/atmos6081154.

Malm, W.C., 2016. Chapter 2 - On the Nature of Light and Its Interaction with Atmospheric Particles, in: Malm, W.C. (Ed.), Visibility. Elsevier, pp. 29 – 72. URL: *http://www.sciencedirect.com/science/article/pii/B9780128044506000024*, doi:10.1016/B978-0-12-804450-6.00002-4.

Mandelbrot, B., 1967. How long is the coast of britain? statistical self-similarity and fractional dimension. science 156, 636–638.

Mandelbrot, B., 1977. Fractals: Form, Chance, and Dimension. W. H. Freeman, 1977.

Mandelbrot, B.B., 1974. Intermittent turbulence in self-similar cascades: divergence of high moments and dimension of the carrier. Journal of fluid Mechanics 62, 331–358.

Mandelbrot, B.B., Mandelbrot, B.B., 1982. The fractal geometry of nature. volume 1. WH freeman New York.

Manwell, J.F., McGowan, J.G., Rogers, A.L., 2010. Wind energy explained: theory, design and application. John Wiley & Sons.

Marsan, D., Schertzer, D., Lovejoy, S., 1996. Causal space-time multifractal processes: Predictability and forecasting of rain fields. Journal of Geophysical Research: Atmospheres 101, 26333–26346. URL: *https://agupubs.onlinelibrary.wiley.com/doi/abs/10.1029/96JD01840*, doi:https://doi.org/10.1029/96JD01840, arXiv:https://agupubs.onlinelibrary.wiley.com/doi/pdf/10.1029/96JD01840.

Marshall, J.S., Palmer, W.M.K., 1948. The distribution of raindrops with size. Journal of Meteorology 5, 165–166. URL: *https://journals.ametsoc.org/doi/abs/10.1175/1520-0469%281948%29005%3C0165%3ATDORWS%3E2.0.CO%3B2*, doi:10.1175/1520-0469(1948)005<0165:TDORWS>2.0.CO;2.

Marzano, F.S., Cimini, D., Montopoli, M., 2010. Investigating precipitation microphysics using ground-based microwave remote sensors and disdrometer data. Atmospheric Research 97, 583–600. URL: *https://www.sciencedirect.com/science/article/pii/S0169809510000682*, doi:https://doi.org/10.1016/

j.atmosres.2010.03.019. from the Lab to Models and Global Observations: Hans R. Pruppacher and Cloud Physics.

Masson-Delmotte, V., Zhai, P., Pirani, A., Connors, S.L., Péan, C., Berger, S., Caud, N., Chen, Y., Goldfarb, L., Gomis, M., et al., 2021. Climate change 2021: the physical science basis. Contribution of working group I to the sixth assessment report of the intergovernmental panel on climate change 2.

McMurry, P.H., 2000. A review of atmospheric aerosol measurements. Atmospheric Environment 34, 1959–1999. URL: *https://www.sciencedirect.com/science/article/pii/S1352231099004550*, doi:https://doi.org/10.1016/S1352-2310(99)00455-0.

Mei, L., Guan, P., Yang, Y., Kong, Z., 2017. Atmospheric extinction coefficient retrieval and validation for the single-band Mie-scattering Scheimpflug lidar technique. Optics Express 25, A628. URL: *https://www.osapublishing.org/abstract.cfm?URI=oe-25-16-A628*, doi:10.1364/OE.25.00A628.

Meneveau, C., Sreenivasan, K.R., Kailasnath, P., Fan, M.S., 1990. Joint multifractal measures: Theory and applications to turbulence. Phys. Rev. A 41, 894–913. URL: *https://link.aps.org/doi/10.1103/PhysRevA.41.894*, doi:10.1103/PhysRevA.41.894.

Mineo, C., Ridolfi, E., Moccia, B., Russo, F., Napolitano, F., 2019. Assessment of Rainfall Kinetic-Energy–Intensity Relationships. Water 11, 1994. URL: *https://www.mdpi.com/2073-4441/11/10/1994*, doi:10.3390/w11101994.

Miriovsky, B.J., Bradley, A.A., Eichinger, W.E., Krajewski, W.F., Kruger, A., Nelson, B.R., Creutin, J.D., Lapetite, J.M., Lee, G.W., Zawadzki, I., Ogden, F.L., 2004. An Experimental Study of Small-Scale Variability of Radar Reflectivity Using Disdrometer Observations. Journal of Applied Meteorology 43, 106–118. URL: *http://dx.doi.org/10.1175/1520-0450(2004)043<0106:AESOSV>2.0.CO;2*.

Mitchell, J., 1976. An overview of climatic variability and its causal mechanisms. Quaternary Research 6, 481–493. URL: *https://www.sciencedirect.com/science/article/pii/0033589476900211*, doi:https://doi.org/10.1016/0033-5894(76)90021-1.

Mohamadi, M.A., Kavian, A., 2015. Effects of rainfall patterns on runoff and soil erosion in field plots. International Soil and Water Conservation Research 3, 273–281. URL: *https://www.sciencedirect.com/science/article/pii/S209563391530071X*, doi:https://doi.org/10.1016/j.iswcr.2015.10.001.

Morgan, R.P.C., Quinton, J.N., Smith, R.E., Govers, G., Poesen, J.W.A., Auerswald, K., Chisci, G., Torri, D., Styczen, M.E., 1998. The European Soil Erosion Model (EUROSEM): a dynamic approach for predicting sediment transport from fields and small catchments. Earth Surface Processes and Landforms 23, 527–544. URL: *https://onlinelibrary.wiley.com/doi/abs/10.1002/%28SICI%291096-9837%28199806%2923%3A6%3C527%3A%3AAID-ESP868%3E3.0.CO%3B2-5*, doi:10.1002/(SICI)1096-9837(199806)23:6<527::AID-ESP868>3.0.CO;2-5.

Nebuloni, R., 2005. Empirical relationships between extinction coefficient and visibility in fog. Applied Optics 44, 3795. URL: *https://www.osapublishing.org/abstract.cfm?URI=ao-44-18-3795*, doi:10.1364/AO.44.003795.

Novikov, E., Stewart, R., 1964. The intermittency of turbulence and the spectrum of energy dissipation fluctuations. Izv. Geophys. Ser 3, 408–413.

Obligado, M., Cal, R.B., Brun, C., 2021. Wind turbine wake influence on the mixing of relative humidity quantified through wind tunnel experiments. Journal of Renewable and Sustainable Energy 13, 023308.

Oboukhov, A.M., 1962. Some specific features of atmospheric tubulence. Journal of Fluid Mechanics 13, 77–81.

Obukhov, A., 1941. Spectral energy distribution in a turbulent flow. Izv. Akad. Nauk. SSSR. Ser. Geogr. i. Geofiz 5, 453–466.

Olsson, J., Niemczynowicz, J., 1996. Multifractal analysis of daily spatial rainfall distributions. Journal of Hydrology 187, 29–43. URL: *http://www.sciencedirect.com/science/article/pii/S0022169496030855*, doi:10.1016/S0022-1694(96)03085-5.

OTT, 2014. Operating instructions, Present Weather Sensor OTT Parsivel2 .

Parisi, G., Frisch, U., 1985. On the singularity structure of fully developed turbulence in Turbulence and predictability in geophysical fluid dynamics and climate dynamics. Turbulence and Predictability of Geophysical Flows and Climate Dynamics 88.

Parisi, G., Frisch, U., et al., 1985. A multifractal model of intermittency. Turbulence and predictability in geophysical fluid dynamics and climate dynamics , 84–88.

Park, S., Mitchell, J., Bubenzer, G., 1982. Splash erosion modelling: physical analyses [Impact of water drops on soil]. Transactions of the ASAE [American Society of Agricultural Engineers] URL: *http://agris.fao.org/agris-search/search.do?recordID=US19830881711*.

Petan, S., Rusjan, S., Vidmar, A., Mikoš, M., 2010. The rainfall kinetic energy–intensity relationship for rainfall erosivity estimation in the mediterranean part of Slovenia. Journal of Hydrology 391, 314 – 321. URL: *http://www.sciencedirect.com/science/article/pii/S0022169410004695*, doi:https://doi.org/10.1016/j.jhydrol.2010.07.031.

Picard, A., Davis, R.S., GlÃ€ser, M., Fujii, K., 2008. Revised formula for the density of moist air (cipm-2007). Metrologia 45, 149. URL: *https://dx.doi.org/10.1088/0026-1394/45/2/004*, doi:10.1088/0026-1394/45/2/004.

Pimentel, D., 2006. Soil Erosion: A Food and Environmental Threat. Environment, Development and Sustainability 8, 119–137. URL: *https://doi.org/10.1007/s10668-005-1262-8*, doi:10.1007/s10668-005-1262-8.

Pond, S., Stewart, R., Burling, R., 1963. Turbulence spectra in the wind over waves. Journal of the Atmospheric Sciences 20, 319–324.

Pruppacher, H., Klett, J., 1996. Microphysics of Clouds and Precipitation. Atmospheric and Oceanographic Sciences Library, Springer Netherlands. URL: *https://books.google.fr/books?id=1mXN_qZ5sNUC*.

Pöschl, U., 2005. Atmospheric aerosols: Composition, transformation, climate and health effects. Angewandte Chemie International Edition 44, 7520–7540. URL: *https://onlinelibrary.wiley.com/doi/abs/10.1002/anie.200501122*, doi:https://doi.org/10.1002/anie.200501122, arXiv:https://onlinelibrary.wiley.com/doi/pdf/10.1002/anie.200501122.

Quérel, A., Monier, M., Flossmann, A.I., Lemaitre, P., Porcheron, E., 2014. The importance of new collection efficiency values including the effect of rear capture for the below-cloud scavenging of aerosol particles. Atmospheric Research 142, 57–66. URL: *https://www.sciencedirect.com/science/article/pii/S0169809513001877*, doi:https://doi.org/10.1016/j.atmosres.2013.06.008. the 16th International Conference on Clouds and Precipitation.

Renard, K.G., Agricultural Research Service, W., Foster, G.R., Weesies, G.A., McCool, D.K., Yoder, D.C., 1997. Predicting soil erosion by water: a guide to conservation planning with the Revised Universal Soil Loss Equation (RUSLE) URL: *http://agris.fao.org/agris-search/search.do?recordID=XF2015047686*.

Richardson, L.F., 1920. The supply of energy from and to atmospheric eddies. Proceedings of the Royal Society of London. Series A, Containing Papers of a Mathematical and Physical Character 97, 354–373.

Richardson, L.F., 1961. The problem of contiguity: an appendix to statistics of deadly quarrels. General systems yearbook 6, 139–187.

Roy, A., Chatterjee, A., Ghosh, A., Das, S.K., Ghosh, S.K., Raha, S., 2019. Below-cloud scavenging of size-segregated aerosols and its effect on rainwater acidity and nutrient deposition: A long-term (2009â2018) and real-time observation over eastern himalaya. Science of The Total Environment 674, 223–233. URL: *https://www.sciencedirect.com/science/article/pii/S0048969719316948*, doi:https://doi.org/10.1016/j.scitotenv.2019.04.165.

Sabetghadam, S., Khoshsima, M., Ahmadi-Givi, F., 2017. Effects of cloud and humidity on atmospheric extinction coefficient derived from visual range observations in Iranian major airports: EFFECTS OF CLOUD AND HUMIDITY ON ATMOSPHERIC EXTINCTION COEFFICIENT. International Journal of Climatology 37, 1474–1482. URL: *http://doi.wiley.com/10.1002/joc.4791*, doi:10.1002/joc.4791.

Sachs, J., Kroll, C., Lafortune, G., Fuller, G., Woelm, F., 2022. Sustainable development report 2022. Cambridge University Press.

Salles, C., Poesen, J., Sempere-Torres, D., 2002. Kinetic energy of rain and its functional relationship with intensity. Journal of Hydrology 257, 256–270. URL: *https://linkinghub.elsevier.com/retrieve/pii/S0022169401005558*, doi:10.1016/S0022-1694(01)00555-8.

Schertzer, D., Lovejoy, S., 1984. On the dimension of atmospheric motions. volume 505. Elsevier, North-Holland, Amsterdam.

Schertzer, D., Lovejoy, S., 1985. The dimension and intermittency of atmospheric dynamics, in: Turbulent Shear Flows 4: Selected Papers from the Fourth International Symposium on Turbulent Shear Flows, University of Karlsruhe, Karlsruhe, FRG, September 12–14, 1983, Springer. pp. 7–33.

Schertzer, D., Lovejoy, S., 1987. Physical modeling and analysis of rain and clouds by anisotropic scaling multiplicative processes. Journal of Geophysical Research: Atmospheres 92, 9693–9714. URL: *https://agupubs.onlinelibrary.wiley.com/doi/abs/10.1029/JD092iD08p09693*, doi:10.1029/JD092iD08p09693.

Schertzer, D., Lovejoy, S., 1988. Multifractal simulations and analysis of clouds by multiplicative processes. Atmospheric Research 21, 337–361. URL: *http://www.sciencedirect.com/science/article/pii/016980958890035X*, doi:10.1016/0169-8095(88)90035-X.

Schertzer, D., Lovejoy, S., 1989. Nonlinear Variability in Geophysics: Multifractal Simulations and Analysis. Springer US, Boston, MA. pp. 49–79. URL: *https://doi.org/10.1007/978-1-4899-3499-4_3*, doi:10.1007/978-1-4899-3499-4_3.

Schertzer, D., Lovejoy, S., 1992. Hard and soft multifractal processes. Physica A: Statistical Mechanics and its Applications 185, 187–194. URL: *https://www.sciencedirect.com/science/article/pii/037843719290455Y*, doi:https://doi.org/10.1016/0378-4371(92)90455-Y.

Schertzer, D., Lovejoy, S., 1993. Nonlinear Variability in Geophysics 3 (NVAG3): Scaling and Multifractal Processes, Institut D'études Scientifiques de Cargèse, September 10-17, 1993. Institut d'études scientifiques de Cargèse.

Schertzer, D., Lovejoy, S., 1997. Universal multifractals do exist!: Comments on âa statistical analysis of mesoscale rainfall as a random cascadeâ. Journal of Applied Meteorology 36, 1296 – 1303. URL: *https://journals.ametsoc.org/view/journals/apme/36/9/1520-0450_1997_036_1296_umdeco_2.0.co_2.xml*, doi:10.1175/1520-0450(1997)036<1296:UMDECO>2.0.CO;2.

Schertzer, D., Lovejoy, S., 2011. MULTIFRACTALS, GENERALIZED SCALE INVARIANCE AND COMPLEXITY IN GEOPHYSICS. International Journal of Bifurcation and Chaos 21, 3417–3456. URL: *https://www.worldscientific.com/doi/abs/10.1142/S0218127411030647*, doi:10.1142/S0218127411030647.

Schertzer, D., Tchiguirinskaia, I., 2020. A century of turbulent cascades and the emergence of multifractal operators. Earth and Space Science 7, e2019EA000608. URL: *https://agupubs.onlinelibrary.wiley.com/doi/abs/10.1029/2019EA000608*, doi:10.1029/2019EA000608, arXiv:https://agupubs.onlinelibrary.wiley.com/doi/pdf/10.1029/2019EA000608. e2019EA000608 10.1029/2019EA000608.

Schertzer, D., Tchiguirinskaia, I., Lovejoy, S., Hubert, P., 2010. No monsters, no miracles: in nonlinear sciences hydrology is not an outlier! Hydrological Sciences Journal–Journal des Sciences Hydrologiques 55, 965–979.

Seinfeld, J.H., Pandis, S.N., 2016. Atmospheric chemistry and physics: from air pollution to climate change. John Wiley & Sons.

Sempere-Torres, D., Porrà, J.M., Creutin, J.D., 1998. Experimental evidence of a general description for raindrop size distribution properties. Journal of Geophysical Research: Atmospheres 103, 1785–1797. URL: *http://doi.wiley.com/10.1029/97JD02065*, doi:10.1029/97JD02065.

Seuront, L., Schmitt, F.G., 2005a. Multiscaling statistical procedures for the exploration of biophysical couplings in intermittent turbulence. part i. theory. Deep Sea Research Part II: Topical Studies in Oceanography 52, 1308–1324. URL: *https://www.sciencedirect.com/science/article/pii/S0967064505000470*, doi:https://doi.org/10.1016/j.dsr2.2005.01.006. observations and modelling of mixed layer turbulence: Do they represent the same statistical quantities?

Seuront, L., Schmitt, F.G., 2005b. Multiscaling statistical procedures for the exploration of biophysical couplings in intermittent turbulence. part ii. applications. Deep Sea Research Part II: Topical Studies in Oceanography 52, 1325–1343. URL: *https://www.sciencedirect.com/science/article/pii/S09670645050*

00482, doi:https://doi.org/10.1016/j.dsr2.2005.01.005. observations and modelling of mixed layer turbulence: Do they represent the same statistical quantities?

Seuront, L., Yamazaki, H., Schmitt, F., 2005. Intermittency. Marine turbulence: Theories, observations and models , 66–78.

Shah, S., Mughal, S., Memon, S., 2015. Theoretical and empirical based extinction coefficients for fog attenuation in terms of visibility at 850 nm, in: 2015 International Conference on Emerging Technologies (ICET), IEEE, Peshawar, Pakistan. pp. 1–4. URL: *http://ieeexplore.ieee.org/document/7389190/*, doi:10.1109/ICET.2015.7389190.

Sheng-Jie, J., Da-Ren, L., . Optimal Forward-Scattering Angles of Atmospheric Aerosols in North China , 8.

Shin, S.S., Park, S.D., Choi, B.K., 2016. Universal Power Law for Relationship between Rainfall Kinetic Energy and Rainfall Intensity. URL: *https://www.hindawi.com/journals/amete/2016/2494681/*, doi:https://doi.org/10.1155/2016/2494681.

Shojaei, S., Kalantari, Z., Rodrigo-Comino, J., 2020. Prediction of factors affecting activation of soil erosion by mathematical modeling at pedon scale under laboratory conditions. Scientific Reports 10, 20163. URL: *https://doi.org/10.1038/s41598-020-76926-1*, doi:10.1038/s41598-020-76926-1.

Sinha, A., Kathayat, G., Cheng, H., Breitenbach, S.F., Berkelhammer, M., Mudelsee, M., Biswas, J., Edwards, R., 2015. Trends and oscillations in the indian summer monsoon rainfall over the last two millennia. Nature communications 6, 6309.

Smith, D.D., Wischmeier, W.H., 1962. Rainfall Erosion, in: Norman, A.G. (Ed.), Advances in Agronomy. Academic Press. volume 14, pp. 109–148. URL: *http://www.sciencedirect.com/science/article/pii/S006521130860437X*, doi:10.1016/S0065-2113(08)60437-X.

Smith, J.A., De Veaux, R.D., 1992. The temporal and spatial variability of rainfall power. Environmetrics 3, 29–53. URL: *https://onlinelibrary.wiley.com/doi/abs/10.1002/env.3170030103*, doi:10.1002/env.3170030103, arXiv:https://onlinelibrary.wiley.com/doi/pdf/10.1002/env.3170030103.

Smith, P.L., Kliche, D.V., Johnson, R.W., 2009. The Bias and Error in Moment Estimators for Parameters of Drop Size Distribution Functions: Sampling from Gamma Distributions. Journal of Applied Meteorology and Climatology 48, 2118–2126. URL: *http://journals.ametsoc.org/doi/10.1175/2009JAMC2114.1*, doi:10.1175/2009JAMC2114.1.

Smith, S.E., Travis, K.N., Djeridi, H., Obligado, M., Cal, R.B., 2021. Dynamic effects of inertial particles on the wake recovery of a model wind turbine. Renewable Energy 164, 346–361. URL: *https://www.sciencedirect.com/science/article/pii/S0960148120314579*, doi:https://doi.org/10.1016/j.renene.2020.09.037.

Steiner, M., Smith, J.A., 2000. Reflectivity, Rain Rate, and Kinetic Energy Flux Relationships Based on Raindrop Spectra. JOURNAL OF APPLIED METEOROLOGY 39, 18.

Sylos Labini, F., Pietronero, L., 1996. Statistical properties of galaxy distributions. Nonlinear Processes in Geophysics 3, 274–283. URL: *https://npg.copernicus.org/articles/3/274/1996/*, doi:10.5194/npg-3-274-1996.

Tamai, K., 2016. Big whorls, little whorls. Nature Physics 12, 197–197. URL: *https://doi.org/10.1038/nphys3697*, doi:10.1038/nphys3697.

Tang, I.N., 1996. Chemical and size effects of hygroscopic aerosols on light scattering coefficients. Journal of Geophysical Research: Atmospheres 101, 19245–19250. URL: *http://doi.wiley.com/10.1029/96JD03003*, doi:10.1029/96JD03003.

Tessier, Y., Lovejoy, S., Schertzer, D., 1993. Universal multifractals: Theory and observations for rain and clouds. Journal of Applied Meteorology and Climatology 32, 223 – 250. URL: *https://journals.ametsoc.org/view/journals/apme/32/2/1520-0450_1993_032_0223_umtaof_2_0_co_2.xml*, doi:10.1175/1520-0450(1993)032<0223:UMTAOF>2.0.CO;2.

Testud, J., 2001. The Concept of "Normalized" Distribution to Describe Raindrop Spectra: A Tool for Cloud Physics and Cloud Remote Sensing. JOURNAL OF APPLIED METEOROLOGY 40, 23.

ThiesCLIMA, 2013a. 3d ultrasonic anemometer, instructions for use .

ThiesCLIMA, 2013b. Clima sensor us, instructions for use .

Thurai, M., Bringi, V.N., 2005. Drop Axis Ratios from a 2D Video Disdrometer. Journal of Atmospheric and Oceanic Technology 22, 966–978. URL: *https://journals.ametsoc.org/doi/full/10.1175/JTECH1767.1*, doi:10.1175/JTECH1767.1.

Thurai, M., Peterson, W.A., Tokay, A., Schutz, C., Gatlin, P., 2011. Drop size distribution comparisons between Parsivel and 2-D video disdrometers. Advances in Geosciences 30, 3–9.

Tokay, A., Short, D.A., 1996. Evidence from Tropical Raindrop Spectra of the Origin of Rain from Stratiform versus Convective Clouds. Journal of Applied Meteorology 35, 355–371. URL: *https://journals.ametsoc.org/doi/abs/10.1175/1520-0450%281996%29035%3C0355%3AEFTRSO%3E2.0.CO%3B2*, doi:10.1175/1520-0450(1996)035<0355:EFTRSO>2.0.CO;2.

Torres, D.S., Porrà, J.M., Creutin, J.D., 1994. A General Formulation for Raindrop Size Distribution. Journal of Applied Meteorology 33, 1494–1502. URL: *https://journals.ametsoc.org/doi/abs/10.1175/1520-0450%281994%29033%3C1494%3AAGFFRS%3E2.0.CO%3B2*, doi:10.1175/1520-0450(1994)033<1494:AGFFRS>2.0.CO;2.

Uhlig, E.M., von Hoyningen-Huene, W., 1993. Correlation of the atmospheric extinction coefficient with the concentration of particulate matter for measurements in a polluted urban area. Atmospheric Research 30, 181–195. URL: *https://linkinghub.elsevier.com/retrieve/pii/016980959390022G*, doi:10.1016/0169-8095(93)90022-G.

Uijlenhoet, R., 2001. Raindrop size distributions and radar reflectivity–rain rate relationships for radar hydrology. Hydrology and Earth System Sciences 5, 615–628. URL: *https://www.hydrol-earth-syst-sci.net/5/615/2001/*, doi:https://doi.org/10.5194/hess-5-615-2001.

Uijlenhoet, R., Stricker, J., 1999. A consistent rainfall parameterization based on the exponential raindrop size distribution. Journal of Hydrology 218, 101–127. URL: *https://linkinghub.elsevier.com/retrieve/pii/S0022169499000323*, doi:10.1016/S0022-1694(99)00032-3.

Ulazia, A., Gonzalez-Rojí, S.J., Ibarra-Berastegi, G., Carreno-Madinabeitia, S., Sáenz, J., Nafarrate, A., 2018. Seasonal air density variations over the east of scotland and the consequences for offshore wind energy, in: 2018 7th International Conference on Renewable Energy Research and Applications (ICRERA), pp. 261–265. doi:10.1109/ICRERA.2018.8566716.

Ulbrich, C.W., 1983. Natural Variations in the Analytical Form of the Raindrop Size Distribution. Journal of Climate and Applied Meteorology 22, 1764–1775. URL: *https://journals.ametsoc.org/doi/abs/10.1175/1520-0450%281983%29022%3C1764%3ANVITAF%3E2.0.CO%3B2*, doi:10.1175/1520-0450(1983)022<1764:NVITAF>2.0.CO;2.

UN, 2019. World urbanization prospects: The 2018 Revision (ST/ESA/SER.A/420). United Nations and Department of Economic and Social Affairs and Population Division, United Nations New York.

UN, 2022. Un-energy plan of action towards 2025. https://un-energy.org/wp-content/uploads/2022/05/UN-Energy-Plan-of-Action-towards-2025-2May2022.pdf .

Van Oost, K., Govers, G., Desmet, P., 2000. Evaluating the effects of changes in landscape structure on soil erosion by water and tillage. Landscape Ecology 15, 577–589. URL: *https://doi.org/10.1023/A:1008198215674*, doi:10.1023/A:1008198215674.

Vassoler, R., Zebende, G., 2012. Dcca cross-correlation coefficient apply in time series of air temperature and air relative humidity. Physica A: Statistical Mechanics and its Applications 391, 2438–2443. URL: *https://www.sciencedirect.com/science/article/pii/S0378437111009125*, doi:https://doi.org/10.1016/j.physa.2011.12.015.

Vestas Wind Systems A/S, V., 2023. V90-2.0 mw™ iec iia/iec s turbines. URL: *https://www.vestas.com/en/products/2-mw-platform/V90-2-0-MW*.

Waas, S., 2008. Field test of forward scatter visibility sensors at german airports, in: WMO Technical Conference on Instruments and Methods of Observation (TECO-2006), pp. 1–17.

Weichel, H., 1990. Laser Beam Propagation in the Atmosphere | (1990) | Weichel | Publications | Spie. volume TT03. SPIE, Bellingham WA. URL: *https://spie.org/Publications/Book/3993?print=2&SSO=1*.

Wilken, F., Baur, M., Sommer, M., Deumlich, D., Bens, O., Fiener, P., 2018. Uncertainties in rainfall kinetic energy-intensity relations for soil erosion modelling. CATENA 171, 234–244. URL: *https://linkinghub.elsevier.com/retrieve/pii/S034181621830273X*, doi:10.1016/j.catena.2018.07.002.

Willebrand, H., Ghuman, B.S., 2002. Free space optics: enabling optical connectivity in today's networks. SAMS publishing.

Williams, P.D., Alexander, M.J., Barnes, E.A., Butler, A.H., Davies, H.C., Garfinkel, C.I., Kushnir, Y., Lane, T.P., Lundquist, J.K., Martius, O., Maue, R.N., Peltier, W.R., Sato, K., Scaife, A.A., Zhang, C., 2017. A census of atmospheric variability from seconds to decades. Geophysical Research Letters 44, 11,201–11,211. URL: *https://agupubs.onlinelibrary.wiley.com/doi/abs/10.1002/2017GL075483*, doi:https://doi.org/10.1002/2017GL075483, arXiv:https://agupubs.onlinelibrary.wiley.com/doi/pdf/10.1002/2017GL075483.

Wiser, R., Yang, Z., Hand, M., Hohmeyer, O., Infield, D., Jensen, P., Nikolaev, V., O'Malley, M., Zervos, G., 2011. Ipcc special report on renewable energy sources and climate change mitigation: Wind energy. IPCC, Cambridge, UK and New York, NY, USA, Tech. Rep .

WMO, et al., 2022. Provisional state of the global climate in 2022 .

WMO-No. 8, t.C.G., 2018. Guide to Instruments and Methods of Observation. WMO, World Meteorological Organization, Geneva.

Wolfensberger, D., Gires, A., Tchiguirinskaia, I., Schertzer, D., Berne, A., 2017. Multifractal evaluation of simulated precipitation intensities from the COSMO NWP model. Atmospheric Chemistry and Physics 17, 14253–14273. URL: *https://www.atmos-chem-phys.net/17/14253/2017/*, doi:10.5194/acp-17-14253-2017.

WWA, 2019. Human contribution to record-breaking June 2019 heatwave in France, howpublished = *https://www.worldweatherattribution.org/human-contribution-to-record-breaking-june-2019-heatwave-in-france/*, note = Accessed: 2023-02-20.

Yaglom, A., 1966. The influence of fluctuations in energy dissipation on the shape of turbulence characteristics in the inertial interval, in: Sov. Phys. Dokl., pp. 26–29.

Zebende, G., Brito, A., Silva Filho, A., Castro, A., 2018. dcca applied between air temperature and relative humidity: An hour/hour view. Physica A: Statistical Mechanics and its Applications 494, 17–26. URL: *https://www.sciencedirect.com/science/article/pii/S0378437117312748*, doi:https://doi.org/10.1016/j.physa.2017.12.023.

Zhang, L., Wang, X., Moran, M.D., Feng, J., 2013. Review and uncertainty assessment of size-resolved scavenging coefficient formulations for below-cloud snow scavenging of atmospheric aerosols. Atmospheric Chemistry and Physics 13, 10005–10025. URL: *https://acp.copernicus.org/articles/13/10005/2013/*, doi:10.5194/acp-13-10005-2013.

Zieger, P., Fierz-Schmidhauser, R., Weingartner, E., Baltensperger, U., 2013. Effects of relative humidity on aerosol light scattering: results from different European sites. Atmospheric Chemistry and Physics 13, 10609–10631. URL: *https://acp.copernicus.org/articles/13/10609/2013/*, doi:10.5194/acp-13-10609-2013.

Appendix A.

Appendix A.1. Method of moments (formulation of moment estimators)

Gamma distribution parameters were estimated from second, fourth and sixth moments using following relations:

M234:

$$D_m = M_4/M_3 \tag{A.1}$$

$$\eta = \frac{(M_3^2)}{(M_2 M_4)} \tag{A.2}$$

$$\mu = \frac{1}{(1-\eta-1)} - 4 \tag{A.3}$$

$$\Lambda = \frac{M_2}{M_3}(\mu+3) \tag{A.4}$$

$$N_0 = \frac{M_2 \Lambda^{(\mu+3)}}{\Gamma(\mu+4)} \tag{A.5}$$

Appendix A.2. Multifractal and DSD parameters

UM parameters: event based analysis from 2013 to 2015 (in section 2.1)

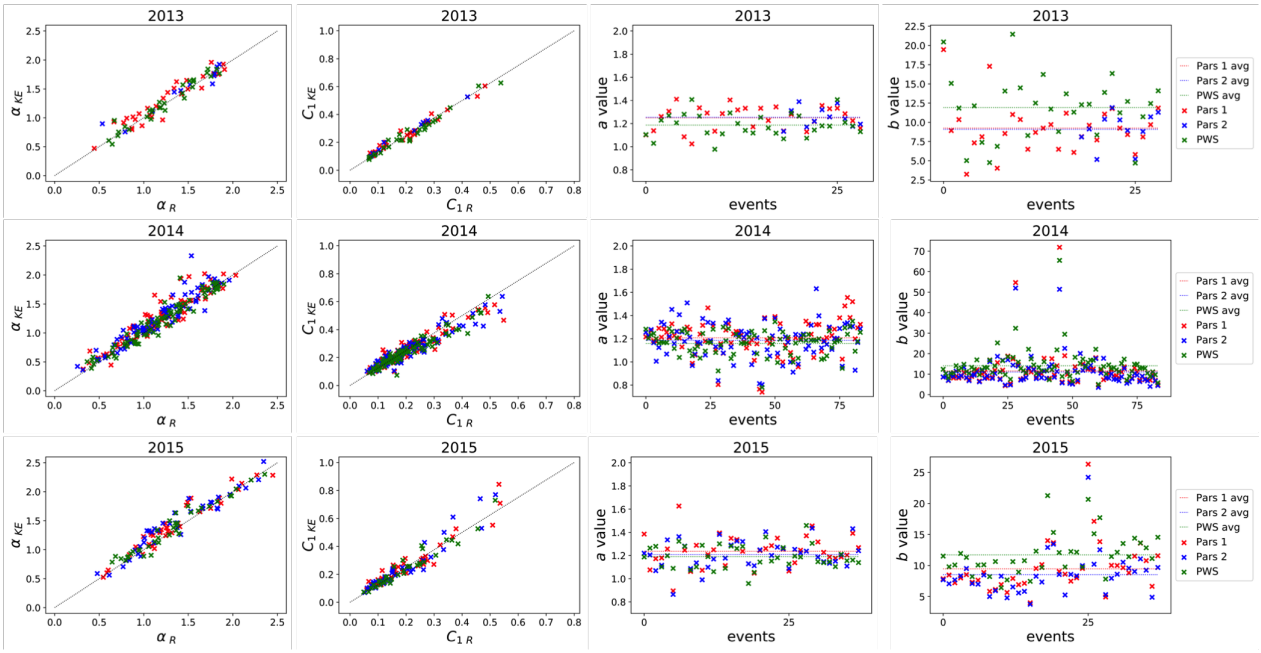

Figure A1: Year wise α and C_1 variation on event based analysis 2013 to 2015.

DSD parameters and power-law coefficients (in section 2.1)

				from DSD moments						from UM	
			# events	μ	N_0	Λ	RMSE$_{DSD}$	a_{DSD}	b_{DSD}	a_{UM}	b_{UM}
					$(m^{-3}mm^{-1-\mu})$	(mm^{-1})	$(m^{-3}mm^{-1})$		$(Jm^{-2}mm^{-a}h^{a-1})$		$(Jm^{-2}mm^{-a}h^{a-1})$
Pars 2	very light	$R<1$	190	2.53	1.36×10^{7}	6.59	19.78	1.196	10.180	1.246	8.097
	light	$1\leq R<2$	160	1.61	1.20×10^{8}	4.70	24.81	1.229	12.630	1.202	9.262
	moderate	$2\leq R<5$	101	0.82	1.66×10^{6}	3.19	20.93	1.260	15.026	1.208	9.911
	heavy	$5\leq R<10$	28	0.26	2.72×10^{4}	2.14	23.85	1.281	17.171	1.247	10.140
	very heavy	$10\leq R<20$	8	-0.38	5.81×10^{2}	1.36	21.20	1.317	19.951	1.098	19.997
	extreme	$R\geq20$	6	-0.94	6.16×10^{2}	1.07	57.99	1.363	15.593	1.180	19.040
PWS	very light	$R<1$	163	2.79	7.82×10^{6}	4.73	10.95	1.187	10.95	1.194	12.070
	light	$1\leq R<2$	176	2.65	2.64×10^{7}	4.15	14.30	1.195	14.30	1.154	12.703
	moderate	$2\leq R<5$	152	1.87	4.73×10^{3}	2.85	14.98	1.216	20.024	1.169	13.136
	heavy	$5\leq R<10$	46	1.16	2.82×10^{3}	1.96	18.90	1.253	24.439	1.193	13.933
	very heavy	$10\leq R<20$	18	0.59	7.07×10^{2}	1.51	19.24	1.266	20.834	1.133	18.983
	extreme	$R\geq20$	6	0.53	4.09×10^{2}	1.28	20.63	1.26	21.031	1.165	18.016

Table A1: Variation of DSD parameters and power law coefficients according to the type of rainfall (R = average of rainy data points)

				from DSD moments						from UM	
			# events	μ	N_0	Λ	**RMSE**$_{DSD}$	a_{DSD}	b_{DSD}	a_{UM}	b_{UM}
					$(m^{-3}mm^{-1-\mu})$	(mm^{-1})	$(m^{-3}mm^{-1})$		$(Jm^{-2}mm^{-a}h^{a-1})$		$(Jm^{-2}mm^{-a}h^{a-1})$
Pars 1	very light	$R < 1$	13	3.82	1.30×10^7	8.19	8.19	1.161	9.471	1.245	8.396
	light	$1 \leq R < 2$	82	2.63	7.76×10^6	6.39	15.96	1.191	10.962	1.271	8.747
	moderate	$2 \leq R < 5$	235	2.04	1.10×10^5	5.32	21.77	1.213	12.528	1.227	9.119
	heavy	$5 \leq R < 10$	134	1.44	2.22×10^7	4.19	24.79	1.235	13.826	1.225	9.369
	very heavy	$10 \leq R < 20$	54	0.51	4.55×10^3	2.67	20.75	1.269	16.214	1.197	11.697
	extreme	$R \geq 20$	38	-0.22	1.77×10^3	1.67	26.84	1.314	26.84	1.147	16.642
Pars 2	very light	$R < 1$	13	4.27	2.02×10^7	8.94	6.75	1.154	9.097	1.217	7.833
	light	$1 \leq R < 2$	82	2.97	2.96×10^6	7.04	15.74	1.183	10.165	1.253	8.245
	moderate	$2 \leq R < 5$	215	1.99	9.38×10^7	5.43	22.15	1.214	11.857	1.212	8.810
	heavy	$5 \leq R < 10$	112	1.17	3.20×10^6	3.94	24.33	1.239	12.969	1.222	9.280
	very heavy	$10 \leq R < 20$	42	0.39	5.92×10^3	2.74	25.49	1.276	15.369	1.196	10.696
	extreme	$R \geq 20$	29	-0.63	1.78×10^3	1.55	35.88	1.343	18.133	1.192	13.445
PWS	very light	$R < 1$	6	3.84	3.39×10^4	6.15	6.78	1.16	13.92	1.223	13.322
	light	$1 \leq R < 2$	61	3.26	5.29×10^4	5.27	10.13	1.175	14.687	1.187	11.997
	moderate	$2 \leq R < 5$	201	2.59	1.91×10^7	4.20	12.56	1.195	17.258	1.176	12.602
	heavy	$5 \leq R < 10$	168	2.32	2.78×10^6	3.50	14.65	1.202	19.013	1.168	12.702
	very heavy	$10 \leq R < 20$	75	1.72	3.31×10^3	2.65	16.90	1.223	20.846	1.155	14.401
	extreme	$R \geq 20$	50	0.67	1.11×10^3	1.69	19.48	1.264	20.879	1.156	15.430

Table A2: Variation of DSD parameters and power law coefficients according to the type of rainfall (R = maximum value of 10 minute moving average)

Appendix A.3. UM plots of dry event as an ensemble for all fields

UM plots of dry events at RW-Turb mast, location 1: all fields at resolution of 15 s (in section 3.1)

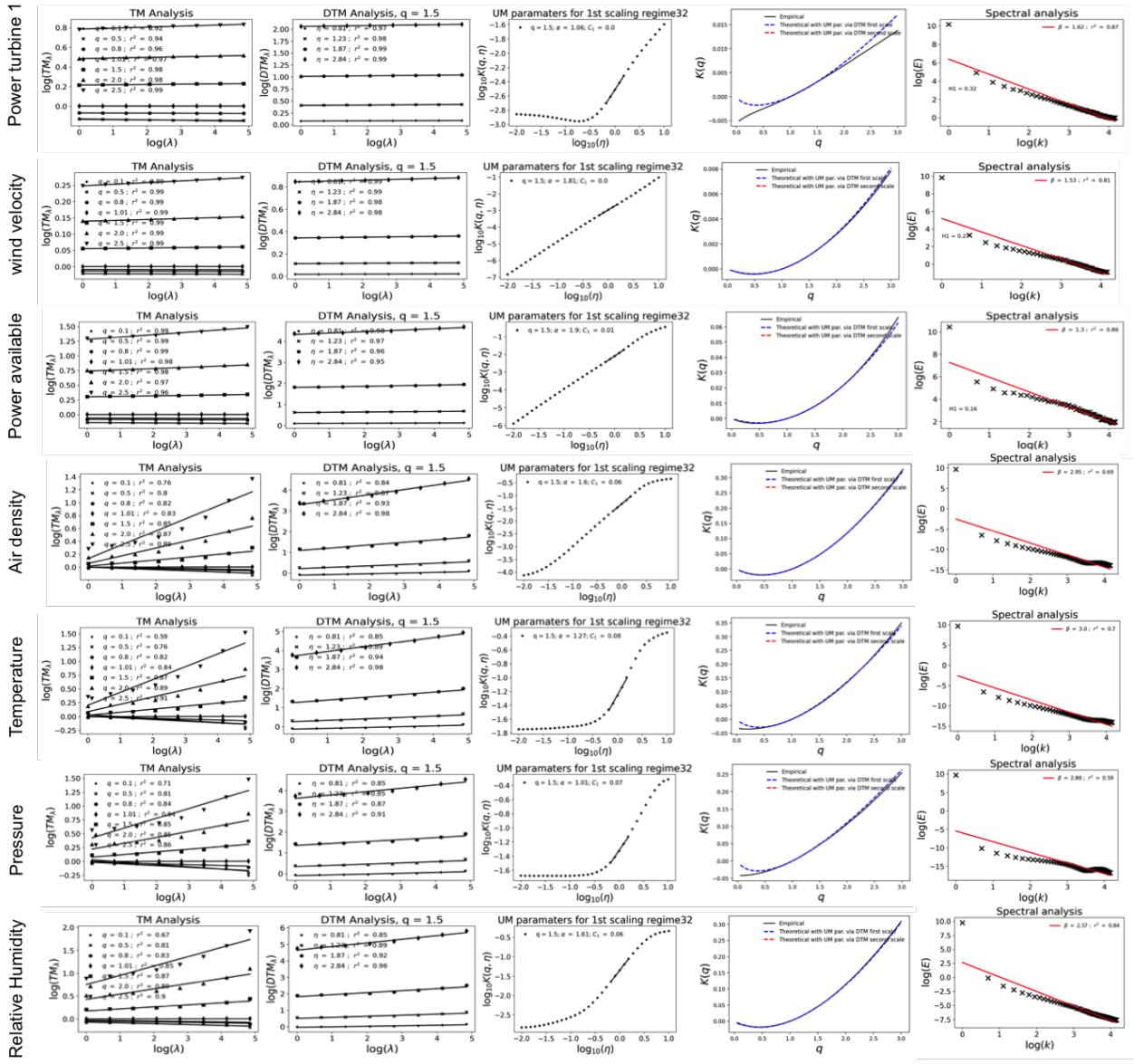

Figure A2: UM plots of rain events from 11 Dec 2020 to 03 June 2021 (6 months) for all fields studied at the lowest instrumental resolution of 15 s (except for Rain rate at 30 s). Ensemble of 213 events at a sample size of 128 (32 min), fluctuations of the field were used for station fields while direct field for rest; spectral plots here are from direct data.

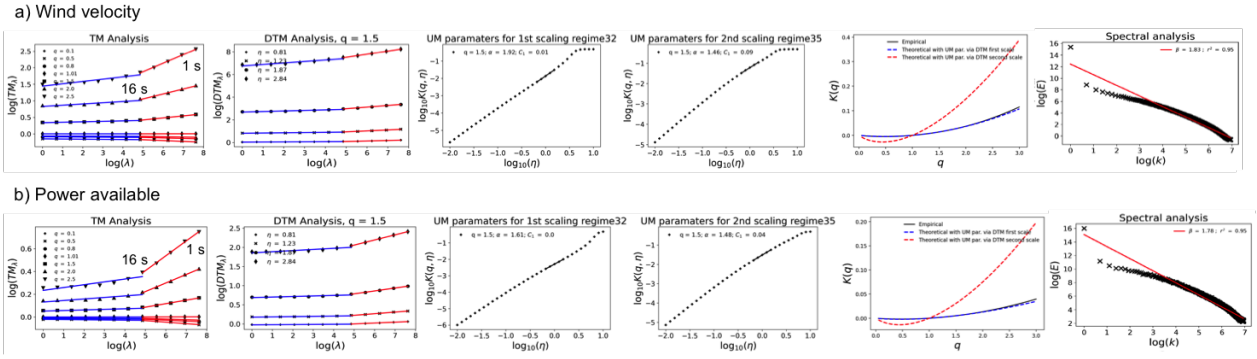

Figure A3: UM plots of dry events from 11 Dec 2020 to 03 June 2021 (6 months) for a) wind velocity and b) power available studied at the lowest instrumental resolution of 1 Hz. Ensemble of 213 events at a sample size of 2048 ($\approx$ 32 min); α was estimated from the slope of DTM curve at $\eta = 0$. FIF of the field was used; spectral plots here are from direct data.

Appendix B.

Appendix B.1. Internship co-supervision during PhD

During PhD research, I co-supervised internship projects of Mateus Seppe Silva and Rodrigo Vieira Casanova Monteiro at HM&Co laboratory. Dr. Auguste Gires was the main supervisor of the projects.

The objective was to compare rain measurements from disdrometers and mini doppler radar (from meteorological station) using multifractal tools. The data from meteorological mast at pays d'Othe wind farm, from RW-Turb project (section 1.1.3) was used for this purpose. Using UM framework, the devices were compared between individual rain events and as an ensemble. The analysis considered the measurement differences between devices at two vertical locations along with the influence D_m and wind has on it. Below is the abstract accepted at EGU General Assembly 2023 (*https://egu23.eu*, session HS7.1) from this work.

EGU23-706 : Multi-scale comparison of rainfall measurement with the help of a disdrometer and a mini vertically pointing Doppler radar

Mateus Seppe Silva[2], Rodrigo Vieira Casanova Monteiro[2], Jerry Jose[1], Auguste Gires[1], Ioulia Tchiguirinskaia[1], Daniel Schertzer[1]

[1]HM&Co, École des Ponts ParisTech, 77455 Champs-sur-Marne, France
[2]Military Institute of Engineering (IME), Rio de Janeiro, Brazil

Local rainfall measurements can be done in a significant range of methods which rely on very different underlying measurement concepts and assumption. As an illustration, mechanical rain gauges collect small rainfall amounts, optical disdrometers assess size and velocity of each drop passing through a sampling area while Doppler sensors derive a rain rate from estimated average fall velocity. Hence, the quality of the measurements can vary a lot, depending on factors such as rain drop drop size, wind velocity, rain rate etc. Understanding the differences between various technologies enables to determine the most reliable device depending on each raining condition. This research aims to compare the performance of two of those devices: the optical disdrometer Parsivel2 (manufactured by OTT) and a mini Doppler radar part of a mini Meteorological Station (manufactured by Thies). The comparison was done with two research focuses: by evaluating the scaling features of the fields measured by both instruments utilizing the framework of Universal Multifractals (UM) to have a performance assessment valid across scales and not only a separated scales, and by analyzing the influence of physical parameters namely drop size, wind velocity and rainfall rate in the performance of the devices.

The data used was collected on a meteorological mast located in the Pays d'Othe wind farm, 110km southeast of Paris. This measurement campaign is part of the RW-Turb project (*https://hmco.enpc.fr/portfolio-archive/rw-turb/*; supported by the French National Research Agency (ANR-19-CE05-0022). The mast is operated with two sets of devices, one around 75m of height and the other around 45m. The observation time steps of the Parsivel2 is of 30 seconds and it measures full binned drop size and velocity distribution, while the mini station provides data (rainfall, 2D wind, temperature, pressure, humidity) with 1 second time step. In general the mini-doppler radar is found to measure smaller amount of rain with regards to the Parsivel2. More precisely, we found that the mini doppler radar returned very low rain measurements when subjected to rain conditions with bigger mean drop size (Dm), and that heavy wind was related to a non-detection of the field in situations with light rain. Scaling analysis enabled to show that mini Doppler radar exhibited white noise from observation scale smaller than 4s. Hence, it was used only with large time steps. UM analysis also revealed different scaling behaviour for mini Doppler radar rain data at finer temporal resolution than that of Parsivel (30 s).

keywords: rainfall; wind; disdrometer; Doppler radar; multifractal; drop size

Session HS7.1 – Precipitation variability from drop scale to catchment scale : measurement, processes and hydrological applications (*https://meetingorganizer.copernicus.org/EGU23/session/45359*)

Publications.

Journal papers:-

- Jose, J., Gires, A., Tchiguirinskaia, I., Roustan, Y., Schertzer, D. (2022). Scale invariant relationship between rainfall kinetic energy and intensity in Paris region: An evaluation using universal multifractal framework. Journal of Hydrology, 609, 127715, *https://doi.org/10.1016/j.jhydrol.2022.127715*

- Gires, A., Jose, J., Tchiguirinskaia, I., and Schertzer, D.: Three months of combined high resolution rainfall and wind data collected on a wind farm, Earth Syst. Sci. Data Discuss., in review, 2022. *https://doi.org/10.5194/essd-2021-463*

Conference presentations:-

- Jose, J., Gires, A., Schertzer, D., Roustan, Y., Ruas, A., and Tchiguirinskaia, I.: Variability in Rainfall and Kinetic Energy across scales of measurement: evaluation using disdrometers in Paris region, EGU 2020, Online, 4–8 May 2020, EGU2020-994, *https://doi.org/10.5194/egusphere-egu2020-994,2019*

- Jose, J., Gires, A., Tchiguirinskaia, I., and Schertzer, D.: Multifractal analysis of extinction coefficient and its consequences in characterizing atmospheric visibility, EGU 2021, online, 19–30 Apr 2021, EGU21-11242, *https://doi.org/10.5194/egusphere-egu21-11242,2021*

- Jose, J., Gires, A., Schertzer, D., Roustan, Y., Ruas, A., and Tchiguirinskaia, I.: Application of universal multifractals framework in estimating a scale invariant power law relation between kinetic energy and intensity of rainfall, *https://nscct20.sciencesconf.org/312009*

- Jose, J., Gires, A., Tchiguirinskaia, I., and Schertzer, D.: Influence of lower threshold on empirical data in estimation of multifractal parameters (using atmospheric extinction coefficient as the field of study), AGU 2021, New Orleans, LA online everywhere, 13–17 Dec 2021, AGU21- 891651, *https://agu.confex.com/agu/fm21/meetingapp.cgi/Paper/891651*

- Jose, J., Gires, A., Schnorenberger, E., Tchiguirinskaia, I., and Schertzer, D.: Combined multifractal analysis of wind power production and atmospheric fields using simultaneous measurement of high-resolution data, EGU 2022, Vienna, Austria, 23–27 May 2022, EGU22-6858, *https://doi.org/10.5194/egusphere-egu22-6858,2022*

Journal papers (from previous works):-

- Varghese, M., Jose, J., Anu, A.S. et al. Cloud and aerosol characteristics during dry and wet days of southwest monsoon over the rain shadow region of Western Ghats, India. Meteorol Atmos Phys 133, 1299–1316 (2021). *https://doi.org/10.1007/s00703-021-00811-3*

- Varghese, M., Jose, J., Anu, A.S., Konwar, M., Murugavel, P., Kalarikkal, N., Deshpande, M. and

Prabha, T.V., 2021. Vertical profile of aerosol characteristics including activation over a rain shadow region in India. Atmospheric Environment, 262, p.118653. *https://doi.org/10.1016/j.atmosenv.2021.118653*

- Mercy Varghese, Neelam Malap, Mahen Konwar, Sudarsan Bera, Jerry Jose, Shivdas P. Bankar, P. Murugavel, and Thara V. Prabha 2023. Impact of monsoon on below cloud base aerosol hygroscopicity over a rain shadow region of India. Atmospheric Research, 285, p.106630. *https://doi.org/10.1016/j.atmosres.2023.106630*